MULTI-LEVEL FILTER BASED ON H SHAPED CHANNELS

by

GUANXIONG WANG

A thesis submitted to
The University of Birmingham
for the degree of
DOCTOR OF PHILOSOPHY

Mechanical Engineering Department
School of Engineering
The University of Birmingham
September 2016

ABSTRACT

Micro and nano filtration is a crucial fundamental process in biological, biomedical and chemical engineering fields. By elimination of irrelevant factors, nanofiltration is able to improve the accuracy, efficiency and reliability of experiments. It is essential for treatments and preparation of high quality specimens, separation and purification of specific components, and control of reaction processes. However, it is difficult to separate complex mixtures such as blood into multi groups in chip level. The nanofilters are under threat of adhesion and clogging. This project aims to establish a multilevel filter for separation and purification complex bio-components mixtures by size in both micro and nano scales; generalize the design methodology of this multi level filter; optimise traditional nanofilter and eventually develop a multi level filter for rapid micro volume sample filtration.

During the study and improvement of traditional filter, a new type of multi level filter for sequential separation based on H shaped channels were put forward in this thesis. The methodology of designing this type multi level filter was built and verified with simulations. A general path for multi level filter chip design was established and demonstrates with examples and experiments. A new fabrication process for multi depths channel on the same surface was put forward during the examples design. The fabrication experiments on photolithography, Inductively Coupled Plasma Reactive Ion Etching (ICP RIE), and Focused Ion Beam (FIB) milling demonstrated the feasibility of this fabrication process and the recipes of these three fabrication processes were given by the experiments. Simulations on both 2D and 3D filters were described and discussed. The angle effect of angular H shaped channels was studied with COMSOL Multiphysics® Modelling Software.

ACKNOWLEDGEMENTS

My heartiest gratitude goes to my supervisors Dr Carl J Anthony and Prof Phil D Prewett who guided my study and research with patience, wisdom and enthusiasms. I would like to appreciate Dr Robert Nordon for his key suggestions on my project during my visit to University of New South Wales. Special thanks go to Prof Graham J Davids and Universitas 21 who gave me a chance to visit Sydney. Thanks for China Scholarship Council funding my PhD study. Special thank for Zahra and Aydin who helped me a lot during my research. Thanks for my friends Chongfeng Wei, Yang Yue, Zongcheng Lin, Kaijie Lin, Gang Liu, Qi Chen, Mofei Guo, Wenlin Xia and Bing Liu, Wenxia Yu, Luya Li who share happiness and sorrow with me during my British time.

Last but not least, I would like to thank my parents. Your love is the power supporting me to explore this beautiful big world. Thanks.

TABLE OF CONTENTS

LIST OF FIGURES

LIST OF TABLES

LIST OF SYMBOLS

a_i	Width of the i^{th} level sieves' channel, assuming its width equals to its depth;
a_j	Diameter of component j;
[B]	Matrix function of inverted binary diffusion coefficients;
c_j	Molar concentration of component j;
$c_{i,j}^{\text{Capture}}$	Capture concentration of component j at the i^{th} level;
$c_{0,j}^{\text{Sample}}$	Inlet sample concentration of component j;
d	Depth of inlet channel;
D_j	Diffusion coefficient for component j;
D_{ij}	Diffusion coefficient component j in the i^{th} level sieve;
D_r	Hydraulic diameter of the microchannel;
F	Faraday constant;
F_b	Body force;
F_D	Dean drag force;
F_L	Inertial lift force;
h_i	The length of the i^{th} level sieve channel
i	Number of sieves' level;
j	Species of components;
J_j	Flux of component j;
J_{diff}	Diffusion flux;
J_{conv}	Convection flux;
l_i	Distance between two levels of sieves;

L	Length of the channel;
n	Number of different species components;
N_i	The minimum number of the i^{th} level sieves in H shaped channel series;
P	Pressure;
Q	Volume flow rate of laminar flow in a straight channel;
R	Gas constant;
R_j	Net mass production rate in chemical reactions;
R_h	Hydrodynamic resistance of the microchannel;
t	Time;
T	Temperature;
$T_{i,j}$	Response time of component j at i^{th} level in a multi-level filter;
v_c	Convective velocity field;
w	Width of the sample inlet entrance
w_i	Distance between two adjacent sieves;
z_j	Valence of component j;
γ	Constant;
$[\Gamma]$	Matrix of thermodynamic factors;
δ_i	Error of capture concentration in level i;
δ_{ij}	Constrictivity, defined as $\frac{a_j}{a_i}$;
ε_t	Porosity, which equals $\frac{a_i^2}{d(a_i+w_{i)}}$;

η	Viscosity;
θ	Angle;
μ	Viscosity of the liquid;
ρ	Density of fluid;
Φ	Electric potential;
ψ	Electric potential due to surface charge;
φ	Electric potential caused by stream;
∇	Gradient operator;
Δ	Difference operator.

CHAPTER 1

INTRODUCTION

1.1 Background

Microminiaturization is undoubtedly one of the most significant achievements of humans in recent decades. The development of nanotechnology provides powerful tools to scientists and engineers. The volume produced of economic[1], safe[2], clean[3], accurate and fast response[4-6] micro and nano devices has already changed peoples' lives. In the area of medical science, bioscience, bio-medical engineering and chemical engineering; nanofiltration is an essential process for treatment and preparation of high quality specimens[7, 8], separation and purification of specific components[9, 10], and control of reaction processes. By elimination of irrelevant factors, nanofiltration is able to improve the accuracy, efficiency and reliability of experiments [4, 11]. Therefore nanofilters are widely used for microdetermination, single molecule detection and precise reaction process control.

The multi-level nanofilter research project described in this thesis is a subproject of a Transdermal Patchlab Blood Analyzer System project which is a collaboration project among University of Birmingham, University of New South Wales (Australia) and Harbin Institute of Technology (China). The transdermal patchlab blood analyzer system project aims at developing a Lab-On-Chip system which is able to detect multi bio-markers with painless blood sample collection. This system is designed for rural area medical care and early diagnoses. It is able to work under low gravity in space as well. Figure 1.1 shows a concept

drawing of the Transdermal Patchlab Blood Analyzer System. It consists of microneedles collecting human blood; multi-level filtration module diluting blood and separating bio-components; bio-marker detection module and pump module. The microneedles fabrication is another PhD project of Miss Zahra Faraji Rad, who is a U21 joint PhD student of University of Birmingham and University of New South Wales.

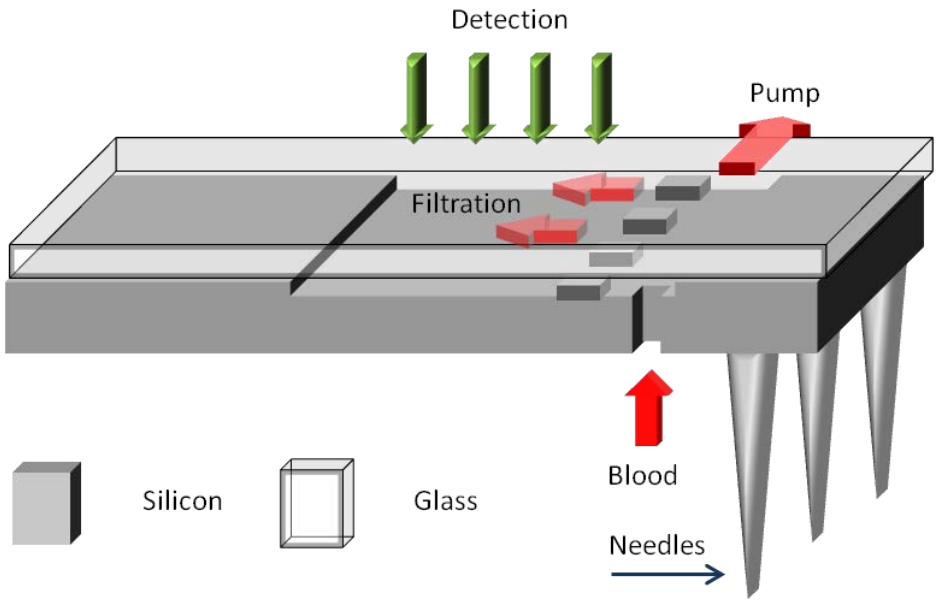

Figure 1.1 Transdermal Patchlab Blood Analyzer System

Consequently a multi-level micro and nano filter for whole human blood separation is demanded for the thransdermal patchlab blood analyzer system. The diameter of blood cells, microvesicles, proteins and other components in blood varies from microns to several nanometres. It is difficult to microminiaturize filters for separation in such a large range of scales down to chip level. Considering the differences of micro and nano fabrication techniques, the varieties of diameters result in a complex fabrication process. Pumping for fine channels needs high pressure while for coarse channels low pressure is enough, thus an appropriate pumping strategy for multi-level filtration is desired. For filtration of complex

fluids such as blood, the clogging and adhesion threat the function of filter[12, 13]. Methodology of multi-level filter design for both the micro and nano components are essential for multi-level filter development.

1.2 Aims and Objectives

The aims of this research project are to establish a multilevel filter for separation and purification complex bio-components mixtures by size in both micro and nano scales; generalize the design methodology of this multi-level filter; optimise traditional nanofilter and eventually develop a multi-level filter for rapid micro volume sample filtration.

Consequently the objectives of this project are set out as below:

1. Review the current development of nanofilters, including but not limited to the transport theory, fabrication techniques, and relevant applications.
2. Analyse and optimise traditional filters to reduce the possibility of clogging and adhesion which block the sieves of filter.
3. Analyse and optimise the traditional filter to seek for a solution of multi-level separation in chip level, where the diameters of target components cover from nanometres to microns.
4. Study the interaction among each level of filter.
5. Generalize the design principles of multi-level filter with mathematical formulas. All physical features of a filter should be able to be described by mathematics.
6. Verify the mathematical formulas by simulations.

7. Generalize the methodology of multi-level filter chip design. Design multi-level chips following the flow process to demonstrate the feasibility of design path.

8. Give a feasible fabrication process of multi-level filter chip.

1.3 Thesis Structure

This thesis contains seven chapters. Chapter 1 introduces the background, aims and objectives of multi-level nanofilter research project. A reading guide for this thesis is set out in this chapter.

Chapter 2 reviews the applications and development progress of micro and nano filtration technology, theory for transport phenomena in nanochannels, guidelines for micro- and nanofluidic chip design and fabrication techniques of lab on a chip micro and nano filter. In the review, answers for the following questions are given: why micro and nano filters are necessary, what kind of micro and nano filter is desired for bio-medical application, and how to design and fabricate a micro and nano filter chip?

Chapter 3 analyses and optimises the model of nanofilter step by step, and then introduces the H shaped channels which is the fundamental basis of the research in thesis. Based on the H shaped channels, a new design of multi-level nanofilter for sequence filtration process is put forward. The theoretical design principles related to this multi-level micro- and nano-filter are discussed in this section.

To improve the capture concentration in the multi-level filter, sieve channel series are applied. Chapter 4 studies the mass transfer process and flow properties of semi-H, H and angular H shaped channels series with finite element software COMSOL. Based on these

analyses, models of multi-level nanofilter is built and simulated. The theoretical design principles are verified with these simulations.

Chapter 5 describes the 3D infinite element modelling of angular H shaped channels series and studies their flow properties. Slip boundary condition is applied with same models for more accurate simulations. Then a 3D model of a three-level nanofilter based on semi-H shaped channels is discussed; the results of simulation demonstrate the feasibility and disadvantage of semi-H shaped channel series.

Chapter 6 illustrates a general chip design path for a multi-level micro- and nano-filter. Two patterned multi-level nanofilter chips are designed as examples following this design flow. A new fabrication process for multi-level nanofilter chip is put forward in these designs. Experiments are made to verify the feasibilities of fabrication process. Reasonable recipes for each step of fabrication process are given by experiments as well. At the end of this chapter, alternative fabrication paths are introduced.

Overall discussions and conclusions are made in Chapter 7. Then the whole thesis is summarized and the future work is introduced briefly.

1.4 Summary

This chapter illustrates the importance of microminiaturization a multi-level nanofilter down to chip level. The aims and objectives of this research project are introduced. An overview of this thesis is given. Although the main motivations of this research are to establish and verify a design methodology for multi-level nano filter separating multi bio-components, develop a multi-level filter and its fabrication process; it also opens up new applications of bio-medical and chemical engineering.

CHAPTER 2

LITERATURE REVIEW

2.1 Introduction

In this chapter, the applications and development progress of micro and nano filtration technology, theory for transport phenomena in nanochannels, and fabrication techniques of lab on a chip micro and nano filter are reviewed. The questions: why micro and nano filters are necessary, what kind of micro and nano filter is desired for bio-medical applications, and how to design and fabricate a micro and nano filter; are answered.

2.2 Review on Traditional Accurate Size Separation Techniques

Accurate size separation and size measurement of various kinds of particles, including polymer beads, ceramics, cells, pharmaceutical emulsions, proteins and DNA molecules, are one of the most important technologies in the fields of analytical and bio-analytical chemistry, biology and bio-medical research, industrial production, and environmental assessment. A lot of studies have developed and demonstrated methods on particle separation, such as field flow fractionation (FFF) [14-18], split flow thin fractionation (SPLITT) [19-21], hydrodynamic chromatograph (HDC) [22-24], capillary hydrodynamic fractionation (CHDF) [25-28], ultracentrifugation [29, 30], and electrokinetic methods [31]. In this section, brief reviews on these methods will be taken.

2.2.1 Field Flow Fractionation (FFF)

Field flow fraction (FFF) was first conceptualized and reported by JC Giddings *et al* in 1976[32]. An external physical field perpendicular with the parabolic flow in a long narrow channel is applied to separate particles into different streams. Thus each group of particles achieves a different velocity based on their position (field direction) in the parabolic flow. These differences of velocity separate the particles into different groups by the end of the channel. (Figure 2.1) The fields or gradients can be flow field (flow FFF), thermal gradients (thermal FFF), centrifugal forces (sedimentation FFF or centrifugal FFF), electrical field (electrical FFF)[14] and magnetic field (magnetic FFF)[33]. Species which range in size from ~10^{-3} to 10^{2}µm can be accurately separated with FFF technology. FFF is a measurement method as well. Currently, various commercial FFF systems are widely used in laboratories for particle analysis. Although FFF is an extremely versatile technique, it has some disadvantages. The first disadvantage is that the separation time is relatively long. The second is that FFF is not a continuous separation method. Thus it is not a powerful tool for particle preparation. Thirdly, FFF requires a complicated outer device for small volume sample injection. What is more, comparing with microfluidics separation devices, a FFF system is comparative complex and expensive.

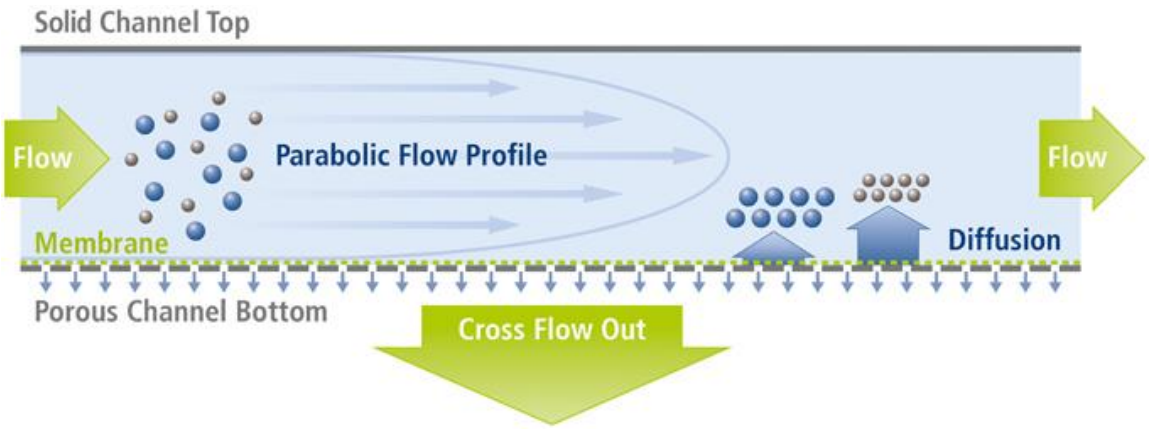

Figure 2.1 Field Flow Fractionation with cross flow field[34]

2.2.2 Split Flow Thin Fractionation (SPLITT)

Split flow thin fractionation is a continuous separation method for micro particles. It was developed based on flow FFF by JC Giddings as well [19]. Figure 2.2 illustrates the principle of SPLITT. There are two inlets, one for sample solution while the other is for a buffer fluid (carrier flow). The carrier stream normally injects with a higher flow rate than the sample inlet. So the sample stream is focused to a narrow band along the inlet splitting plane. Without an external field, all particles go with the sample stream and exit from the outlet opposite the inlet. When an external field (gravity, electric field, or magnetic field) is applied, susceptible particles are pushed towards the outlet splitting plane. Consequently the sample is separated to two groups. Comparing with the FFF method, SPLITT achieves a continuous separation thus it is used for particle preparation rather than measurement. However, SPLITT can only separate micro or submicron particles. Both FFF and SPLITT require external fields and so they become complicated systems. Recently, some studies demonstrated the miniaturization of SPLITT as microfluidics devices, reducing the cost of the SPLITT system and achieving a relatively high flow rate [20, 35].

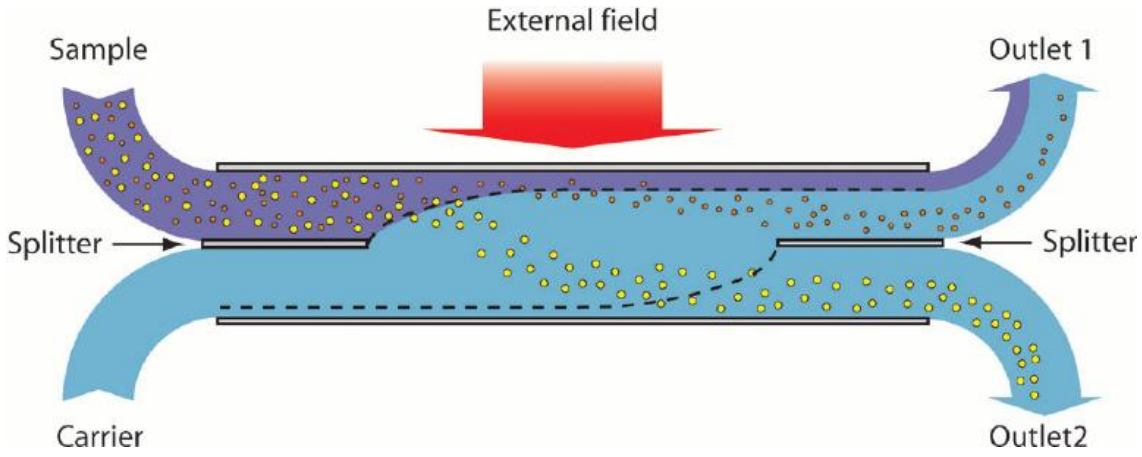

Figure 2.2 Principle of Split Flow Thin Fractionation [36]

2.2.3 Hydrodynamic Chromatograph (HDC)

In 1974, Small showed that colloid particles in an aqueous suspension emerged from packed beds of spherical particles according their size sequence, the largest first while the smallest last [22]. This is because that in a narrow conduit, larger particles (size range from 0.002 to 0.2 of the conduit size [23]) cannot fully access the stream near the conduit walls. Due to the properties of parabolic flow, the flow rate towards the boundary is lower. Thus larger particles achieve a higher velocity than smaller ones. However, the absorption and clogging of colloidal particles in the packing columns limit its application [37]. By using a capillary channel (diameter is 250 μm) rather than a bed packed by solid nonporous particles, capillary hydrodynamic chromatograph (CHDC) was developed [38, 39]. Silebi *et al* pointed out that "the separation mechanism results from the eluant's parabolic velocity profile rather than through the partitioning of the species to be fractionated between two phases, as in typical chromatographic separations, this technique is not a chromatographic separation" [25]. Thus they rephrased capillary hydrodynamic chromatograph (CHDC) as capillary hydrodynamic fractionation (CHDF). Both HDC and CHDF are separation methods without external fields. Although the CHDF increases the separation efficiency comparing with HDC, there are no apparent improvements on resolution. Comparing with the FFF methods, the resolution of HDC and CHDF is their main disadvantage.

2.2.4 Ultracentrifugation

Since Svedberg and his collaborators first introduced the method of centrifugation (1923) [40] and ultracentrifugation (1924) [29], the huge developments of this technique have made ultracentrifugation a common and important tool in analytical chemistry and bioscience, especially Proteomics [30]. There are three areas of ultracentrifugation based on

the transport process and detection methods: sedimentation velocity, sedimentation equilibrium and the approach to sedimentation. Very high resolution of molecular mass can be achieved by analytical ultracentrifuge. Preparative ultracentrifuges are used for pelleting of fine particulate fractions and gradient separation. However, ultracentrifugation is a time consuming process. The high price and complicated systems also limited its applications. For a small volume (nL) sample, the sample needs to first be diluted to a larger volume before ultracentrifugation can take place, which is not necessary for lab-on-chip devices.

2.2.5 Electrophoresis and Electro-osmosis

Electro-osmosis and electrophoresis are two typical electrokinetic separation processes. According to the electrical double layer theory (EDL), if a plane charged surface is in contact with liquid and an electric field is applied parallel to the solid surface, liquid adjacent to the interface moves [31]. This phenomenon is called electro-osmosis. Electrophoresis, in contrast, is the converse process of electroosmosis. It can be viewed as ions movement in fixed liquid. The thickness of the electrical double layer affects the electrophoretic mobility. Schoch made an outstanding review on electrokinetic phenomena in nanofluidics [31]. More details can be referred to that review.

2.2.6 Discussion and Conclusions

In this section, several techniques for particle separation have been reviewed. Each technique has its advantages and disadvantages. In these methods, FFF, HDC, CHDF, ultracentrifugation and electrokinetic method are mainly used for particle or molecule analysis. Except the ultracentrifugation and electrokinetic techniques; FFF, HDC and CHDF are based on the flow rate distribution in parabolic flow. Ultracentrifugation, FFF, electrophoresis and electro-osmosis require external fields such as centrifuge, cross-flow or

electric field. In contrast, external fields are not necessary for HDC and CHDF. Although the separation accuracy is high in these techniques, the time for separation is relatively long. Meanwhile, as these separation methods are not continuous (some preparative ultracentrifuges are continuous with complicated outer injection and collection devices, while most ultracentrifuges are not), they are not used for preparation of particles. The advantages of continuous flow separation were summarised by Pamme as: continuous introduction of sample, continuous readout of separation efficiency, lateral separation of sample components, potential for integration, and Label-free [20].

SPLITT fractionation, however, is a continuous separation technique which requires external physical field as FFF, ultracentrifugation and electrokinetic methods. Thus SPLITT fractionation is mainly used for particle preparation. As the microfluidics chips show significant advantages on their low cost, safety, high efficiency and accuracy; some researchers focused on the microminiaturization of these methods [23, 31]. Even though the miniaturized chips showed enhancements comparing with the traditional machines, the disadvantages of these techniques are still problems. Thus simple label-free continuous flow separation methods for micro and nano components without external fields are demanded. In the next section, micro and nano filters will be reviewed and discussed.

2.3 Review on Micro and Nano Filtration

2.3.1 Classifications of Micro and Nano Filter

Generally, separation by size (mass) and separation by charge are the common ways of classifying micro and nano components separation. Another way of classification is by active and passive separation techniques based on whether external physical fields are applied.

Filtration is a typical separation by size process and in most time is passive. Electrophoresis [41-43] and electroosmosis [44-46] are widely used methods for separation by charge and they are typical active methods. However, the boundaries of these two types of separation are not clear nowadays. A lot of designs of filter take advantages of both of active and passive methods [47, 48].

There are several different classifications of filtration methods; by the filtration process difference, there are two types, filtration with barriers and continuous flow separation. One way to classify the filters with barriers is based on the differences of their structures. There are (1) weir [49-51], (2) pillar [51-53], (3) membrane [54, 55], types of barrier filters. Another way is according to the direction of flow and filter surface, when the flow direction is perpendicular with filter surface it is called dead-end filtration. In contrast, if the flow direction is parallel with the filter, it is classified as cross-flow filter. Filtration with weir and pillar is a typical dead-end filtration process. Membrane can be used for both dead-end and cross-flow filtration. In lots of articles, membrane filter refers in particular to the membrane filter for dead-end filtration [12].

Continuous separation is generally classified into two types, passive and active. Some continuous separation techniques are able to separate mixtures into plural groups by size. Passive structures such as pinched channels (pinched flow fractionation)[20, 56, 57], obstacles array (obstacle induced separation)[58-61], hydrodynamic filtration[20, 62, 63] and spiral channel (inertia flow) [64, 65], are able to separate multi micro components continuously without external physical fields. When external physical fields, such as electric[66], magnetic[67], gravity[16] or sound field[68], are applied; it is the active continuous separation. More details will be discussed in following section for each method.

2.3.2 Filtration with Barriers

2.3.2.1 Weir, pillar and membrane

A weir in a micro- or nano- channel reduces the depth of the channel, thus it can block the flow of large particles (Figure 2.3a). The weir filter is applied for nano volume separation especially for single molecule separation (entropic trapping[31]). Filters with a row of pillars perpendicular with the flow direction reduce the width of flow path (Figure 2.3b). Comparing with the weir filter, the pillars filter is more easily fabricated and it has a longer working time and larger separation volume. Some publications reported filters which combined the weir and pillar, in these reports both the width and depth of flow pathway were declined [51, 69]. Some continuous separation methods (such as obstacles array) took advantages of array of pillars (more than one row) [58, 69, 70], which are distinct from pillars filters. A membrane with arrays of holes to reduce the width of the flow pathway is also used for barrier filtration (Figure 2.3c). A lot of membrane filters are not patterned such

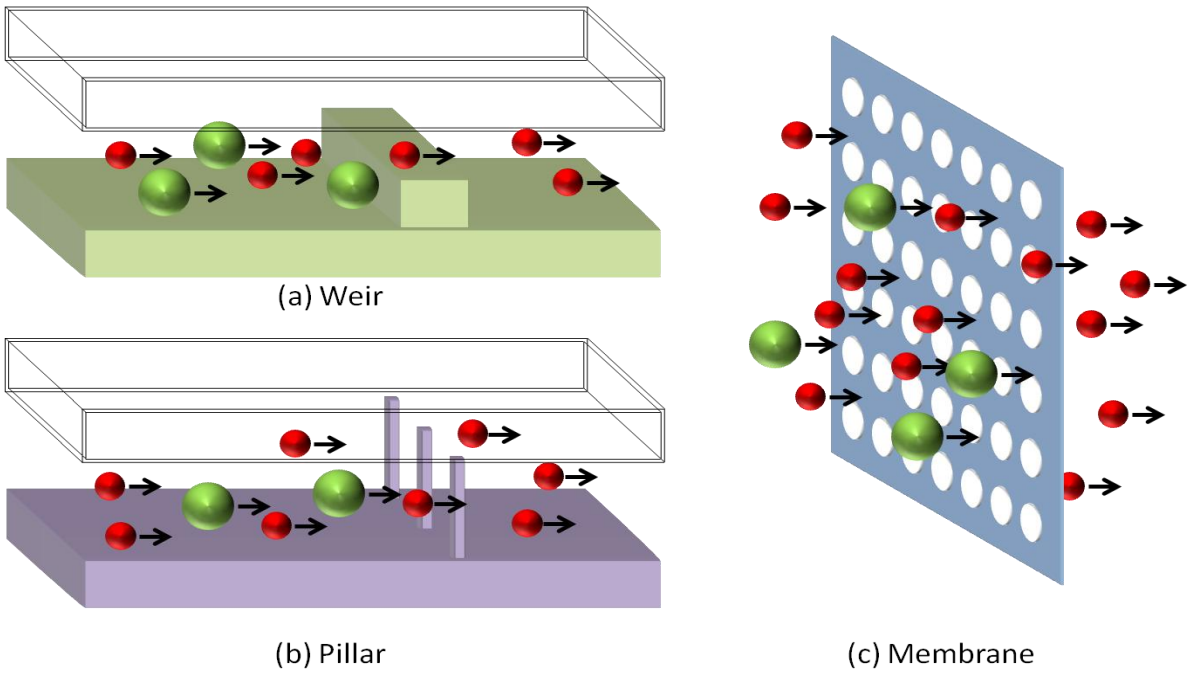

Figure 2.3 Principle of filter with barriers: (a) Weir, (b) Pillar and (c) Membrane.

as gel and some polymer membranes [71] which means the holes are not uniform and the channels are windy. This kind of membrane filter is more easily to be blocked and the filtration efficiency is lower than the well patterned membrane filter. Comparing with the pillars filter, a membrane filter can deal with a larger volume filtration as the overall flow cross-section is considerable higher.

2.3.2.2 Dead-end and cross-flow filtration

As normally the flow directions in weir, pillar and membrane filter are perpendicular with the filters and large particles are blocked by the filters, they are called dead-end filtration [72, 73]. Dead-end filters are easily blocked due to clogging and jamming [12, 51, 55, 73, 74]. A cake layer that consists of large particles will cover the filter during the filtration and will progressively stop the filtration. In addition some deformable particles such as blood cells can squeeze into the small channels, again blocking the filters and making the filtration becomes less effective over time [51]. P. Bacchin *et al* (2002) described the mathematic modelling of deposit formation and compaction of the cake layer[74]. The concentration of solute has an important role during the deposit process. Lower concentration of solute can slow down the deposit formation process and reduce the thickness of the cake layer[75]. External physical fields such as, pulsed electric field, high voltage electrical discharges and ultrasound, are able to improve the performance of dead-end filters [75-78]. However, these external physical fields only slow down the process but are not able to stop the deposition process completely. Cross-flow filtration is a better solution for avoiding the cake layer.

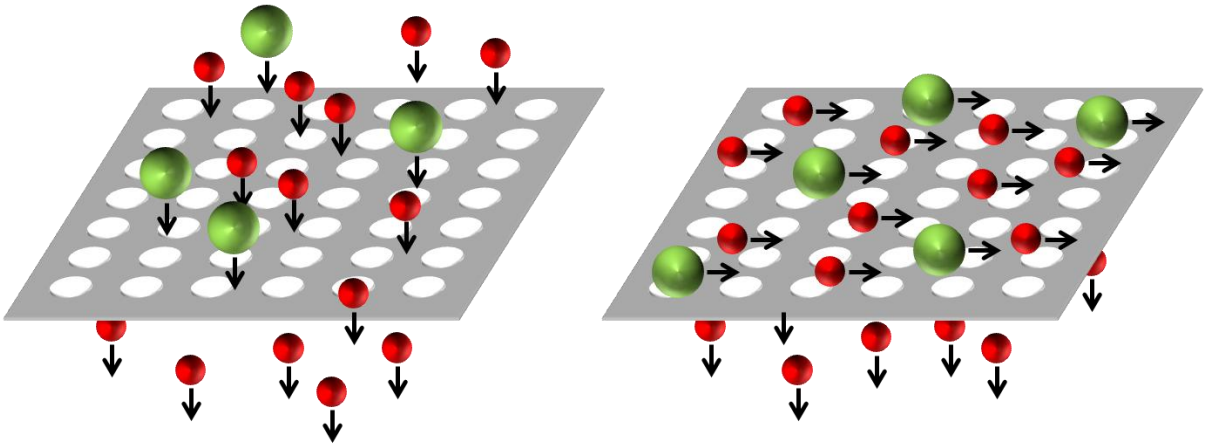

(a) Dead-end filtration (b) Cross-flow filtration

Figure 2.4 Dead-end and cross-flow filtration with membrane.

In a cross-flow filtration the flow direction is parallel with the filter surface, which is shown in Figure 2.4b. Small particles are trapped in the filter due to the mass transfer. As the majority of the feed flow travels tangentially across the surface of the filter, it washes away large components; hence the cross-flow filtration avoids the filter cake layer so that it enhances the useful time and throughput of a filter. However, many reports [79-81] demonstrated that the filter cake layer was gradually but finally formed after a long term of filtration. The reason is that some large components are captured on the surface of filter. Luis Seminario (1997) *et al* studied the pore blocking and permeability reduction in a cross-flow membrane filter and built a mathematic model [82]. For small volume diluted solution separation, the cake layer can be ignored. What's more, because the majority of feed flow is along the surface of the filter, there are very weak forces to push the large components through the holes. Therefore the cross-flow filter is able to achieve high filtration efficiency and long useful time for deformable particles. External physical fields are able to enhance the cross-flow filtration process as well[83, 84]. It should be pointed out that the electric field enhanced filtration is only acceptable when the membrane and all solute particles have

the same sign of ζ-potentials. Surface modification of filters such as, to produce a hydrophobic surface, is an alternative way to improve the cross-flow filtration[85]. Consequently, the cross-flow filter has a better performance than the dead-end filter under similar conditions.

All of these three types of barrier filters (weir, pillar and membrane, dead-end or cross-flow) separate the components in solution into two groups: small group and mixture group. The weir, pillar and membrane filters are suitable for different volume separations. Fine patterned filters show better selectivity. The membrane filters without uniform patterns are not able to separate similar sized particles. Cross-flow filtration improves the useful time and filtration efficiency comparing with the dead-end filtration. When there are multi species of components which need to be separated, barrier filters become less effective tools. The filtration efficiency of middle sized components is low due to the Brownian movement of smaller particles. Thus other treatments such as external physical fields, dilution and concentration are necessary.

2.3.3 Continuous Flow Separation Techniques

2.3.3.1 Pinched Flow Fractionation

Pinched flow fractionation uses two inlets; one is a liquid stream with particles and one is a buffer stream without particles. (Figure 2.5) By controlling the laminar flow rate of each inlet, the particles in the pinched segment move aligned to one side wall. Due to the different force exerted on larger and smaller particles at the outlet of pinched segment, larger particles move towards the middle of the microchannel while smaller particles move towards the side wall of microchannel. Thus the position difference of different sized particles separates the particles perpendicularly with the flow direction. This method was

developed by Seki and Yamada (2004).[56] Pinched flow fractionation is a high throughput, label free, and particle sized based separation method. As the dimension of the pinch segment relates to the size of particles, a significant amount of design work is necessary to arrange for different size particles separation. The outlets which collect the different sized particles are all distributed on the upper half of the microchannel. Therefore limited amounts of outlet groups are possible due to space restrictions.

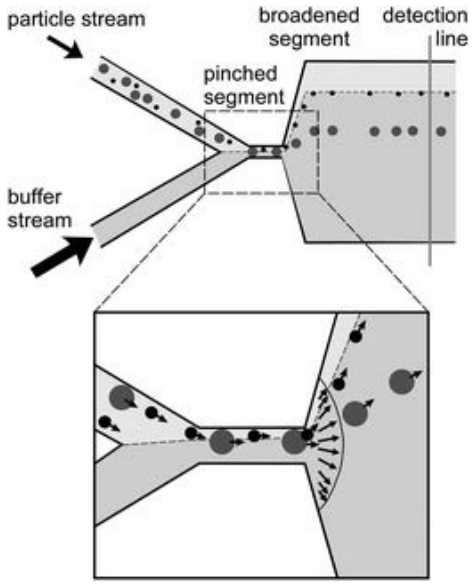

Figure 2.5 Principle of pinched flow fractionation. [20]

2.3.3.2 Obstacles Induced Separation

In obstacles induced separation (also called deterministic lateral displacement), the pillars or posts are not acting as barriers to block components anymore. The distance between adjacent pillars is fixed and slightly bigger than the diameter of the largest component; and each row of pillars is shifted a little to the next. After a few rows, the pillars repeat as the first row. If the diffusion can be neglected, the small particles move with the laminar flow and exit the obstacles array at same position on x direction (Figure 2.6). However, as a comparison, the large components enter the array at centre of a gap between posts; then

the inertia force will push them to the shifted side of next gap. Thus the large components move out of the original laminar stream and exit the obstacles array with the neighbouring stream. The mixture is thus separated into different positions on y direction. The paths of all particles are pre-designed with the geometry of the obstacle array, which results in a narrow outlet stream band. Consequently obstacles induced separation is a very accurate and very fast separation method without any labelling. David W. Inglis *et al* made the relevant theoretical analysis as a guidance for posts arrays design[61]. As the diffusion results in some off-path particles, higher flow rate is demanded for a better resolution. It is necessary to carefully design the arrays for different mixtures separation missions. And the gap between particles size are limited.

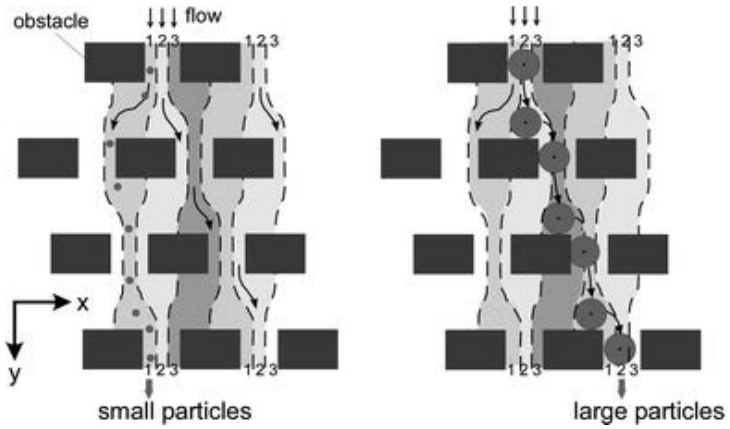

Figure 2.6 The principle of particle separation via lateral displacement around obstacles. Small particles follow the laminar flow streams (shaded in grey) in the y-direction, whereas large particles are continuously forced to change the laminar flow stream and are thus continuously displaced in the x-direction. [20]

As the diffusion coefficient is positively related with molecule mass, there is another way to separate particles by size with obstacles arrays which is called “Brownian ratchet” [86]. A typical application of Brownian ratchet is DNA separation. Different sized molecules are pumped into the array under low flow rate (y direction). Small molecules which have higher diffusion coefficient diffuse faster. Therefore small molecules achieve larger average

movement on x direction while large molecules experience less average movement on x direction during same periods. Comparing with the obstacles induced separation, Brownian ratchet asks for a very slow inlet flow rates (few μm s^{-1}) so that the separation process is slow as well. Because Brownian ratchet separates particles based on probability of diffusion movement, the path of each sized group is not pre-designed. So the band of each sized components is wide.

2.3.3.3 Hydrodynamic Filtration

Hydrodynamic filtration (HDF) was first reported and demonstrated by Masumi Yamada and Minoru Seki in 2005[62]. The principle of hydrodynamic filtration is shown in Figure 2.7. When the diameter of the side channel is small, the majority of the parabolic-flow flows from left to right in main channel and only a small portion flows into the side channels. All particles of solutes cannot enter the side channels; therefore the side channels concentrate and align the micro particles along the side walls of main channel eventually. Then the particles can be selected and collected by size sequence in different sized outlet channels positioned sequentially after the small side channels.

The volume flow rate of laminar flow in a straight channel is described as, Q = ΔP × $(D_r^2 wd/32\mu L) = \Delta P \times (1/R_h)$, where ΔP is the pressure loss between channel ends, L is the length of the channel, μ is the viscosity of the liquid, D_r is the hydraulic diameter of the microchannel, and R_h is the hydrodynamic resistance of the microchannel. Considering the situation at a cross section, only the flow near the side walls can enter the side channel which is the grey section in Figure 2.8. Thus the particles of which their centre is outside of the grey section (the diameter is larger than w_1) cannot flow into the side channel due to the property of laminar flow; even if the diameter of particles is smaller than the entrance of

side channel. Sari Sugaya *et al* studied the situation when the particles were nonspherical and which may rotate [63]. This paper demonstrated that HDF can be used for continuous shaped based separation.

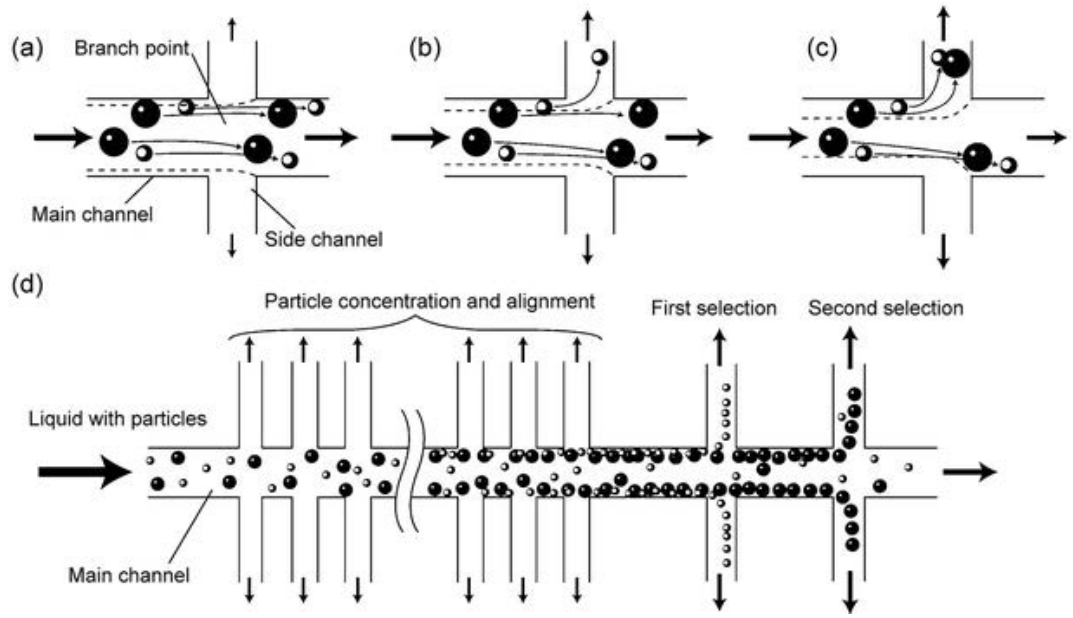

Figure 2.7 The principle of hydrodynamic filtration (a) shallow side channels align particles against the main channel wall. (b) Due to the higher flow rate in larger side channels, small particles are able to enter side channels. (c) Finally, if a relatively large portion of the flow enters the side channels, both small and large particles can enter the side channels. (d) Design of hydrodynamic filtration channel network for enrichment of small and large particles. [62]

Consequently, hydrodynamic filtration is a high throughput (100 000s particles per hour), label free, continuous separation or concentration method for micro and sub-micron particles. In the HDF scheme, the particles are viewed as solid phase and the diffusion of particles in two-phase flow is ignored. However, for nano particles, the diffusion flux of the mass transfer is so significant therefore HDF scheme is not suitable to solve nano particles separation. Although its filtration efficiency cannot be as high as 100%, it needs minimal tuning for different situation so that the devices are easy to operate as compared with the

pinched flow fractionation, pinched flow fractionation and obstacles induced separation methods.

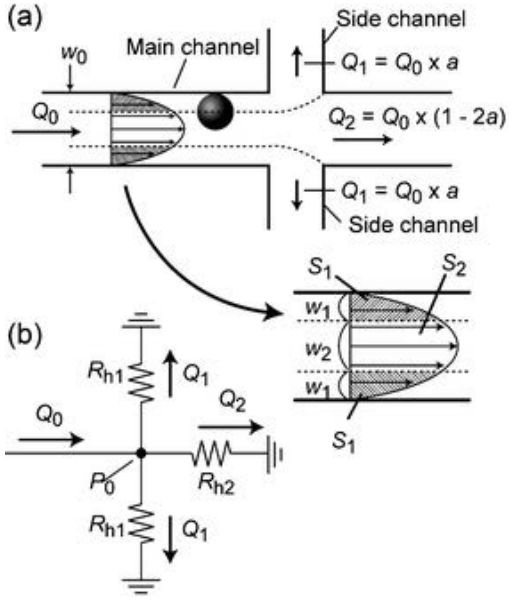

Figure 2.8 Relation between the channel geometry, filtered particle size, and flow rate distribution. (a) Flow rate distribution at a branch point. (b) Diagram of a resistive circuit corresponding to the microchannel structure. [62]

2.3.3.4 Inertia Flow Filtration

Lateral migration due to inertial lift forces was first experimentally shown by Segré and Silberberg[87]. Under the influence of the inertial forces, neutrally buoyant particles flowing in a microchannel migrate to stable equilibrium positions. Di Carlo et al. showed that by employing a curvilinear channel the Dean vortices can be used to reduce the number of equilibrium positions to one[64, 88]. Sathyakumar et al made improvements by adding a cross section at the inlet[65]. Figure 2.9 describes the principle of inertia flow in spiral channels. Where F_L is the inertial lift force and F_D is the Dean drag force. The ratio of F_L and F_D determined the position of different diameter particles.

Inertia flow in a spiral micro channel is able to separate label free micro particles with a high throughput. The separation efficiency is around 90%[65]. Some publications reported applications of inertia flow on cell sorting and alignments[89, 90]. The significant amount of tuning required for different diameter components limits its application. It is also not suitable for nano-particles.

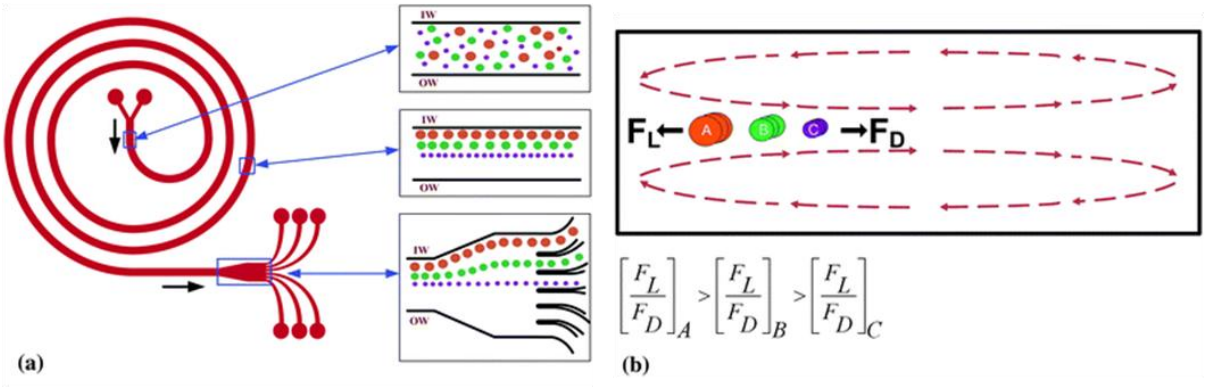

Figure 2.9 The principal of inertia flow filtration (a) Schematic of the spiral microparticle separator. The randomly dispersed particles equilibrate at different equilibrium positions along the inner wall (IW) of the spiral microchannel under the influence of F_L and F_D. Separation between individual particle streams is enhanced by opening the spiral channel into a wider straight channel before extracting the individual streams using a multiple outlet design. (b) Microchannel cross-section illustrating effects of F_L and F_D on particles. The ratio of forces (F_L/F_D) is the determining factor in where a particle of given size (diameter) equilibrates.[65]

2.3.3.5 Active Continuous Flow Separation

There are a lot of reports on blood cells separation with continuous separation techniques [91, 92]. Rapid, high throughput, multi components purifications can be achieved by these methods. However, when the mixtures are complex and contain various diameters components, a large area for filtration is needed but it is still difficult to separate similar

diameter components. For a better filtration, an external field is introduced, which are the active continuous separation methods.

There are various active continuous separation techniques; such as split thin flow fractionation[19], acoustophoresis[93], dielectrophoresis[66], and magnetophoresis[67]; which need an external field applied [36]. These fields can enhance the selectivity; however more complex devices are needed. For a lot of situations, such as electroneutral or antimagnetic particles separation, or space application, external fields do not help. There are also problems when the size order and charge order of components are different in complex mixtures such as whole blood. As the external fields may harm the bio-activity of cells and other bio-components, the active continuous separation is limited for some particular applications. Thus a passive continuous separation method which is label free and without any external physical field has more comprehensive applicability and thus is demanded. In this thesis, filtration without external fields is mainly concerned. For more information about active continuous separation please refer to the references.

2.3.3.6 Discussion and Conclusions

In this section 2.3.3, several continuous separation techniques have been reviewed. It was mentioned in section 2.2.6 that simple label-free continuous separation methods for micro and nano components without external fields are desired. Therefore this thesis mainly concerns the passive continuous separation. The accuracy and efficiency of separation, throughput, particle size area, output band numbers, complexity of the device, and tolerance of the sample composition variation are key issues for continuous flow separation.

The PFF, HDF and obstacles induced separation (except the Brownian ratchet) view particles as solid phase thus the diffusion can be neglected. The separation accuracy of pinched flow fraction (PFF) and obstacles induced separation is very high (can be almost 100%). Meanwhile the inertia flow filtration achieves higher flow rate but lower separation accuracy. The throughput of hydrodynamic filtration (HDF) is the highest in these four techniques, while the separation accuracy is the lowest.

The PFF, HDF and inertia flow filtration are all passive continuous methods for micro and sub-micron components separation with high throughput. In contrast, the obstacles induced separation is able to separate nano-particles such as DNA molecules or micro components.

Although the PFF and inertia flow filtration are able to achieve high separation accuracy, the narrow area for the species band limits the complexity of carrier liquid composition. In other words, only a few amounts of species can be separated with these two methods. By careful design and increasing the number of rows and columns of obstacles, the obstacle induced separation can distinguish more species of components. Similarly, the HDF method is able to collect more species of particles by simply adding different size outlet capillaries. Therefore HDF can deal with very complex mixtures separations (but not complete separation).

Except hydrodynamic filtration, all other methods require numerous tuning (geometry design, injection or collection) to adjust to different separation conditions such as flow rate, carrier liquid composition or instrumental parameters. Thus the HDF method is simple for design and use with the highest tolerance of separation conditions.

Consequently, the comparisons of these techniques are not straightforward. There is no "one size fits all" method. A simple high throughput continuous flow separation method for complex mixture which contains both micro and nano particles is still a blank area.

2.3.4 Development Progress of Micro and Nano Filters

Before the patterned nanofilters can be easily fabricated, gel was widely used as a nanofilter in biological and biomedical research which can be found in various publications. A lot of applications of gel filters have still been reported in last two decades. [4, 94-96] Gel can be easily and economically achieved without expensive nanofabrication equipments. Although some applications take advantage of it absorption[97], the irregular poles and the winding channels limit the application of gel filter. What is more, it is complex to use gels for the fabrication of micro structures which are desired on chips. All these reasons limit the applications of gel filter and push scientists and engineers to chase well patterned nanofilters.

The membrane filter is one option to replace the gel filter. The studies of transport theory in nanopores date back to early in 20th century. Ferry (1936) derived the hindrance factor (partition coefficient Φ) at the nanopore entrance[54], and Pappenheimer *et al*. (1951)[98] and Renkin (1954)[99] derived the other factors representing hydrodynamic hindrance. Deen published an outstanding review paper in 1987 which listed all the relevant experimental and theoretical references in the field up to that time.[100] The review made by Han (2008) presented the progress of membrane research in the 1990s and early 21th century.[101] The recent research was focused on the applications of different material and sized membranes. Various materials, such as Si, polymer, anodic alumina, were used for membranes with different applications especially in the biomedical field.

With the development of nanofabrication technology, well patterned nanochannels are capable to be fabricated fast with low cost [101, 102]. The accurate geometric sizes and low surface roughness of patterned filters offer a more controllable filtration process. Single molecule separation in a nanochannel has been reported by Fu[103], Park[103], Diehl[104] and others.

The other important achievements are the various separation methods which have been introduced in the former section. Lots of gel-free continuous separation devices were developed in the last ten years. Figure 2.10 shows an anisotropic nanosieve array filter designed by Fu as an example of active continuous separation[47].

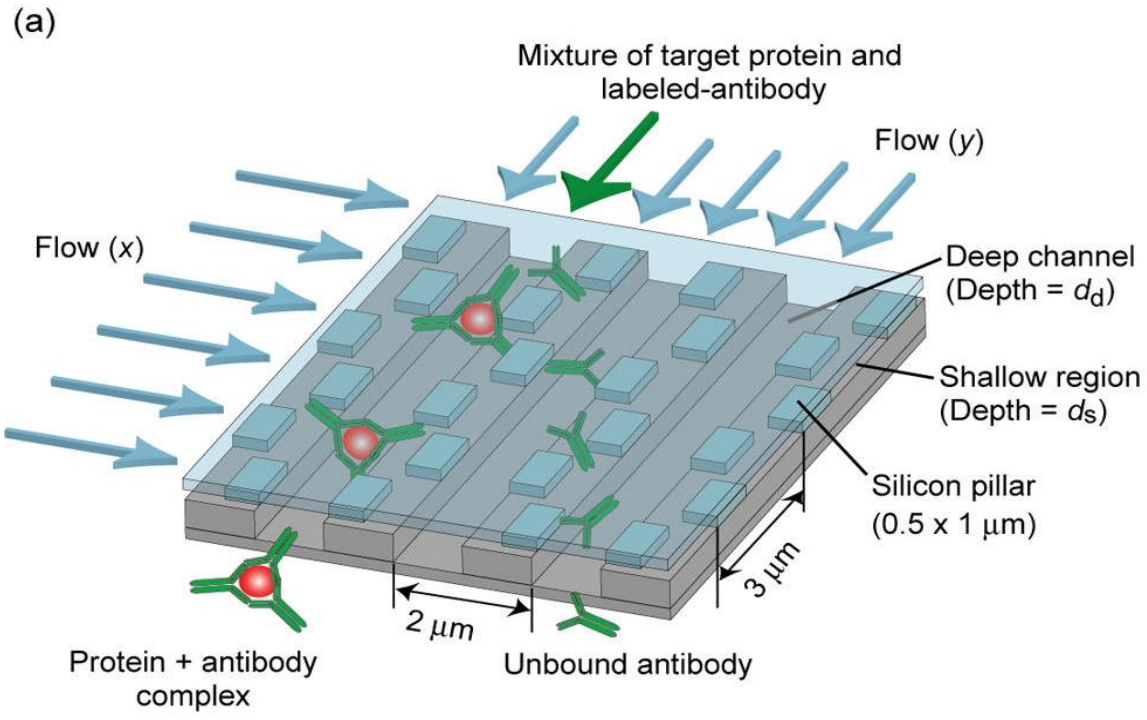

Figure 2.10 Concept of the anisotropic nanofilter array (ANA) [47, 101]

2.3.5 Applications of Micro and Nano Filters

Filtration of micro or nano components is a fundamental operation in biological, biomedical [2] [5]and chemical engineering fields[105]. For clinical diagnoses, many of the detection techniques need to remove the blood cells before detection. There are various filter chips designed for blood cell separation. [106-108] Escosura-Muniz *et al* reported a membrane sensor for cancer bio-marker CA15-3 detection in 2011.[4] Nanofilter applied on other biomarker detections can also be seen in other numerous reports. [1, 109-111] Membrane filtration is also one of the key processes of water purification [10, 105, 112].

Typical pore diameter of commercial membrane filters using in bio-laboratories are 0.1, 0.2, 0.45, 0.65, 0.8, 1, 1.2, 3, 5, 8, 12um. Table 2.1 lists the sizes of human blood cells and other components in blood which gives the concept of what filter to use for bio-components separation.

Table 2.1 Size Table of blood components[113]

Typical Particles	General Size (nm)
White blood cells	7,000~20,000
Red blood cells	2,400~8,000[114]
Platelets	4000[115]
Microvesicles	100~1,000[116]
Hemoglobin	6
Insulin	5
DNA diameter	2
Glucose	1
Sodium	0.102

2.4 Review on Transport Phenomena in nano channels

2.4.1 Electrical Double Layer Theory

The fixed surface charge on the solid-liquid interface causes an opposite charged layer in the liquid to keep electro neutrality. This screening layer is known as the Electrical Double Layer (EDL). Schoch published a review paper on transport phenomena in nanofluidics 2008 where summarized the theory for EDL.[31] The Gouy-Chapman-Stern model is commonly used to describe EDL. (Figure 2.11) (Reprinted figure with permission from Schoch, R.B., J.Y. Han, and P. Renaud, *Transport phenomena in nanofluidics*. Reviews of Modern Physics, 2008. 80(3): p. 839-883. Copyright (2008) by the American Physical Society.) This model contains three layers. The first layer is at the inner Helmholtz plane. The co-ions and counter ions are not hydrated on this layer and are specifically adsorbed to the surface. The second layer consists of a layer of bound, hydrated and partially hydrated counter ions. The third layer is the diffuse layer at the outer most part of the EDL, composed of mobile co-ions and counter ions. Equations for the surface potential, Debye length of EDL, surface change density and surface conductance were introduced clearly in that review paper. The EDL layer is the fundamental effect for understanding the transport process in a nanochannel.

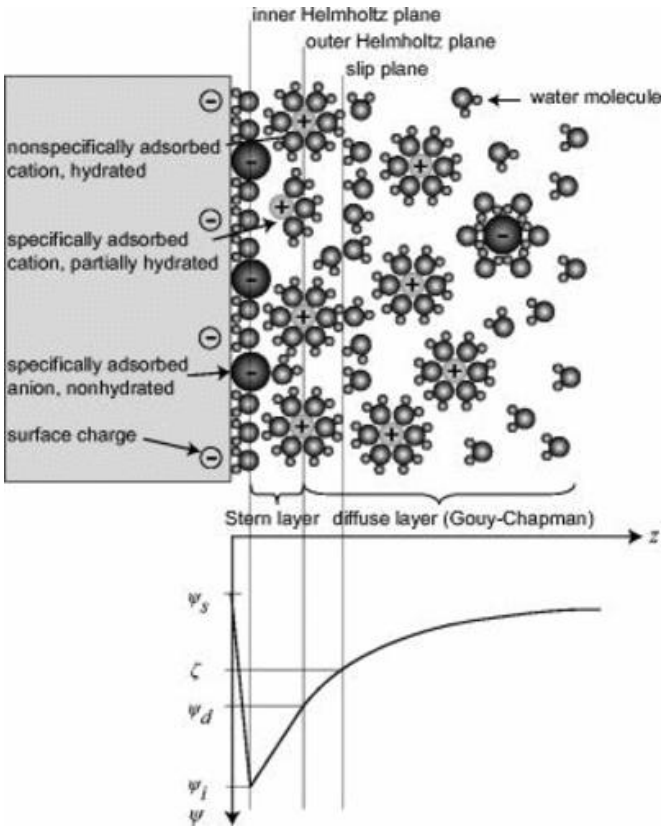

Figure 2.11 Gouy-Chapman-Stern model of the solid-electrolyte interface, with the corresponding potential distribution ψ vs the distance z from the wall. The solid is illustrated with a negative surface potential ψ_s, described by three layers in solution. The inner Helmholtz plane layer (ψ_i) consists of nonhydrated co-ions and counterions, whereas the outer Helmholtz plane layer (ψ_d) is built up of only hydrated counterions. The diffuse layer is defined beyond the outer Helmholtz plane. At the slip plane, the ζ potential can be experimentally investigated, and as the distance between the outer Helmholtz plane and the slip plane is negligible in most cases, the ζ potential is usually equal to ψ_d. [31]
http://dx.doi.org/10.1103/RevModPhys.80.839

2.4.2 Mass Transfer in nanochannels

The mass transfer process consists of diffusion and convection. Fick's laws illustrate the diffusion progress. The First Fick's Law is,[117]

$$J_{diff} = -D\nabla c \qquad \text{Equation 2.1}$$

And the Second Fick's Law is,

$$\frac{dc}{dt} = -D\nabla^2 c \qquad \text{Equation 2.2}$$

The convection flux is,

$$J_{conv} = \pm v_c c \qquad \text{Equation 2.3}$$

Considering the EDL theory, there is a flux generated by electric potential which is:

$$J_{\Phi} = -\frac{z_j F}{RT} D_j \cdot c_j \nabla \Phi \qquad \text{Equation 2.4}$$

Consequently, the transport progress of component j is able to be described by the extended Nernst-Planck equation [31]

$$J_j = -D_j \nabla c_j \pm v_c c_j - \frac{z_j F}{RT} D_j \cdot c_j \nabla \Phi \qquad \text{Equation 2.5}$$

Where J_j is the flux of component j,

∇ represents gradient,

c_j is the molar concentration of component j,

v_c is convective velocity field,

z_j is the valence of component j,

F is the Faraday constant,

R is the gas constant,

T is the temperature,

Φ is the electric potential,

D_j is the diffusion coefficient for component j.

The continuity equation of mass transfer is:

$$\frac{\partial c_j}{\partial t} + \nabla \cdot \left(-D_j \nabla c_j\right) + u \cdot \nabla c_j = R_j \qquad \text{Equation 2.6}$$

Where u is the velocity vector;

R_j is the net mass production rate in chemical reactions and $\sum_j R_j = 0$.

2.4.3 Diffusion Coefficient for Multicomponent Mass Transfer

For a mixture of components in a porous medium the diffusion coefficient D_{ij} for the component j in the i^{th} level sieve should be used instead of D_j, which is defined as:[118, 119]

$$D_{ij} = \frac{\varepsilon_t \delta_{ij}}{\tau} D_j = \frac{a_i a_j}{d(a_i + w_i)} D_j \qquad \text{Equation 2.7}$$

Where a_j is the diameter of component j;

a_i is the width of the i level sieves' channel, assuming its width equals to its depth;

d is the depth of inlet channel;

w_i is the distance between two adjacent sieves;

ε_t is the porosity, which equals $\frac{a_i^2}{d(a_i + w_{i)}}$;

δ_{ij} is the constrictivity, defined as $\frac{a_j}{a_i}$

τ is the tortuosity.

With the tortuosity equal to 1 in this case, we have,

$$D_{ij} < D_j \qquad \text{Equation 2.8}$$

This means that components are less likely to do Brownian movement in a narrow space. Thus we can answer why it is time consuming to filter small particles. It is not only due to the low flow rate in finer channels, but also the lower diffusion coefficient.

When similar diameter components are mixed together, the interactions among similar components result in a multicomponent Fick diffusion coefficient of liquid mixtures. This diffusion coefficient can be estimated by the formula $[\mathbf{D}_{ij}] = [\mathbf{B}]^{-1}[\mathbf{\Gamma}]$, where $[\mathbf{B}]$ is the matrix function of inverted binary diffusion coefficients, $[\mathbf{\Gamma}]$ is the matrix of thermodynamic factors. [117](Taylor, R. and R. Krishna, *Multicomponent mass transfer*, section 4.2.2)

2.4.4 Continuity and Navier-Stokes Equations

For incompressible Newtonian fluids and assuming constant viscosity, the continuity equation and the Navier-Stokes equation describe the laminar flow in channels, which are: [31, 120]

$$\nabla v_c = 0 \qquad \text{Equation 2.9}$$

$$\eta \nabla^2 v_c - \nabla P - F_b \sum_{j=1}^{n} z_j c_j \nabla \psi - F_b \sum_{j=1}^{n} z_j c_j \nabla \varphi = \rho \frac{\partial v_c}{\partial t} \qquad \text{Equation 2.10}$$

Where P is the external pressure,

η is the viscosity,

F_b is the body force,

n is the number of different species components,

ψ is the electric potential due to surface charge,

φ is the electric potential caused by stream,

ρ is the density of fluid,

t is the time,

other terms are as introduced previously.

Equation 2.9 is the continuity equation. Momentum conservation equation 2.10 describes the viscous force results from convective movement of fluid, and three other forces working on any volume elements of the flow. The first term is the viscous force. The second term shows a mechanical force due to the pressure gradient. The third term illustrates body forces caused by the polarization of EDL, and the forth part relates to another body force due to the streaming potential. For a steady flow, the viscous force balances all the other three forces. If the components are electro neutral, Equation 2.9 can be simplified as

$$-\nabla p + \eta \nabla^2 v_c = 0 \qquad \text{Equation 2.11}$$

2.4.5 Casson fluid

For non-Newtonian fluids such as Casson fluid, however, the Navier-Stokes equation is not able to describe the flow properties accurately. Casson fluid was defined as a shear thinning liquid which is assumed to have an infinite viscosity at zero rate of shear, a yield stress below which no flow occurs and a zero viscosity at an infinite rate of shear. Blood is viewed as one of the typical Casson fluids[121]. Casson 's constitutive equation is shown below:

$$\sqrt{\tau} = \sqrt{\tau_y} + \sqrt{-\mu_x \frac{du}{dr}}\ ,\quad if\ \tau \geq \tau_y \qquad \text{Equation 2.12}$$

$$\frac{du}{dr} = 0, \qquad if\ \tau \leq \tau_y \qquad \text{Equation 2.13}$$

Where τ is the shear stress; τ_y is the yield stress; μ_x donates the Casson viscosity; u is the axial velocity; and r is the distance towards axes of tube. The boundary condition is:

$$u = 0, \qquad \text{when } r = R \qquad \text{Equation 2.14}$$

where R is the radius of tube. In this thesis, the Newtonian fluid is mainly concerned at a start point of multi-level nanofilter. As the blood is too complex for a design verifying, the aqueous dextran solution is selected as a test solution which is Newtonian fluid [122].

2.5 Review on Fabrication Techniques Used in This Thesis

The fabrication techniques used in this thesis are photolithography, ICP Reactive Ion Etching, and Focused Ion Beam machining.

2.5.1 Photolithography

Photolithography is a process which transfers the 2D geometric patterns from a mask to 3D light sensitive chemical photoresist modules[123]. It is easy to fabricate micro structures with photolithography.[124, 125] The whole process is: pre-treatments, photoresist coating, soft bake, exposure, hard bake (post-exposure bake), develop and clean. During the soft bake, the solvent that the photoresist is dissolved in evaporates and the photoresist loses its liquidity and adheres with substrate the wafer. [126]

Photochemical reaction takes place in photoresist during the exposure to UV light. For positive photoresist, such as MICROPOSIT S1800 SERIES photoresist [127], the exposure area is soluble in developer. For negative photoresist, such as SU-8 [128], cross-link structures forms during the photochemical reaction and post exposure. These cross-link structures are not soluble in developer. The hard bake improves the adhesion force between photoresist and the substrate, and reduces the standing wave phenomena caused by the destructive and constructive interference patterns of the incident light. After development, the modules of photoresist are fabricated.

2.5.2 Inductively Coupled Plasma Reactive Ion Etching

Inductively coupled plasma reactive ion etching is widely applied in industry for fabrication of MEMS systems. Figure 2.12 illustrates the main structure of the ICP RIE system. The

inductively coupled plasma has high density ion fluxes for anisotropic dry etching under low pressure.[129] A RF source is applied on a coil wrapped around the RIE plasma discharge region, to generate inductively coupled plasma. As the density of the plasma and the momentum imparted to the ions can be controlled separately, high aspect ratio structures are achievable by ICP RIE.

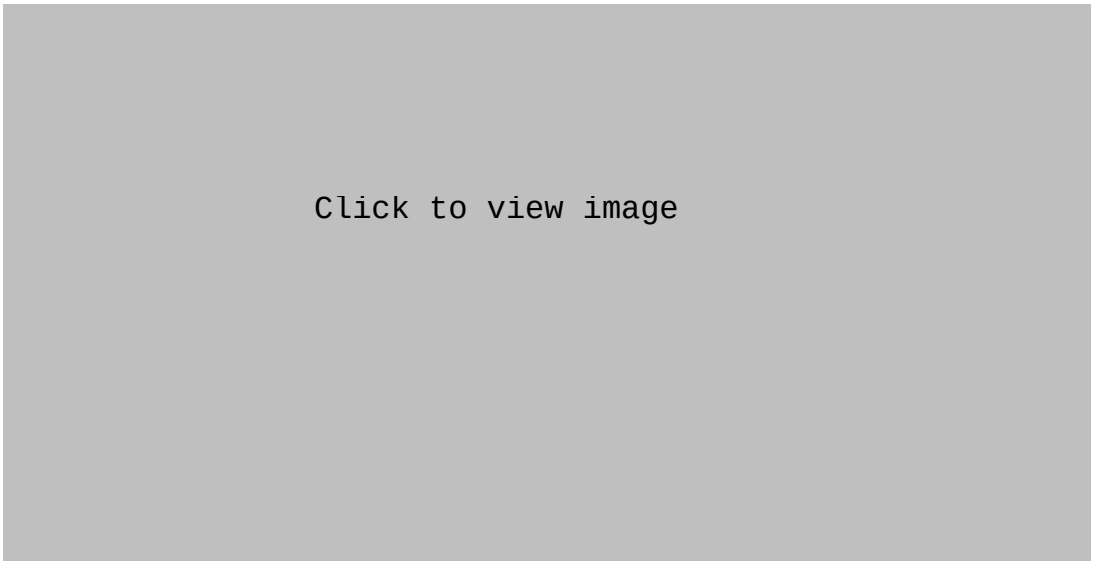

Figure 2.12 Schematic figure of STS ICP system (www.stsystems.com)

The reactive ion etching proceeds with chemistries which are classified as etching gas and passivate gas. Etching chemistries are normally sulfur-hexafluoride (SF_6) or the combination of tetrafluoromethane (CF_4) mixed with oxygen (O_2). For SF_6, the ICP controls the density of F ions in the plasma while the electrode power of capacitive coupled plasmas (CCP) (Forward Power) controls the momentum applied. In this situation, there are three basic etching mechanisms for silicon: firstly F ions reach attach and chemically combine with the Si to form a volatile SiF_4, and then are pumped away (chemical etching); secondly F ions impinge on the substrate and hit Si ions away (mechanical etching), and thirdly F ions impinge on the substrate, chemically bind with the Si (ion assisted etching).[130, 131] In the

passivate cycle, octafluorocyclobutane (C_4F_8) forms a passivation layer on the surface of substrate and protects the side walls during the etch periods. [85] As the photoresist has a high etch resistance, there is a high etch selectivity.

2.5.3 Focused Ion Beam

The Focused Ion Beam was developed in late of 1970s as a microscope[132]. Currently FIB is wildly used in semiconductor research, processing environments, failure analysis TEM treatments and chip-design centres. As the FIB system enables localized milling and deposition of conductors and insulators in nanoscale, it shows advantages at device modification[133], mask repair[134], process control[135] and failure analysis[136].

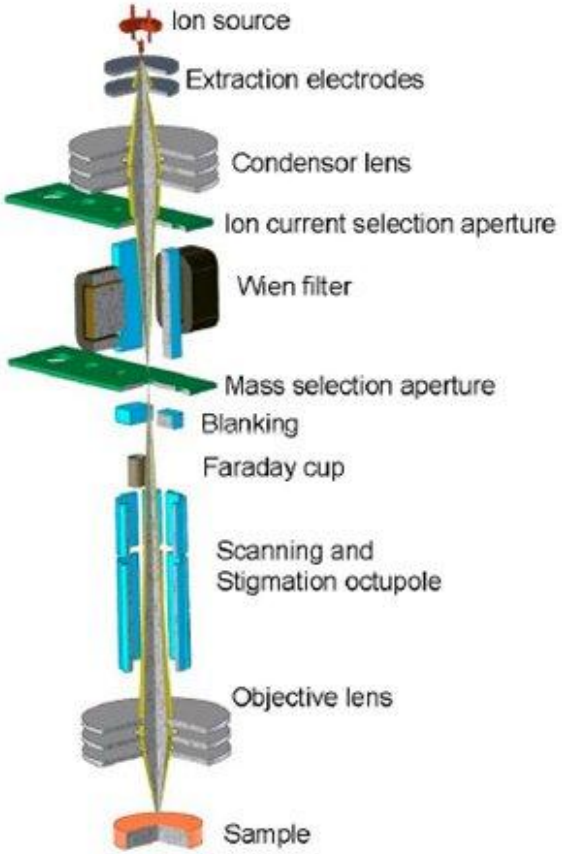

Figure 2.13 Schematic diagram of Focused Ion Beam ion column
(http://www.wikiwand.com/en/Focused_ion_beam)

Figure 2.13 shows the focused ion beam system. It consists of the liquid metal ion source[137], and focusing lens columns with mass separation capability[138] etc. There are various ion species for the liquid metal ion source; such as Ga, Au, Si, Be, B, As, P, etc. [139] [140, 141]. When the ion incidents on a solid surface; the sputtering of ions, emitting of electrons and chemical reactions all occur. Some atoms move away from their equilibrium positions, and ions implant into the solid, altering solid properties. The sputtering and implantation are widely used in semiconductor device fabrication [142-144] and in other fields[145]. FIB is able to induce deposition with chemical vapour assistance. [142] It is convenient and flexible to milling various sized nanochannels with FIB systems [146-148].

2.6 Summary

In this chapter, several traditional accurate size separation methods were reviewed and discussed. Due to the demand of continuous flow separation without external physical field and the development of microfluidics, numerous micro and nano devices were investigated and reported in the last two decades. The classifications of these separation methods were illustrated. References relating to each type of filter were given. The filters with barriers which are weir, pillar or membrane were discussed. According to the direction of inflow and outflow, there are two kinds of filtration process with barriers, dead-end and cross-flow. The clogging issues related were reviewed. The cross-flow filtration can reduce the cake layer significantly. For similar reason, the continuous flow separation methods avoid the severe problem caused by clogging. The filter with barriers can separate mixture into two groups: small group and the mixture.

Then continuous separation technologies were introduced, some of which can separate mixtures into plural bands. These methods exhibit advantages of high throughput, low blocking possibilities, and accurate label-free multi targets separation. What's more, with these methods, the continuous introduction of sample, continuous readout of separation efficiency, and lateral separation of sample components were realized and showed great potential for integration. However most of the structures of continuous separation devices are complex and need to be designed and tuned carefully to adjust to different separation conditions; and there are still problems to separate complex mixtures containing both micro and nano particles, such as human blood. Due to the wide range of component diameters, various and complex properties of particles; continuous separation devices are difficult to be designed. The properties of particles limited the application of external physical field. The complicated outer devices on the other hand increase the cost thus reducing the demand of active continuous flow separation. The reviews on transport theory offered mathematic tools to analyse transport process in nanofilters, which is essential for the multi-level filter design. The brief review on photolithography, ICP RIE and FIB is a basis fundamental for fabrication process design.

CHAPTER 3

H SHAPED CHANNELS AND A NEW DESIGN OF A MULTI-LEVEL FILTER

3.1 Introduction

This chapter builds analyses and optimises the model of a nanofilter aiming at a new design of multi-level nanofilter for sequence filtration process. The theoretical design principles related to this multi-level micro- and nano-filter are discussed.

The study in this chapter starts from an analysis of transport phenomena in dumbbell shaped channels (Figure 3.1b&c), which is the basis of traditional filtration by size. The dumbbell shape channel can be viewed as a unit of a pillar or membrane filter, or two symmetric weirs (dead-end filter). Then the dumbbell shaped channels were improved to semi-H (cross-flow filter) and H shaped channels (Figure 3.1d&e). After studying the static and dynamic properties of H shaped channels (Figure 3.1f), an angular is introduced to the H shaped channels. The effects of angle were analysed and confirmed with COMSOL Multiphysics® finite element software. Based on these results, theoretical design principles of this type of multi-level micro- and nano-filters are discussed. Then a new model of a multilevel filter is built with these principles.

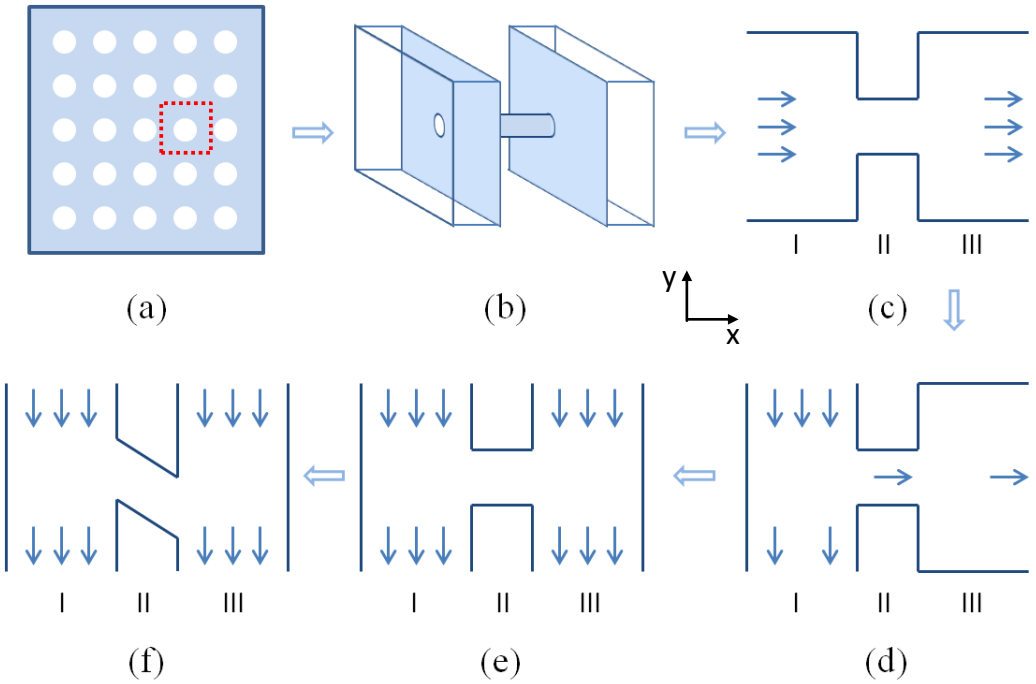

Figure 3.1 From the dumbbell channel to the angular H shaped channels (a), (b) and (c) Dumbbell model; (d) Semi-H shaped channels; (e) H shaped channels; (f) Angular H shaped channels

3.2 Transport Phenomena in Dumbbell and Semi-H Shaped Channels

Traditionally a filter is something porous which is able to separate mixture components by size. Ideally it can be viewed as a union of uniform pores. Each pore is combined with two volumes beside it as a dumbbell shape, which is the basis of H shaped channels that are discussed in this chapter. (Figure 3.1a, b&c) Here these three channels from left to right were named as: sample inlet channel (I), sieve channel (II) and capture channel (III) respectively. The study of dumbbell and H shaped channels is helpful to understand the filtration process.

In the following study it is assumed that there are i $(i = 1,2, \dots, n)$ levels of filter and j $(j = 1,2, \dots, n)$ levels of components in the mixture. However, additionally before building the model of dumbbell channels, certain other assumptions must be made. These are, that

all particles in the mixture are spheres, the diameter of the biggest particles are smaller than the distance between adjacent pores' centre which is w_i, and the smallest particles are smaller than the diameter of the pore a_i (otherwise it cannot be simplified to a dumbbell model). All entrances of channel I, II and III are square. As not all mixture components are able to separate by charge and sometimes electric fields mix different sized particles together by their electric properties, it is assumed in this chapter that the components studied are electro neutral.

Then the particles were separated into two groups; a big group for which the diameters are bigger than the pore size and a small group in which the diameters are smaller than the pore size. It was also assumed that during the filtration process the big group is blocked, while the small group can pass through the pore or sieve channel II. For both groups, their transport progress of component j is able to be described by the extended Nernst-Planck equation (Equation 2.5), when the particles are electro natural ($z_j = 0$), the equation can be simplified as follows:

$$J_j = -D_j \nabla c_j \pm v_c c_j \qquad \text{Equation 3.1}$$

For the big group, the diffusion coefficient in the sieve channel (II) must be 0. That is,

$$D_{\text{big}} = 0 \qquad \text{Equation 3.2}$$

Thus the big group particles are blocked by sieve channel (II), and their movements are limited to the sample inlet channel (I). Navier-Stokes equations are used to illustrate the steady laminar flow in channels, and with a no slip boundary condition applied are

$$\nabla v_c = 0 \qquad \text{Equation 2.9}$$

$$\eta \nabla^2 v_c - \nabla p = 0 \qquad \text{Equation 3.3}$$

COMSOL Multiphysics® Modelling Software is a finite element simulation software. The Laminar Flow module and Transport of Dilute Species module were used to assist the analysis in all simulation results in this thesis. The Navier-Stokes equation is used in the laminar flow module.

3.2.1 Static Properties of Dumbbell Channels

In this model, the pressure difference between inlet and outlet was 100 Pa; the density of liquid was 1050 kg/m^3; the dynamic viscosity was 0.03 Pa·s; the diffusion coefficient was 3.28e-10 m^2/s; the inlet and outlet channels (I and III) was 1x1.5 μm^2; and the sieve channel (II) was 0.5x0.5 μm^2. The free triangular mesh was drawn by COMSOL Multiphysics®, of which the maximum element size was 20nm while the minimum size was 3 nm. No-slip boundary condition was used in this simulation.

The typical velocity and its streamline graphs of Newtonian liquid flow through a dumbbell channel are exhibited in Figure 3.2, which represents the small group transport as well. The concentration after filtration reaches the same value as the inlet. The flux and flow rate through the sieve channel of the big group are zero, while the concentration is raised in channel I. A problem, however, is produced due to the big group concentration magnitude. The high concentration of big particles on the interface between channel I and II may block the entrance of channel II, which means the transport of the small group may be stopped by the filtration process naturally. To avoid this potential blocking, the direction of the fluid inlet and outlet of channel I were changed to the y-axis orientation. As a result semi-H shaped channels were achieved which is the basis of cross flow filtration (Figure 3.1d), these will be discussed in the next section.

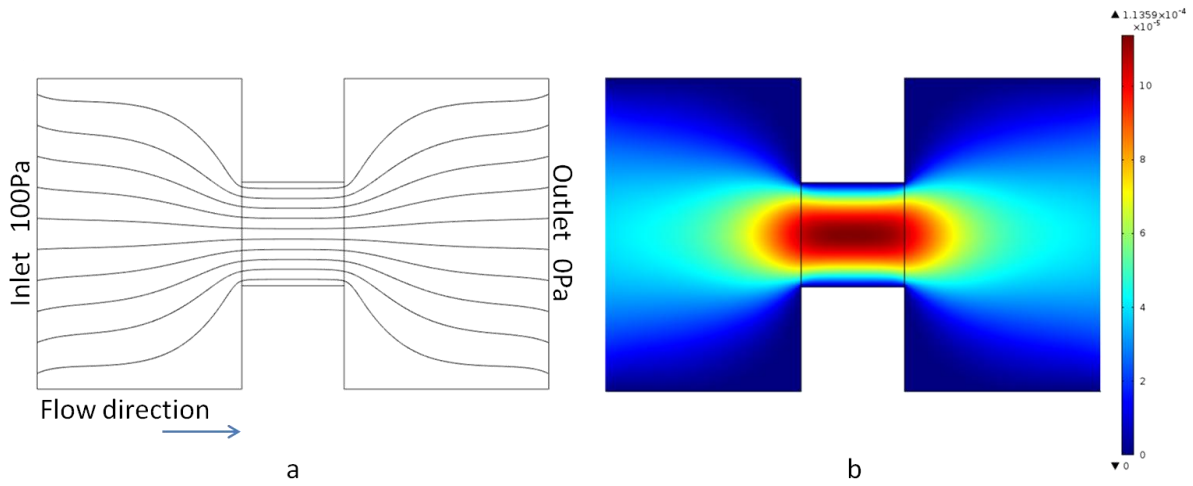

Figure 3.2 Dumbbell channels (a) velocity streamline; (b) velocity magnitude.

3.2.2 Transport Properties of Semi-H Shaped Channels

In this model, the pressure difference between inlet and outlet was 100 Pa; the density of liquid was 1050 kg/m^3; the dynamic viscosity was 0.03 Pa·s; the diffusion coefficient of small group in the sieve was 3.28e-10 m^2/s; the inlet and outlet channels (I and III) was 1x1.5 μm^2; and the sieve channel (II) was 0.5x0.5 μm^2. The free triangular mesh was drawn by COMSOL Multiphysics®, of which the maximum element size was 20 nm while the minimum size was 3nm. No-slip boundary condition was used in this simulation. All initial values were zero.

The velocity streamline of semi-H shaped channels (Figure 3.3) shows that due to the initial inlet velocity the big group and parts of the small group flow down along the sample inlet channel (I). Comparing with the dumbbell shaped channels; the semi-H shaped channels result in the big group moving along channel I and eliminating the dead volumes; thus reducing the probability of clogging. However, the bifurcation of streamlines towards channel II illustrates a tendency of sieve channel (II) to concentrate the big group components[62]. As the particle size is more similar with the pore diameter, there is a higher probability of the particle to be trapped. In other words, the more similar the size of

the particle blocked by a filter to the filter pore diameter, the higher chance it has to block the filter. This result fits the former study of cross-flow filtration [149]. So that semi-H shaped channels are not able to eliminate cluster but to ease the blocking. This result answers why cross-flow filtration still forms a cake layer after long term use and therefore fits the reports[79, 80, 150]. A smaller pore size and a higher inlet velocity are helpful to reduce blocking. The right part of the semi-H shaped channels showed an extension of streams which potentially can be used for continuous separation[56, 62].

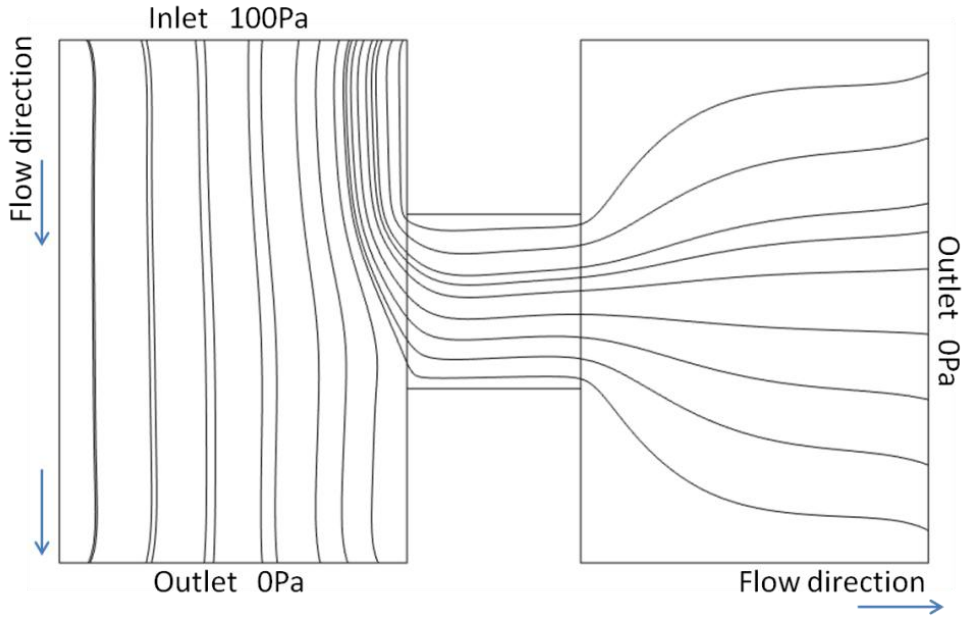

Figure 3.3 Velocity streamline of Semi-H shaped channels

For the small group, a multi-component mass transfer (convection) takes place in channels. A same concentration of small group as the inlet sample is achieved at the end of the capture channel (III). Comparing with dumbbell channels, the convection flux and especially the flow rate in the capture channel III reduce. It is because portions of small particles escape from capture and flow through the new outlet of channel I. So that it takes longer time for the concentration in channel III to get same level as in the dumbbell model.

Consequently, semi-H shaped channels (cross-flow filtration) have a potential to reduce cluster; but sacrifice target amounts of substance collected after filtration, and extend response time. A more important disadvantage is the difficulty of pumping flow through the sieves due to the pressure drop during the fluid flow through orifices [151, 152]. Next to improve the fluid kinetics properties, an H shaped channels model is studied.

3.3 Transport Phenomena in H Shaped Channels

3.3.1 Static Flow Properties of H Shaped Channels

As is shown in Figure 3.1e, H shaped channels consist of two parallel inlet channels and one connected channel perpendicular to them, which are geometrically symmetric. In the sample inlet channel, channel I, the input solution is awaiting separation; and the capture channel, channel III, inputs a buffer solution. If there is no electric field or components in solution are electro neutral (as assumed in these studies), there is purely multicomponent mass transfer between these two inlet channels. If the two inlet flows have the same velocity or are under the same pressure, in other words, the flows in these two channels are symmetric; there is only diffusion in channel II. This phenomenon can be explained by the symmetry. For the big group, the flow is similar to the semi-H shaped channels result. It can be seen from the velocity streamline shown in Figure 3.4 clearly that the two inlets flow separately.

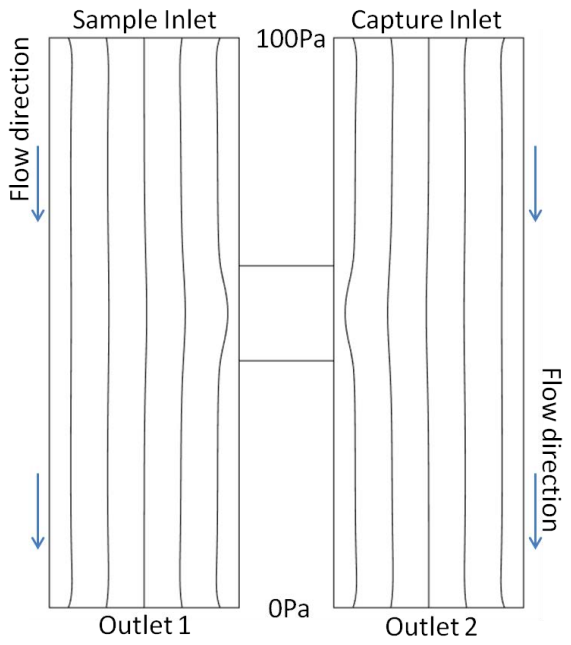

Figure 3.4 Velocity streamline of H shaped channels

The flux streamlines of the small group are shown in Figure 3.5. Components enter the sample inlet channel, diffuse through the sieve channel, and then diffuse to the lowest concentration part which is the inlet of the capture channel. That is why U shaped (or sometimes shallow w shaped) flux streamlines appear.

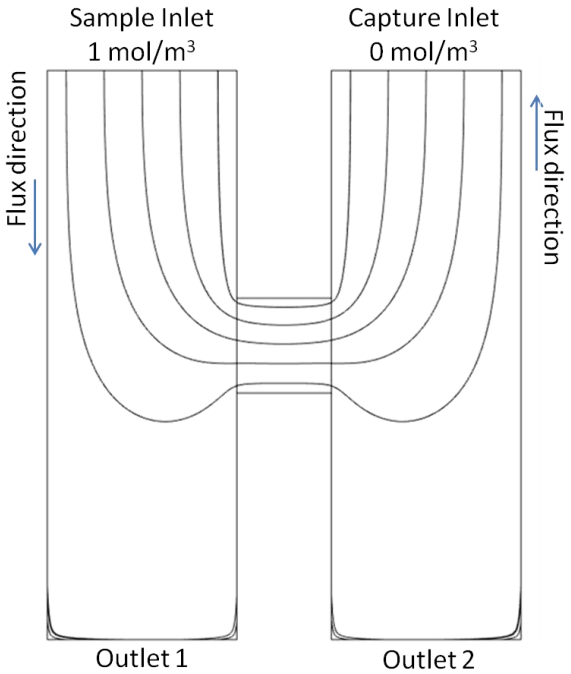

Figure 3.5 Flux streamline of Small group components in H shaped channels

The velocity magnitude and contour pressure are shown in Figure 3.6 and 3.7 respectively. The force generated by the pressure gradient along channel I and III pushes fluid to flow along these two channels and eliminates the dead volumes both sides. Thus relieves the adhesion and clogging around the sieve channel. As the pressure gradient is symmetric, no flow is seen in channel II. For steady laminar flow, the static and dynamic results on velocity and pressure are same. In this model, the pressure difference between the inlet and outlet was 100 Pa; the density of liquid was 1050 kg/m^3; the dynamic viscosity was 0.03 Pa·s; the diffusion coefficient of small group in the sieve was 3.28e-10 m^2/s; the inlet and outlet channels (I and III) was 1 x 3 µm^2; and the sieve channel (II) was 0.5 x 0.5 µm^2. The free triangular mesh was drawn by COMSOL, of which the maximum element size was 20 nm while the minimum size was 3 nm. No-slip boundary condition was used in this simulation.

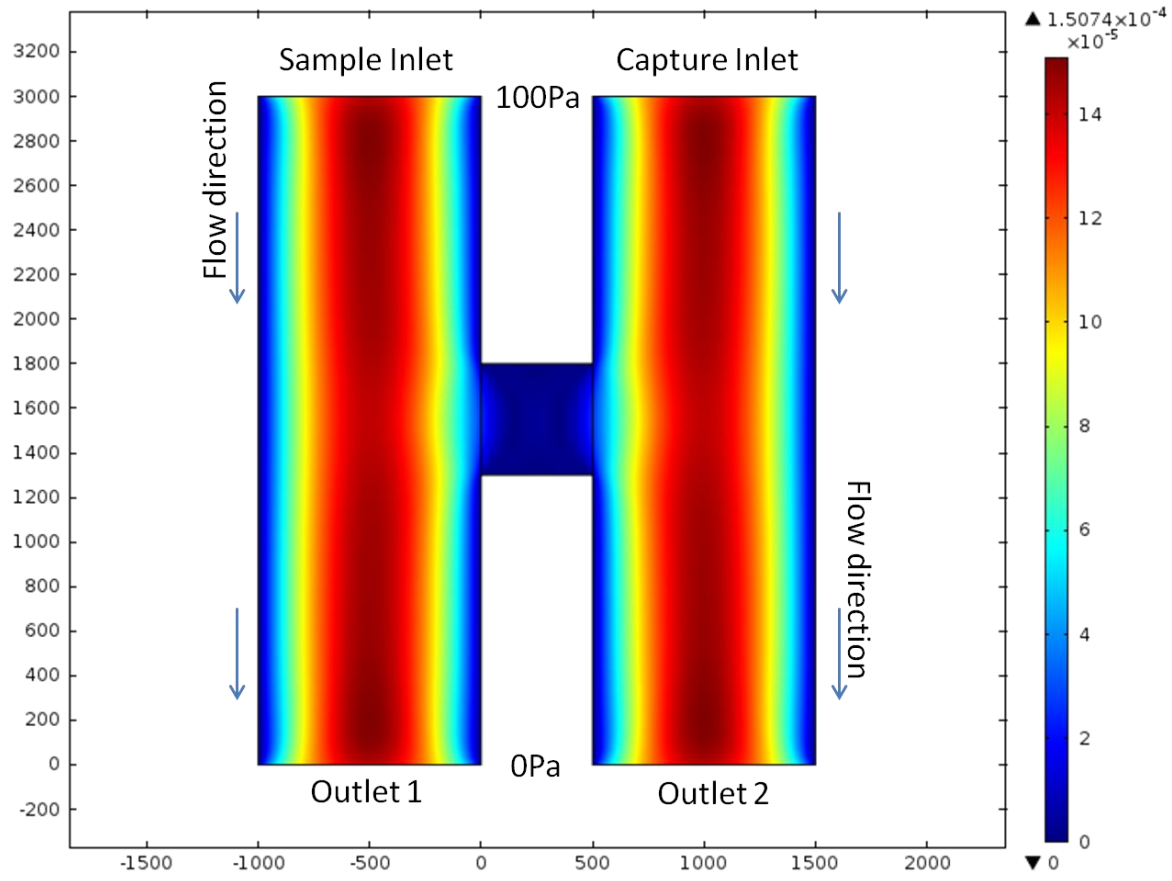

Figure 3.6 Velocity magnitude of H shaped channels (m/s)

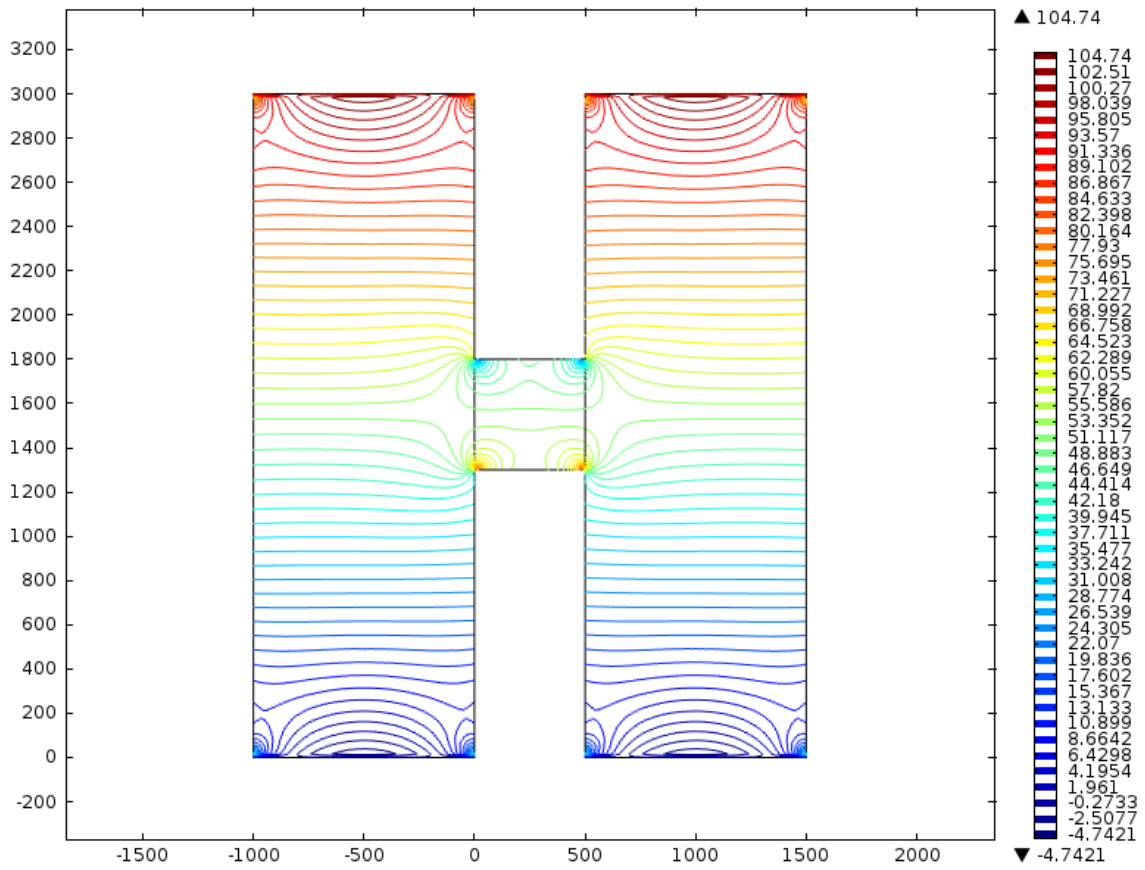

Figure 3.7 Contour Pressure of H Shaped Channels (Pa)

3.3.2 Static Concentration vs. Channel Size of H Shaped Channels

Figure 3.8 exhibits the concentration magnitude in H shaped channels. The big group keeps its concentration after filtration while parts of the small group diffuse into the buffer flow. Now considering purely the small group, it can be seen that the concentration at the outlet of the capture channel is not able to reach the same level as was seen in the dumbbell or semi-H shaped model anymore. Based on Fick's Second Law (Equation 2.2), the width and depth of sieve channel, a_i; the length of the sieve channel which is h_i and diffusion coefficient D_j decide the concentration diffusing to the capture channel. It was assumed that the inlet concentration of channel I is unit one, and the inlet concentration of channel III is zero, that is:

$$c_{0,j}^{\text{Sample}} = 1, \quad c_{0,j}^{\text{Capture}} = 0. \qquad \text{Equation 3.4}$$

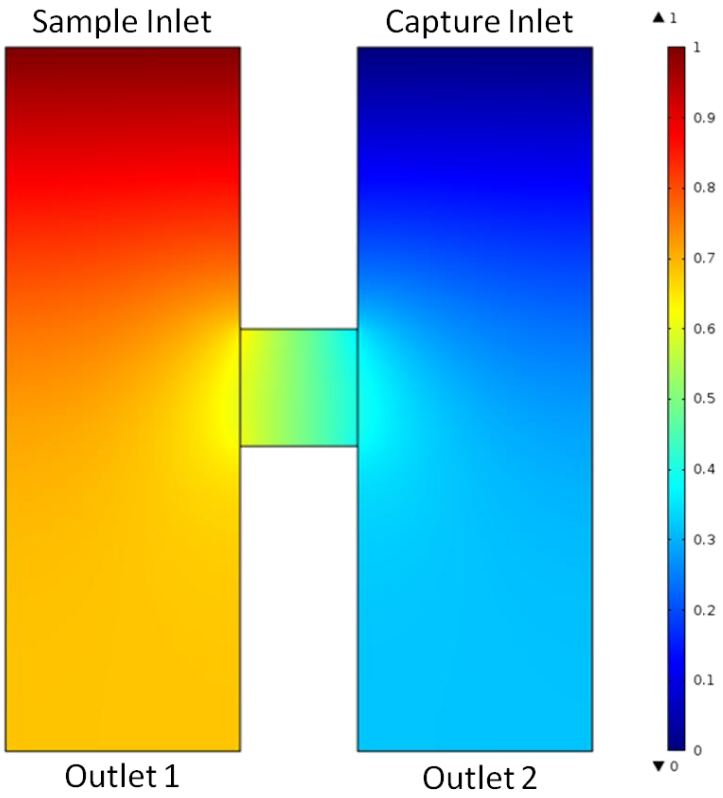

Figure 3.8 Concentration Magnitude of H Shaped Channels ($\mathrm{mol/m^3}$)

To simplify the model, it is assumed that the diffusion coefficient is constant everywhere in the model. Table 3.1 exhibits the outlet concentration of channel III ($c_{i,j}^{\mathrm{Capture}}/c_{0,j}^{\mathrm{Sample}} \times 100\%$) with different $a_i$and h_i, while $w = 1\mu\mathrm{m}$. When $a_i \geq w$, H shaped channels does not function as a filter anymore, and under this condition $D_{ij} = D_j$. The highest concentration of small group in channel III without external field assistance is 50% of the input. This is due to its symmetry. It can be explained by Fick's Second Law or the Second Law of Thermodynamics.

Table 3.1 Concentration at the outlet of capture channel with different sieve size (%)

(m)	$a_i = 0.5$	$a_i = 1$	$a_i = 4$	$a_i = 8$	$a_i = 10$
$h_i = 0.5$	47.37	48.76	49.97	50.00	50.00
$h_i = 1$	45.89	47.97	49.90	50.00	50.00

It is understandable that due to the inlet convection velocity, components are more likely to move along the sample inlet channel rather than enter the sieve channel. The analysis of Equation 2.8 in the previous chapter illustrated that the diffusion is anisotropic in porous medium. These are two reasons why H shaped channels used as a filter cannot capture as much as 50% of the inlet target components. To achieve a concentration as high as 50% of the inlet at the capture side, higher integration of flux on the cross sectional area is demand. Hence higher flux or larger cross-section area are required. A shorter sieve channel can increase the concentration gradient in the sieve channel thus increases the diffusion flux. The larger pore area (no larger than the sample inlet) can be achieved by adding the number of sieve channels which is the H shaped channel series (Figure 3.9). Further discussions on the sieve series will be illustrated in the next chapter.

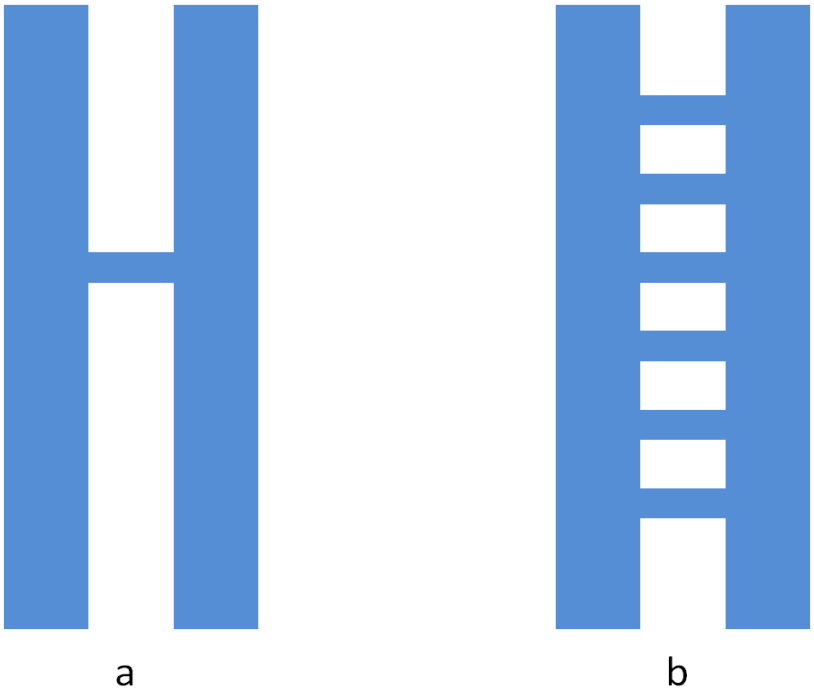

Figure 3.9 (a) a single sieve H shaped channels; (b) H shaped channel series

3.3.3 Dynamic Model of H Shaped Channels

For a steady fully developed laminar flow, the time dependent solution is the same as the static result. The response time of the filter which is defined as the time taken by the capture channel to achieve a steady outlet concentration, marked as $T_{i,j}$. Therefore there is,

$$\frac{dc_{i,j}}{dt} = 0, \text{ when } t \geq T_{i,j} \qquad \text{Equation 3.5}$$

It is difficult to give a generalized solution of $T_{i,j}$, but CFD software is helpful to give a numerical result for specific models. In this model, there are $w = 100\ \text{nm}, a_i = 50\ \text{nm}$, $h_i = 100\ \text{nm}$, and $D_{i,j} = 3.28\text{e}-10\ \text{m}^2/\text{s}$. The simulation settings were the same as the one in section 3.4, besides the solver was time dependent rather than stationary. Figure 3.10 exhibits a curve of $c_{i,j}^{\text{Capture}}(\text{t})$, which was drawn by COMSOL finite element software. For this curve, the mass transfer process took only a second to reach a steady concentration output, in other words a steady flux of component j. Figure 3.11 illustrates the total flux changing at the outlet of the capture channel, which is $J_{i,j}^{\text{Capture}}(t)$.

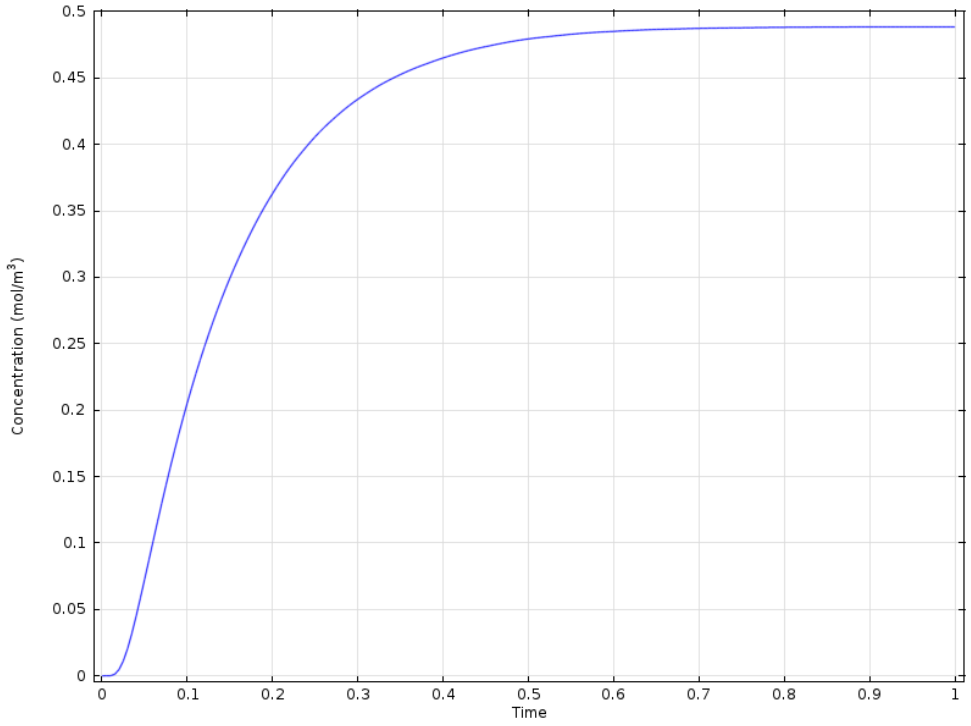

Figure 3.10 Concentration in capture channel corresponding with time (s)

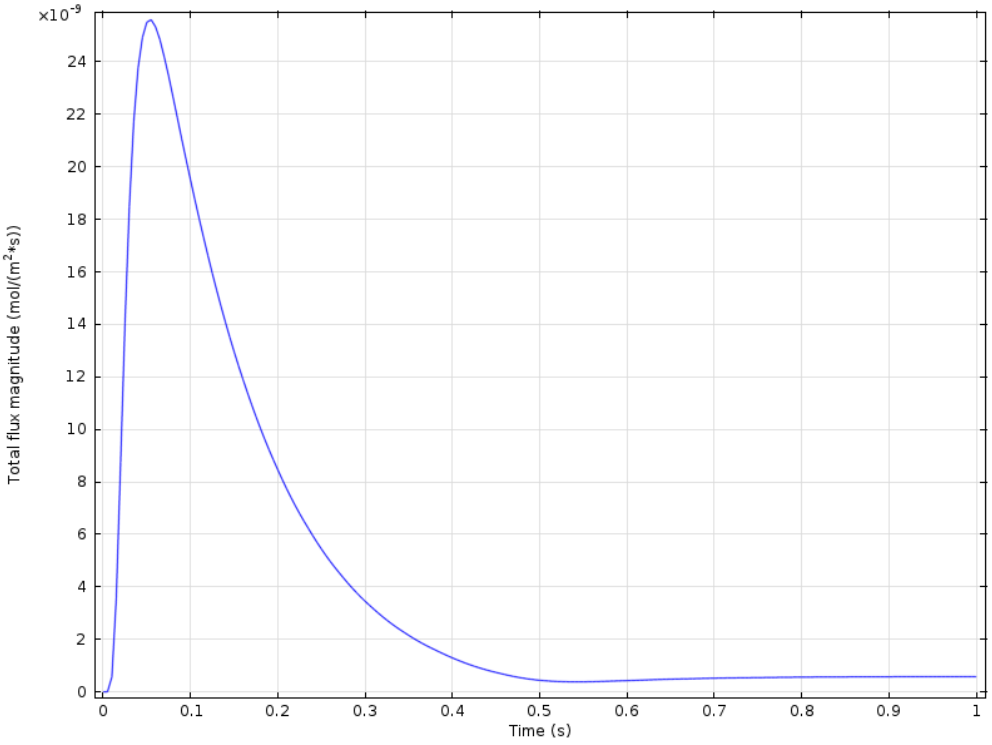

Figure 3.11 Flux in capture channel corresponding with time.

As a higher flux is able to expedite the mass transfer process, according to the extended Nernst-Planck equation (Equation 2.5) a larger gradient of concentration and a higher diffusion coefficient should be chosen to create a higher flux. For H shaped sieves, most geometric sizes and the diffusion coefficient are fixed by the application except for the length of the sieve channel. Thus a shorter sieve channel can be used to reduce response time.

3.3.4 Conclusions

H shaped channels are high throughput filters. The flows along the interface between channel I & II, II & III reduce the possibility of adhesion at the solid-liquid interface. In addition as the concentration in the capture channel (II) is always lower than the concentration in the channel I, the concentration of the small group in the sample inlet channel reduces (thus there is a negative concentration gradient) during the mass transfer

process (due to the Fick's law); hence the chance of clogging further declines due to this dilution phenomenon. However, a filter based on H shaped channels cannot capture the target components to a level as high as 50% of the concentration of the inlet sample. Thus for applications which ask for keeping the target concentration, a concentration process is necessary. By extending the sieves of H shaped channels, an H shaped channels series is able to improve the capture concentration with the same inlet sample concentration.

3.4 Transport Phenomena in Angular H Shaped Channels

To enhance the convection in the sieve channel (channel II) of H shaped channels, an angle is introduced to make the channels asymmetric (Figure 3.12). Choosing the position sieve channel of the standard previously discussed symmetric H shaped channels as the positive x-axis, and the sample inlet flow direction as the negative y-axis; the angle that the sieve channel is rotated through is defined as $\theta \in (-90°, 90°)$. The angle θ for H shaped channels is zero. Thus angular H shaped channels are built when angle θ is not equal to zero. This subsection introduces the transport phenomena in angular H shaped channels, especially the changes caused by the angle.

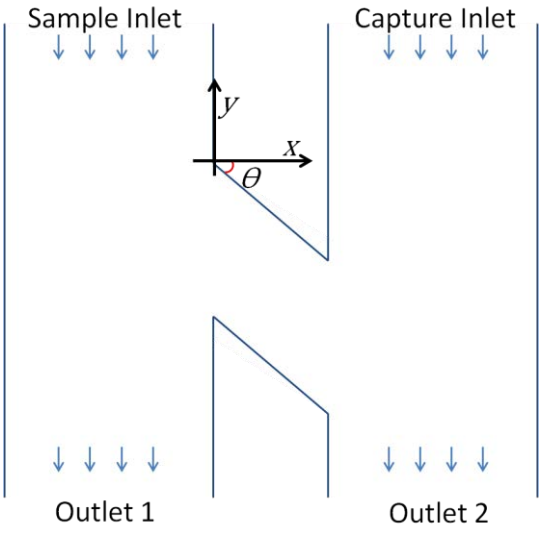

Figure 3.12 Angular H shaped channels

In this model, the pressure difference between inlet and outlet was 100 Pa; the density of liquid was 1050 kg/m^3; the dynamic viscosity was 0.03 Pa·s; the diffusion coefficient of small group in the sieve was 3.28e-10 m^2/s. The free triangular mesh was drawn by COMSOL Multiphysics®, of which the maximum element size was 20nm while the minimum size was 3nm. No-slip boundary condition was used in this simulation. All initial values were zero.

3.4.1 Static Flow Properties of Angular H Shaped Channels

The angle θ destroys the geometric symmetry of the H shaped channel; so if the inlet keeps the same conditions as subsection 3.2.3, convection appears in sieve channel II (Figure 3.13). This convection is caused by the inertia of fluid and the concentration gradient around channel II. There are 20 streamlines in Figure 3.13. Thus the flow rate through the sieve channel is around fifth of the inlet flow rate.

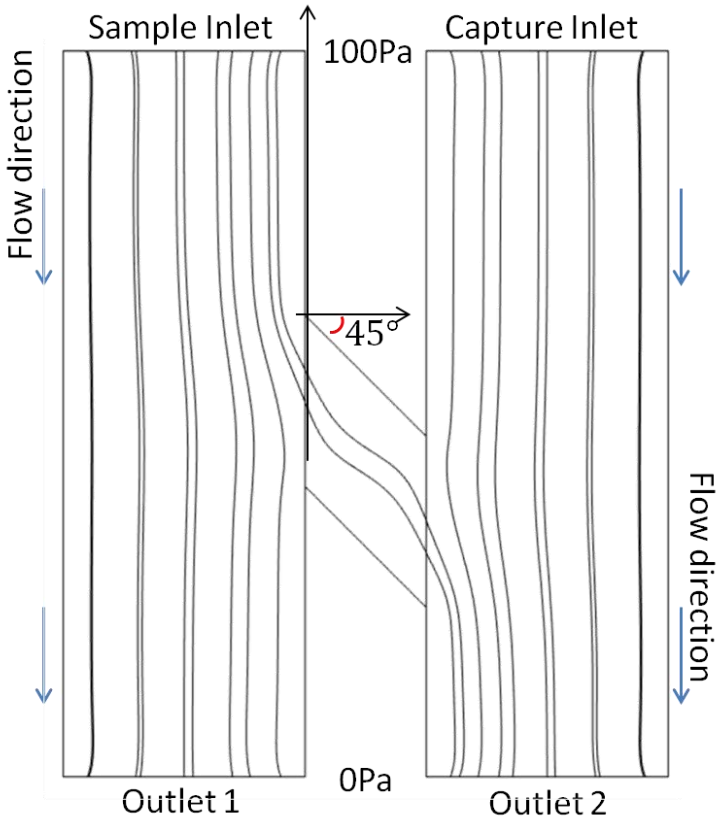

Figure 3.13 Velocity streamline of angular H shaped channel

In Figure 3.14, that shows contour pressure, it can be seen that the pressure in channel I and II drops down nonlinearly. The sieve channel connects the two channels and there is a tendency to equilibrate the pressure beside its two entrances. Comparing with the contour pressure of H shaped channels (Figure 3.7), the angular sieve channel changes the pressure gradient in channel I and II, and reduces the pressure difference at the two ends of the sieve channel (If there were no sieve channels, the pressure difference between the start point and end point of sieve channel should be higher). Due to the inertia of the fluid and the additional pressure gradient on the sieve channel, a bigger angle magnitude results in a higher y direction velocity component. Thus a higher convection velocity is achieved in channel II with a larger angle magnitude. For no slip boundary condition, fine sieve channels reduce or even prevent the convection in them.

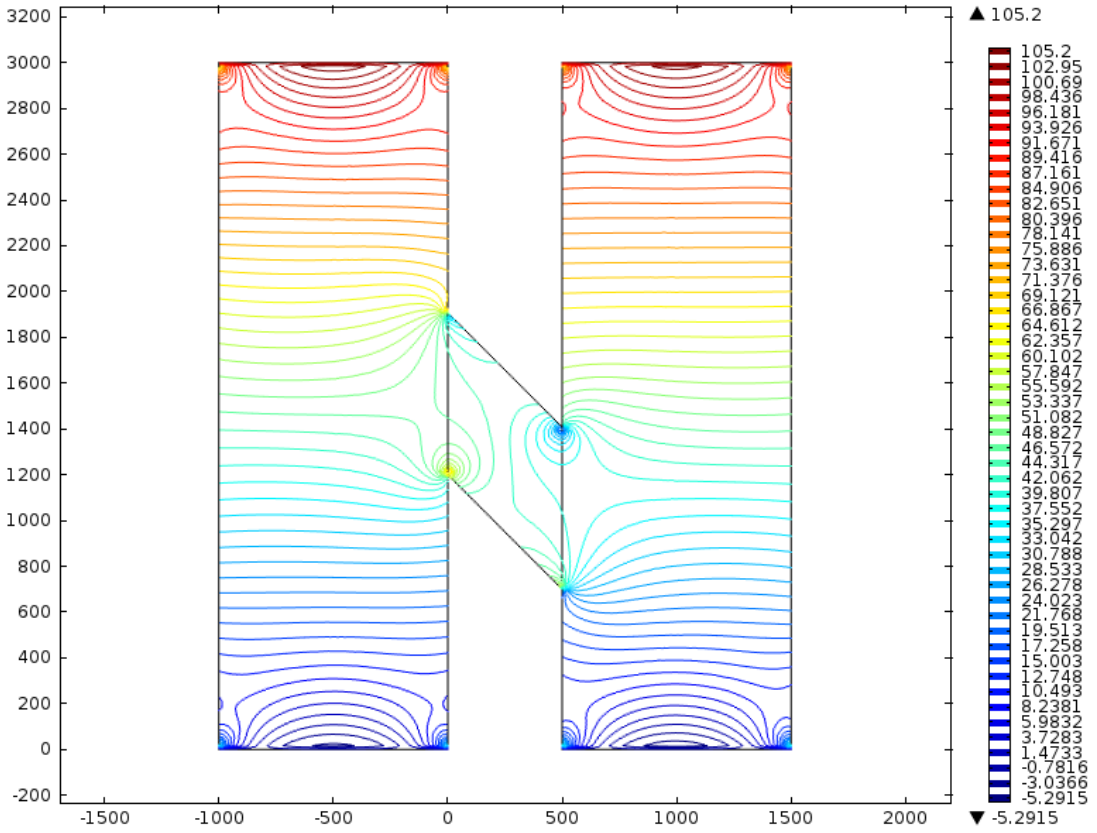

Figure 3.14 Contour pressure (Pa) of Angular H shaped channels (-45°)

The direction of convection is dependent on whether the angle is positive or negative. A positive angle results in convection from the capture channel to the sample inlet channel. It is helpful to reduce adhesions on the interface between channel I and II and adhesions inside sieve channel as well, while dilute the sample solution in channel I. For a negative angle the convection is from channel I to III, which is helpful for the capture progress in the capture channel and reduces the response time. However the extended length of channel II increases the chance of clustering inside it. According to the Navier-Stokes equation, the convection in the sieve channel reduces by the diameter of sieve channel. Hence the angle effect declines with the diameter of sieve channel.

Figure 3.15 illustrates the velocity magnitude in the angled H shaped channels. A weak convection flow in the sieve channel can be seen. While the flux streamline of the small group is shown in Figure 3.16a. Comparing with the U shaped flux streamline of H shaped channel (Figure 3.5), a shift to an asymmetric U shape is seen. This asymmetry results in a different outlet concentration. Figure 3.16b illustrates the situation when the sieve channel is wide enough, where the bottom flux streamline is U shape. However, it cannot work as a filter because all particles injected are able to pass through the sieve channel.

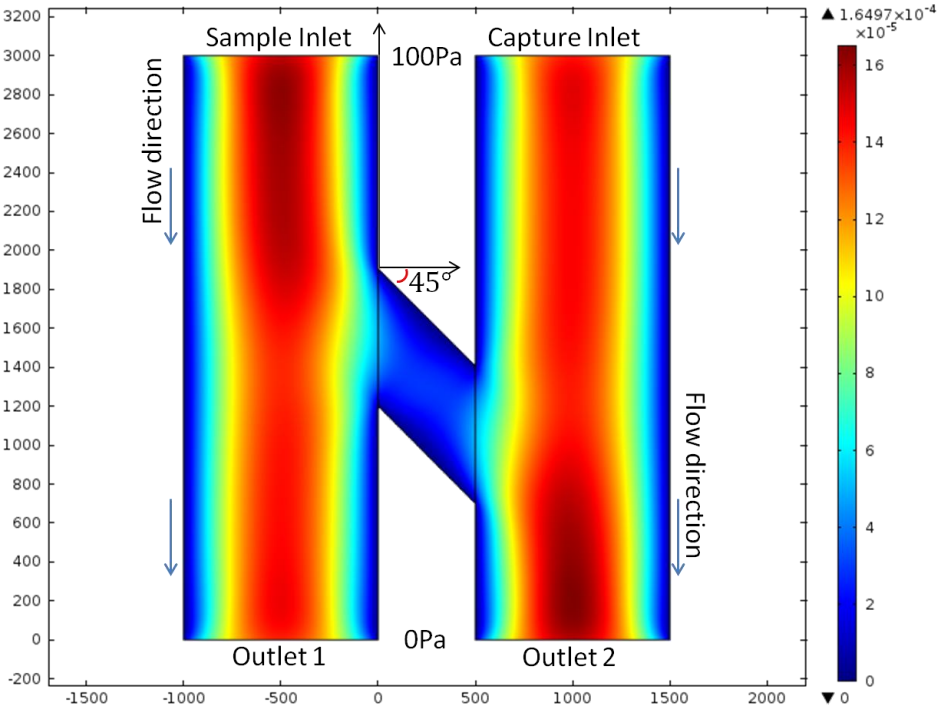

Figure 3.15 Velocity Magnitude of Angular H shaped channels (m/s)

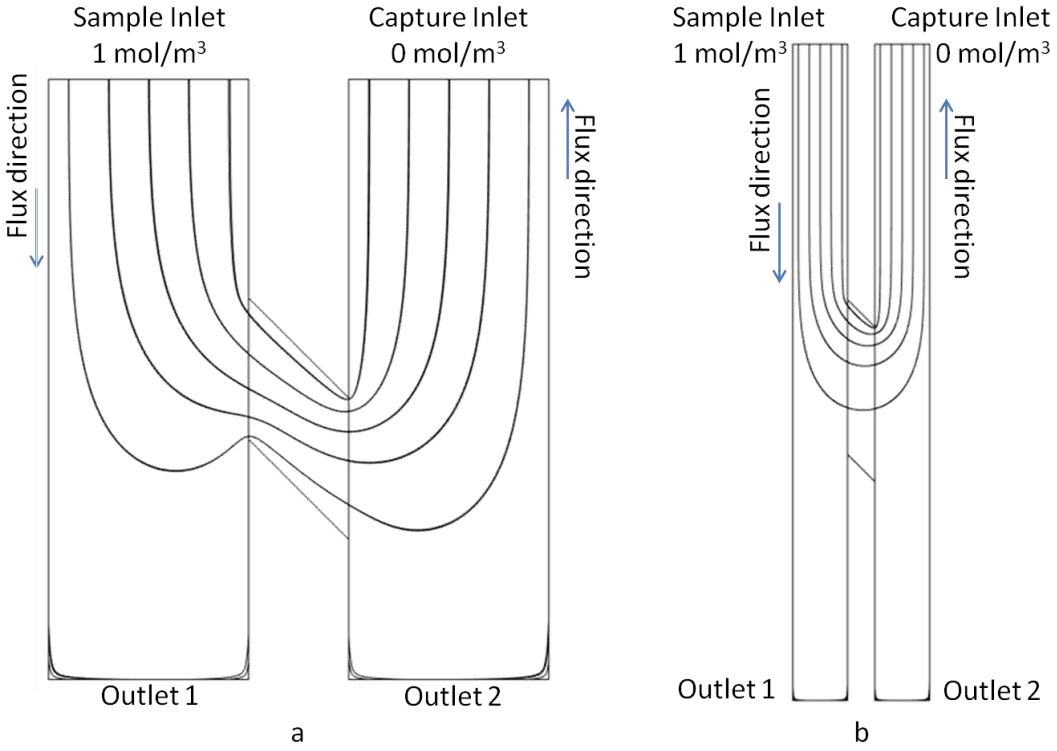

Figure 3.16 Flux Streamline of Small Group (a) Inlet channels are 1x3 μm^2, the distance between two inlet channels is 0.5 µm, and the width of sieve channel is 0.5 µm; (b) Inlet channels are 1x8 μm^2, the distance between two inlet channels is 0.5 µm, and the width of sieve channel is 2 µm. All the other settings of these two models are the same.

3.4.2 Static Concentration VS. Angle

If the same assumptions regarding the inlet concentration are made as in section 3.2 and 3.3.2 (Equation 3.4), the flux streamlines start from the sample inlet and end at the capture inlet. As the flux streamlines are separated evenly almost everywhere (except the area near the wall and around the cross sections, Figure 3.16), concentration can be approximated as a linear reduction along the flux streamline (uniform concentration gradient). Then the concentration distribution issue shifts to a length issue of flux streamline (based on Equation 2.1). Furthermore, it can be approximated by the boundary condition of angled H shaped channels, which are the three red line sections shown in Figure 3.17. Thus a different angle results in a different concentration output, which can be seen in Table 3.2 ($\frac{c_{i,j}^{\text{Capture}}}{c_{0,j}^{\text{Sample}}} \times 100\%$).

Table 3.2 Capture concentration with different angel and sieve size (%)

θ	(0.5, 0.5)	(8, 0.5)
60°	47.07	48.19
45°	47.14	49.54
30°	47.20	49.75
0°	47.37	50.0
−30°	47.78	50.21
−45°	48.08	50.46
−60°	48.47	51.81

It shows clearly that the target concentration increased when the angle decreased. If the sieve channel is big enough (U shaped flux streamline), in the simulation the outlet concentration of the capture channel is not only limited to 50% of input sample. Here the

entrance length of inlet lamina flow is ignored, and the concentration at the sample inlet was fixed as 1 $\mathrm{mol/m^3}$ while at the capture inlet was fixed as 0 $\mathrm{mol/m^3}$. For the continuous flow, in reality, the backward flux in capture channel rise the concentration at the inlet of capture channel thus the concentration cannot be always zero. Moreover, the entrance is much longer than a micro or nano channel; thus these effects are difficult to be observed.

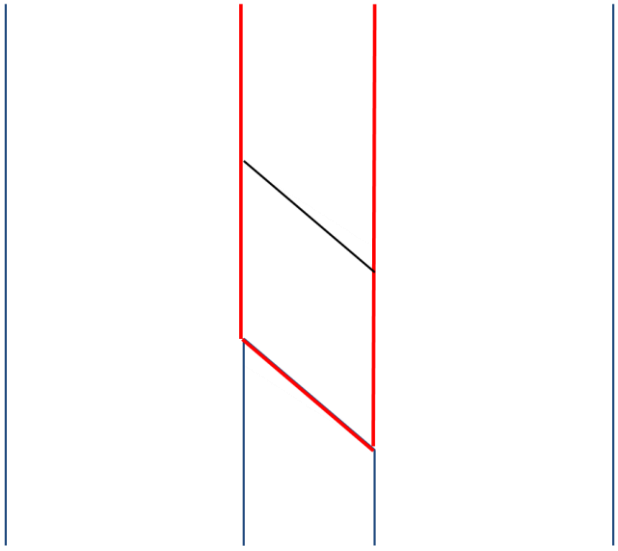

Figure 3.17 Red line sections for the estimation of the concentration variation.

3.4.3 Dynamic Model

As it was mentioned the response time of a filter is related to the length of the sieve channel, angled H shaped channels extended the sieve channel length and thus extended the response time. In addition, in a positive angle sieve, convection is in an inverse direction with the flux which decreases the flux and delays the response time. In contrast the convection in a negative angle sieve channel, increases the flux slightly. However the decrease of flux due to the extended length dominates the total flux, the response time $T_{i,j}$ increases with the magnitude of angle θ,

$$T_{i,j} \propto |\theta| \qquad \text{Equation 3.6}$$

3.5 A New Design of Multi-Level Filter Based on H shaped Channel Series

3.5.1 Introduction of a New Design of Multi-Level Filter

Based on the former discussion, a new multi-level filter is designed as shown in Figure 3.18. The filter is a connection of different sized H shaped channels from the smallest to the biggest in series along the sample inlet channel. So it separates components j $(j = 1,2, \dots, n)$ by size sequence which marked as i $(i = 1,2, \dots, n)$ into n groups. The diameter of component j is market as a_j; and the width of the i level sieves' channel is marked as a_i, assuming its width equals to its depth. It is assumed that $a_i < a_{i+1}$, $a_j < a_{j+1}$; and when $i = j$, $a_j < a_i$. In the sample inlet channel, when $i \geq j$, component j can diffuse through the sieve channels of level i; in contrast when $i < j$, the component j is blocked by the sieves. Their concentrations drop down at each level, if diffusion occurs. So that concentrations of the small group drops down in sequence, and the amount of the substance of the bigger components remains unchanged until their first diffusion; which is:

$$c_{i,j\leq i}^{\text{Capture}} > c_{i+1,j\leq i}^{\text{Capture}} \text{ and } c_{i,j>i}^{\text{Capture}} = 0. \qquad \text{Equation 3.7}$$

Thus for each spices of component j, we have:

$$c_{i,j=i}^{\text{Capture}} > c_{i,j\neq i}^{\text{Capture}} . \qquad \text{Equation 3.8}$$

In other words, each capture channel mainly captures the same number particle group, while removing all of the bigger particle groups and most of the smaller ones. This means particles are purified by size.

As the capture concentration of H shaped channels is lower than 50% of the target components sample inlet concentrations (section 3.3.2); aiming at a higher capture

concentration, a series of sieve channels are applied at each level, which is the H shaped channel series. The maximum capture concentration is 50% of sample inlet concentration for a sufficient diffusion (maximum entropy). Table 3.3 shows the ideal concentrations of component j at the outlet of the i^{th} level capture channel compared with the concentration of inlet sample in an n-level filter based on H shaped channels ($c_{i,j}^{\text{Capture}} / c_{0,j}^{\text{Sample}} \times 100\%$).

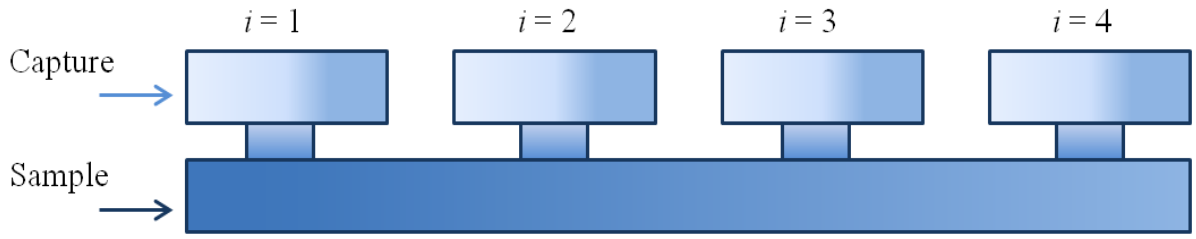

Figure 3.18 Scheme for multi-level filtration in sequence.

Table 3.3 The concentration table of multilevel filter (%)

j	1	2	3	4	n
$i = 1$	50.0	0	0	0	0
$i = 2$	25.0	50.0	0	0	0
$i = 3$	12.5	25.0	50.0	0	0
$i = 4$	6.25	12.5	25.0	50.0	0
$i = n$	$\frac{1}{2^n} \times 100\%$	$\frac{1}{2^{n-1}} \times 100\%$	$\frac{1}{2^{n-2}} \times 100\%$	$\frac{1}{2^{n-3}} \times 100\%$	50.0

The concentration of component j after the i^{th} level filtration in the capture and sample channel is able to be written in geometric progression.

$$c_{i,j}^{\text{Capture}} = c_{i,j}^{\text{Sample}} = \frac{1}{2^i} \cdot c_{0,j}^{\text{Sample}} \quad (i = 1,2,\dots,n) \qquad \text{Equation 3.9}$$

As it was mentioned previously, one disadvantage of filtration by size is that it is only able to purify the small group from a mixture but not big ones. Comparing with a typical filter, the new design of multilevel filter achieves a purer big group also (Figure 3.18). In order to purify each group further, a dilute channel is added in parallel with the sample inlet channel (Figure 3.19). After each level of capture sieve and before the next level, same size sieves repeat again but between the sample inlet channel and the dilute channel. These sieves dilute particle groups which are smaller than the sieves size, and after these diluted sieves the concentrations of these particles drop down to 50% (if they are first time diluted). Thus in the outlet of each capture channel, the concentration of similar but smaller impurities reduces. Table 3.4 shows the concentrations of component j at the outlet of the i^{th} level capture channel with a dilute channel added ($c_{i,j}^{\text{Capture}} / c_{0,j}^{\text{Sample}} \times 100\%$), assuming that sieve channels of each level are isolated.

Table 3.4 The connection table of multilevel filter with a dilute channel (%)

j	1	2	3	4	n
$i=1$	50.0	0	0	0	0
$i=2$	12.50	50.0	0	0	0
$i=3$	9.38	12.50	50.0	0	0
$i=4$	7.03	9.38	12.50	50.0	0
$i=n$	$\frac{3^{n-2}}{2^{2n-1}}\times 100\%$	$\frac{3^{n-3}}{2^{2n-3}}\times 100\%$	$\frac{3^{n-4}}{2^{2n-5}}\times 100\%$	$\frac{3^{n-5}}{2^{2n-7}}\times 100\%$	50.0

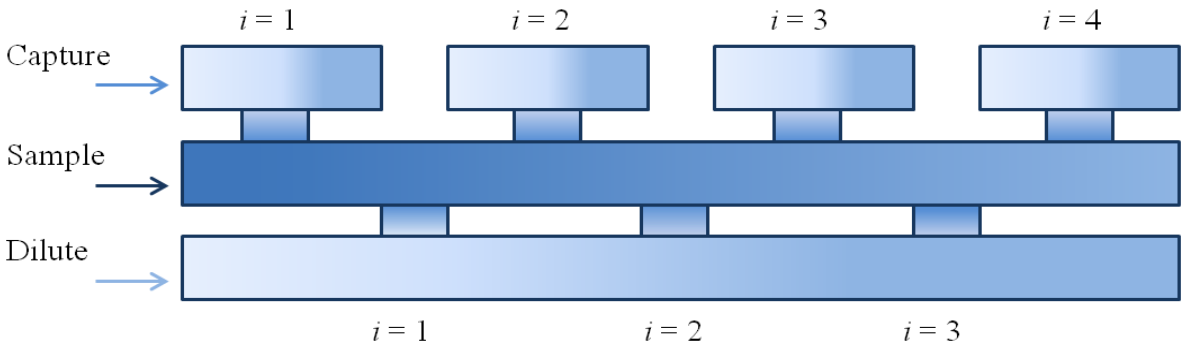

Figure 3.19 A multi-level filter with a dilute channel

The concentration of component j after i level filtration in the capture, sample inlet and dilute channel is able to be written in a geometric progression.

$$c_{i,j}^{\text{Capture}} = c_{i,j}^{\text{Sample}} = \begin{cases} \frac{1}{2} \cdot c_{0,j}^{\text{Sample}} & i = 1 \\ \frac{2}{9} \cdot \left(\frac{3}{4}\right)^{i} \cdot c_{0,j}^{\text{Sample}} & i > 1 \end{cases} \qquad \text{Equation 3.10}$$

$$c_{i}^{\text{Dilute}} = \begin{cases} \frac{1}{4} \cdot c_{0,j}^{\text{Sample}} & i = 1 \\ \frac{1}{3}\left(\frac{3}{4}\right)^{i-1} \cdot c_{0,j}^{\text{Sample}} & i > 1 \end{cases} \qquad \text{Equation 3.11}$$

Because the common ratio $(\frac{3}{4})$ is higher than the one without the dilute channel where the common ratio is $(\frac{1}{2})$; if the particles were diluted by more than three levels of sieves, their concentrations in the capture channel should be no lower than the ones without the dilute channel. Both concentration percentages are lower than 7.03% after three levels dilution. Based on these analyses, a dilute filter is helpful to purify similar sized particles while it declines the concentrations of all components j in all level $i \neq j$.

In this design of multilevel filter, all channels are pumped independently. Laminar streams flow along each channel, which reduces the possibility of adhesion on the surface of the sieves. What's more, small group is diluted during the filtration, which relieves clustering in sieve channels [75]. Filtration in series makes this filter high throughput and it is able to expand levels easily. It is a general well patterned filter that fulfils most application of

separation by size in a huge range of scale, such as blood cells separation and bio-marker detection. All features of this multilevel filter are able to be designed and controlled. So it is reasonable to build standard commercial chips of different range of scale. However, it is difficult to separate components of which sizes are extremely similar or even the same. In this kind of situation, other methods, such as electrophoresis and electroosmosis, can be combined with this filter for further precise purification.

3.5.2 Principles for Multi-Level Filter Design

During the design of this type of multi-level filter, several parameters should be considered.

i) First is the number of channels that are enough for each level of sieves to achieve a sufficient diffusion. Considering the entrance of the sample inlet shall be big enough for all components to pass through; what is the relation among entrance channel size, filter sieve size and the number of filter sieves? This relates to the entrance area of sample inlet channel and the total area of the sieves entrance surface. In this design, the width of all sieves in the i^{th} level is equal to their depth which is a_i, and the distance between two adjacent sieve channels is w_i. It is understandable that the minimum number of the i^{th} level sieves, N_i, is proportional to the width of the sample inlet entrance w and the depth of the inlet entrance d whereas inversely related to the width and depth of the sieve channel a_i, where γ is a constant.

$$N_i \propto \gamma \frac{wd}{a_i^2} \qquad \text{Equation 3.8}$$

Because during the same time 50% of particles entered from the sample inlet diffuse to sieves channel, γ cannot be lower than 0.5. Considering the size effect in nanochannels, finer sieves need a higher γ. That means that γ is a function of the sieve channel geometric scale and the particle size a_j according to the effective diffusion coefficient function

(Equation 2.7). When $\gamma = 1$, the sample inlet entrance area is equal to the total sieves entrance area of this level. γ is a complex function so, a better way to understand it is to find γ for a typical fine nanochannel and examine it for different size sieves. Simulation results on γ are shown in the next chapter.

ii) In a continuous flow diffusion always happens when a concentration difference exists. The second question therefore is that if we want adjacent levels that are independent, how long of a distance between two adjacent levels is enough to ignore the diffusion between them? Considering two adjacent level of sieves i and $i+1$ (Figure 3.20), the concentration of component j at the end of the i^{th} level is $c_{i,j}^{\text{Sample}}$, and the distance between two levels of sieves is l_i, and the distance between the end point of either sieve is L_i. It can be viewed that the later level sieve introduces an additional concentration gradient on the former level. This extra gradient results in a concentration decrease $\Delta c_{i,j}^{\text{Sample}}$, where Δ is the difference operator. If $\Delta c_{i,j}^{\text{Sample}}$ is small enough, the two levels can be viewed as independent, that is $c_{i,j}^{\text{Sample}} \approx 2c_{i+1,j}^{\text{Sample}}$. The average gradient of concentration of component j on l_i is smaller (negative) than the average value on L_i, thus the average concentration gradient of component j on l_i is able to be used to estimate the extra gradient $\Delta c_{i,j}^{\text{Sample}}$ sufficiently. That is,

$$\Delta c_{i,j} \approx N_i w_i \cdot \frac{c_{i,j}^{\text{Sample}} - c_{i+1,j}^{\text{Sample}}}{l_i} \approx \frac{1}{2} N_i w_i \cdot \frac{c_{i,j}^{\text{Sample}}}{l_i} \qquad \text{Equation 3.9}$$

So the error caused by the additional concentration gradient is estimated as,

$$\delta_i = \frac{\Delta c_{i,j}^{\text{Sample}}}{c_{i,j}^{\text{Sample}}} \approx \frac{N_i w_i}{2 l_i} \qquad \text{Equation 3.10}$$

Where now δ_i can be decided by technical requirements or the measurement error demand. Based on this equation the minimum distance between two adjacent level sieves can be estimated under a given error:

$$l_i \geq \frac{N_i w_i}{2\delta_i} \qquad \text{Equation 3.11}$$

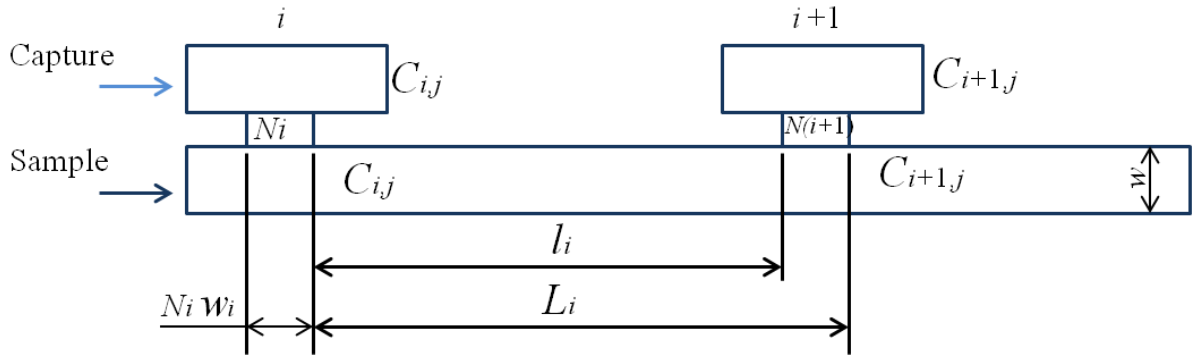

Figure 3.20 Scheme about the distance between two adjacent levels.

iii) Another question to be answered is that if engineers use droplet instead of continuous flow, aiming to take advantages of the angle effect, what angle shall be chosen. A positive angle is better for dilution process while a negative angle is helpful for the capture progress. As the entrance width of the sieve channel and the length of the sieve channel increase with angle magnitude($-90° < \theta < 90°$); the extended sieves due to the angle in one side reduce adhesions inside channels because of the convection introduced, in other side it gives particles which are bigger than the diameter of sieve channels more chance to blocking the at the cross-section[153]. If engineers shorten the sieve channels, more precise fabrication methods would be needed. Normally this means a higher cost. For some fabrication techniques related with removed substrate volume, a bigger angle magnitude needs longer working time or higher energy when the distance between sample inlet and capture channels kept the same. In other words the fabrication cost increases slightly with angle magnitude.

There are some general guidelines for microfluidics chips design as well, which will be discussed in Chanter 6; such as chip's size and material, connection interface and biocompatibility. These issues are not related with the filtration process; so that more specific analyses of these issues are discussed in Chapter 5 where the design of the mask for this multi-level filter is presented.

3.6 Summary

In this chapter, different models of filter element were built and discussed step by step, which is helpful for understanding of the transport phenomena in nano sieves especially the mass transfer process. Then a sequence filtration process was put forward, and a new design of multilevel filter base on H shaped channels was illustrated.

This filter showed potential advantages to reduce adhesion and clustering inside the filter and to purify each group of components by size order in a relatively large scale. The design parameters which affect the performance of the filter were also studied. They will be investigated more specifically in the next chapter through calculation on Semi-H shaped, H shaped and angular H shaped channels series with the finite element simulation software COMSOL Multiphysics®.

CHAPTER 4

2D SIMULATIONS

ON MULTI-LEVEL FILTER

4.1 Introduction

This chapter studies the transport process and flow properties of sieve channel series which forms each level of a multi-level filter and verifies, by simulations, the design principles put forward in the last chapter. Based on these analyses, a three-level nanofilter is designed, modelled and discussed.

This chapter start the analyses from semi-H shaped channels, and then simulations of multi-level filter based on semi-H shaped channels are presented. The transport process and flow properties of H and angular H shaped channels are simulated sequentially. Then a model of a multi-level filter based on H shaped channels was the simulated with the finite element software COMSOL Multiphysics®. During these discussions the estimate formulas illustrated in Chapter 3 were examined. In these simulations the Transport of Diluted Species module and the Laminar Flow module were used to study the flow properties and the mass transfer process. The no-slip flow boundary condition was applied in this.

Dextran is a complex branched glucan which is widely used in bio-medical and bioscience. Commercial dextrans with different standard molecular mass are easily obtained. Numerous publications applied dextran as a bio-label. Thus dextran of which the aqueous solution is

Newtonian fluid is a good option for bio-filter testing [122]. Hence in this chapter and the next chapter, all simulations were applied with dextran solutions. In section 4.2-4, all models were applied with 1 $\mathrm{mol/m^3}$3kDa dextran aqueous solution. The density of liquid was 1050kg/m^3; the dynamic viscosity was 0.03Pa·s; the diffusion coefficient was 7.5e-10m^2/s. The pressure difference between inlets and outlets was 100Pa. 500 and 2,000 kDa dextran were applied in section 4.5. The diffusion coefficient can be calculate by the Equation 2.7

4.2 Simulation on Semi-H Shaped Channels Series

4.2.1 Meshing

This model contained an inlet channel and a capture channel whose size were both 2x25 µm. Between these two channels, there were 100 2 µm x 40 nm sieve channels. The distance between two adjacent sieve channels is 120 nm. The free triangular mesh was drawn by COMSOL Multiphysics® physical-controlled mesh automatically (Fine size option).

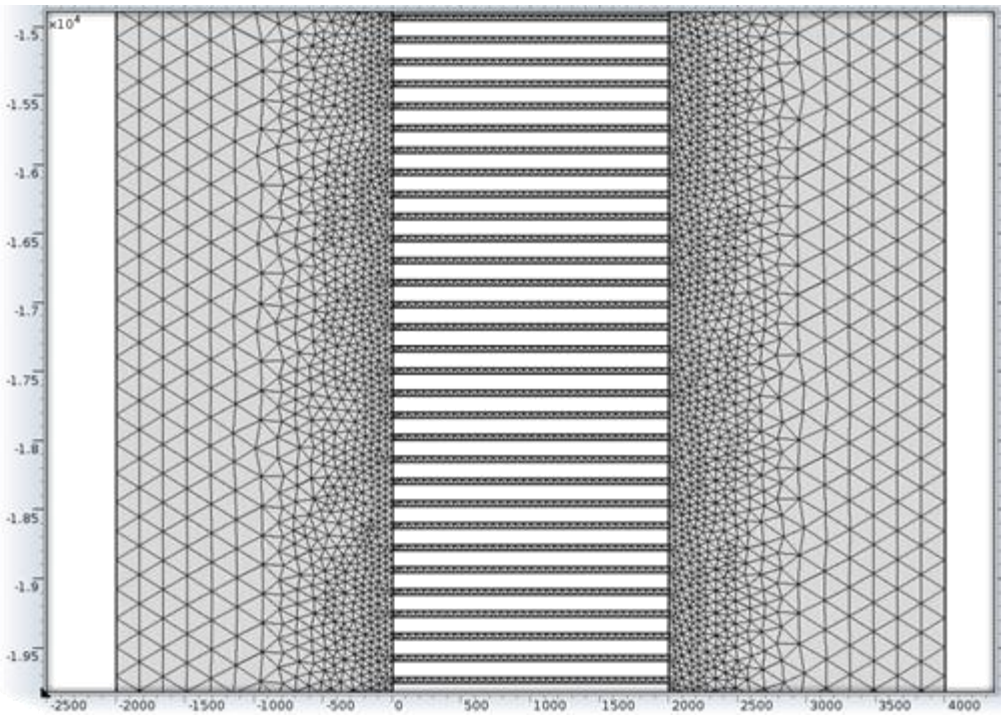

Figure 4.1 Free triangular mesh built by COMSOL Multiphysics® (nm)

4.2.2 Static Flow Properties of Semi-H Shaped Channels series

Figure 4.2a&b exhibit the velocity streamline and velocity magnitude of a semi-H shaped channels series. The main convection took place in the sample inlet channel (I), while few fluids convect through the series of sieves into the capture channel (III). It is well known that the velocity in the sieve channels reduces with channel size, thus for fine sieves the velocity in capture channel is extremely low. The capture channel worked as a reservoir. This is the 'pumping problem' of the semi-H shaped channel series. Contour Pressure is shown in Figure 4.3 which explains this problem. In the sieve channels, pressure dropped rapidly and increasing the inlet pressure did not help significantly with the flow through the sieve channels. One way to solve this problem is to pump both sides of the sieve channels independently, which is achieved in H shaped channels series shown in a later section 4.3.

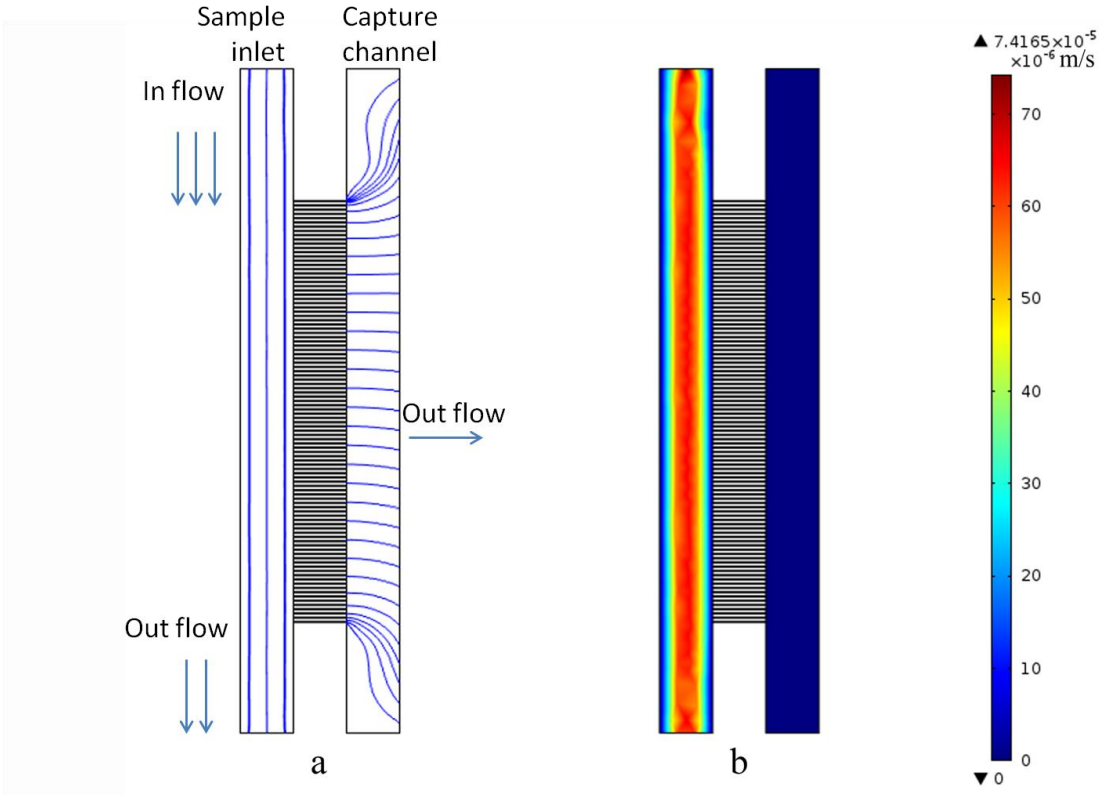

Figure 4.2 Semi-H shaped channels series, (a) Velocity streamline; (b) Velocity magnitude

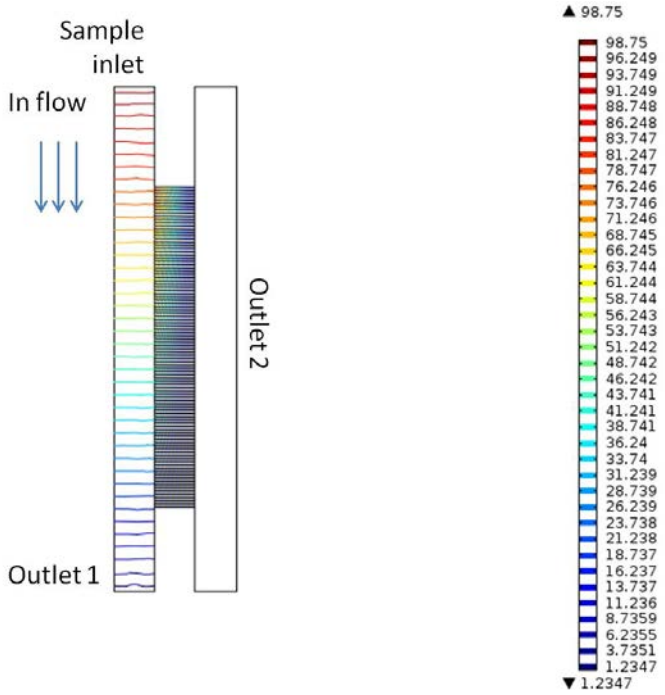

Figure 4.3 Contour pressure in Semi-H shaped channel series (Pa)

Static concentration of target components (Figure 4.4) on both sides of the sieve channels is the same due to the continuous sample input. So a semi-H shaped channel series filter cannot drop down the target component concentration in the sample inlet channel. This phenomenon disables the ability of a multi-level semi-H shaped channels series to purify components except for the smallest target group.

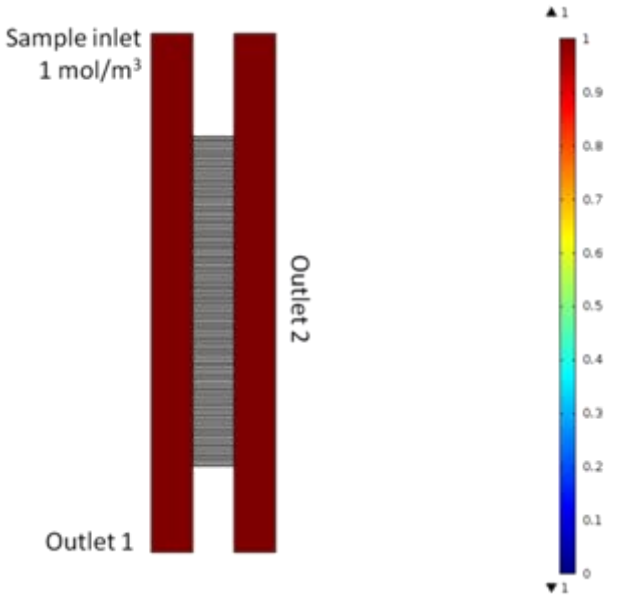

Figure 4.4 Concentration magnitude of 3kDa dextran ($\mathrm{mol/m^3}$)

4.2.3 Multi-level Semi-H shaped channels series

The sample inlet channel was 2 μm x 28 μm and the three capture channels were all 2μmx8μm. There were 400 20 nm sieves, 100 40 nm sieves and 25 80 nm sieves respectively in each level. The spacing between the sieve channels in each level was 20, 40 and 80 nm respectively. All outlet pressures were 0 Pa and the inlet pressure was 100 Pa. The free triangular mesh was drawn by COMSOL physical-controlled mesh automatically (Fine size). Figure 4.5a&b illustrates the velocity streamline and velocity magnitude of 1 mol/m^3 3 kDa dextran aqueous solution in a three-level semi-H shaped channels series filter. Comparing with the capture channels, the sample inlet channel achieved a significantly faster flow which pushed components to keep moving along the inlet channel. Thus it helps to reduce adhesions on the interface between the sieves and the inlet channel. Table 4.1 shows the static flow rates of each channel. It can be seen clearly that there is low flow rate in the capture channels, which means low efficiency of filtration process. The low flow rate also caused a problem in multi-level filtration regarding the concentration, which will be described later.

Table 4.1 2D flow rate for each channel of the three-level semi-H shaped filter ($\mu m^2/s$)

Channel	Sample inlet	Capture 1	Capture 2	Capture 3
Flow rate	88.56	0.4895	0.7411	0.9612

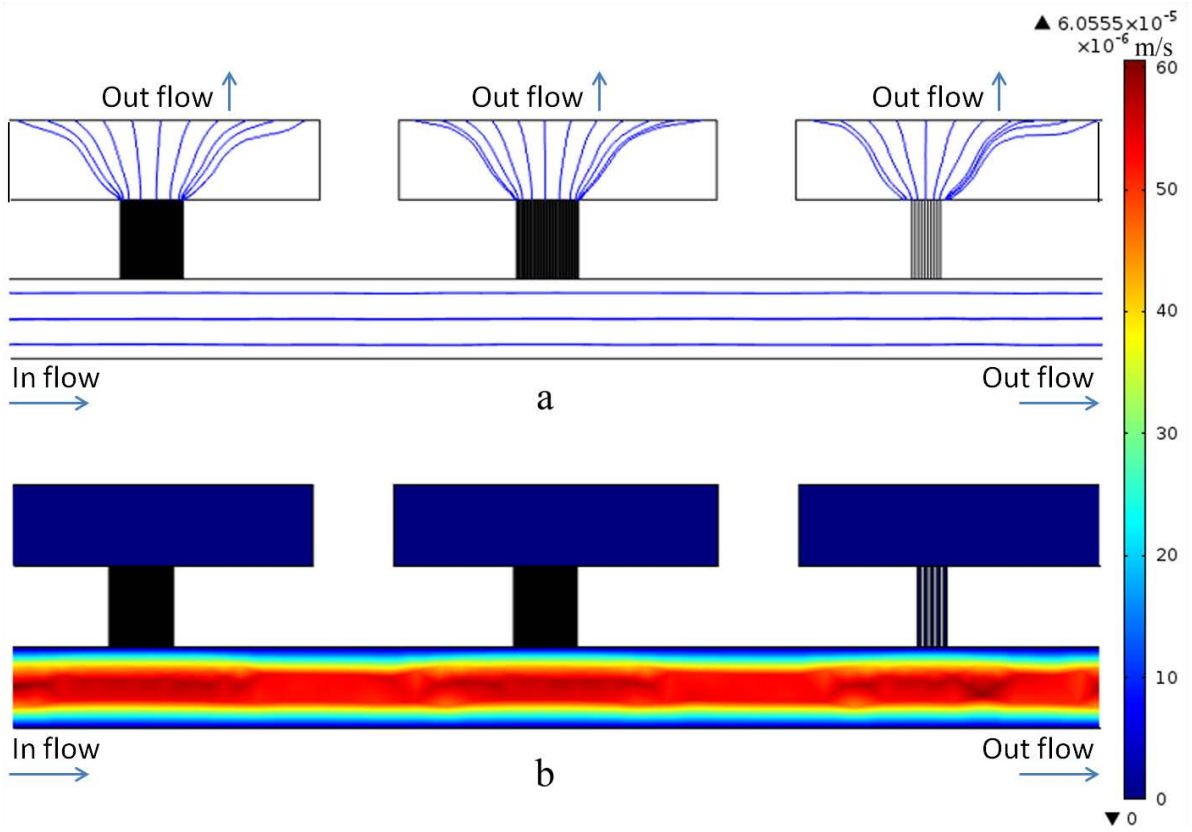

Figure 4.5 Three levels semi-H shaped channel series, (a) Velocity streamline; (b) Velocity magnitude

The response time of the three level semi-H shaped channels series are exhibited in Figure 4.6. The red line shows the concentration $c_{1,1}$ (component 1, the 3kDa dextran, in the first level) at the end of the capture channel 1, the green line represents $c_{2,1}$ of capture channel 2 and the blue line is $c_{3,1}$ of capture channel 3. The initial concentration in the three-level filter was zero. At the beginning the stream flowed into the sieves according to the sequence order. Thus the increasing of concentration in the three-level filter started in spatial sequence. During this period both convection and diffusion occurred. Thus the first level responds fastest. By the end of the simulation, all levels achieved a similar concentration. During the mass transfer process, the outlet concentration increases; this results in the concentration gradient of the small group across the sieve channels reducing until almost zero due to the equilibrium of the concentration. The diffusion flux,

correspondingly, decreases to almost zero. Finally the static concentration of the small group is almost uniform everywhere. The response time relates to the input flow rate and concentration of the sample, the diffusion coefficient and the sieve length. Hence the component 1 (3kDa dextran) responds fastest as it has the highest diffusion coefficient.

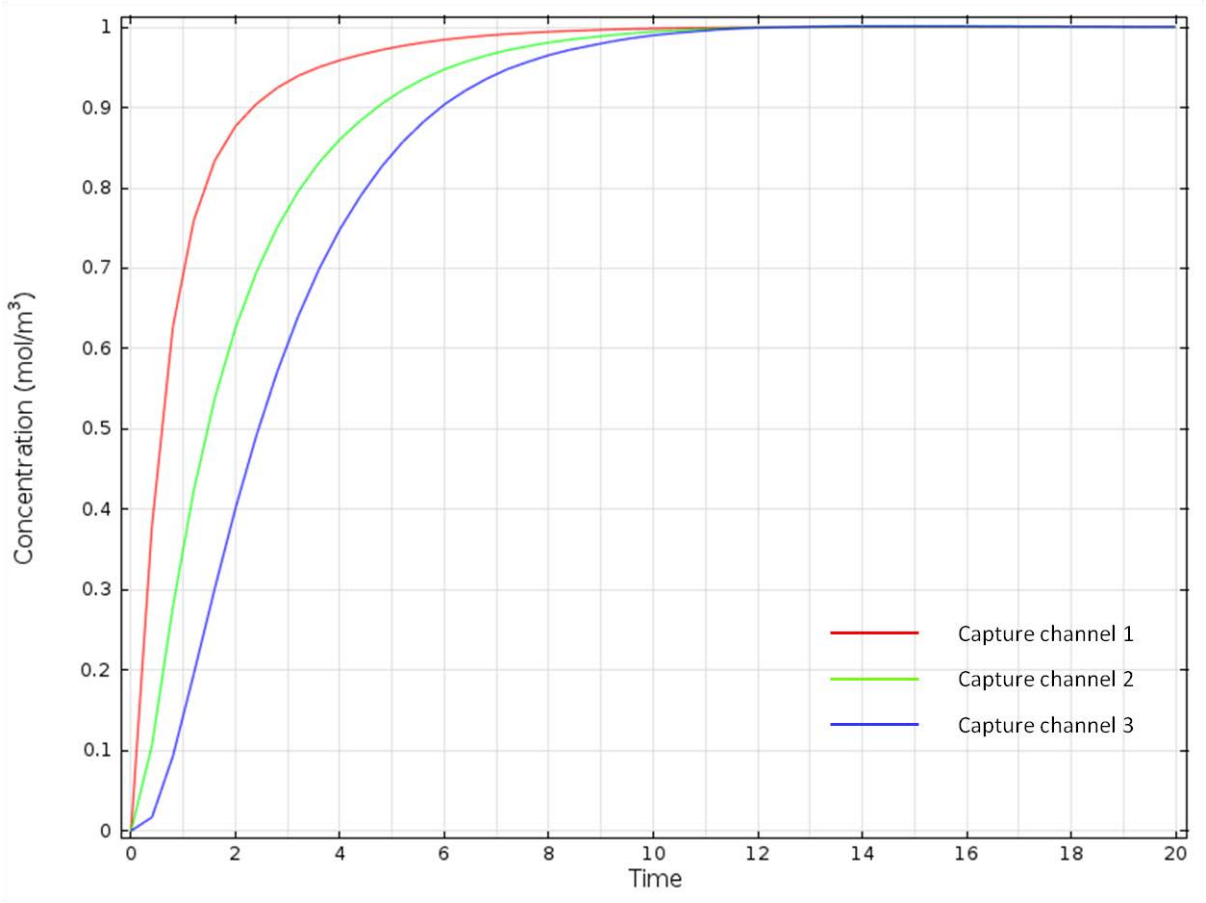

Figure 4.6 Curve of the outlet of each capture channel

The static concentration of 3kDa dextran in the three levels of semi-H shaped channels series is shown in Figure 4.7. The concentration in each capture channel was similar, and did not drop down by 50% after each level of filtration as it was hoped for the multi-level filter based on H shaped channels. This behaviour is because in the semi-H channel series with single inlet, the convection dominates the mass transfer. As the convections of solvent and the small solute are the same; although the diffusion coefficient of each component is different, a uniform concentration is observed. Therefore it is not able to purify the medium

or large components from the small ones. The diffusion coefficient only affects the response time of each component in the same level significantly. For the micro components there is a concentrating effect along the surface of the filter[62], however, the concentrated components at each outlets mixed together again due to the Fick's law. Thus the outlet concentration does not increase due to the concentrating.

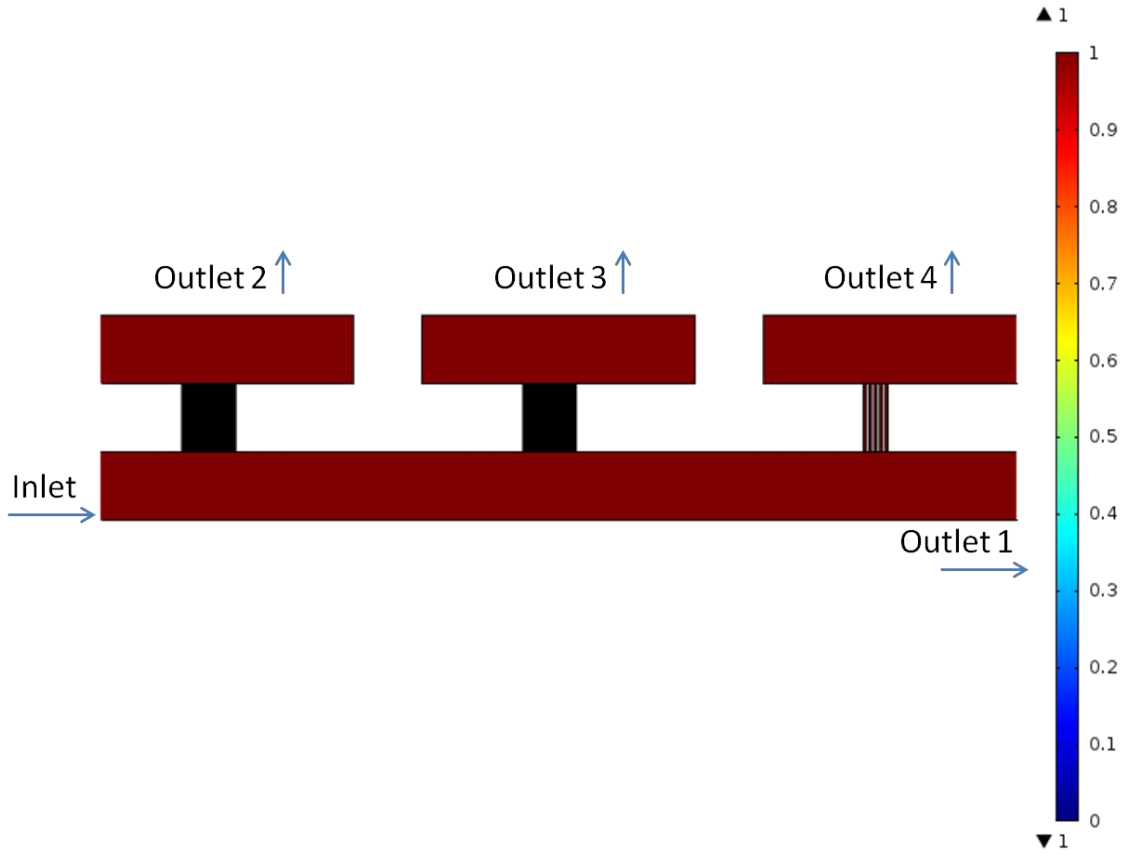

Figure 4.7 Static concentration distribution of a three-level semi-H shaped filter (mol/m^3)

4.3 Simulations on H Shaped Channels Series

As it was introduced in previous section 3.3.2, the simulations on H shaped channels series were studied in this section. In these simulations the similar geometry model were used as the one in section 4.2.1. The sample inlet channel and capture channel were both 2 x 50 µm. The number of the sieve channels will be discussed with different sieve diameter in section

4.3.1. The settings of the laminar flow module were also the same as section 4.2.1 except that there two parallel inlets both with 100 Pa pressure and two outlets with 0 Pa, which are shown in Figure 4.8. The concentration of the 3 kDa dextran solution at the sample inlet was 1 $\mathrm{mol/m^3}$ while 0 $\mathrm{mol/m^3}$ at the capture inlet. The free triangular mesh was drawn by COMSOL Multiphysics® physical-controlled mesh automatically (Fine size option).

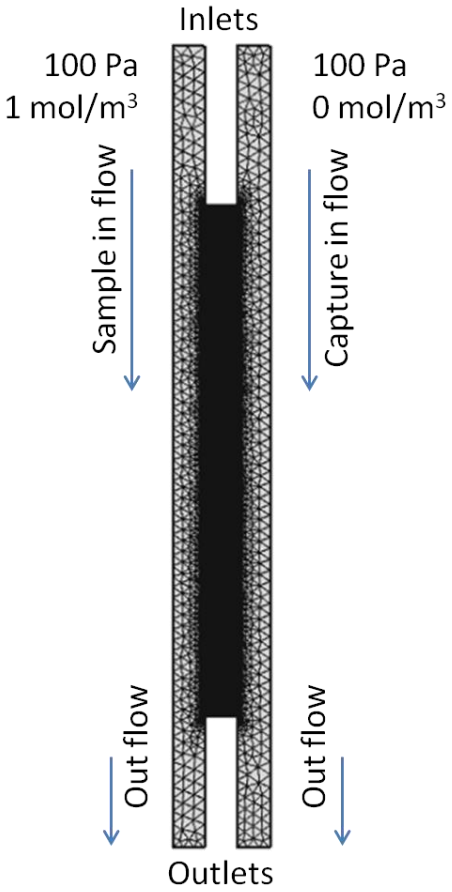

Figure 4.8 The scheme of the H shaped channel series

4.3.1 Statistic concentration vs. Number of H Shaped Channels series

As it was discussed in the previous chapter, the relationship of channel size and number of channels can be described by Equation 3.12, which is

$$N_i \propto \gamma \frac{wd}{a_i^2}$$

Where N_i is the minimum number of i level sieves;

w is the width of sample inlet entrance;

d is the depth of inlet entrance;

a_i is the depth and width of sieve channel;

γ is a constant.

For finding an appropriate value of γ, a group of simulations was designed which are shown in Table 4.2.[154, 155] Because N_i is a natural number, in the group N6, $N_i = 1$. When $\gamma = 1$, the total area of the entrances of sieves is equal to the area of the sample inlet; and the capture concentrations are close to the ideal value from Table 4.2. Thus the Equation 3.12 mostly makes a close but insufficient estimation (except N9) for N_i when $\gamma = 1$. This is because of the isotropic diffusion in porous medium (Equation 2.8). In contrast when $\gamma = 2$, sufficient estimations are achieved in all groups of the table.

Table 4.2 Simulation experiment on constant γ

No.	γ	a_i (nm)	$w = d$ (nm)	N_i	$c_{1,1}(\mathrm{mol/m^3})$
$N1$	1	20	20	1	0.49858
$N2$	1	200	200	1	0.48467
$N3$	1	2000	2000	1	0.42026
$N4$	2	20	200	200	0.5
$N5$	2	200	2000	200	0.5
$N6$	2	2000	20	1	0.5
$N7$	0.5	20	2000	500	0.49882
$N8$	0.5	200	2000	50	0.49879
$N9$	1	20	200	100	0.5

When is $\gamma = 1$ a sufficient index number for the estimation equation 3.12? Table 4.3 studies the relationship between the number of the sieve channels and the concentration of 3 kDa dextran at the capture outlet with different sieve channel sizes; when $\gamma = 1$, $w = 2000$ nm and $d = a_i$. It can be seen that the concentration drops when the diameter of the sieve channel increased over a point between 100 and 200 nm. This is because the distance from the first sieve channel to the last decreases with the increasing sieve diameter. As the flow rate in the sample channel is the same in every simulations in this table, the time cost by the inflow to pass the sieve area declines meanwhile. So less amount of substance of dextran can diffuse through the sieve channels. Hence at the outlet of the capture channel, the capture concentration of the dextran drops down.

Table 4.3 Concentration of 3 kDa dextran at the outlet of capture channel with different size sieves (γ=1) ($\mathrm{mol/m^3}$)

a_i (nm)	20	40	80	100	200	400	800	1000	2000
$c_{1,1}$	0.5	0.5	0.5	0.5	0.4981	0.4729	0.4613	0.4273	0.4203

4.3.2 Static Flow Properties of H Shaped Channels series

After determining the sufficient amount of sieve channels to achieve a maximum concentration in the capture channel, the static flow properties were studied. A 200 40nm H shaped sieve series was simulated. The velocity streamline and velocity magnitude of H shaped channels series are exhibited in Figure 4.9a&b. Comparing with semi-H shaped channels series (Figure 4.2), the flow properties of the inlet sample channels are similar. The only difference is that there is no convection in the sieves channels. It also achieved same velocity in the capture channel as in the sample inlet channel. Thus H shaped channels

series solves the pump problem of semi-H shaped channels series which was discussed in section 4.2 by providing a flow in the capture channel.

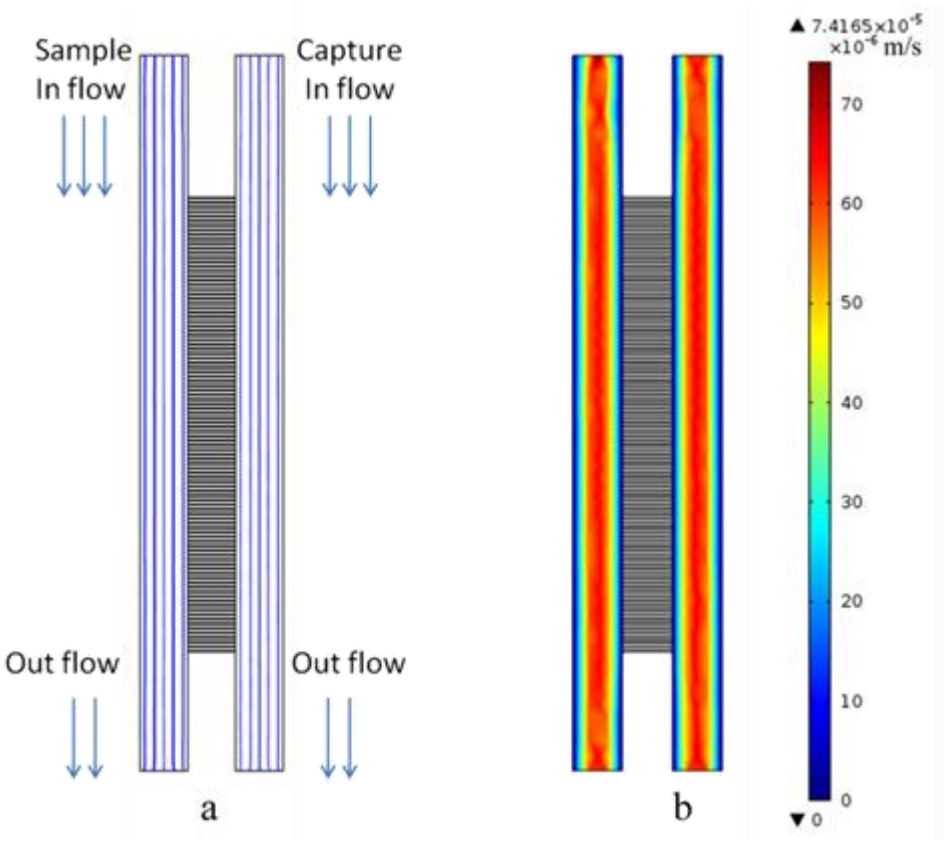

Figure 4.9 H shaped channel series (a) Streamline, (b) Velocity magnitude.

The flux streamline which is shown in Figure 4.10a appeared as a U shape. Thus there were back fluxes towards the inlet of the capture buffer solution (here the buffer is water). The bottom U shape flux streamlines ends at the middle of the sieve series. As the flux streamline starts from the sample inlet where the concentration is 1 $\mathrm{mol/m^3}$ and ends at the capture inlet where the concentration is 0 $\mathrm{mol/m^3}$; obviously the concentration at the middle (bottom) of this flux streamline is 0.5 $\mathrm{mol/m^3}$. After this point, the concentration of downstream flows keeps the same 0.5 $\mathrm{mol/m^3}$. Thus there was sufficient diffusion between the sample inlet channel and capture channel. Whereas the W shaped flux streamline of a single H shaped channel represented insufficient diffusion (Figure 3.5). This is why a single H

shaped channel is not able to achieve a concentration as high as 50% of the inlet concentration. Thus a U shaped flux streamline can be used as a criterion for N_i besides the Equation 3.12.

The contour pressure is shown in Figure 4.10b. Due to the same pressure difference between inlets and outlets, the pressure between two sides of the sieve channels is zero. This is why there is no convection in the sieve channels. If the pressure were asymmetric, there should be convection from the higher pressure side to the lower pressure side. The contour pressure explains the reason of the fast flow in the sample inlet and capture channels as well.

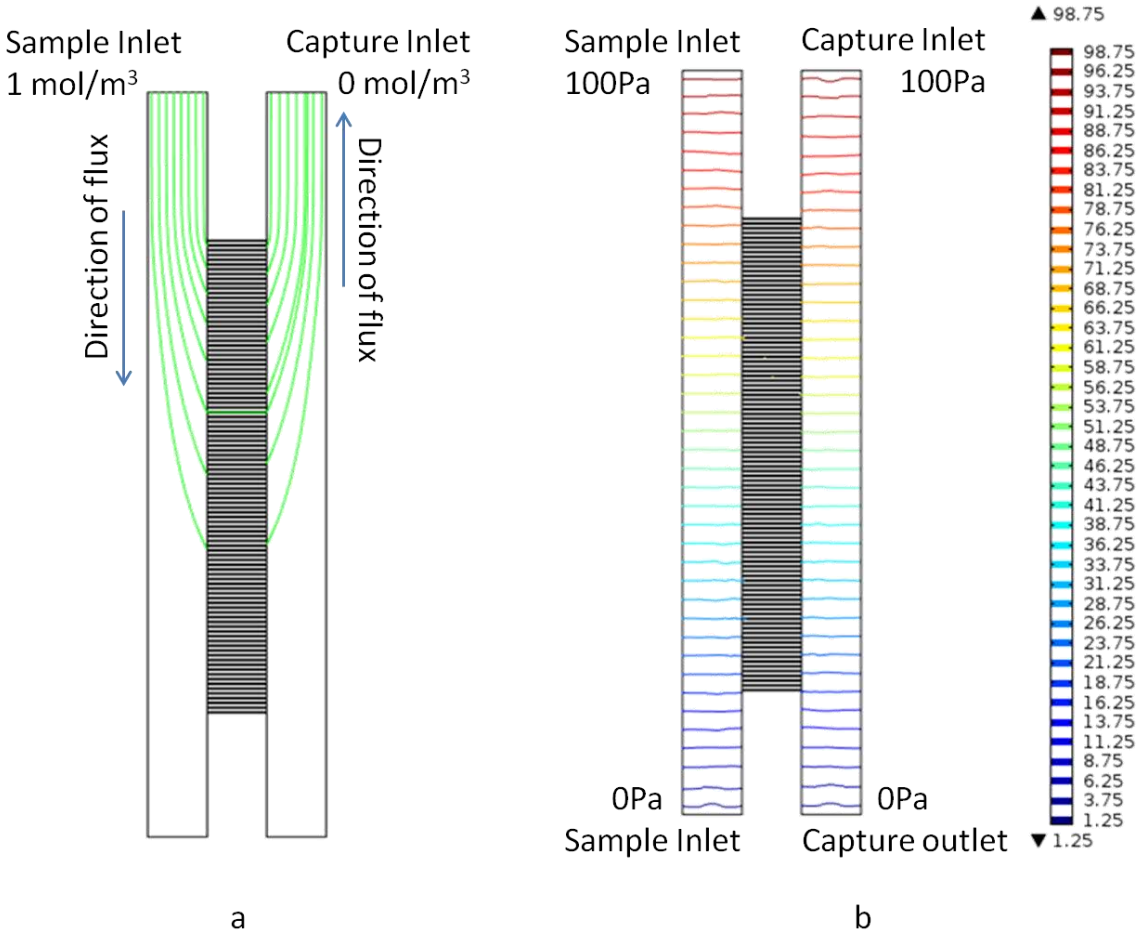

Figure 4.10 H shaped channel series (a) Flux streamline; (b) Contour pressure (Pa).

4.4 Simulation on Angular H Shaped Channels Series

As it was introduced in previous section 3.4, the simulations on angular H shaped channels series were studied in this section. In these simulations the similar geometry model were used as the one in section 4.3. The sample inlet channel and capture channel were both 2 x 50 µm. The angle and number of the sieve channels will be discussed with different sieve diameter in section 4.4.1. The settings of the laminar flow module were also the same as section 4.3 where both inlets pressure were 100 Pa and both outlets were 0 Pa. The concentration of the 3 kDa dextran solution at the sample inlet was 1 $\mathrm{mol/m^3}$ while 0 $\mathrm{mol/m^3}$ at the capture inlet. The free triangular mesh was drawn by COMSOL Multiphysics® physical-controlled mesh automatically (Fine size option).

4.4.1 Concentration vs. Number vs. Angle

As it was mentioned that for a single angular H shaped channel the concentration in the outlet of the capture channel should vary with the angle θ (section 3.4.2) if the inlet length was ignored, the question is now what would happen when there is a series of angular H shaped channels? If the upper limit of concentration is not 50%, what number of sieve channels shall be used to achieve a maximum concentration? Table 4.4 shows the relationship of concentration $c_{1,1}$, angle θ and number of sieve channels; which is $c_{1,1}(\theta, N)$. Here the entrances of the sample inlet channel and the capture channel are both $2\ \mathrm{m} \times 40\ \mathrm{nm}$ and the entrance of sieve channel is $40\mathrm{nm}\times40\mathrm{nm}$. It can be seen from the table that for H shaped channels series ($\theta = 0°$), the upper limit of concentration is 0.5 $\mathrm{mol/m^3}$. When reaching the upper limit, adding sieve channels was not able to increase concentration anymore. For angular H shaped channels series, the concentration increased when the angle decreased, and the minimum channels for sufficient diffusion (maximum

outlet concentration) increased as well. For the 400 channels group, concentration decreased comparing with 300 channels group. There was longer time for the inflow to diffuse due to the increased length of cross section. The capture concentration $c_{1,1}$ in the table i.e. $c_{1,1}(-80,400) = 0.5603,$ exceeds the upper limit which is 50% of the H shaped channel series; due to the entrance length was ignored (Referring to section 3.4.2, Figure 3.17). If the amount of sieve channels are kept increasing, the concentration will finally become 0.5 $\mathrm{mol/m^3}$. Therefore for the number of sieve channels it is not the more the better. Besides the parameters in Equation 3.12; the parameters which affect the best amount of sieve channels are the angle, the distance between the sample inlet channel and capture channel, and the distance between the sieves and the entrance of inlet channel.

Table 4.4 Capture concentration with different angel and number of sieves ($\mathrm{mol/m^3}$)

N	-80°	-70°	-60°	-45°	-30°	-15°	0°
100	0.4977	0.5158	0.5177	0.5139	0.5082	0.5021	0.4955
200	0.5388	0.5250	0.5223	0.5157	0.5091	0.5035	0.50
300	0.5637	0.5378	0.5261	0.5162	0.5097	0.5046	0.50
400	0.5603	0.5360	0.5250	0.5155	0.5093	0.5044	0.50

4.4.2 Static Flow Properties of Angular H Shaped Channels series

The main difference of flow properties between the H shaped channels series and the angular H shaped channels series is the flow rate in the angular sieve channels. The relationship is similar as H shaped channels (section 3.3.1) and angular H shaped channels (section 3.4.1). The convection is caused by the inertia and pressure gradient on the sieve channel series. Although the sieve channels change the pressure distribution in both sample inlet channel and capture channel to reduce the pressure gradient on sieve channels, there

are corresponding increases of pressure gradients on sieve channel series with the angle magnitude, which is shown in Figure 4.11a. It has been mentioned that fine sieve channels are possible to prevent the convection. Here an example of very low convection in sieve channels is exhibited in Figure 4.11b&c. (Figure 4.11b describes the velocity streamlines and Figure 4.11c exhibits the velocity magnitude of angular H shaped channels series.) The flux streamline is shown in Figure 4.11d, which formed an asymmetric U shape. The bottom of U shaped flux streamline does not reach the bottom of sieve channel area, which represents that there is sufficient diffusion.

However, it should be mentioned that due to the no slip boundary condition, the 2D modelling assuming the depth of channels are infinite. Further studies of the 3D modelling of angular H shaped channels series flow properties are discussed in Chapter 6.

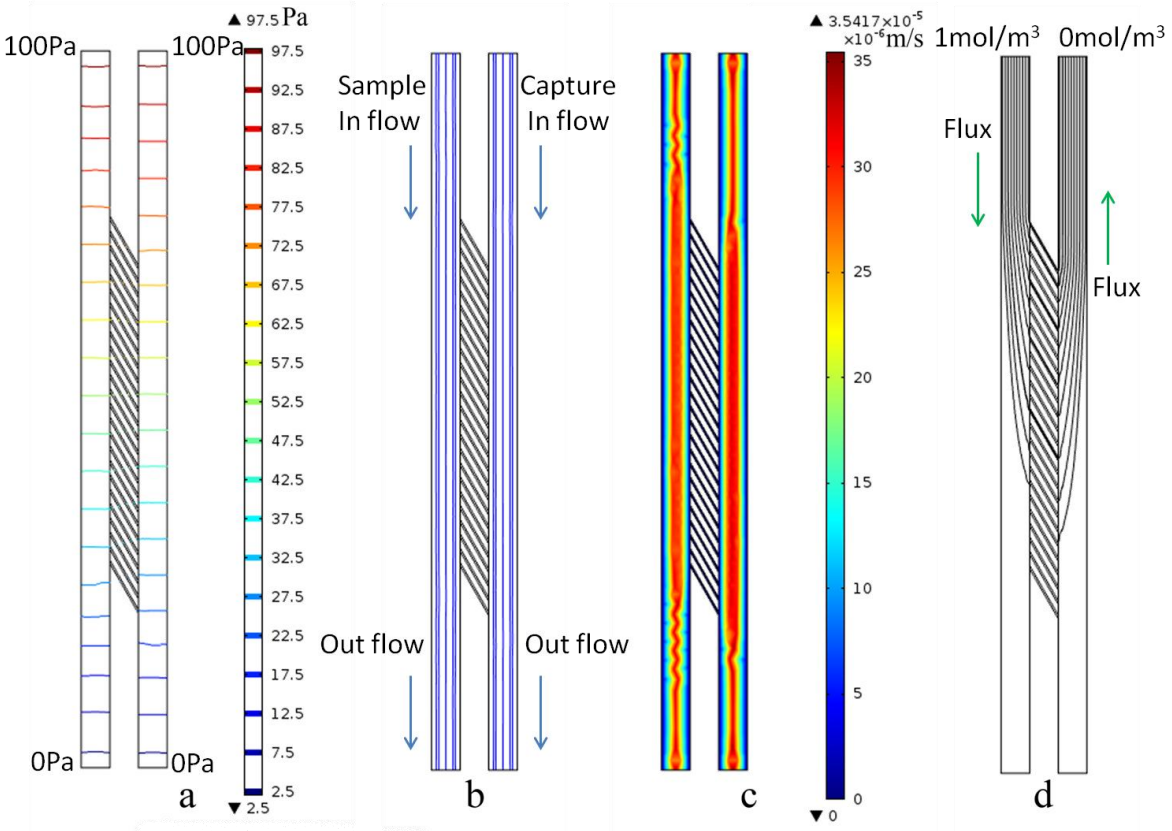

Figure 4.11 Angular H shaped channel series when $\boldsymbol{\theta = -60°}$ (a) Contour Pressure, (b) Velocity streamline, (c) Velocity magnitude and (d) Flux streamline.

4.4.3 Dynamic Properties of Angular H Shaped Channels series

It was mentioned that the response time relates to the volume of sample solution, the diffusion coefficient of target components and the length of the sieve channels. There are no apparent relation among response time, with the size and number (*N*) of sieve channels. So the question is, what is the effect of the amount of sieves? Table 4.5 shows response time $T_{i,j}$ of component j with different size of sieve a_i and different number of sieve channels N; where $w = 2{,}000\ \text{nm}, d = 80\ \text{nm}$. It is seen that a stable output is able to be achieved in one minute. This shows the potential of real time applications.

Table 4.5 Response time for different size and number of sieve channels

a_i (nm)	N	$c_{i,j}$ (mol/m^3)	$T_{i,j}$ (s)
40	100	0.4754	33
40	200	0.4895	42
80	100	0.4866	48
80	200	0.4902	35

4.5 Simulation on Multi-level Filter

For the properties of H shaped channel series discussed above, it is able to be applied with both microcomponents and nanocomponents. Based on the design and analysis of multi-level filters in the last chapter, a 2D three-level filter design is built and simulated with COMSOL Multiphysics® software in this section to examine the design and show its practicability. The amounts and sizes of the three-level sieve channels were $1000\ a_1 = 20\ \text{nm}$, $200\ a_2 = 40\ \text{nm}$ and $40\ a_3 = 80\ \text{nm}$ respectively. (In the 2D simulation the depth is infinite; the number of sieve channels was calculated assuming the depth equal to its

width) For the sample inlet channel and capture channel, there were $w = 2\ \mu\text{m}$ and $d = 1\ \mu\text{m}$. $1\ \text{mol/m}^3$ 3 kDa, 500 kDa and 2000 kDa dextrans were applied as the target components, marking as $j = 1, 2$ and 3 respectively. The diffusion coefficient of 3, 500 and 2000kDa dextran are 7.5e-10, 3.28e-10, and 8.4-e-11 m^2/s respectively. The density of fluid is 1050g/L and the dynamic viscosity is 0.3 Pa·s. All inlets pressures were 100 Pa while outlets pressures were zero. The inlet of capture channel 1,2 and 3 is water where concentration of dextrans was zero. The free triangular mesh was drawn by COMSOL physical-controlled mesh automatically (normal size). The no-slip boundary condition was applied for the laminar flow modules.

Figure 4.12 shows the static concentration distribution $c_{i,1}$ $(i = 1,2,3)$ of $3\ \text{kDa}$ dextran in the three-level filter model. The concentration at each outlet of capture channel is 0.37, 0.05 and $0.01\ \text{mol/m}^3$ respectively. It was mentioned in section 3.5.2 that the ideal outlet concentration should be 0.5, 0.25 and $0.125\ \text{mol/m}^3$ respectively. The difference can be answered by the interaction among different levels. In other words, the distance l_i between adjacent levels is too short. Thus a two level model was simulated first to examine the estimate equation (Equation 3.15) described in section 3.5.2.

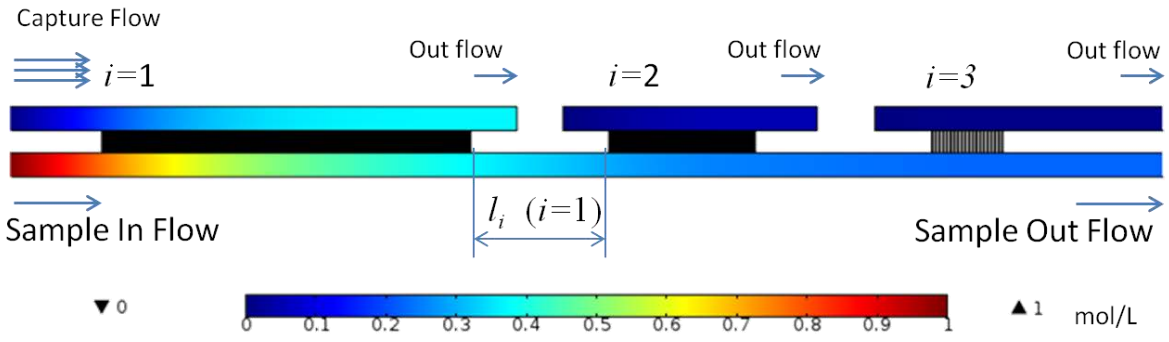

Figure 4.12 Concentration of 3kDa dextran in a three-level filter

4.5.1 Concentration vs. Distance between Adjacent Levels

In this analysis, four different designed errors $\delta_i = \frac{\Delta c_{i,j}^{\text{Sample}}}{c_{i,j}^{\text{Sample}}} = \frac{c_{i,j}^{\text{Designed}} - c_{i,j}^{\text{Sample}}}{c_{i,j}^{\text{Sample}}}$ (Equation 3.14) were given which were 0.5%, 1%, 5% and 10%. $c_{i,j}^{\text{Sample}}$ can be calculated with Equation 3.8. The distance l_i between two adjacent levels ($i = 1,2$) was calculated with Equation 3.15,

$$l_i \geq \frac{N_i w_i}{2\delta_i}.$$

Table 4.6 shows the simulation results where the $N_1 = 250, w_1 = 80\text{nm}, N_2 = 40$ and $w_2 = 160\text{nm}$. Comparing with the demanded error δ_i, the simulated error ($\delta_{\text{simulate}} = \frac{c_{i,j}^{\text{Simulated}} - c_{i,j}^{\text{Sample}}}{c_{i,j}^{\text{Sample}}}$) shows the same tendency. The estimate equation is accurate when $\delta_i = 10\%$. When $\delta_i = 0.1\%$, the result is even better than the designed error.

Table 4.6 Simulation results of capture concentration (mol/m^3) for different l_i

δ_i	0.5%	1%	5%	10%
l_i (mm)	20	2	0.4	0.2
$c_{1,1}^{\text{Simulated}}$	0.4985	0.4901	0.4651	0.4505
$c_{2,1}^{\text{Simulated}}$	0.0145	0.0735	0.1651	0.2339
δ_{simulate}	0.3%	1.98%	6.98%	9.9%

If the application were asked for $\delta_i = 5\%$, a three-level filter is able to be designed based on Equation 3.15 which is shown in Figure 4.13 (using the same settings as Figure 4.12). The capture concentrations of 3kDa, 500kDa and 2000kDa dextran in each level are exhibited in Table 4.7. The errors were similar with the design value. Consequently, Equation 3.15 is suitable for the multi-level filter design.

Table 4.7 Captured concentration of each components when δ_i=5% (mol/m^3)

$c_{i,j}$	$i=1$	$i=2$	$i=3$
$j=1$	0.4586	0.2330	0.1678
$j=2$	0	0.4651	0.1651
$j=3$	0	0	0.5

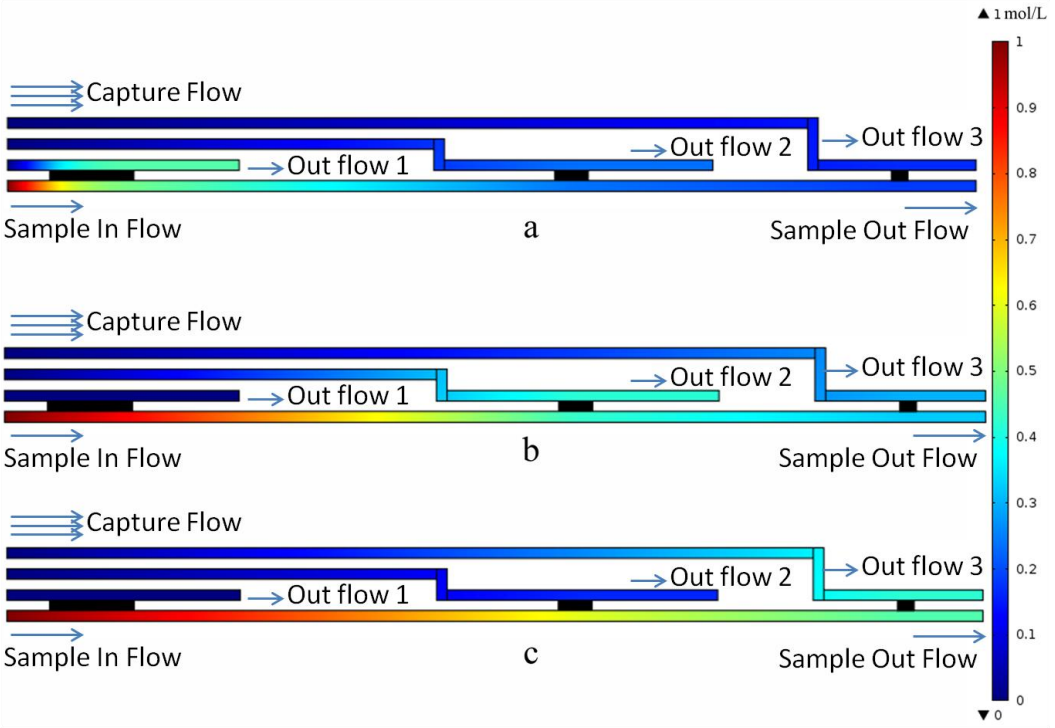

Figure 4.13 Concentration in a three-level filter (a) 3 kDa, (b) 500 kDa, (c) 2,000 kDa dextran

4.5.2 Static Flow Properties of Multi-level Filter

The contour pressure is exhibited in Figure 4.14a. It can be seen that the pressures beside each end of the sieve channels are not equal. Due to the same pump pressure of each channel but different channel length, the pressure gradient varies each channel. Thus there is convection in sieve channels which causes a higher velocity around cross sections. A uniform pressure gradient can be achieved by designing the pump pressure and length of each channel to get steady flow. Figure 4.14b shows the velocity magnitude. A high flow rate in the sample inlet channel and all capture channels can be viewed clearly, which

contributes to adhesion reduction on sieves surface. Hence, comparing with traditional filtration it shows advantages for high throughput applications.

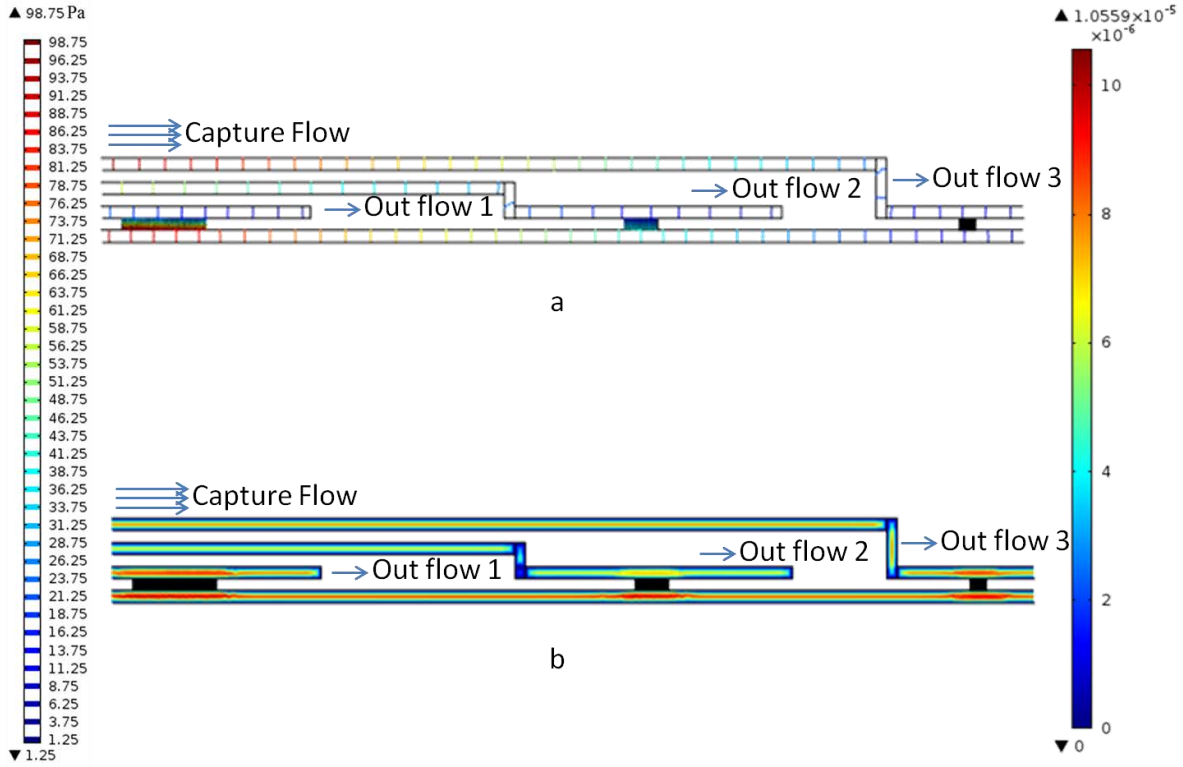

Figure 4.14 The three-level filter (a) Contour pressure, (b) Velocity magnitude m/s.

4.5.3 Multi-level Filter with a Dilute Channel

To improve the performance of a multilevel filter, a dilute channel was added as discussed in section 3.5. So a dilute channel was added on the model which built in last section by creating an additional 'dilute' inlet channel running parallel to the existing inlet and then placing sieves between the new channel and the original inlet (Figure 4.15). The dilute sieves are the same size and number as the former level filter sieves. The simulation result of 3 kDa dextran concentration is illustrated in Figure 4.15 (the inlet pressure of the dilute channel was the same as the other channels i.e. 100 Pa, the outlet pressure was zero, and other conditions are the same as Figure 4.10). Table 4.8 compares the simulation results with ideal values (Equation 3.9), the ones without dilute channel and their ideal values

(Equation 3.8). It can be seen that a dilute channel is able to reduce the concentration of small species ($i < j$) significantly while only decreasing the concentration of the target component ($i = j$) slightly, therefore improving the separation. As the small species are diluted, the chance of clustering reduces as well. Whereas there is a decrease of target component due to the shortened distance between adjacent sieves which is caused by the additional sieves, l_i should be redefined as the distance between the filter sieves and the followed same size dilute sieves. Then the target concentration can keep same level as the ones without a dilute channel which fits the design demands. Consequently the dilute channel is a low cost and efficient tool to assist the multi-level filter to achieve a purer separation.

Table 4.8 Capture concentrations with or without a dilute channel (mol/m^3)

	Without dilute channel	Ideal($c_{i,j}^{\text{Sample}}$)	With a dilute channel	Ideal diluted
$c_{1,1}$	0.4586	0.5	0.4482	0.5
$c_{2,1}$	0.2330	0.25	0.1634	0.125
$c_{3,1}$	0.1678	0.125	0.1338	0.0313
$c_{\text{Sample},1}$	0.1817	0.125	0.1502	0.0313
$c_{1,2}$	0	0	0	0
$c_{2,2}$	0.4168	0.5	0.3677	0.5
$c_{3,2}$	0.3002	0.25	0.2122	0.125
$c_{\text{Sample},2}$	0.3249	0.25	0.2297	0.125
$c_{1,3}$	0	0	0	0
$c_{2,3}$	0	0	0	0
$c_{3,3}$	0.4203	0.5	0.4201	0.5
$c_{\text{Sample},3}$	0.4550	0.5	0.4548	0.5

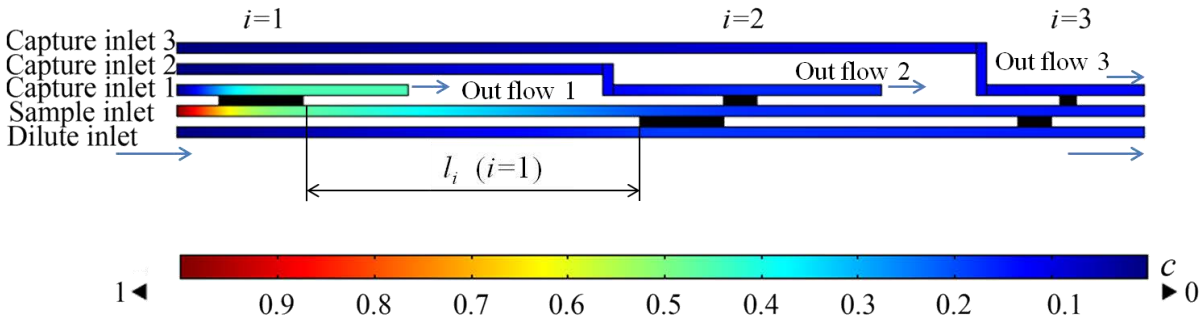

Figure 4.15 Concentration of 3kDa dextran in the three-level filter with a dilute channel

Figure 4.16a shows the contour pressure of a three-level filter with a dilute channel. Because of the pressure difference beside the sieves, convection through the sieve channels dominates the velocity in the sample inlet, capture and dilute channels. So in Figure 4.16b a higher velocity around sieves was observed.

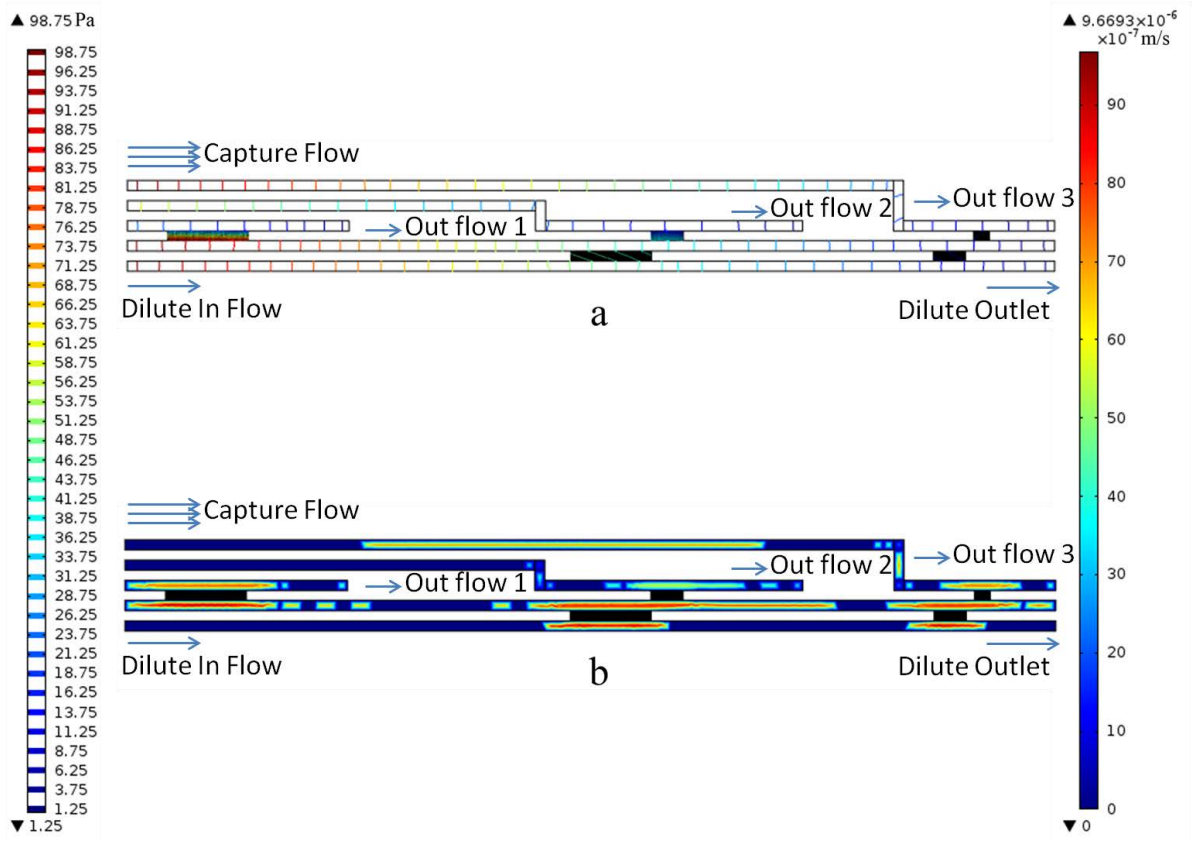

Figure 4.16 The three-level filter with a dilute channel (a) Contour pressure, (b) Velocity magnitude.

4.6 Summary

In this chapter the models discussed in chapter 3, i.e. semi-H shaped channels, H shaped channels and angular H shaped channels; were extended to their series. The mass transfer process was simulated with finite element software COMSOL Multiphysics®. The estimate equations introduced in Chapter 3 were examined as well. Consequently the H shaped channels series showed advantages on relief of adhesion, high throughput and extendibility. Furthermore, simulations on the multi-level filter based on H shaped channels series illustrated the practicability of a filter which consist of H shaped channels series as its basic elements. The principles of a multi-level filter based on H shaped channels series are able to be applied to the design and fabrication of a lab-on-chip multi-level filter. Based on the simulation results in this chapter, chips of multi-level filter are able to be designed. The next chapter will present the progress of multi-level chip design and its fabrication.

CHAPTER 5

3D MODELLING RESULTS

5.1 Introduction

As 2D modelling assumes the depths of each channels are infinite, it is not able to describe the flow properties accurately. In this chapter, further studies on 3D models of one level filters (angular H shaped channels series) are built and analysed with finite element software COMSOL Multiphysics® 4.1a. The results are still given under no-slip boundary condition. Then 3D simulations with slip boundary condition are illustrated and compared with the no-slip results. Finally a 3D model of a three-level filter based on angular semi-H channels is described. It is a model of a simplified angular version of the verification chip designed in chapter 6. The settings of Transport of Diluted Species module and Laminar Flow module are described. The static results of velocity, flow streamline, pressure and concentration distributions are presented and discussed.

5.2 3D No-Slip Modelling of Angular H Shaped Channels Series

5.2.1 Settings and Meshing

In this section, the only variable factor was the angle ($\theta = 0°$, -15°, -30°, -45°, -60° and -75°) of sieve channels. The widths of the sample inlet channel and capture channel were both 5 µm and the depths were both 500 nm. The distance between these two channels was 2 µm. Sixteen sieve channels were applied and the width and depth of them were both 400 nm.

The density, dynamic viscosity and diffusion coefficient of sample fluid were 1050 kg/m^3, 0.03 $Pa \cdot s$ and 1e-9 m^2/s respectively.

The continuity and the Navier-Stokes equations (Equation 2.9 & 2.10) were solved by the Laminar Flow module. The boundary condition in this section is the no-slip condition which means the velocity on the boundary interface is zero. The entrance pressures of both sample inlet and capture channels were 100 Pa, while the exit pressures were 0 Pa. Both the entrance and exit lengths were 1 cm.

The Transport of Dilute Species module was used to solve the continuity and the Nernst-Planck equations (Equation 2.6 & 2.5) with an impenetrable boundary. No reaction and all initial values were set up as zero. The Inlet concentration was 1 mol/m^3 for sample inlet channel and 0 mol/m^3 for the capture channel.

After these settings, the model was meshed by COMSOL. Firstly, free triangular meshes were drawn on the interface between inlet channel and sieve channels. The element sizes were from 50 nm to 200 nm. Then secondly the triangular meshes were swept along the x-axis to form the meshes of sample inlet channel and sieve channels. The swept sizes ranged from 100 nm to 1,000 nm. The third step was drawing the free triangular meshes on the interface between capture channel and sieve channels (50-200 nm). Finally this triangular mesh was swept along the x-axis to form the meshes of capture channel (100-1,000 nm). Figure 5.1 demonstrates the meshes of the 3D model of angular H shaped channel series.

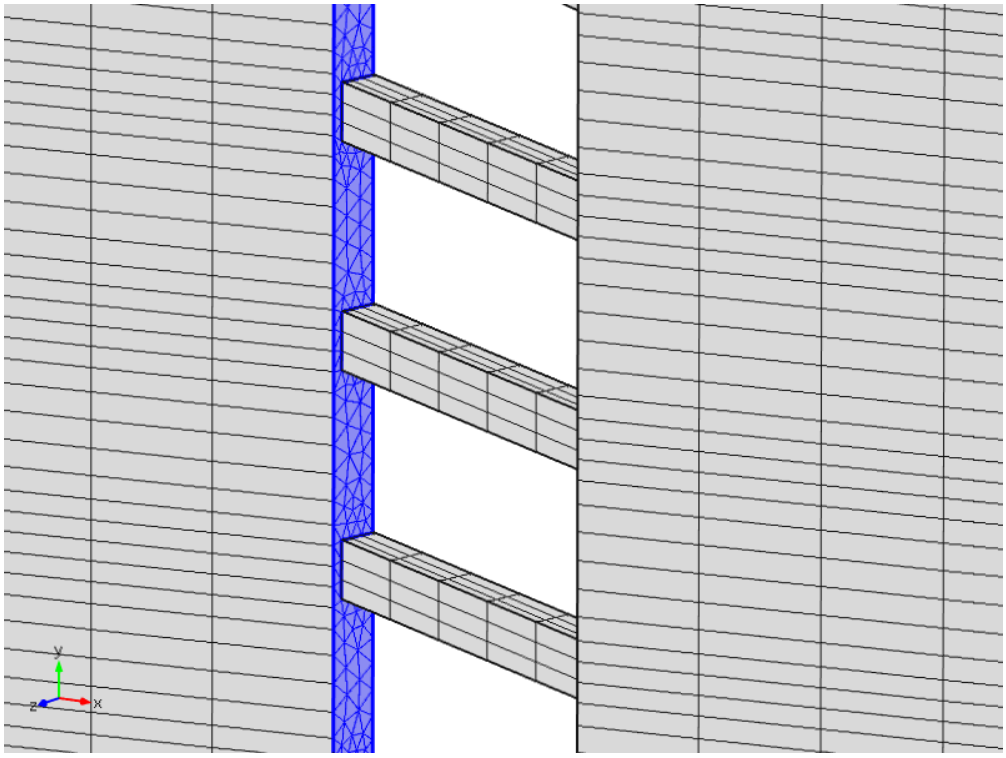

Figure 5.1 Meshing of 3D models ($\boldsymbol{\theta = -15°}$)

5.2.2 Pressure

Figure 5.2a-f shows the contour pressure of the angular H shaped channels series when the angle θ is 0°, -15°, -30°, -45°, -60° and -75° respectively. When θ=0°, the pressure is symmetric on the other side of the sieve channels, which is same as the 2D simulation results. It can be seen that the pressures beside each end of the sieve channel are still similar when the angle magnitude increases, whereas the angle changes the pressure gradient in the sample inlet channel and capture channel. Comparing the results for different angles, there is limited corresponding increase of pressure difference when the angle increased. As finer channels need higher pumping pressure; it is understandable why it is still possible that no convention across in the sieve channel due to the viscose resistance even if the pressure gradient is not zero. More details on the velocity can refer to section 5.2.3 and 5.2.4.

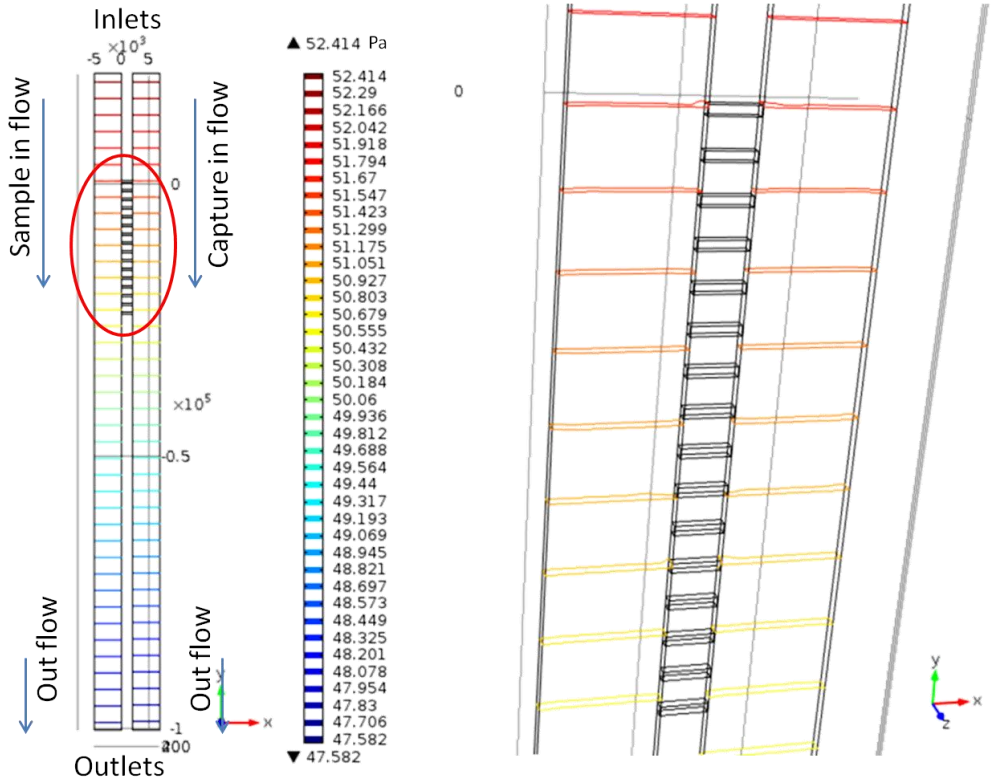

a $\theta = 0^\circ$

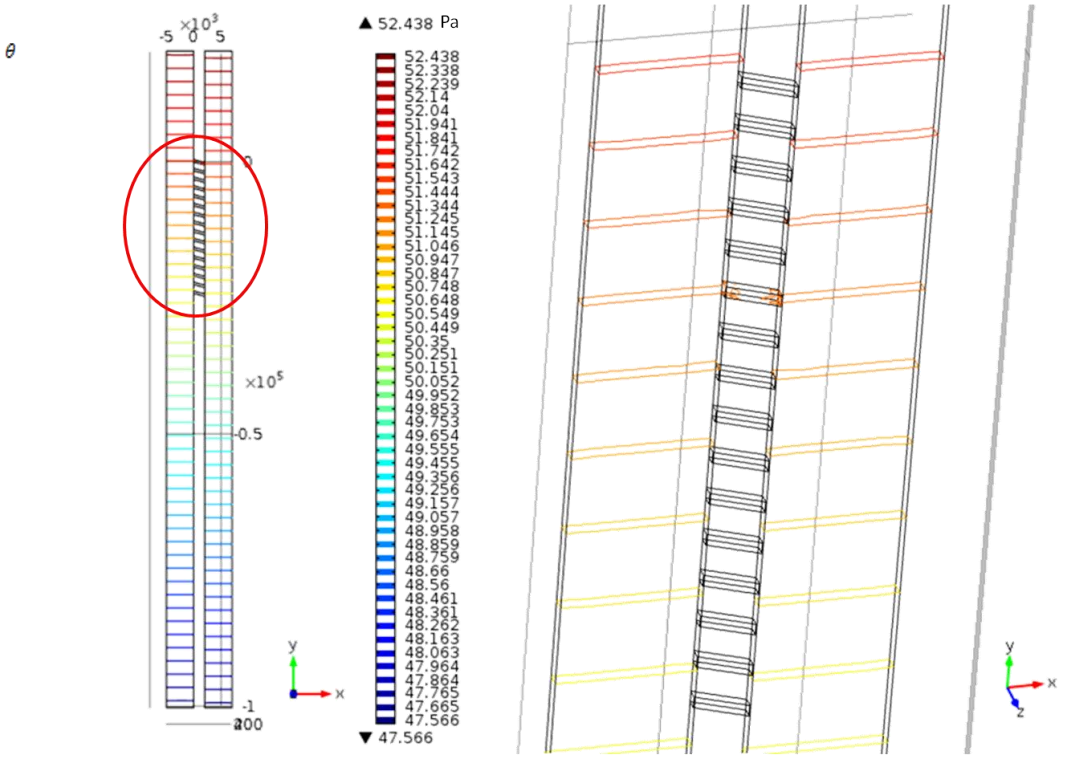

b $\theta = -15^\circ$

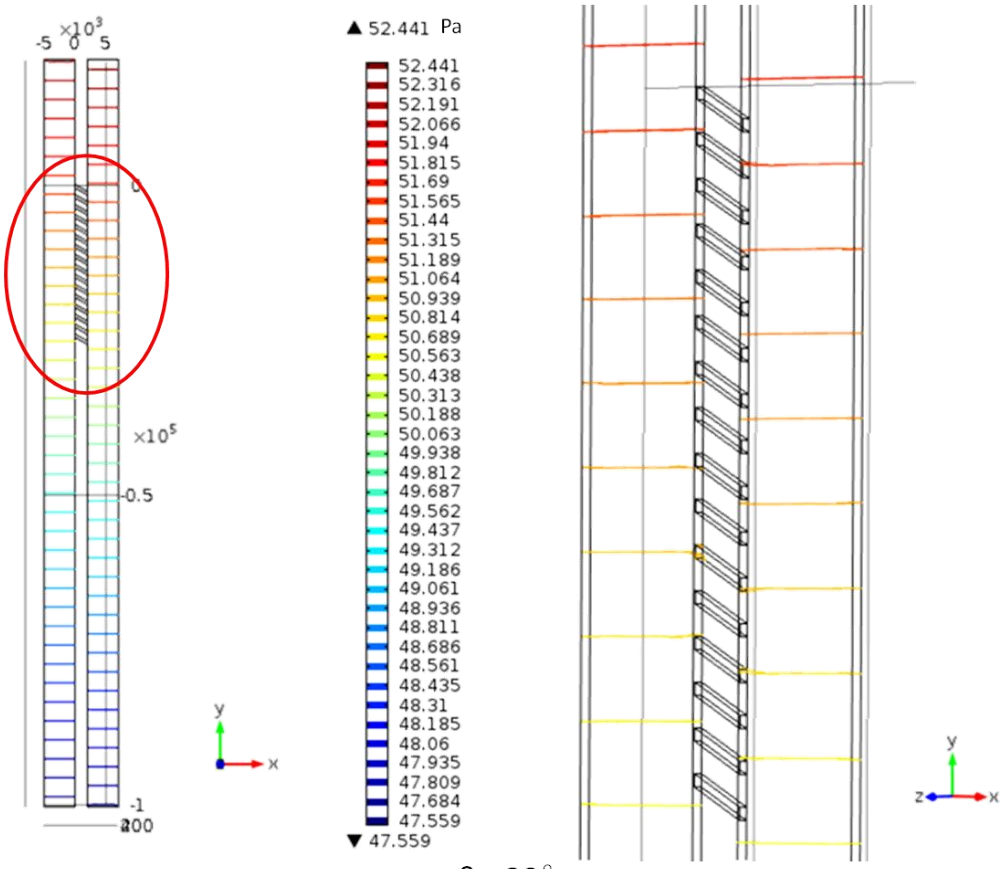
×10³
-5 0 5
×10⁵
-0.5
-1
▲ 52.441 Pa
52.441
52.316
52.191
52.066
51.94
51.815
51.69
51.565
51.44
51.315
51.189
51.064
50.939
50.814
50.689
50.563
50.438
50.313
50.188
50.063
49.938
49.812
49.687
49.562
49.437
49.312
49.186
49.061
48.936
48.811
48.686
48.561
48.435
48.31
48.185
48.06
47.935
47.809
47.684
47.559
▼ 47.559
y
x
z

c θ=-30°

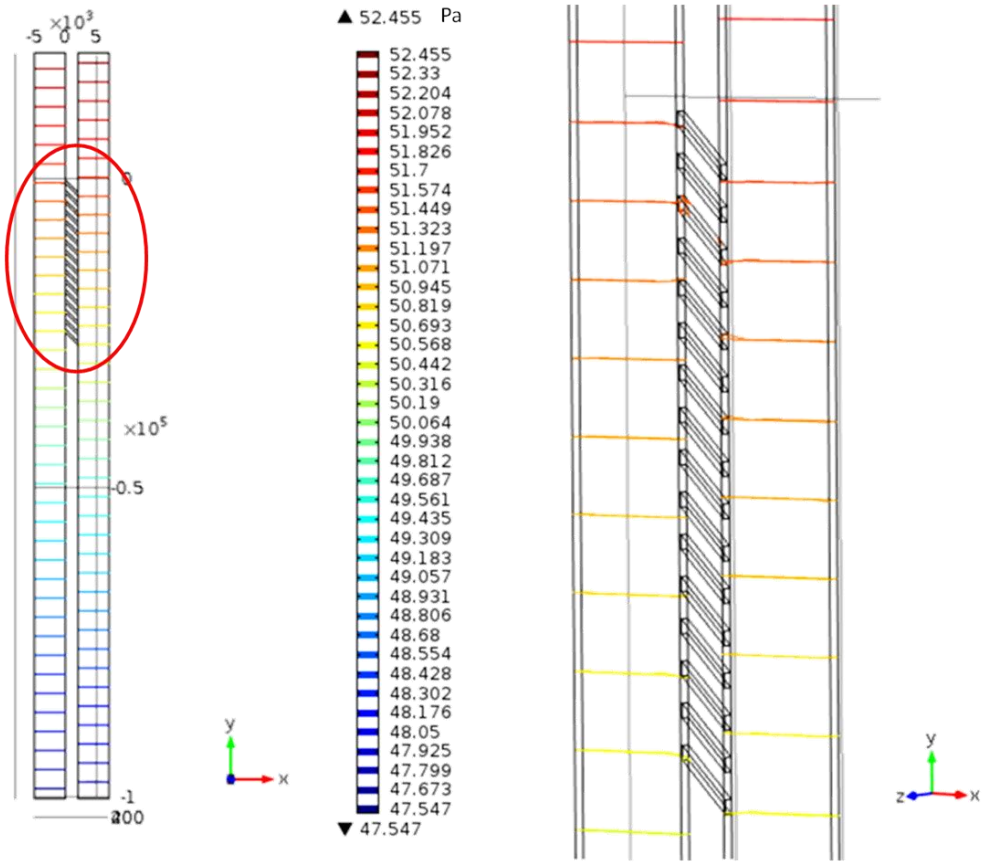
×10³
-5 0 5
×10⁵
-0.5
-1
▲ 52.455 Pa
52.455
52.33
52.204
52.078
51.952
51.826
51.7
51.574
51.449
51.323
51.197
51.071
50.945
50.819
50.693
50.568
50.442
50.316
50.19
50.064
49.938
49.812
49.687
49.561
49.435
49.309
49.183
49.057
48.931
48.806
48.68
48.554
48.428
48.302
48.176
48.05
47.925
47.799
47.673
47.547
▼ 47.547
y
x
z

d θ=-45°

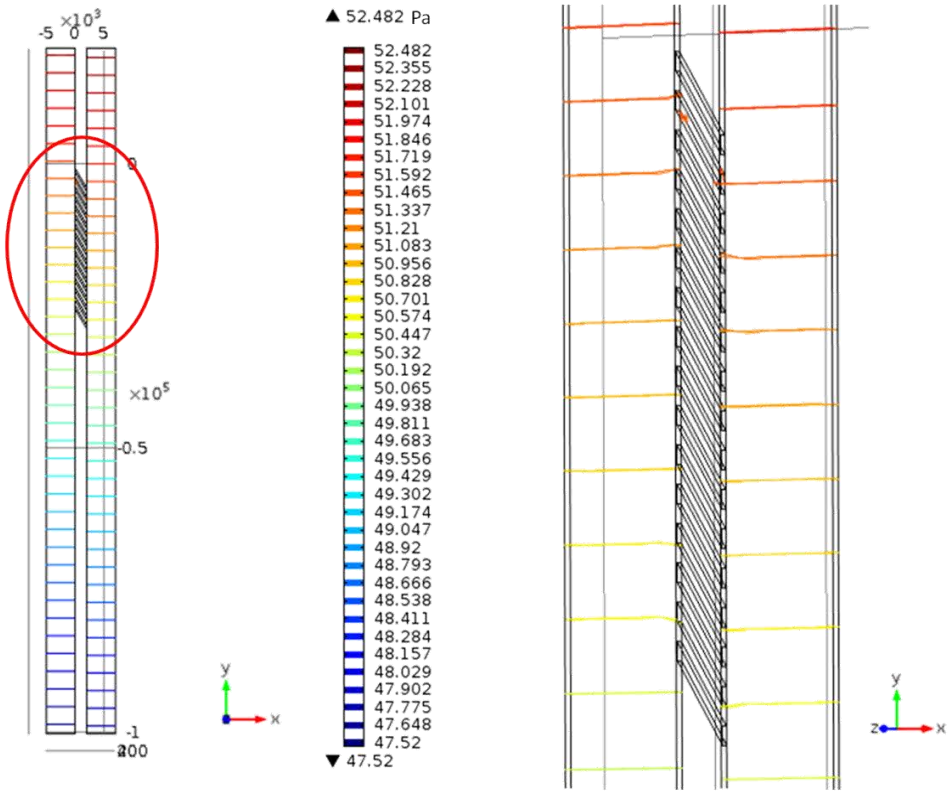

e θ = -60°

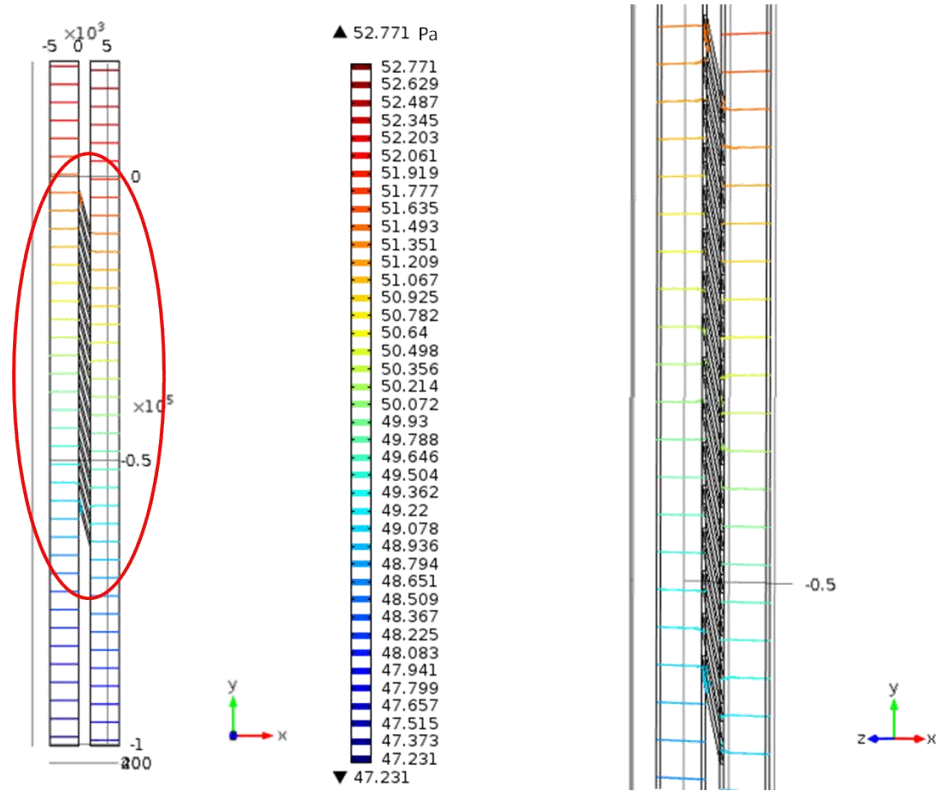

f θ =-75°

Figure 5.2 3D contour pressure of no-slip flow with different angle $\boldsymbol{\theta}$.

5.2.3 Velocity Streamline

The velocity streamlines of different angle angular H shaped channels series are illustrated in Figure 5.3. The streamlines deviate towards the sieve channels on the interfaces between sample inlet channel and sieve channels, and capture channel and sieve channels. A vortex is clearly seen in the sieve channels. This is because of the high aspect ratio of the sieve channel (2 µm/ 400 nm = 5). No vortex was observed in section 3.3.1 due to the low aspect ratio of the sieve channel which was 0.5 µm/0.5 µm = 1. When the angle decreases, the centre of the vortex moves down on the left of the sieve channel and moves up on the right side; accompanied by a decrease of the vortex area.

However, still no convection in the middle of the sieve channels was observed in the streamline. The pressure gradient caused by the angle with a small magnitude was not enough to overcome the viscous resistance. For the large angle magnitude, the increase of the convection in the sieve channels cannot be observed straightforwardly through the streamline pictures compared with the high velocity main flow. Thus more information about convection across the sieve channels refers to the next section about velocity.

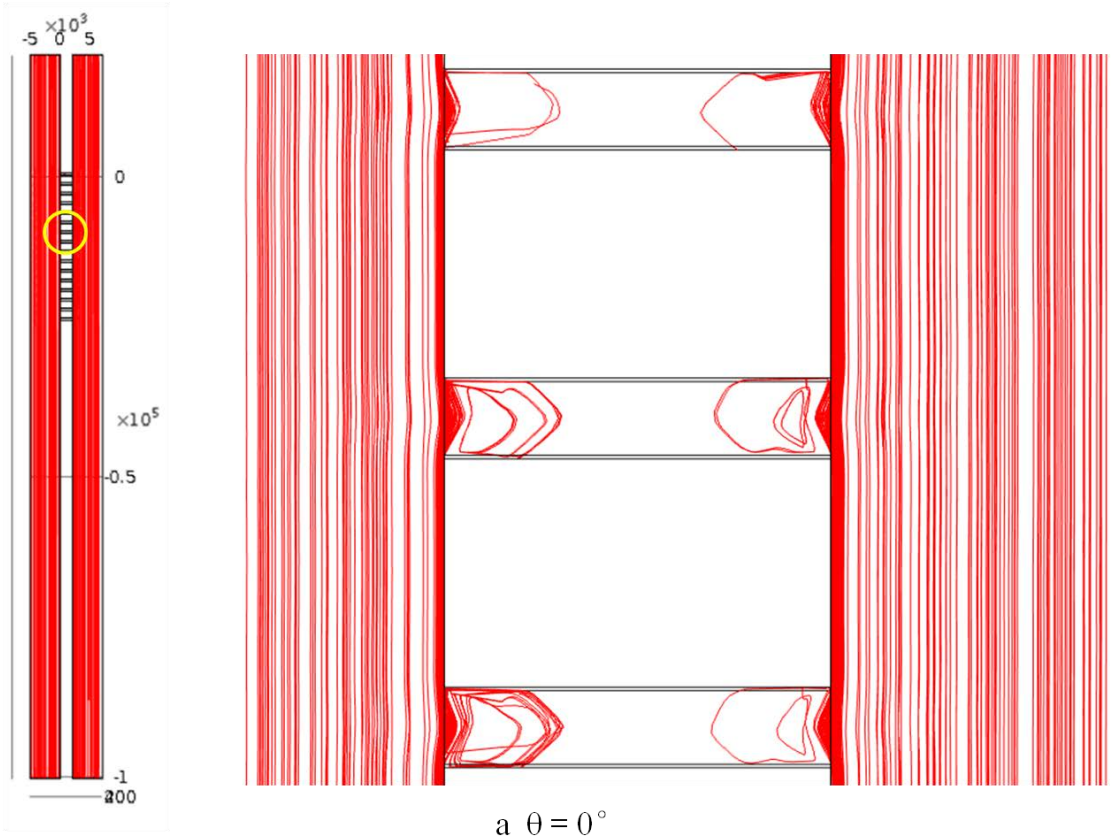

a $\theta = 0^\circ$

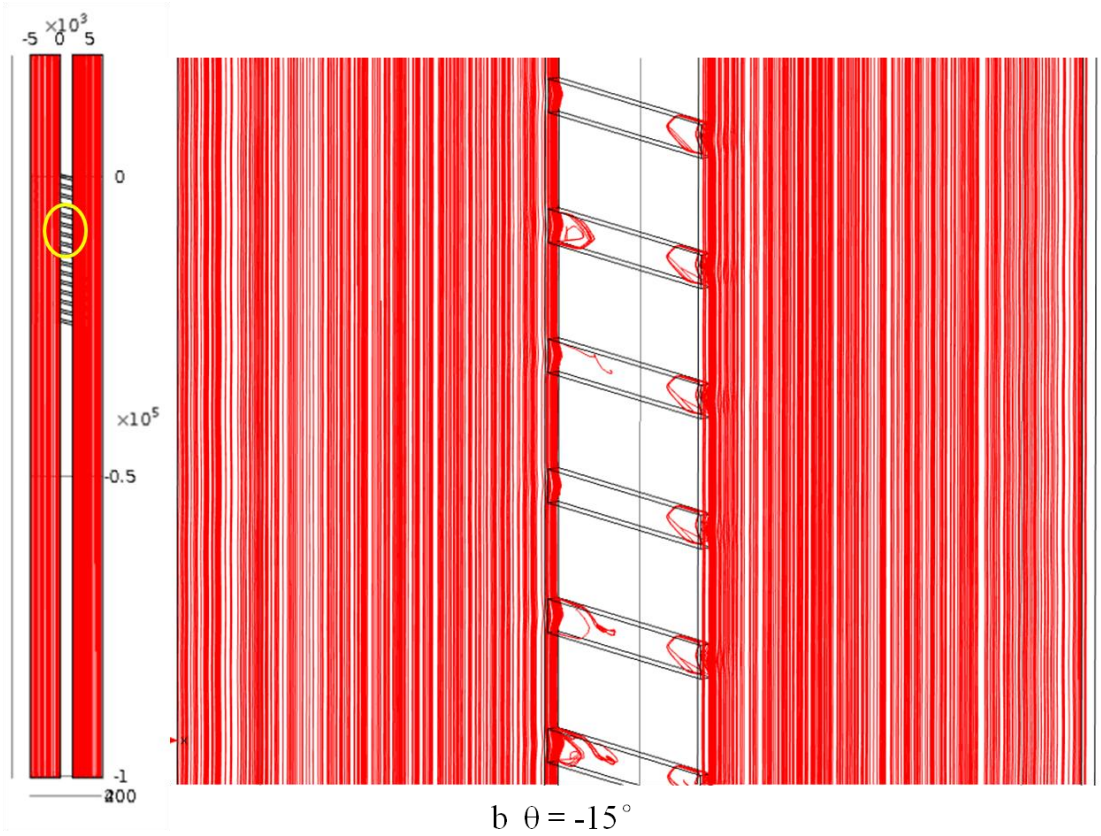

b $\theta = -15^\circ$

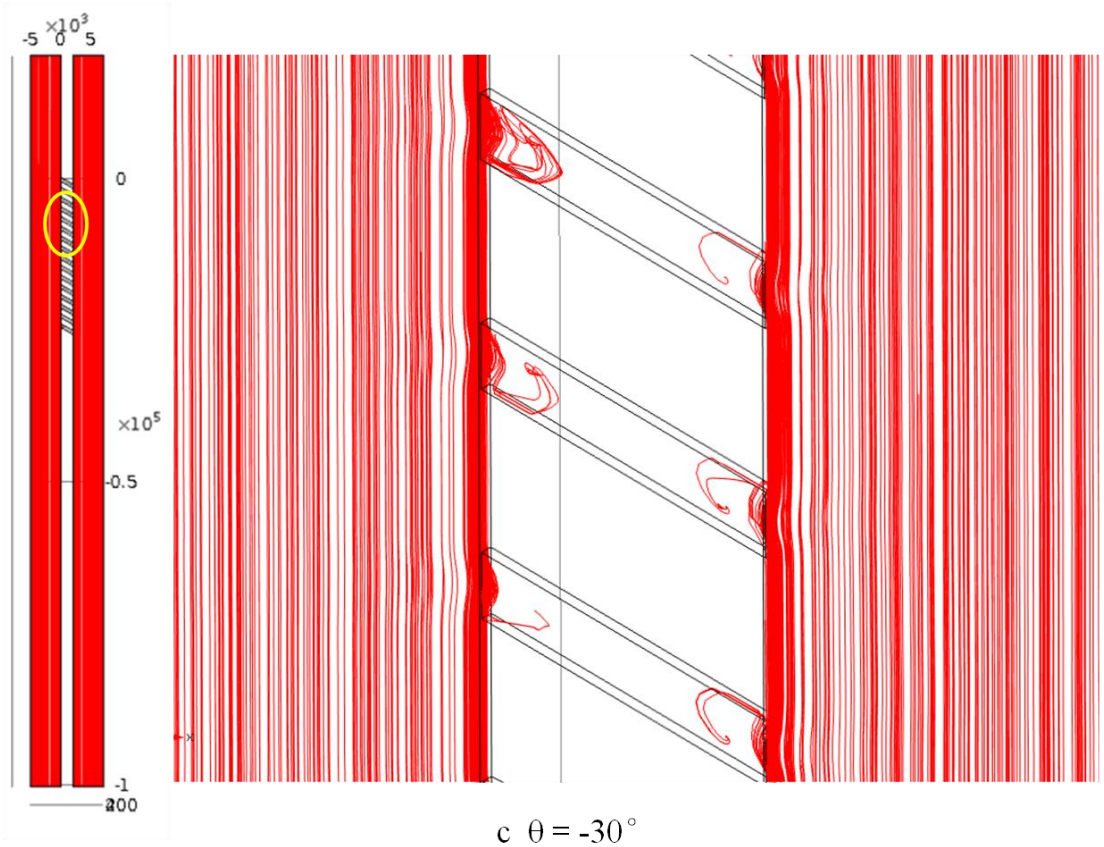

c $\theta = -30^\circ$

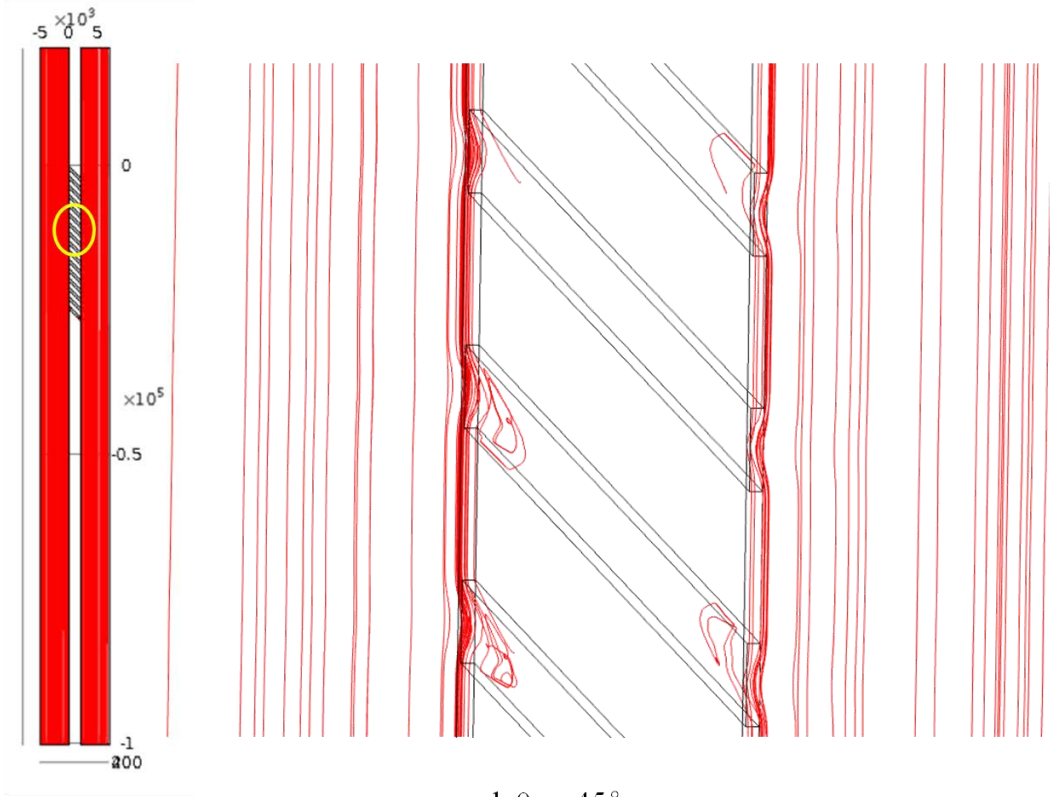

d $\theta = -45^\circ$

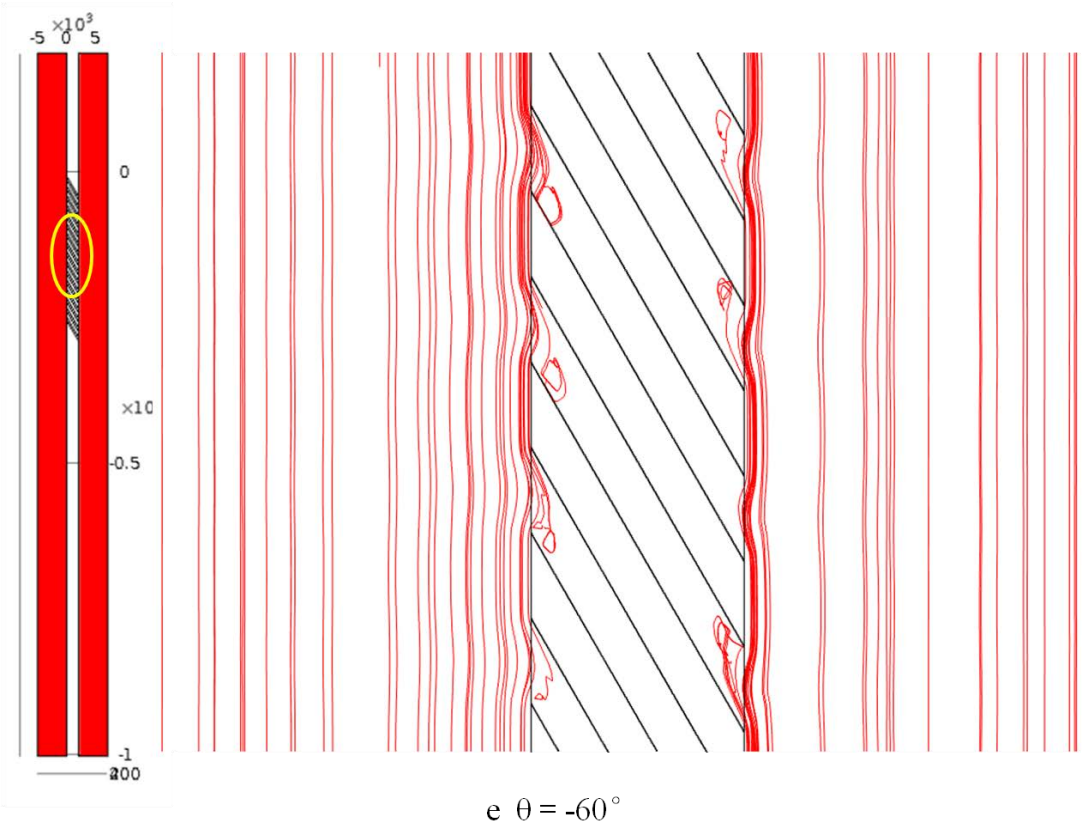

e $\theta = -60^\circ$

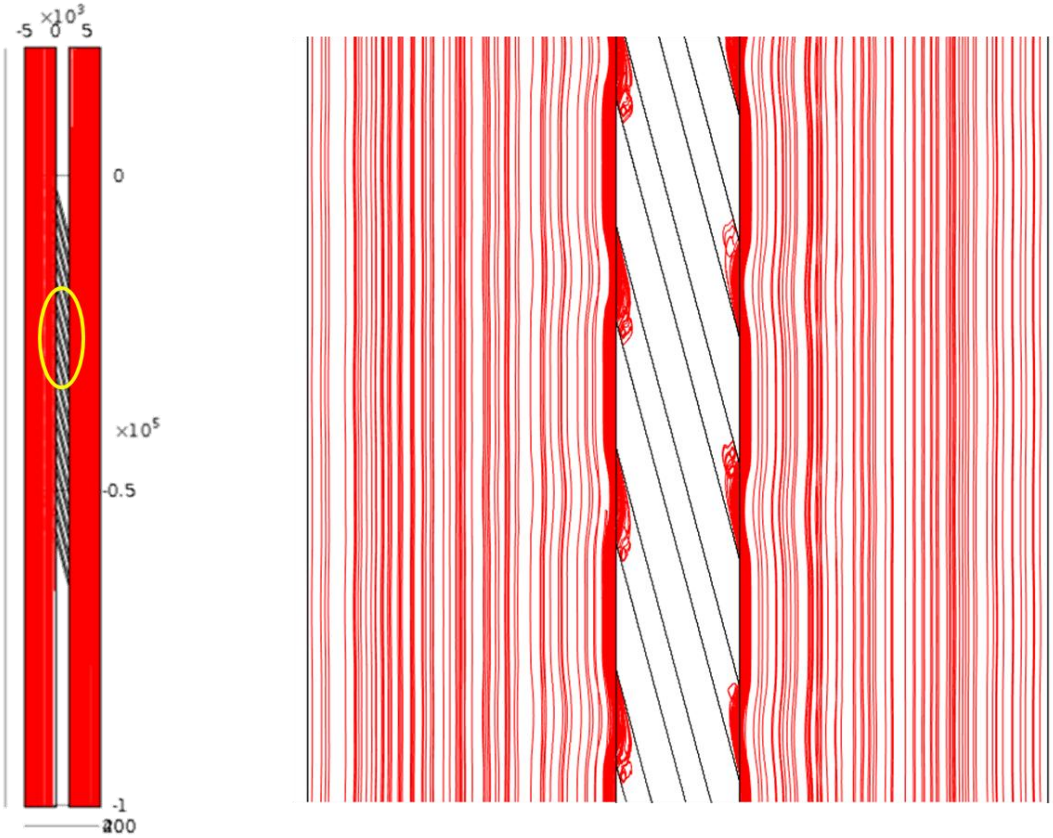

f $\theta = -75^\circ$

Figure 5.3 3D no-slip flow streamline for different angle θ.

5.2.4 Velocity

Figure 5.4 shows the middle slice (xy-planes) of the velocity magnitude in angular H shaped channel series ($\theta = 0°, -15°, -30°, -45°, -60°, \text{and} -75°$). It is similar with the 2D results. However, velocity magnitude cannot fully describe the flow. For a more specific study, the velocity field is introduced. Figure 5.5 describes the x component of velocity. Although the pressures beside the sieve channel were the same when $\theta = 0°$, the x direction velocity *u* was not zero in the sieve channel (Figure 5.5a) due to the osmosis process and trap effect. The trap effect has been shown as the streamlines deviate towards the entrances of the sieve channels in Figure 5.3. Figure 5.6 exhibits the x direction velocity when there is zero inlet concentration at both inlets thus avoiding the osmosis effects. This picture also gives evidence that the x direction vortex occurs in the sieve channels. By calculating the surface integration of *u* on all area of the cross-section with the capture channel, total flow rates out of the sieve channels were achieved which is shown in Table 5.1. Meanwhile, the sample inlet flow rate was 6.38e-20 m^3/s, and the average outlet velocity was 25.5nm/s. The negative value when $\theta = 0°$ demonstrates the osmosis phenomenon.

Table 5.1 Total flow rate across sieve channels (m^3/s) (no-slip)

Angle	0°	-15°	-30°	-45°	-60°	-75°
Flow out	-2.31e-23	6.51e-23	2.69e-22	2.84e-22	4.31e-22	6.50e-22

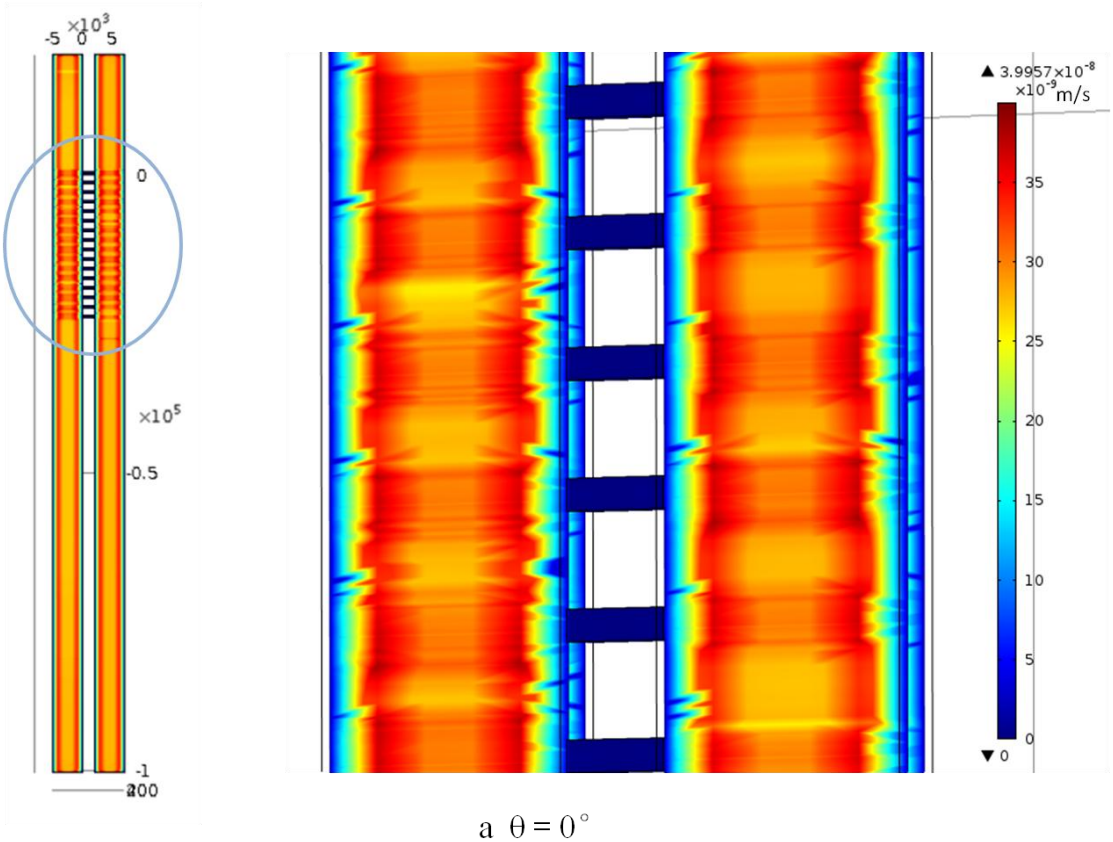

a $\theta = 0^\circ$

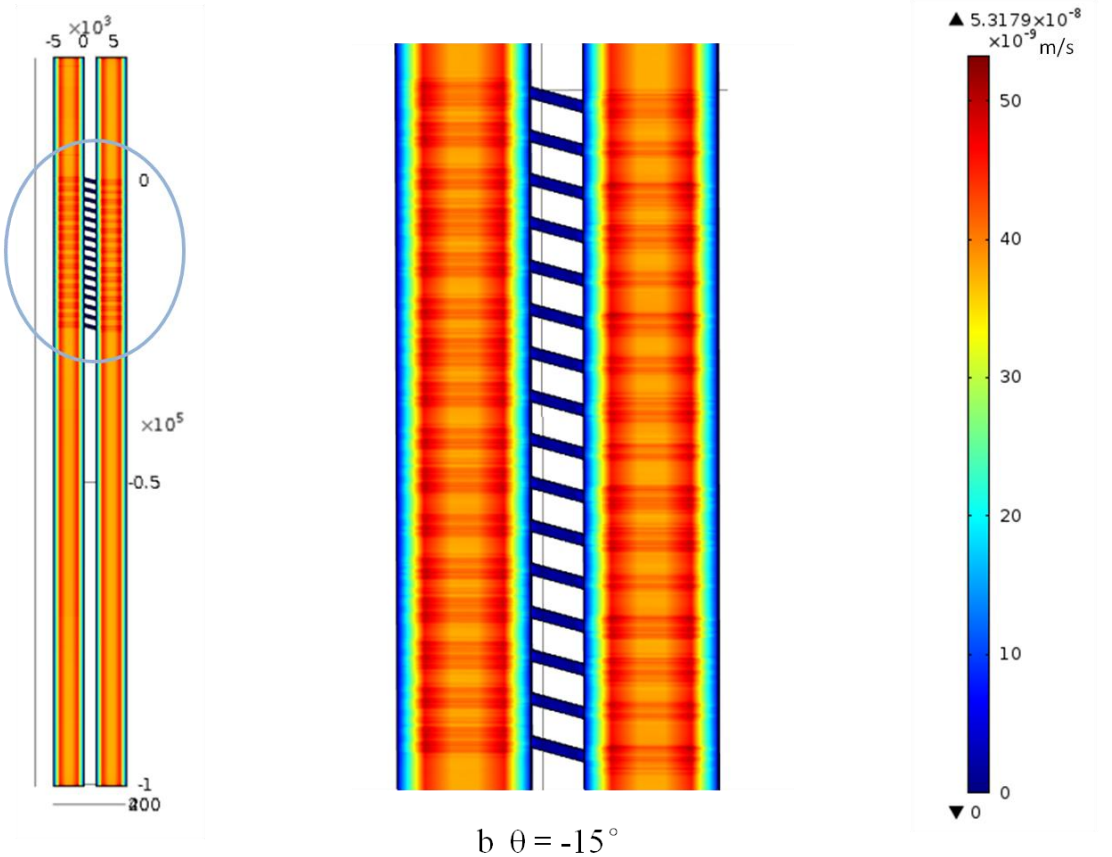

b $\theta = -15^\circ$

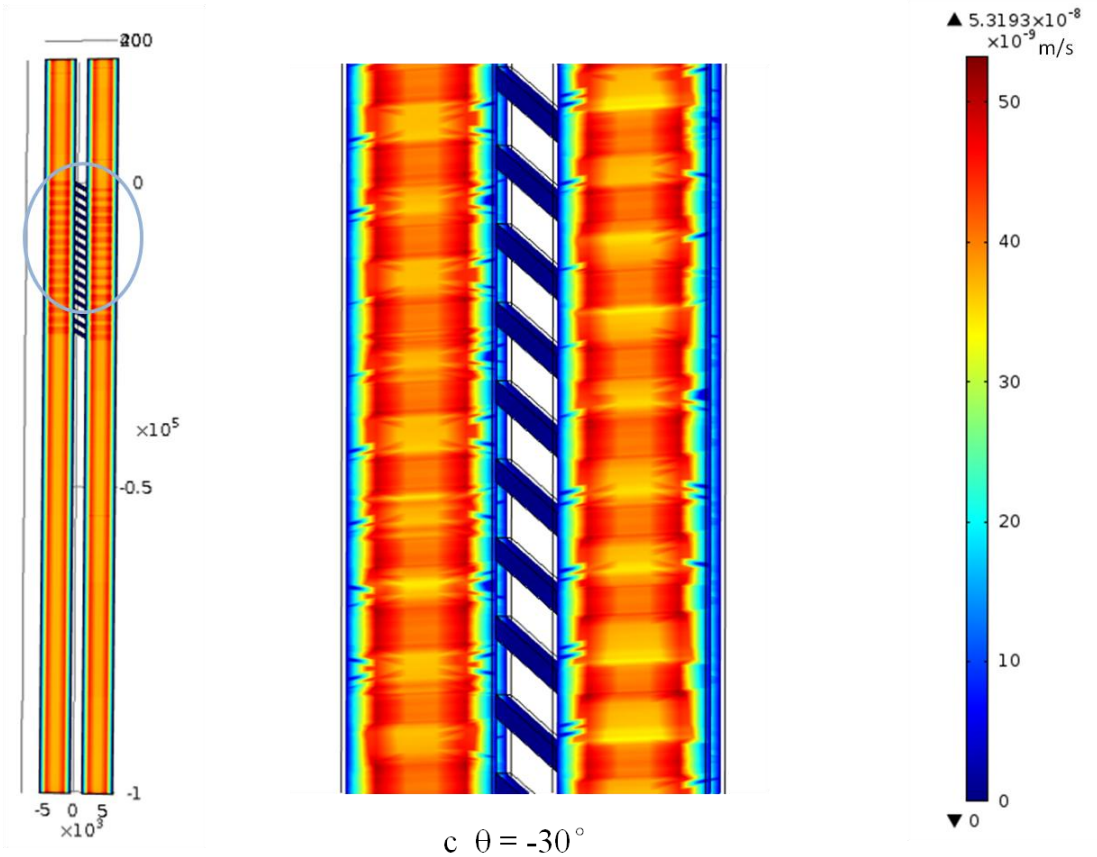

c $\theta = -30^\circ$

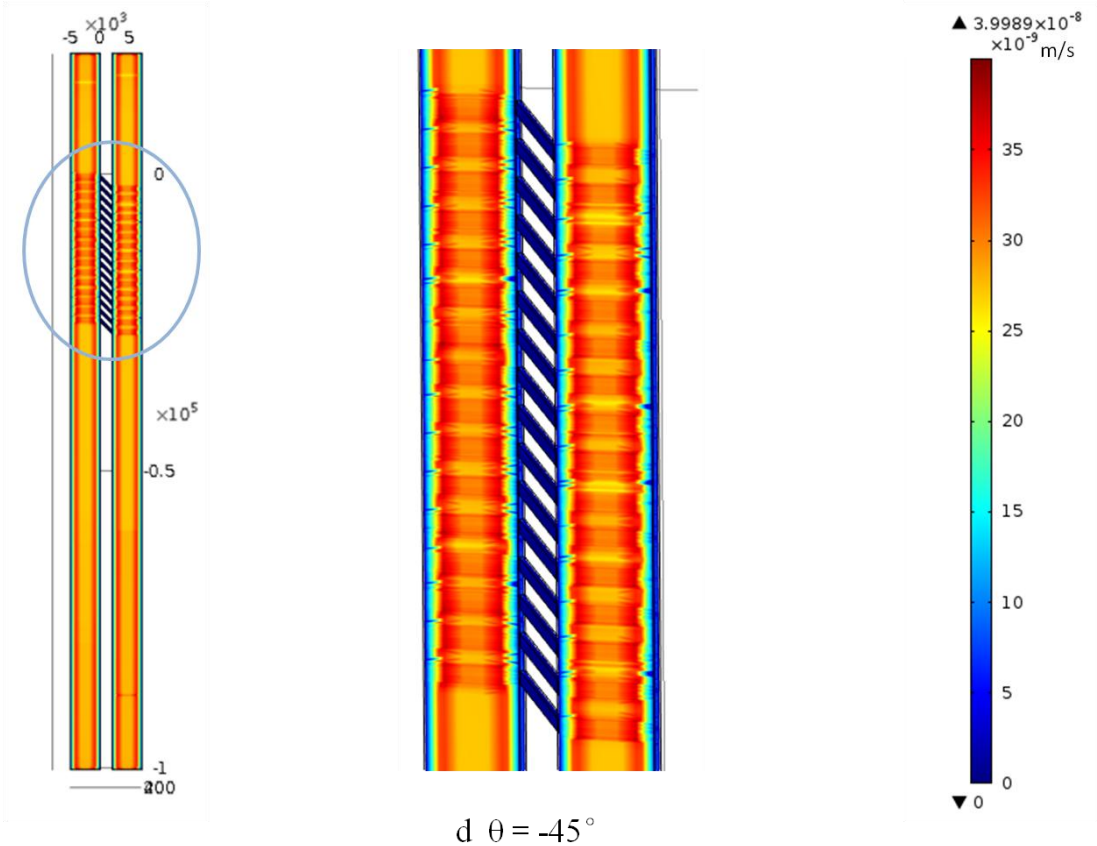

d $\theta = -45^\circ$

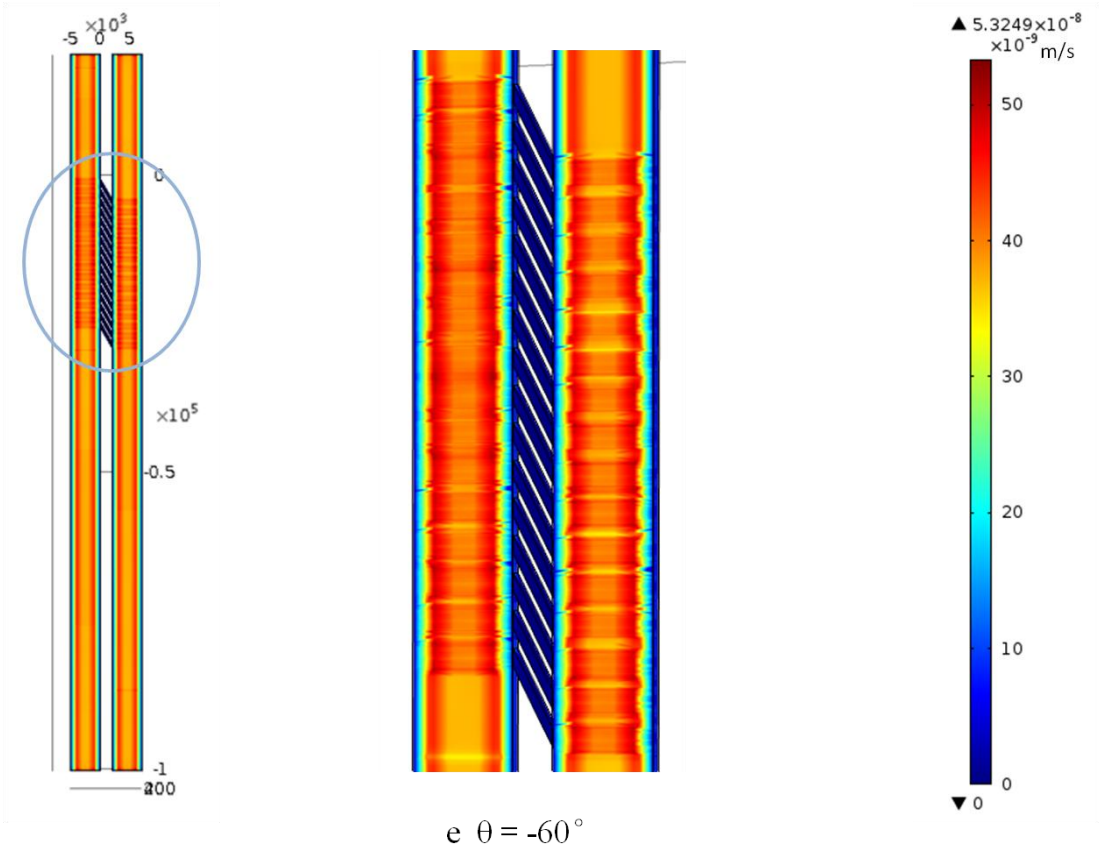

e $\theta = -60^\circ$

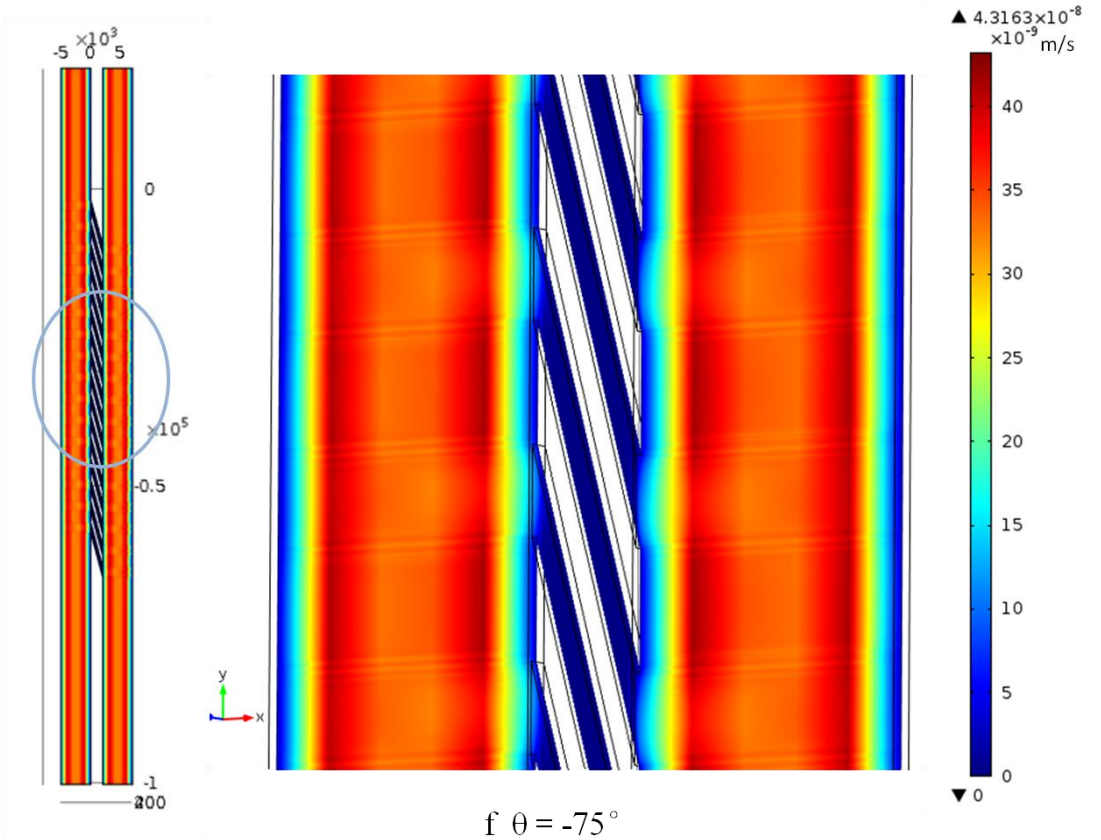

f $\theta = -75^\circ$

Figure 5.4 Velocity magnitude of no-slip flow with different angles.

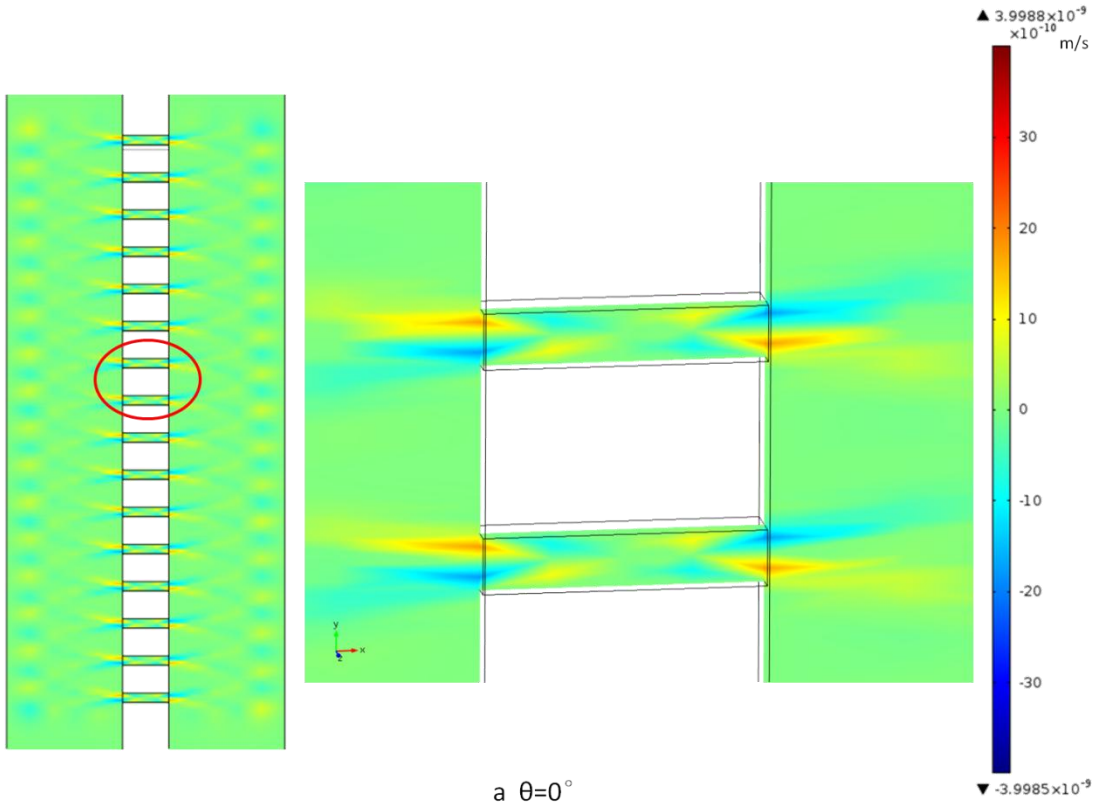
▲ 3.9988×10⁻⁹
×10⁻¹⁰ m/s
30
20
10
0
-10
-20
-30
▼ -3.9985×10⁻⁹

a θ=0°

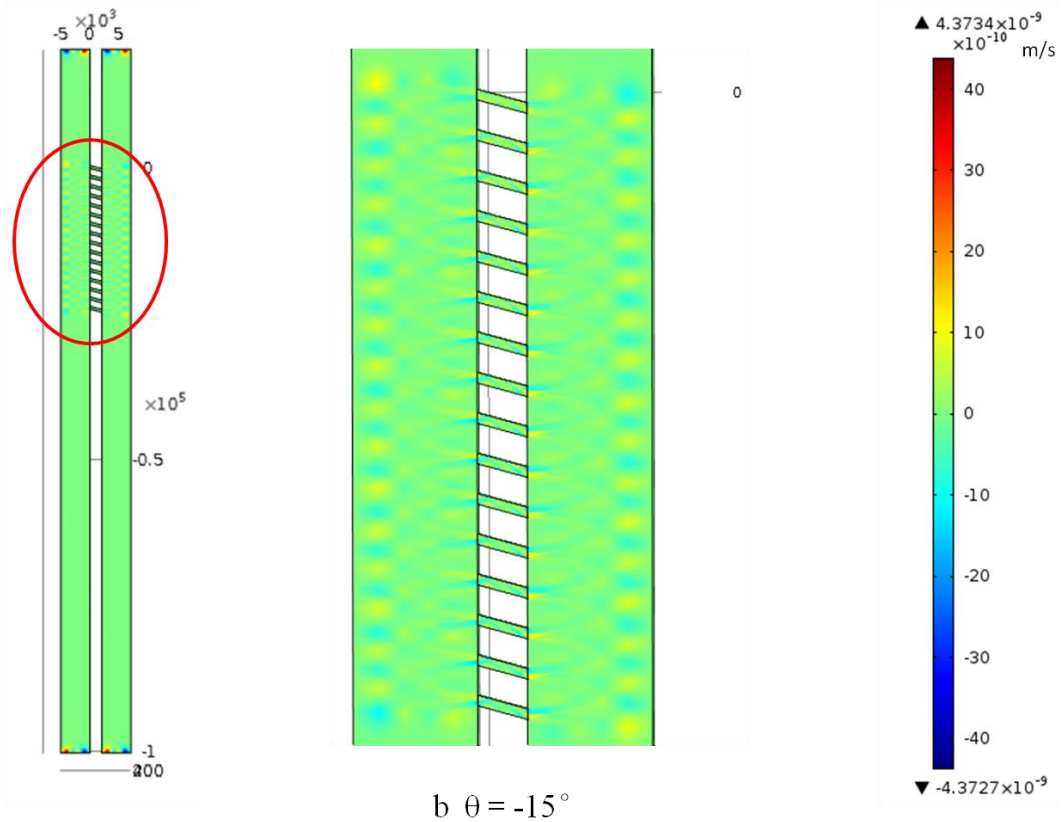
×10³
-5 0 5
0
×10⁵
-0.5
-1
0
▲ 4.3734×10⁻⁹
×10⁻¹⁰ m/s
40
30
20
10
0
-10
-20
-30
-40
▼ -4.3727×10⁻⁹

b θ = -15°

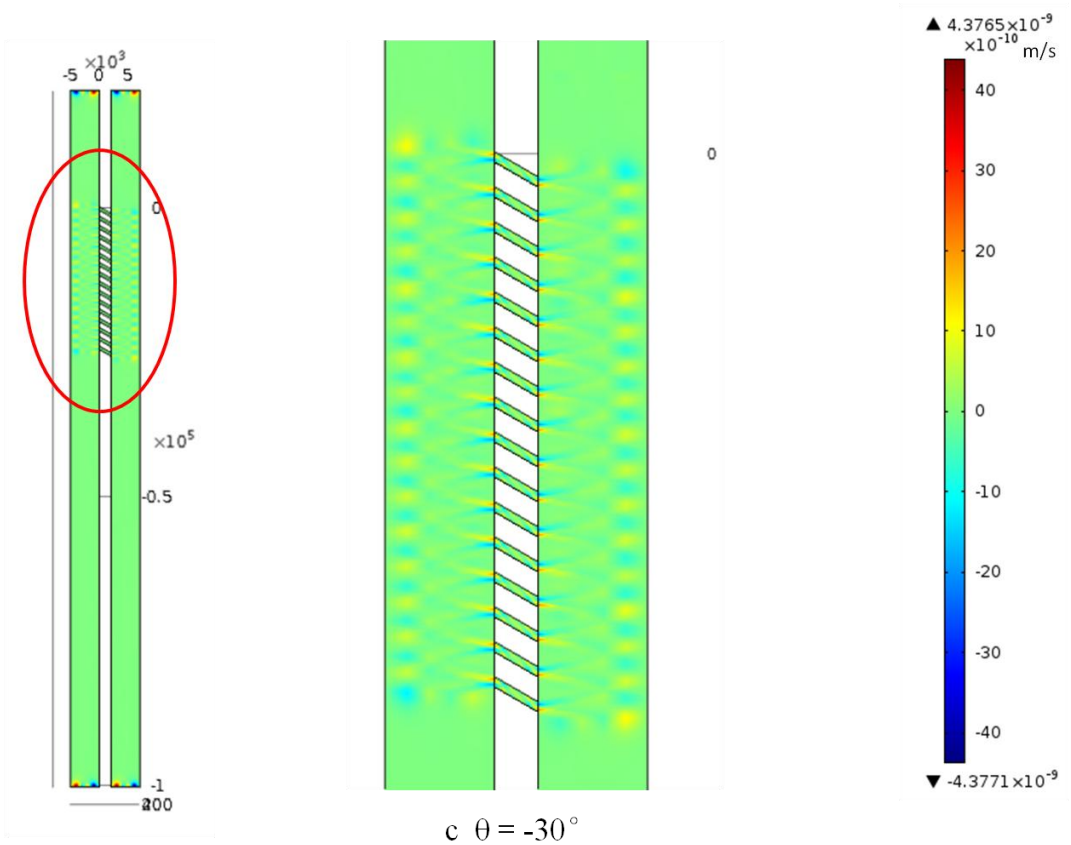

c $\theta = -30^\circ$

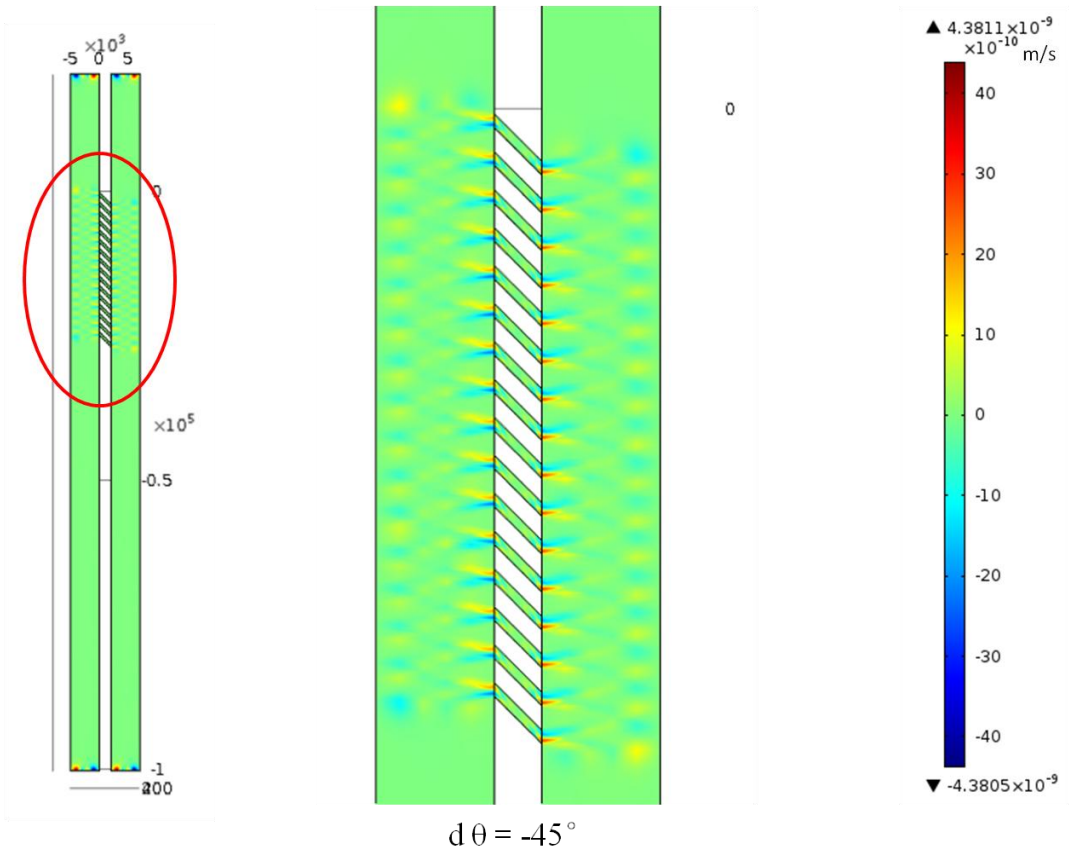

d $\theta = -45^\circ$

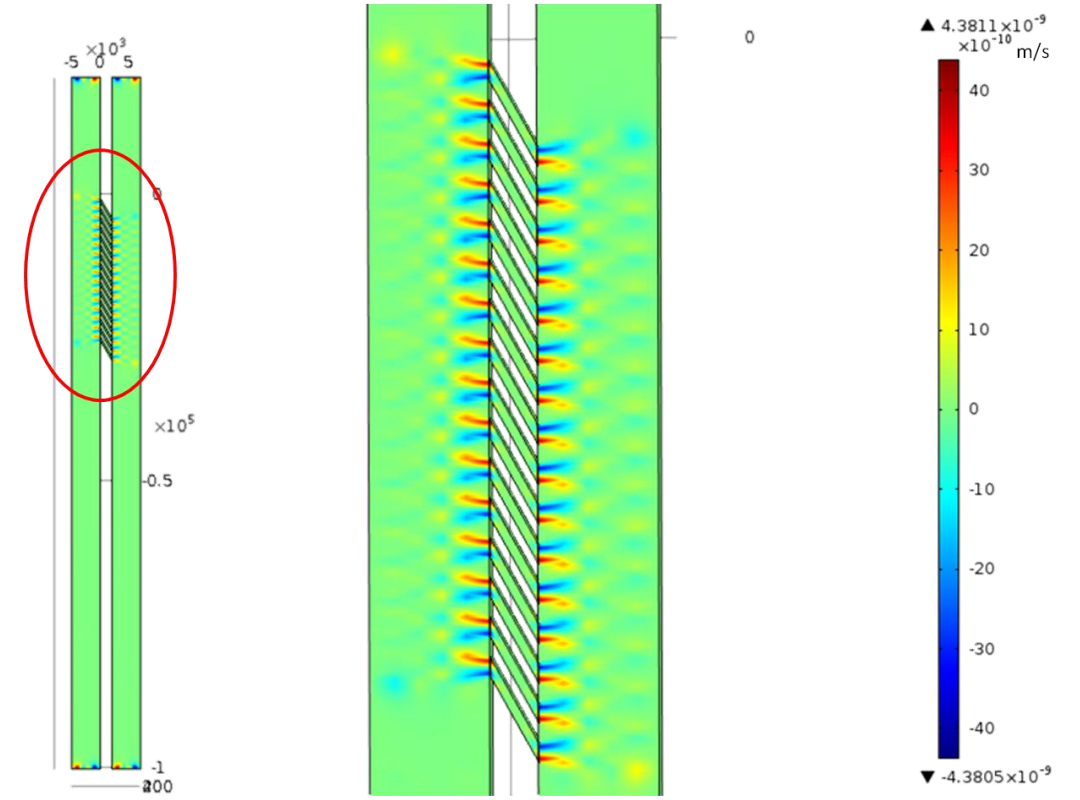

e θ = -60°

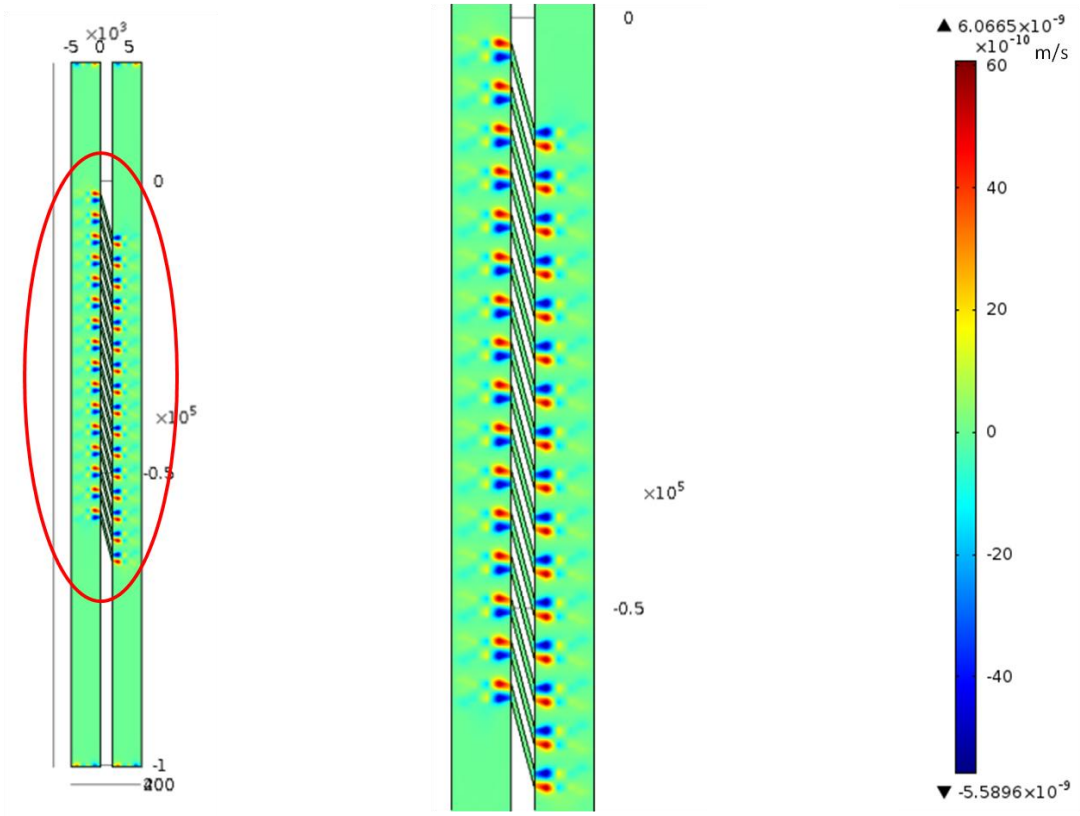

f θ = -75°

Figure 5.5 Velocity x direction component u of no-slip flow with different angle $\boldsymbol{\theta}$.

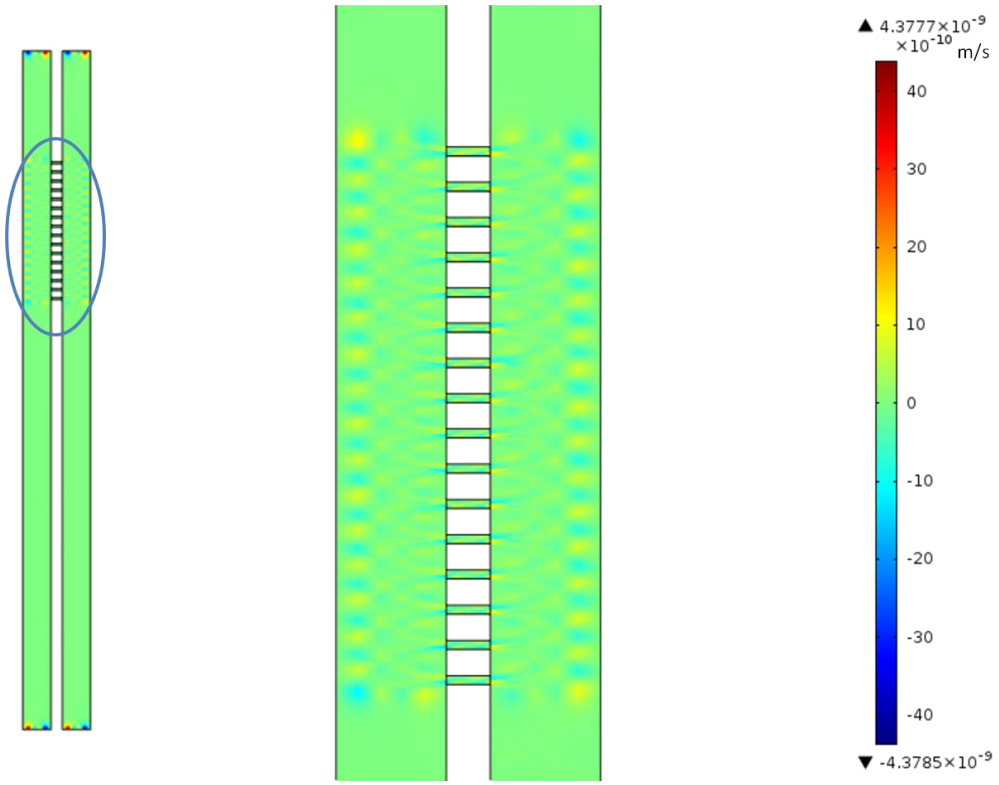

Figure 5.6 X direction velocity component with zero concentration

The y direction velocity *v* is shown in Figure 5.7, which is the main velocity component. So these figures are very similar with the velocity magnitude figures. The pressure difference between inlets and outlets of the sample inlet channel and capture channel decides the y direction velocity component *v*.

Z direction velocity component *w* is exhibited in Figure 5.8. The trap effect is clearly shown in the figure as the rainbow colour stripes. This effect takes place because the depth of the sieve channels is smaller than the depth of the sample inlet and capture channel.

Consequently, due to the inertia of fluid and improvement of pressure gradient on sieve channels caused by angle, higher but limited convection in sieve channels is able to be achieved with bigger angle magnitude.

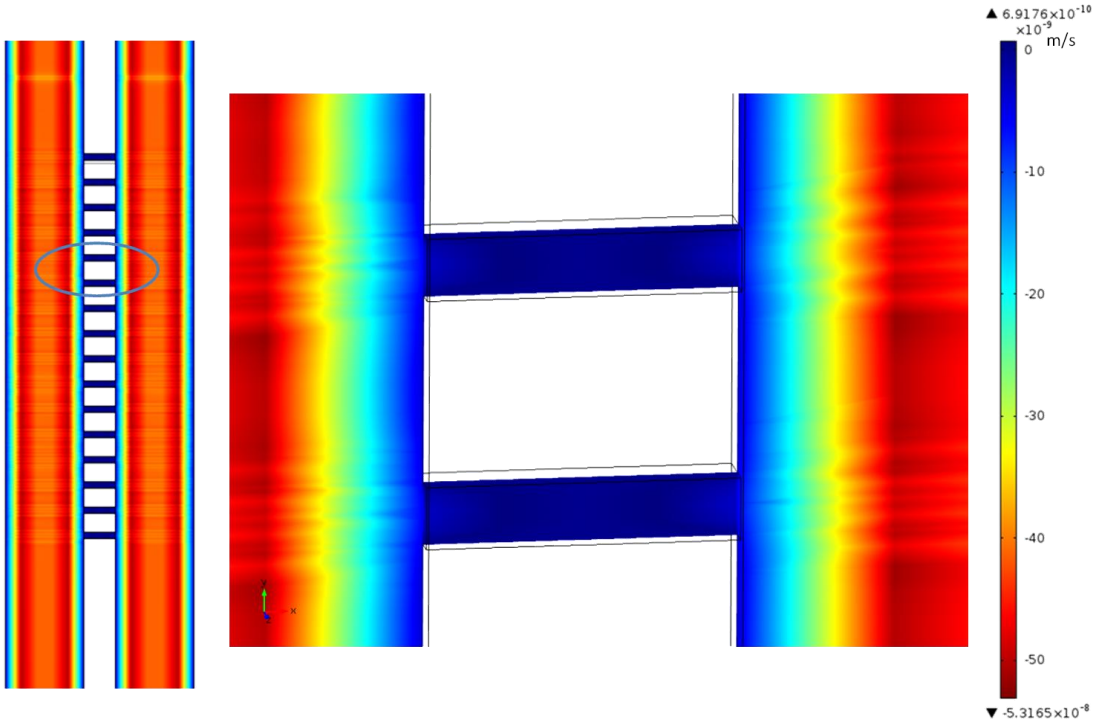

a $\theta = 0^\circ$

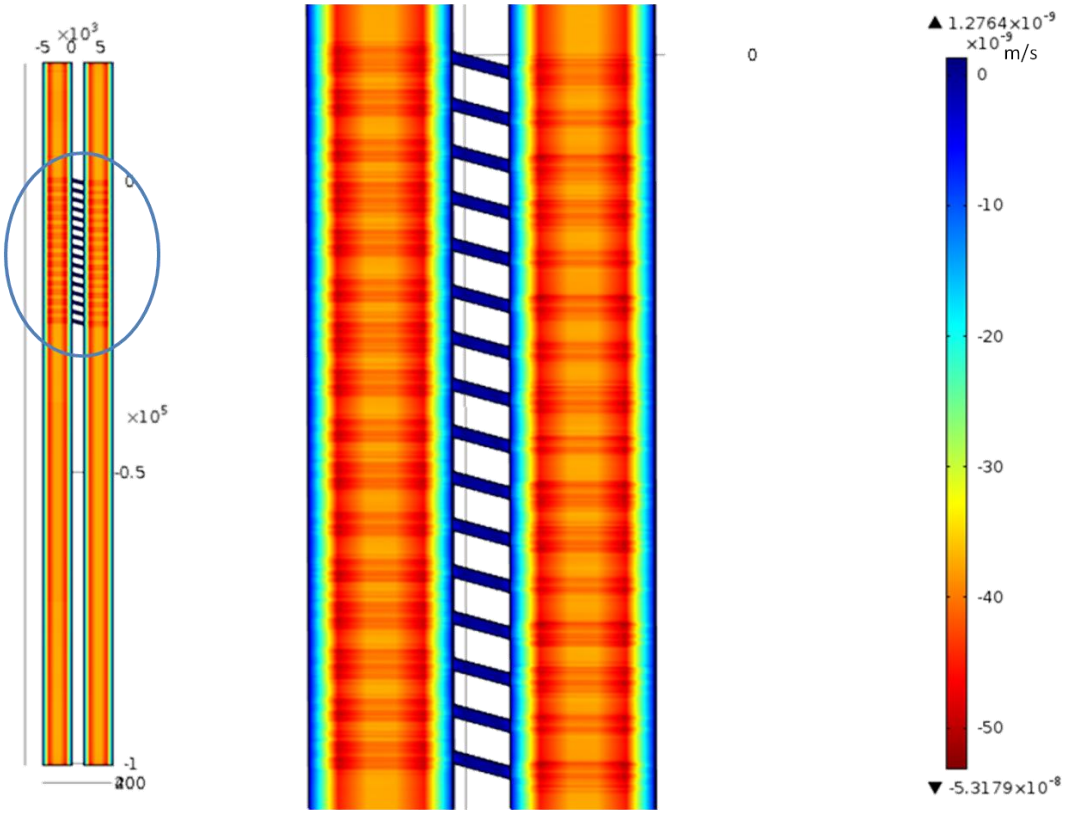

b $\theta = -15^\circ$

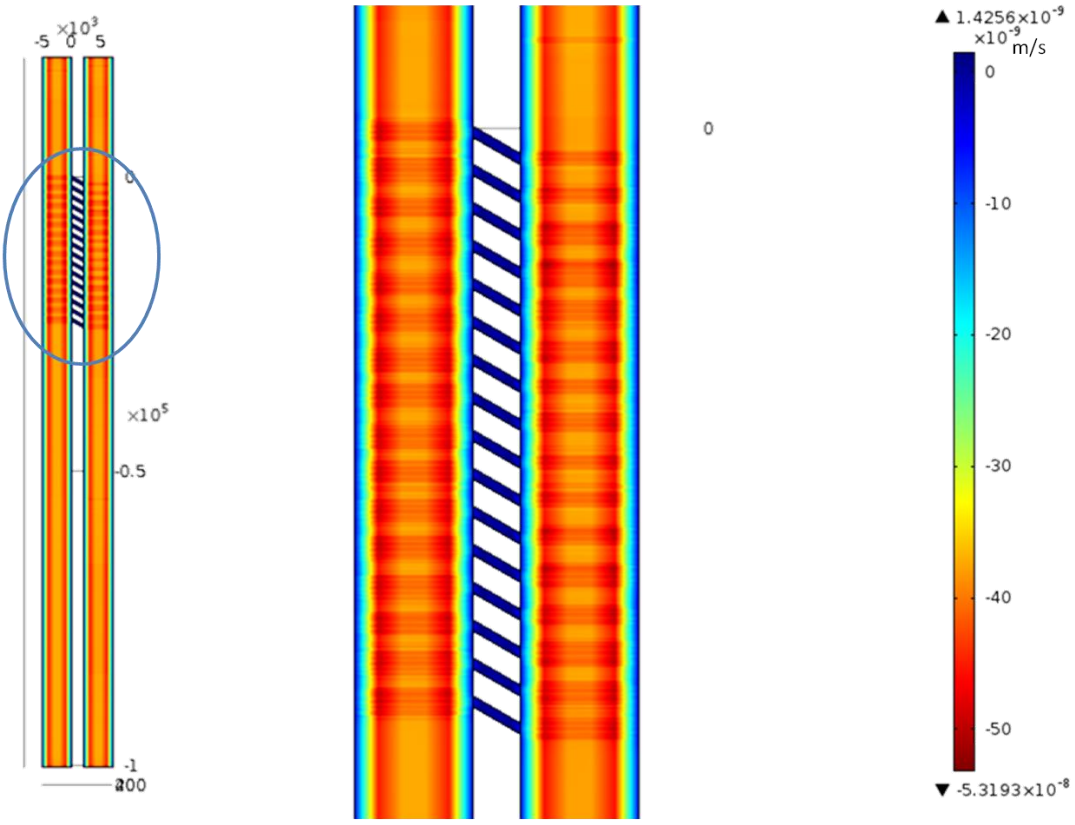

c $\theta = -30^\circ$

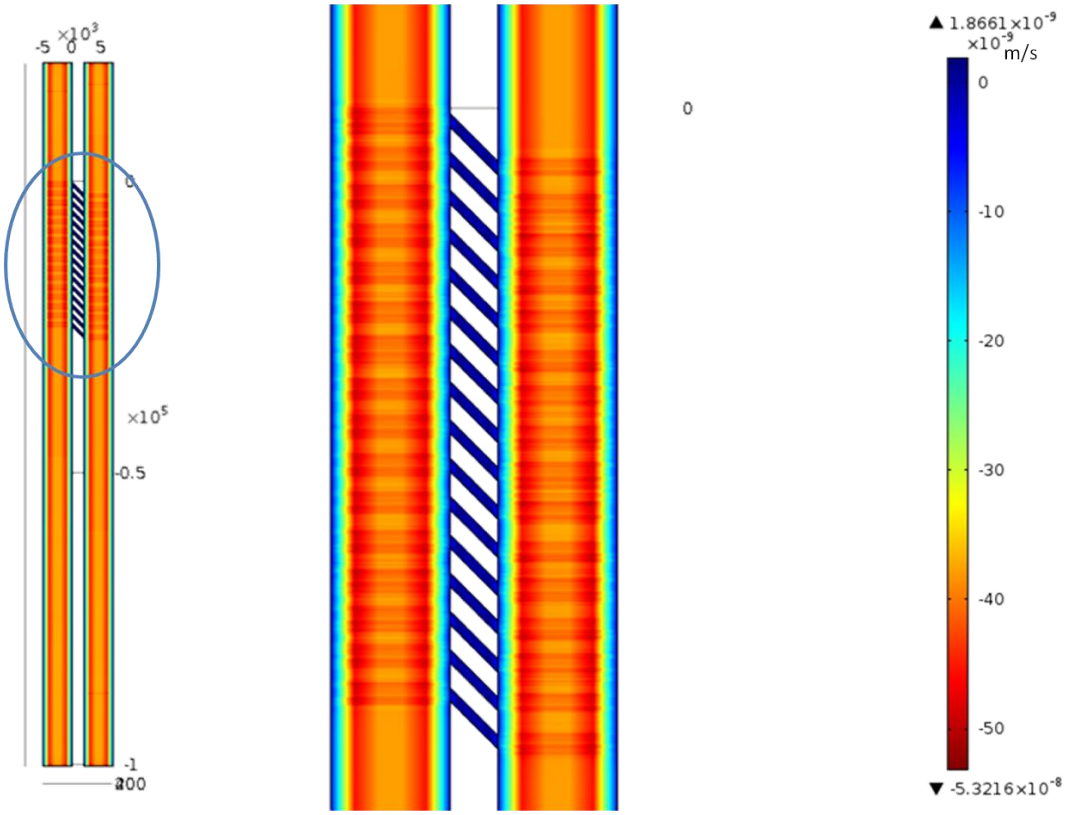

d $\theta = -45^\circ$

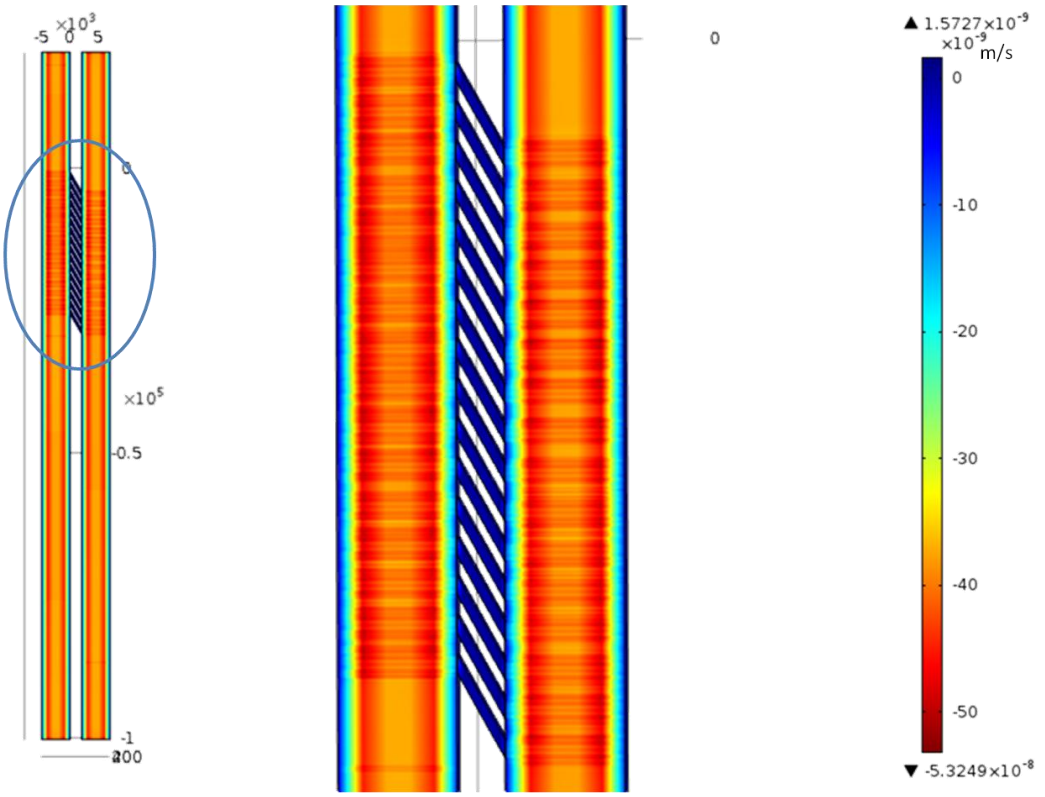

e θ = -60°

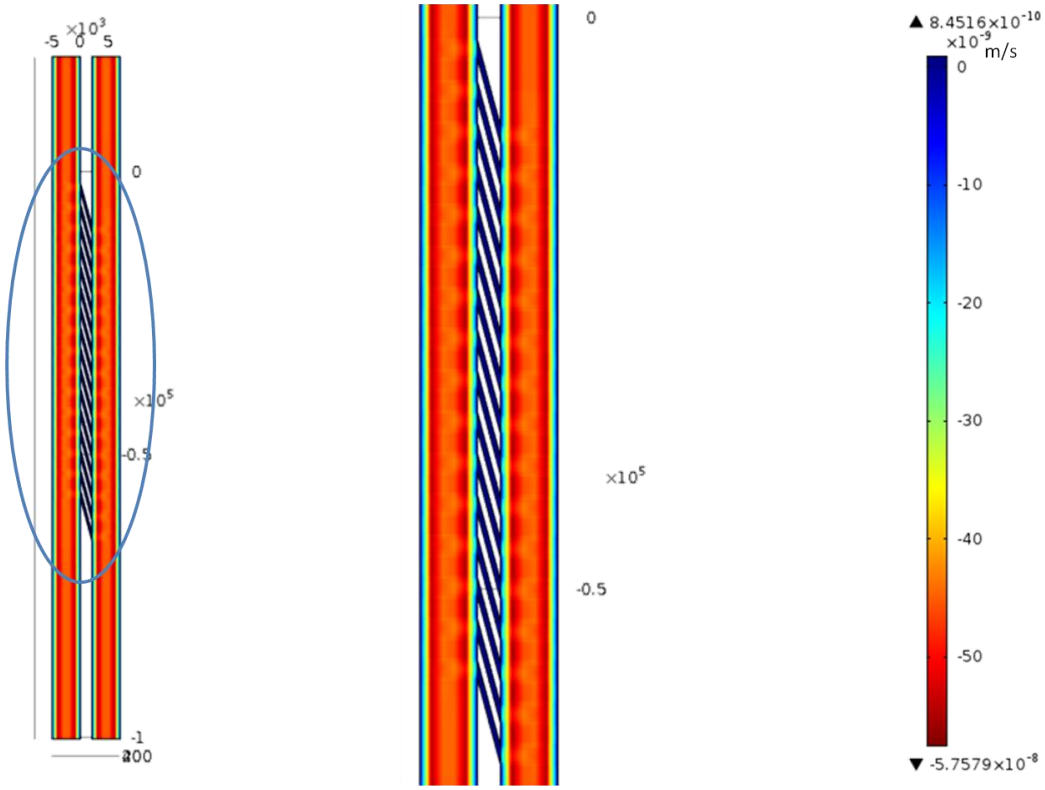

f θ = -75°

Figure 5.7 Y direction velocity components of no-slip flow with different angles.

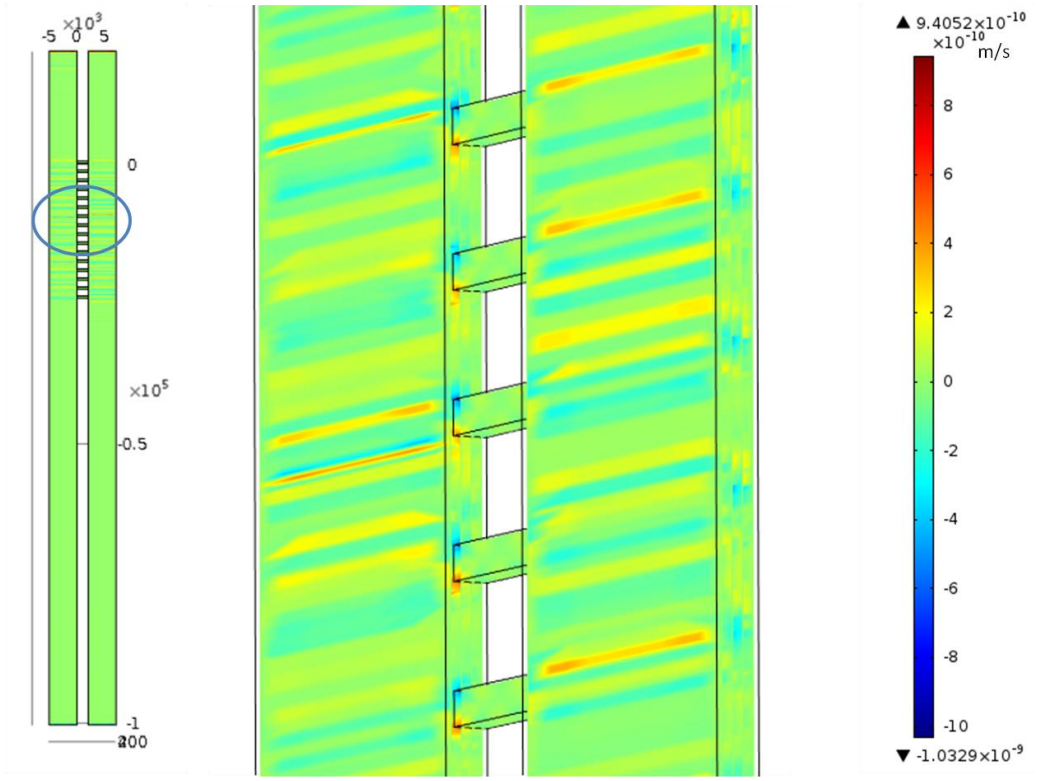

a $\theta = 0^\circ$

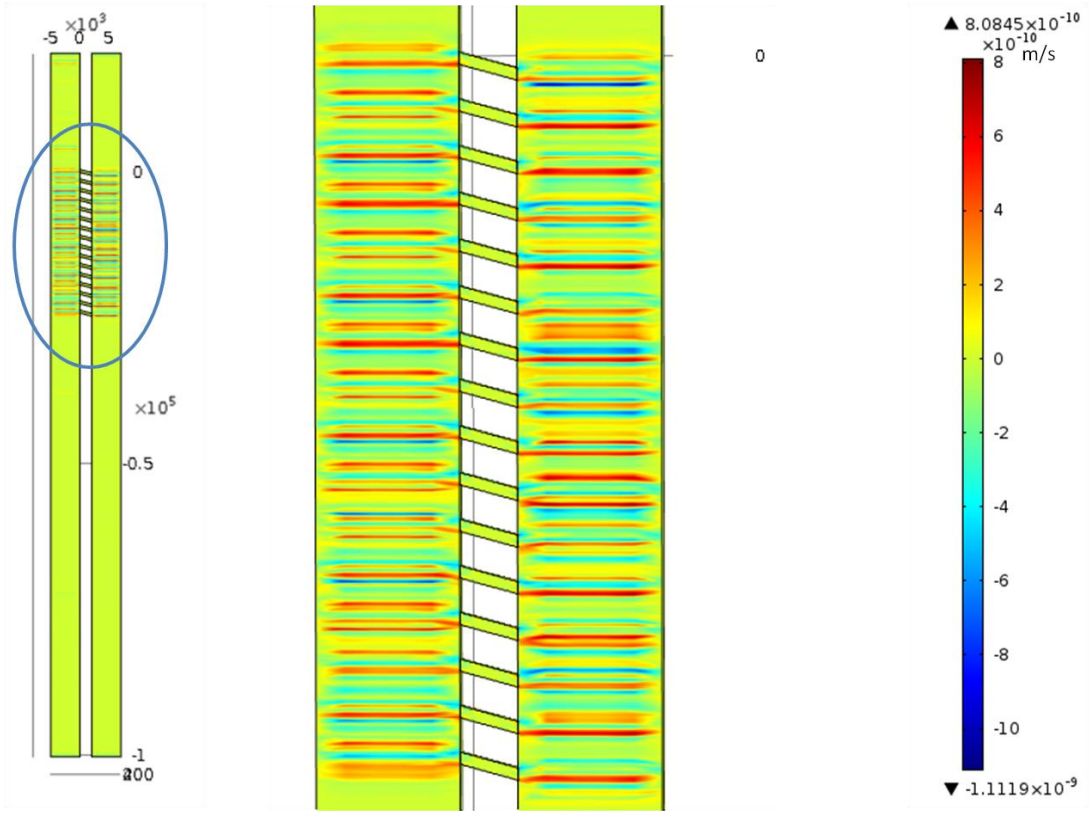

b $\theta = -15^\circ$

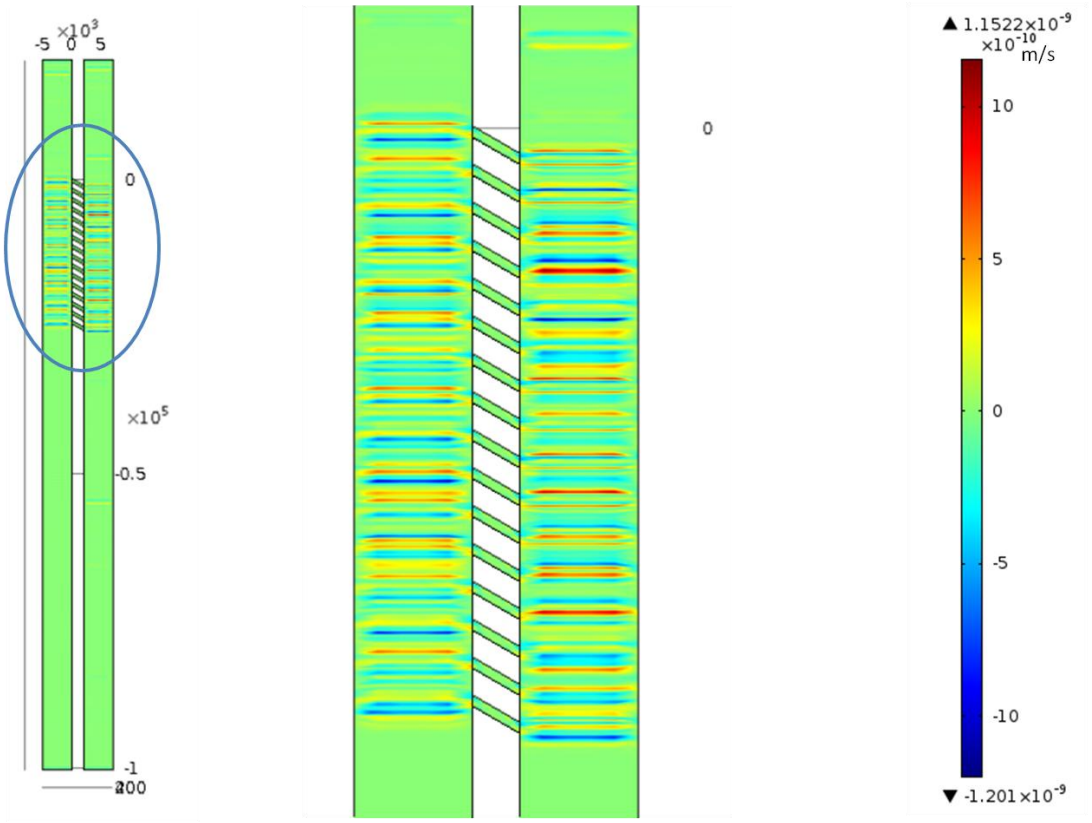

c $\theta = -30^\circ$

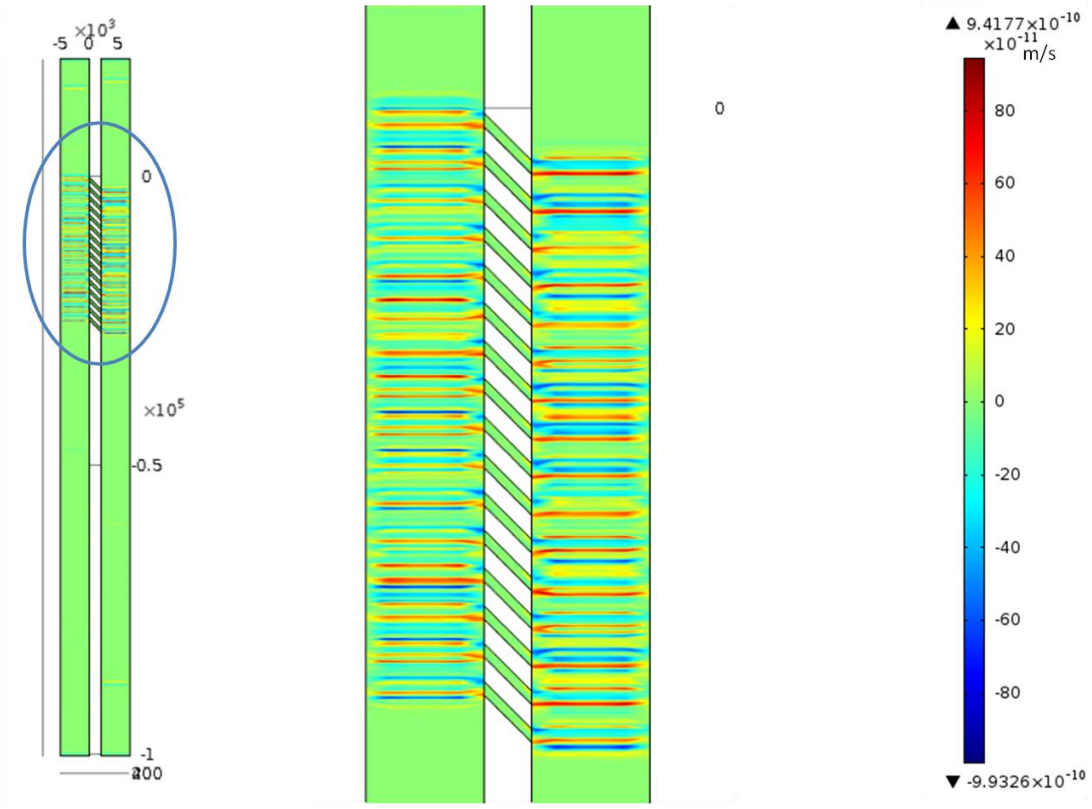

d $\theta = -45^\circ$

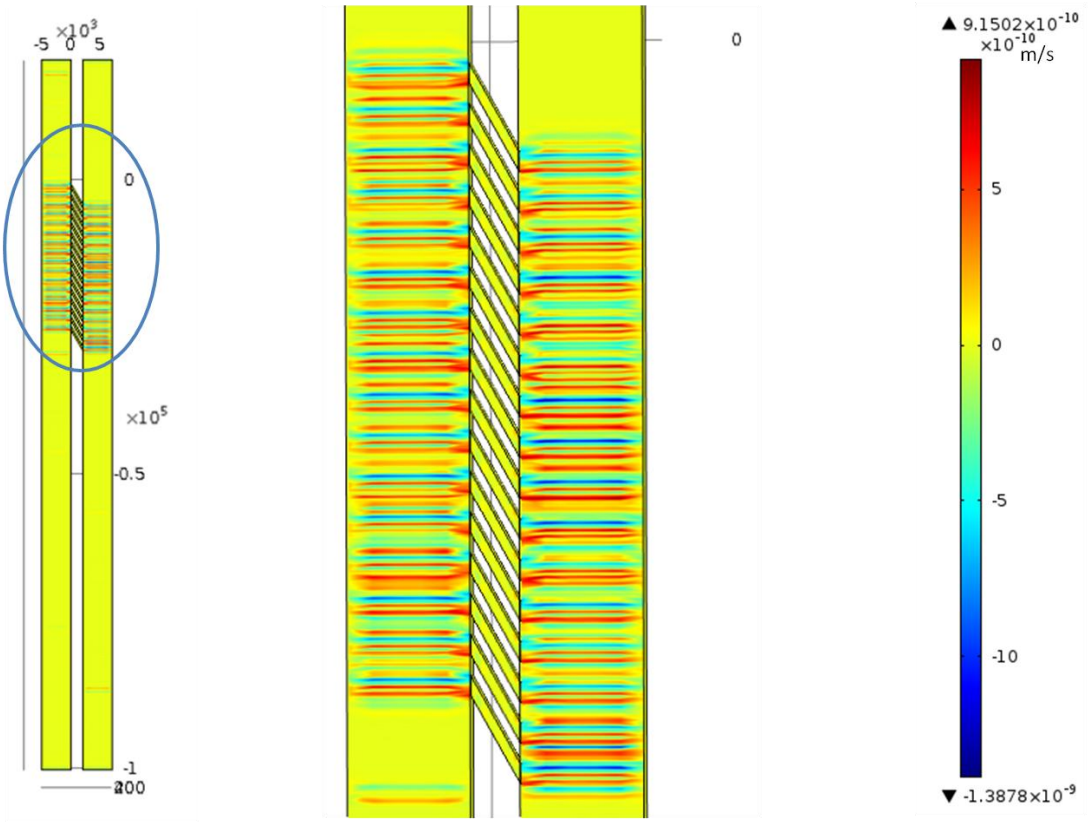

e θ = -60°

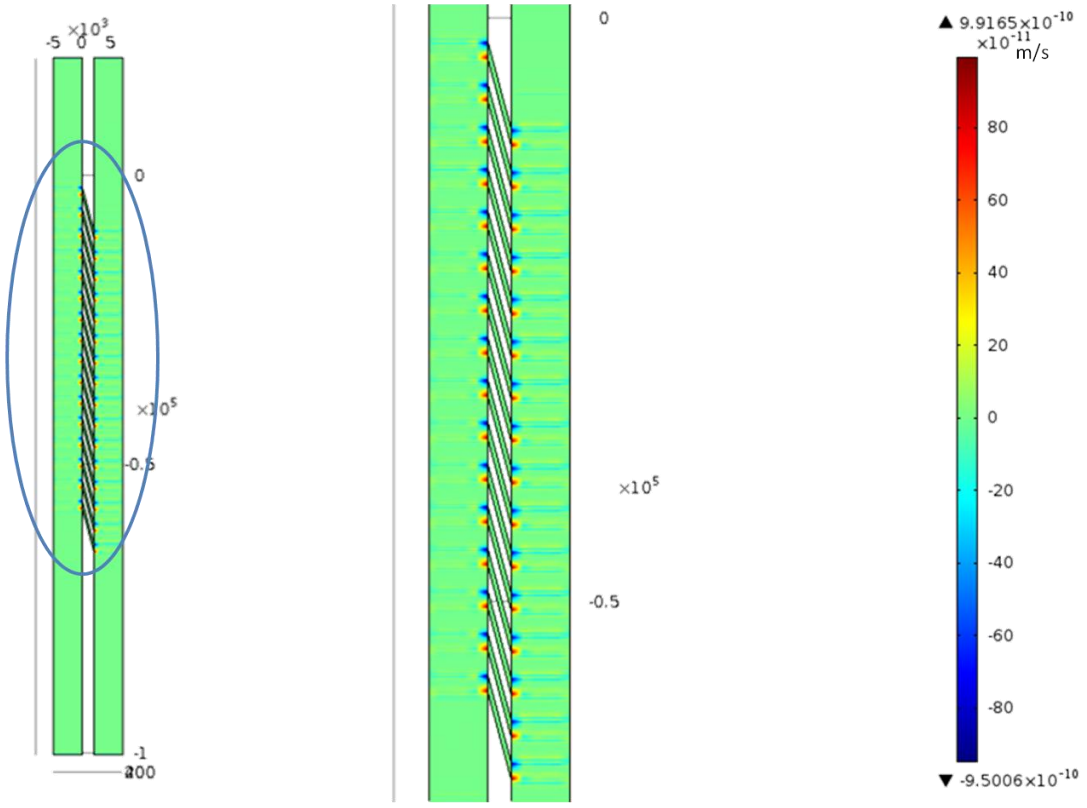

f θ = -75°

Figure 5.8 Z direction velocity components of no-slip flow with different angles.

5.3 Slip Boundary Condition Results

The no-slip boundary condition has been used to solve Navier-Stokes equation since the 19th century[156]. However, a lot of publications reported experimental evidences of slip in variety of situations[157, 158]. For non-Newtonian fluids, such as blood, apparent slips were observed in various experiments[159, 160]. Thus slip boundary condition was applied in this section for more accurate simulations. The boundary condition in laminar module is:

$$\mathbf{u} \cdot \mathbf{n} = 0, \mathbf{K} - (\mathbf{K} \cdot \mathbf{n})\mathbf{n} = 0, \mathbf{K} = [\mu(\nabla \mathbf{u} + (\nabla \mathbf{u})^T)]\mathbf{n}$$

Where $\mathbf{u}$ is the velocity vector, $\mathbf{n}$ is the outer normal vector on $\partial\Omega$, and Ω is a domain. The geometric model and software settings (including the mesh) are the same as section 6.2 except the boundary condition of Laminar Flow module. Thus the simulations in this section can be viewed as the control group of section 6.2. The control variable is the boundary condition of flow.

5.3.1 Velocity

The surface velocity is not zero under slip boundary condition. Comparing with the no-slip simulation results, flow rates in all channels increase significantly. Figure 5.9 exhibits the velocity magnitude (on xy-planes) when θ is $-0°, -15°, -30°, -45°, -60°,$ and $-75°$. Whereas large increases of flow velocity in sample inlet channel and capture channel are seen, relative low velocity layers are observed on the cross sections due to the vortices in the sieve channels. Table 5.2 exhibits the flow rate in single sieve channel when the slip boundary condition was applied. The sample inlet flow rate was 2.55e-15 m^3/s (inlet Pressure 100 Pa), and the average velocities at both outlets were 1.01 mm/s. Comparing with the no-slip results, appreciable increase of flow rate is achieved in all different angle

simulations. It can be seen from the table that the flow rate in the sieve channels increased with the angle magnitude. This relationship is the same as for the no-slip simulation results.

Table 5.2 Total flow rate across the sieve channels (m^3/s) (slip boundary condition)

Angle	0°	-15°	-30°	-45°	-60°	-75°
Flow rate	2.67e-19	8.83e-18	2.47e-17	3.68e-17	6.15e-17	8.58e-17

Figure 5.10 shows the x component of velocity (*u*). The trap effect reduces compared with the no-slip results. Thus a slip flow in filters based on H shaped channels takes a lower possibility of clustering at the entrances of the sieve channels than no-slip flow. The high x direction velocity at the top and bottom of the cross section means that the flow goes around the low velocity layer area. This phenomenon further reduces the possibility of clustering at the cross section.

Figure 5.11 introduces the y direction component of velocity. As the y component is distinct higher than x and z direction components, this figure is similar with Figure 5.9. Z direction velocity component is illustrated in Figure 5.12. The z direction movements are caused by the depth changes (sudden contraction and sudden expansion) in the z direction at the cross-section.

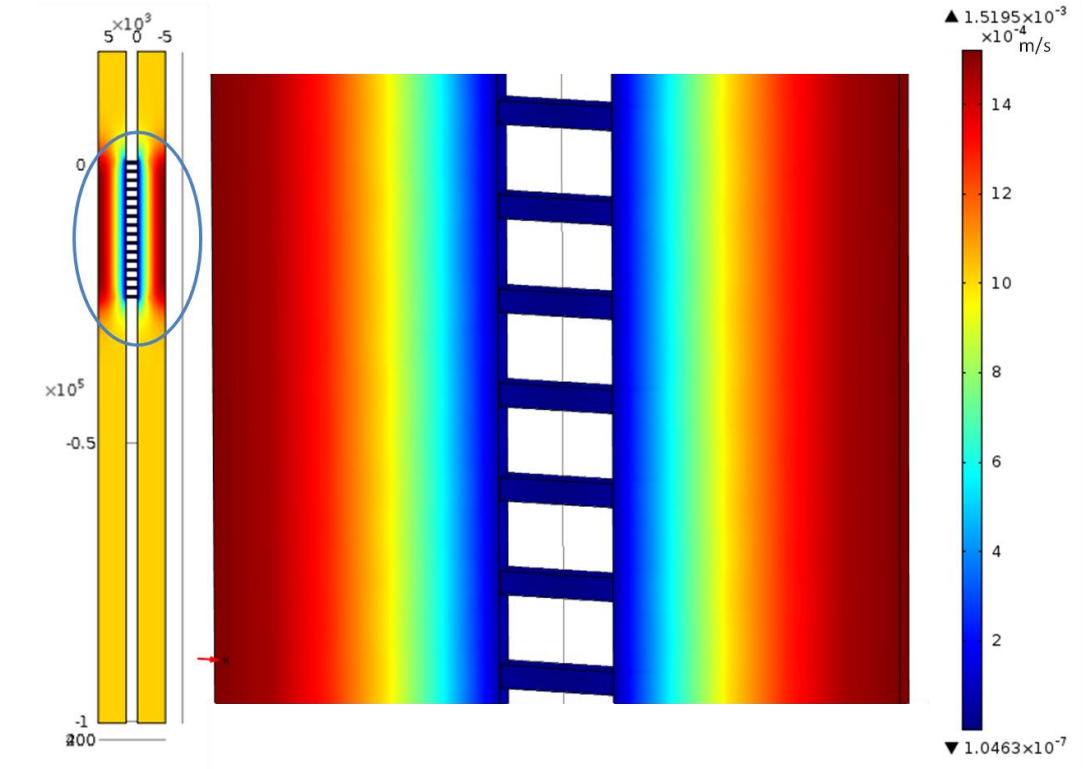

a $\theta = 0^\circ$

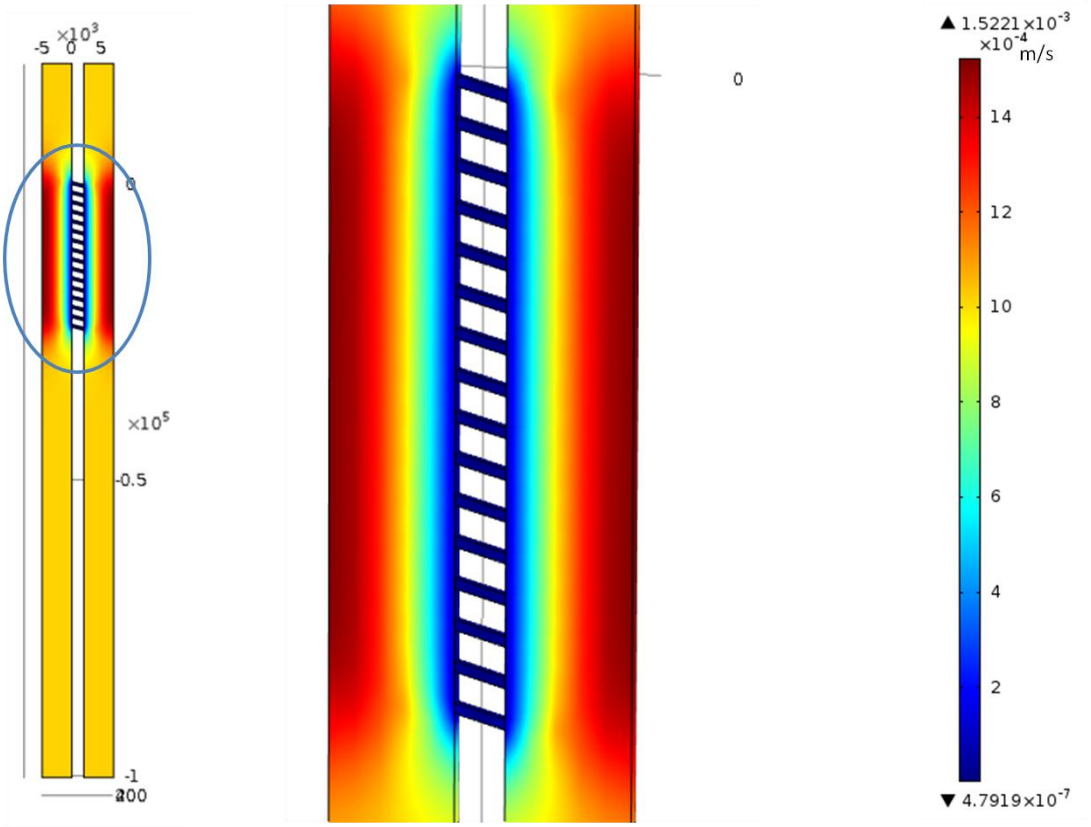

b $\theta = -15^\circ$

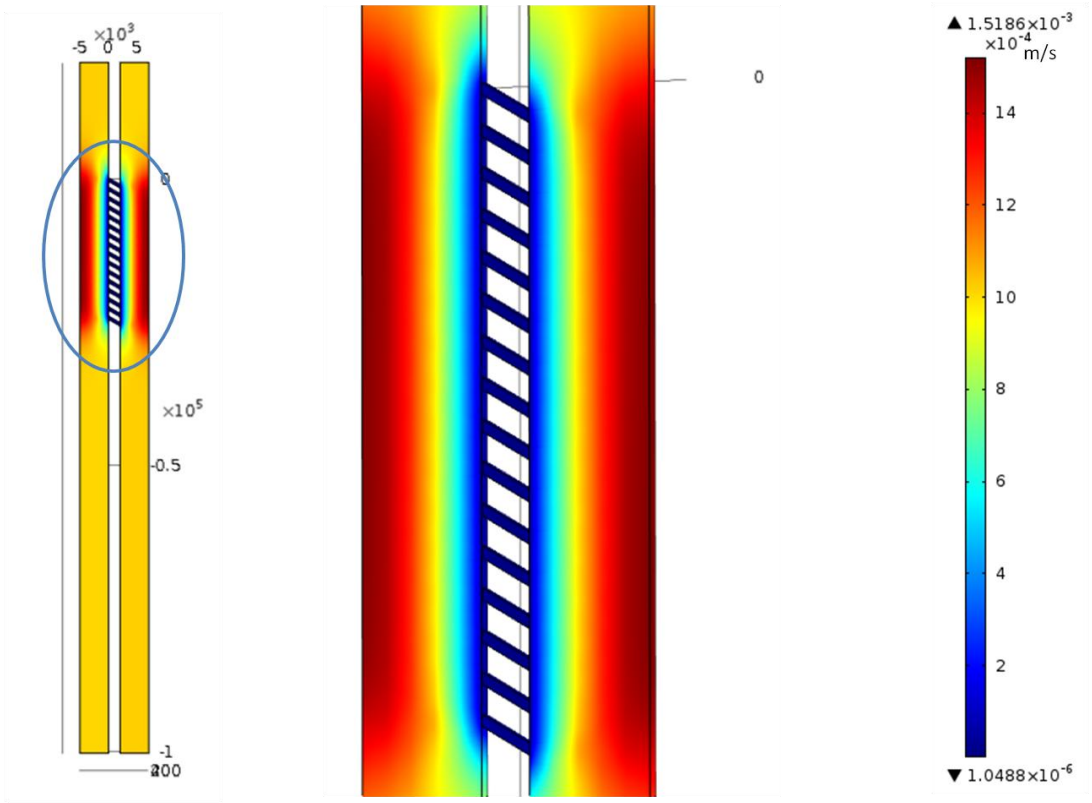

c $\theta = -30^\circ$

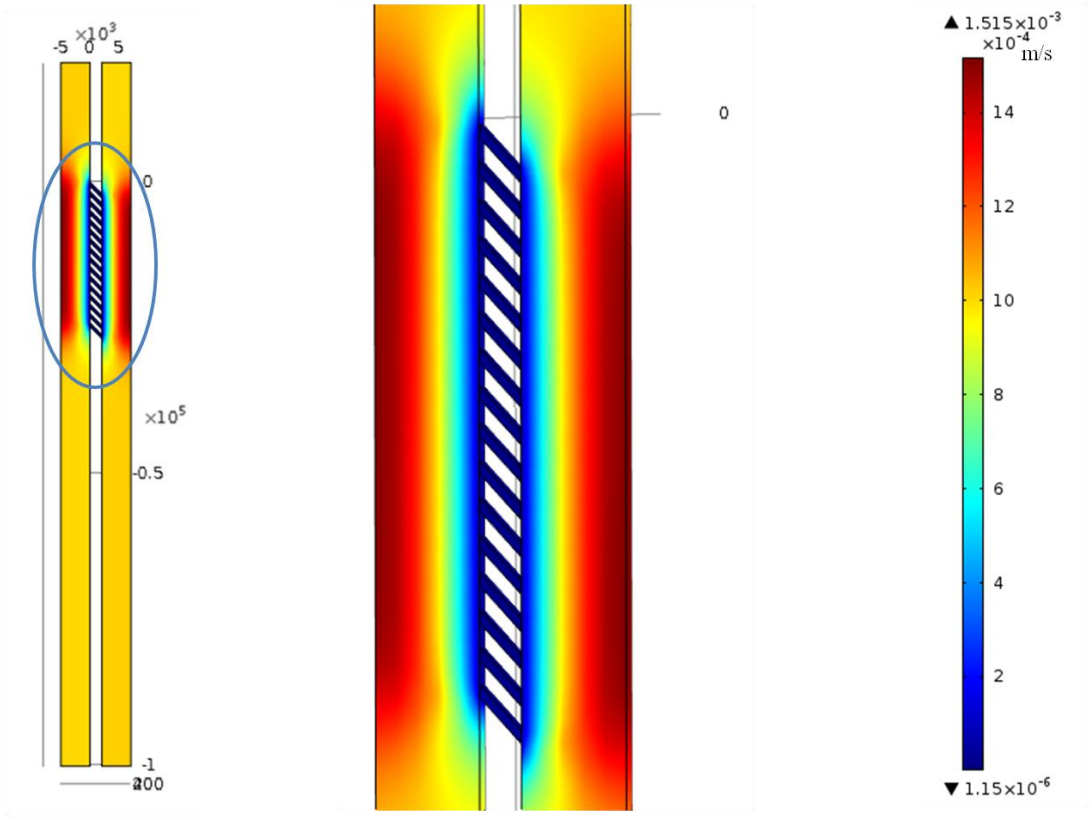

d $\theta = -45^\circ$

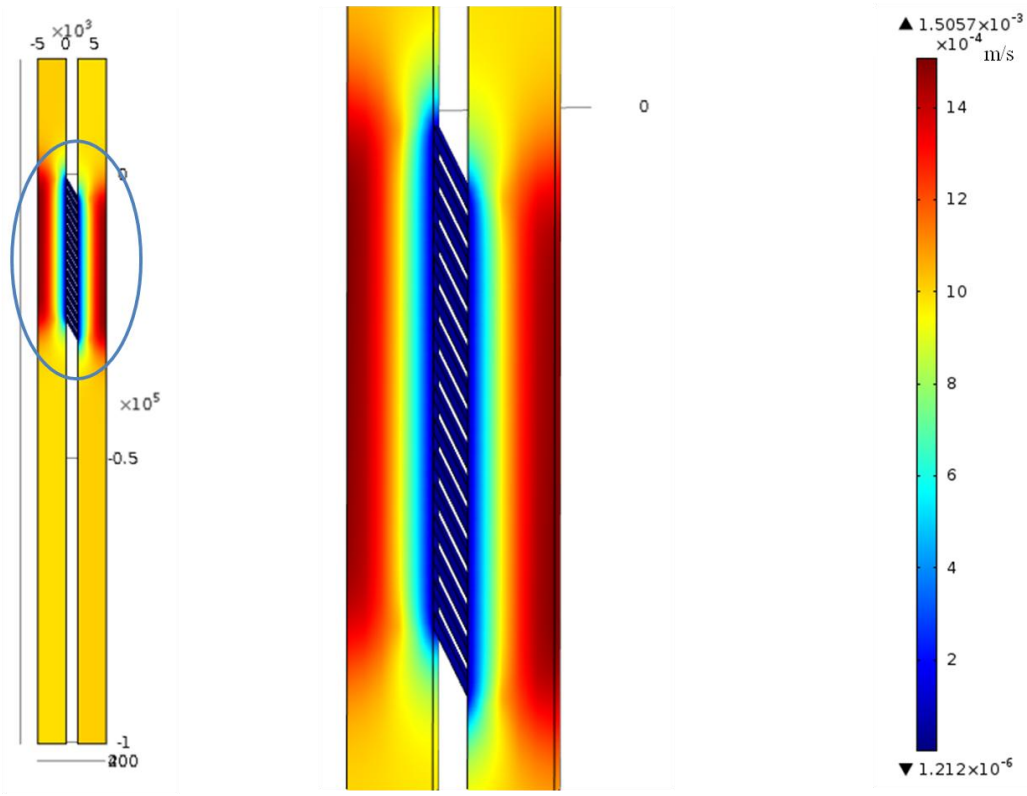

e θ = -60°

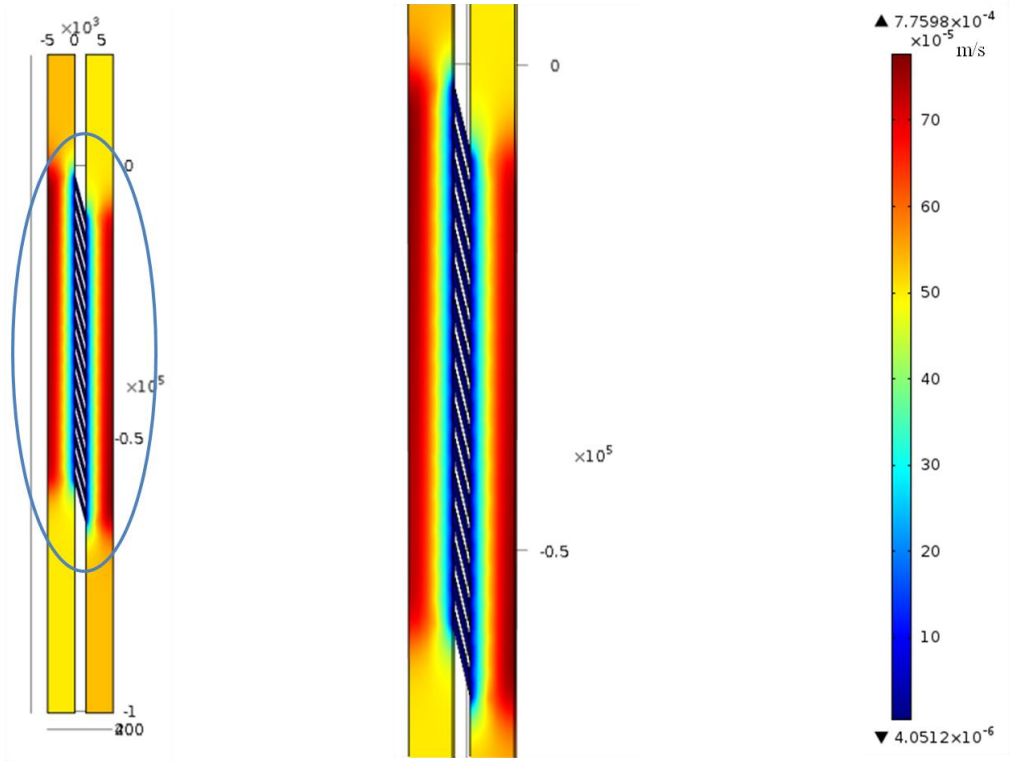

f θ = -75°

Figure 5.9 Velocity magnitude of angular H shaped channel series with slip boundary condition

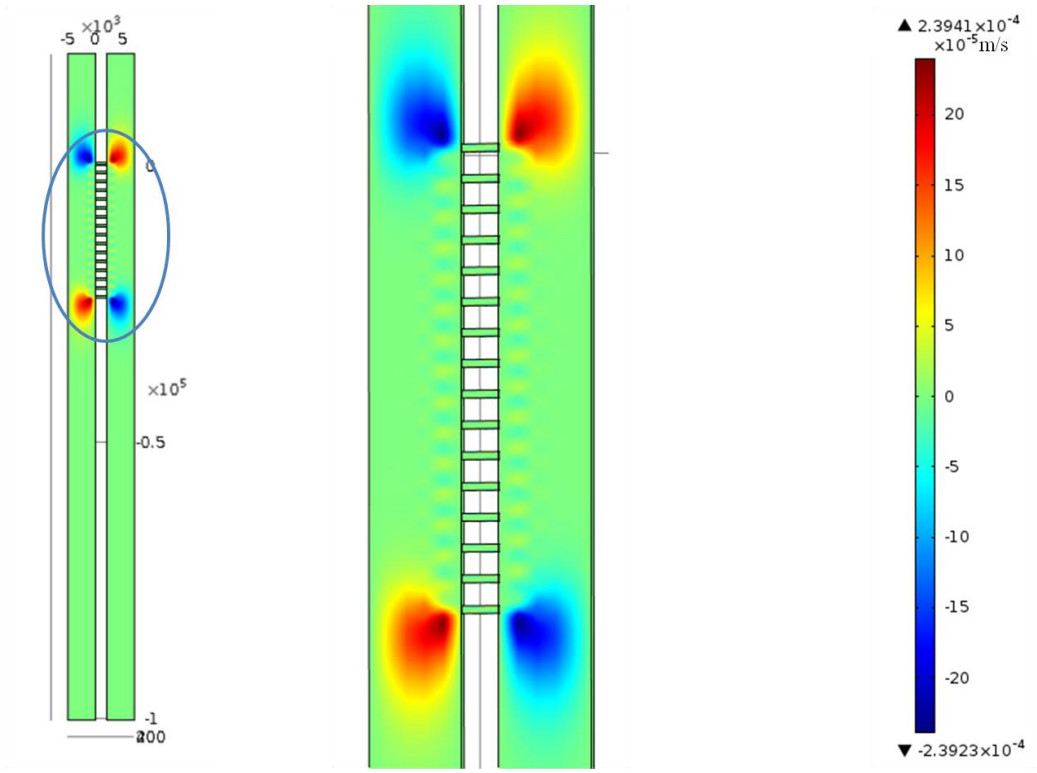

a $\theta = 0^\circ$

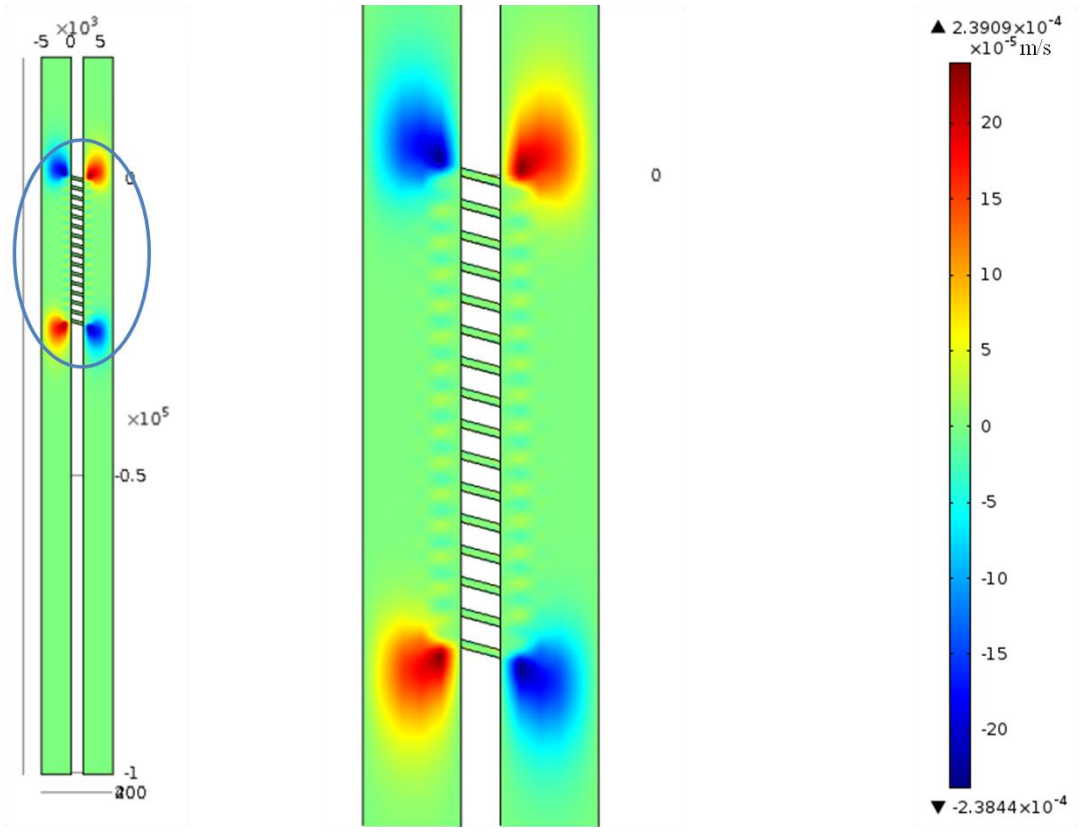

b $\theta = -15^\circ$

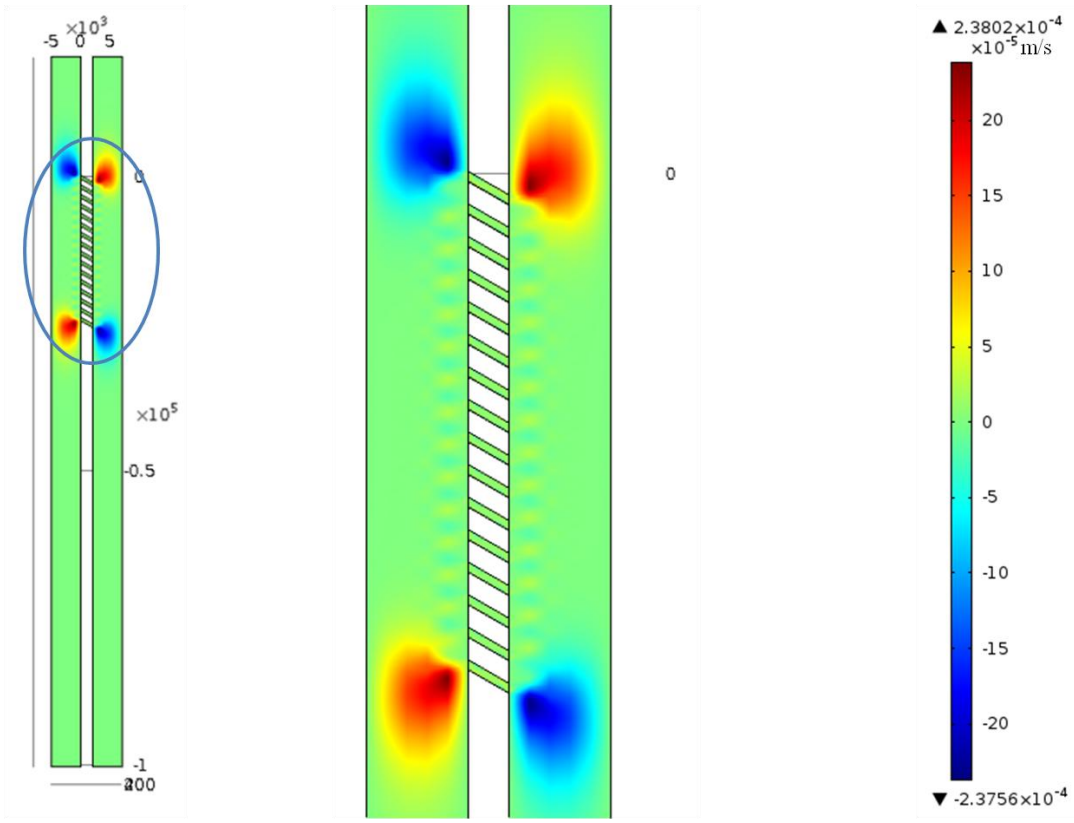

c $\theta = -30^\circ$

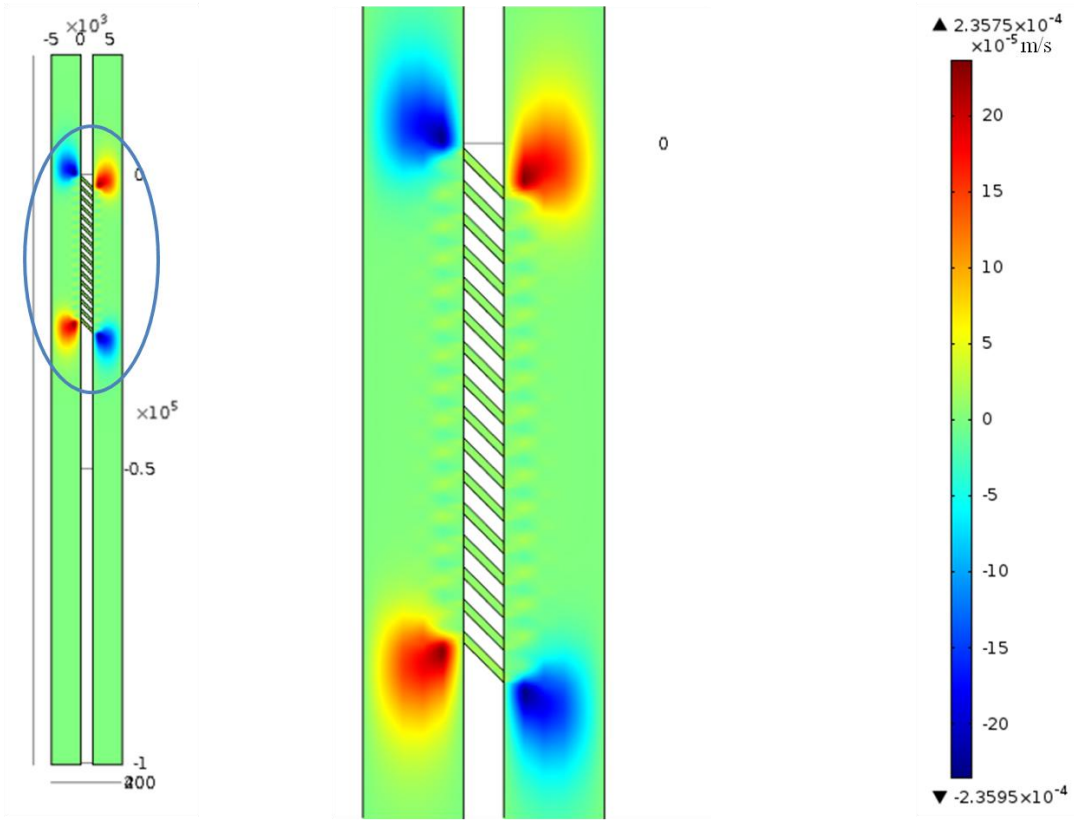

d $\theta = -45^\circ$

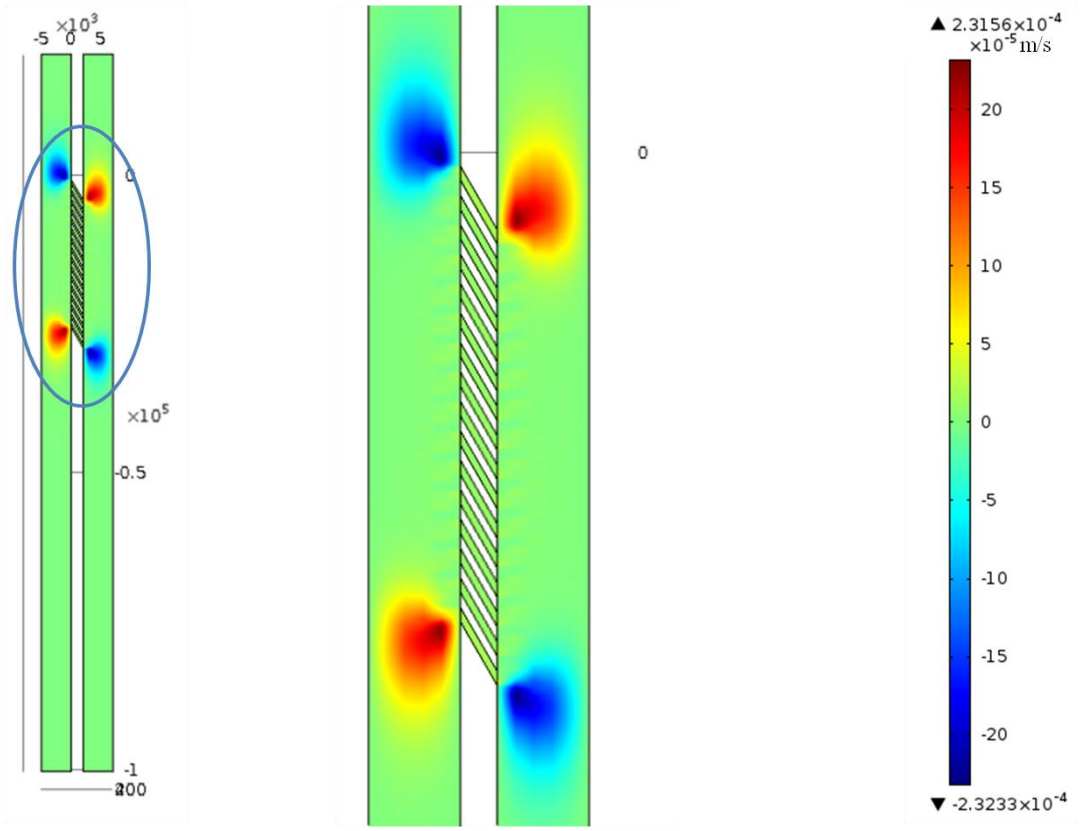

e θ = -60°

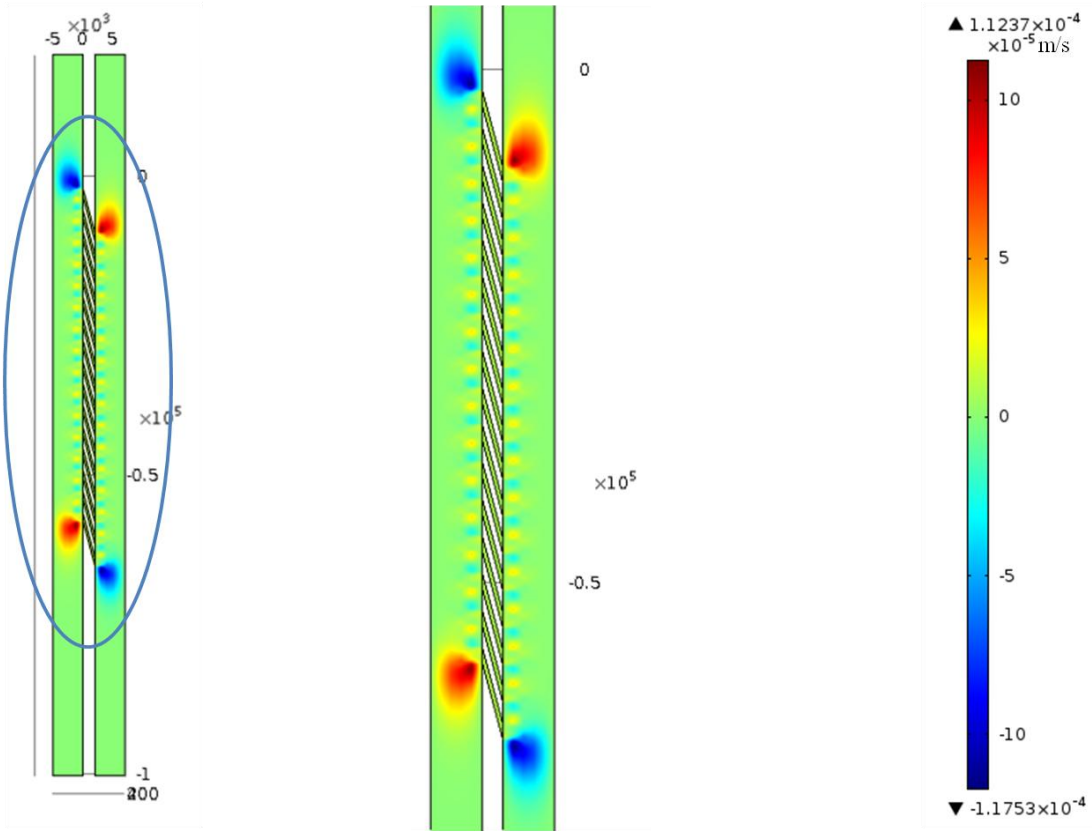

f θ = -75°

Figure 5.10 X direction velocity components (Slip boundary condition)

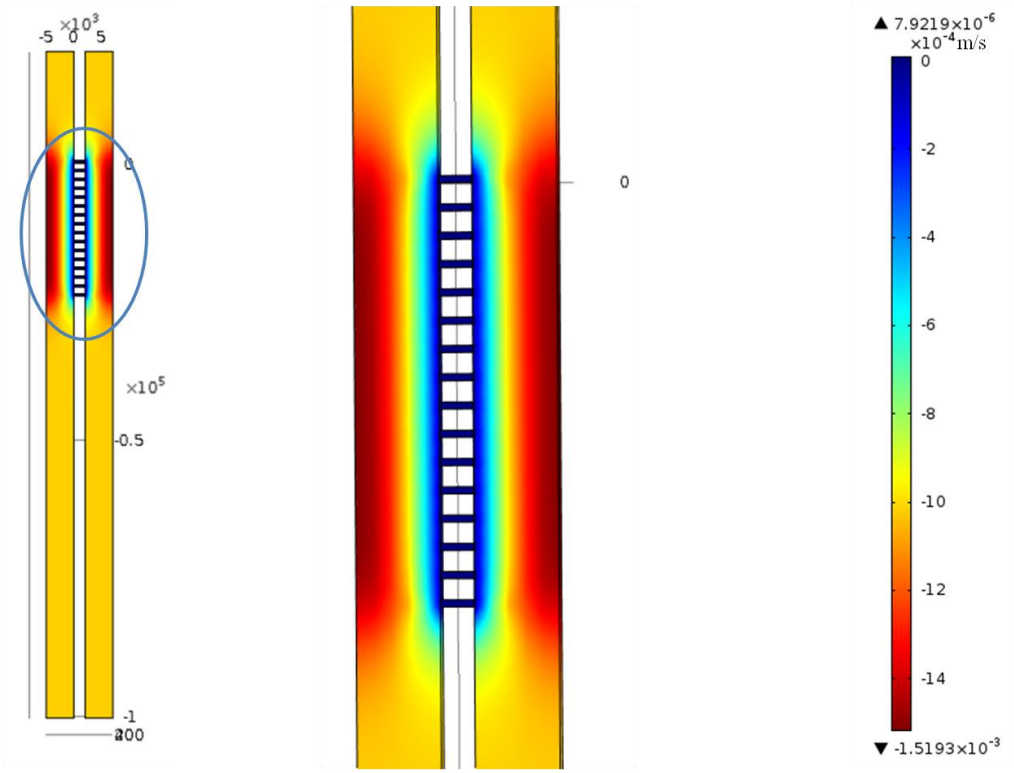

a $\theta = 0^\circ$

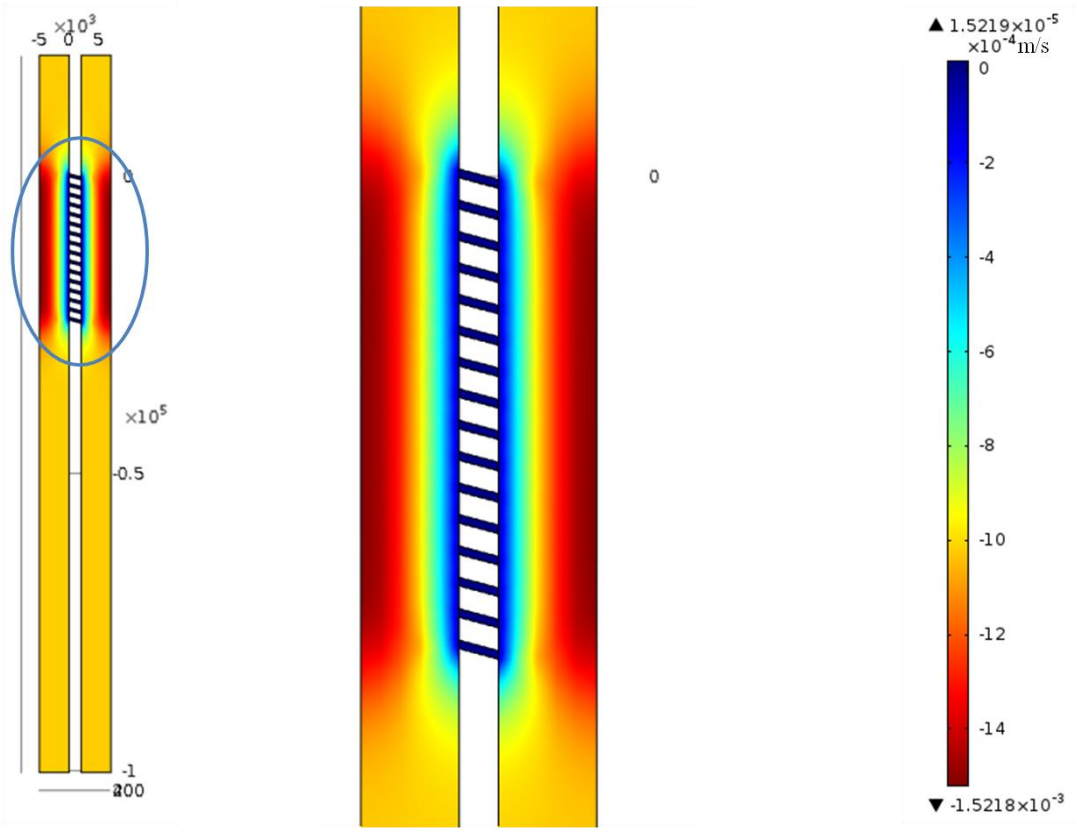

b $\theta = -15^\circ$

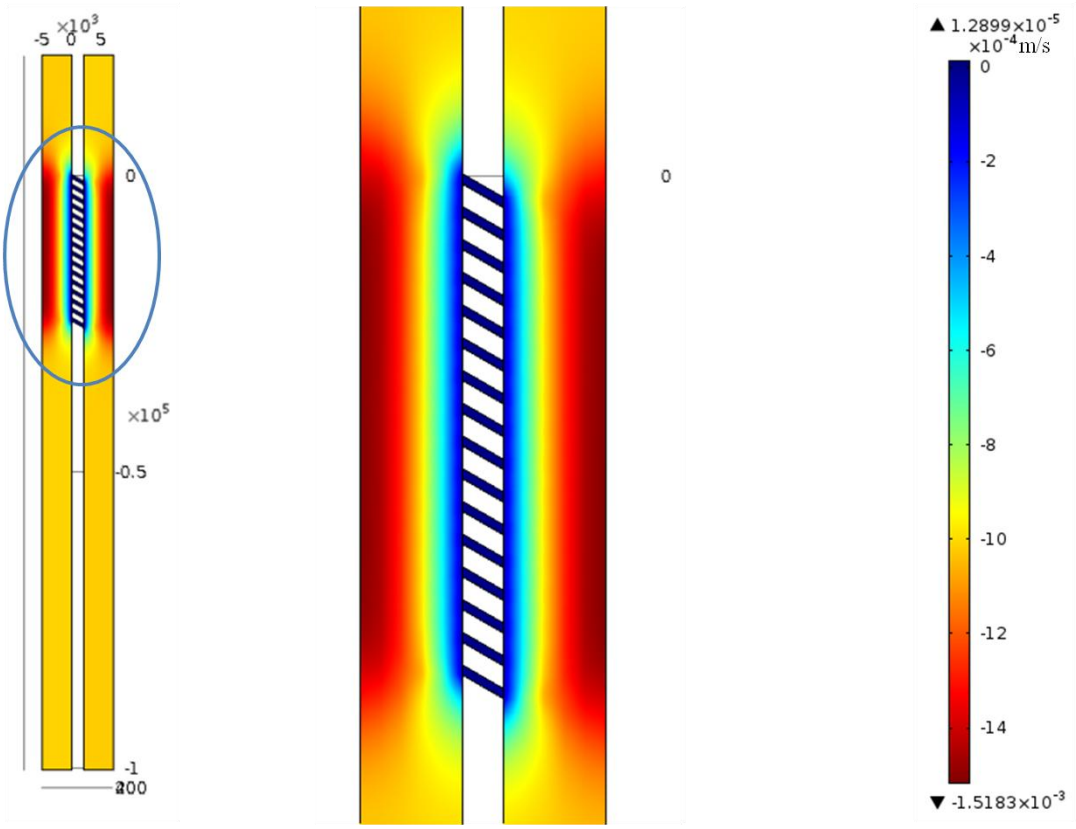

c $\theta = -30^\circ$

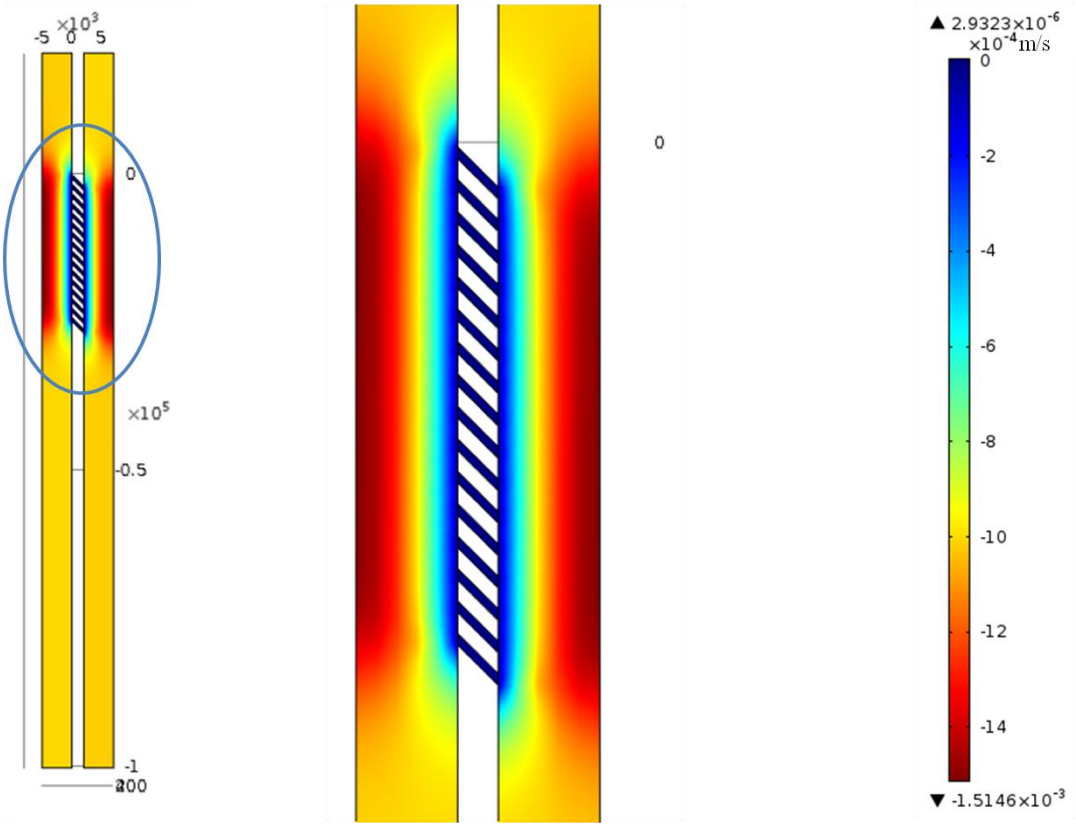

d $\theta = -45^\circ$

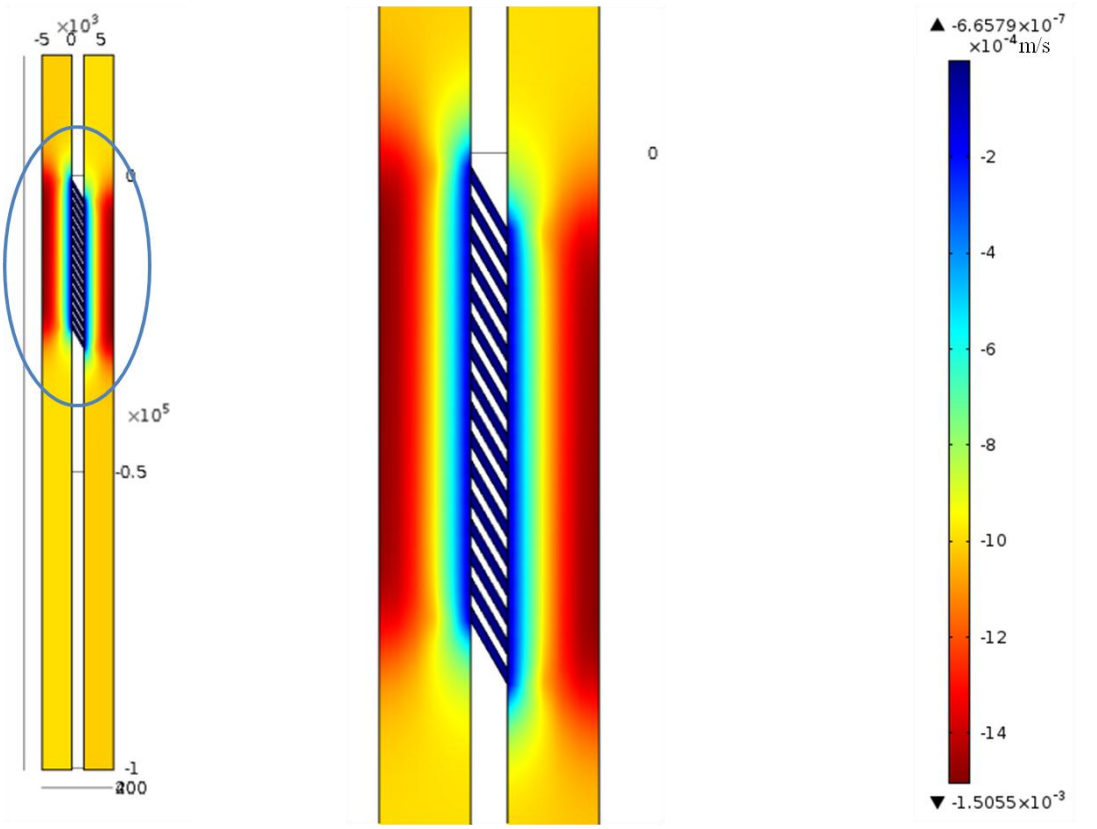

e $\theta = -60^\circ$

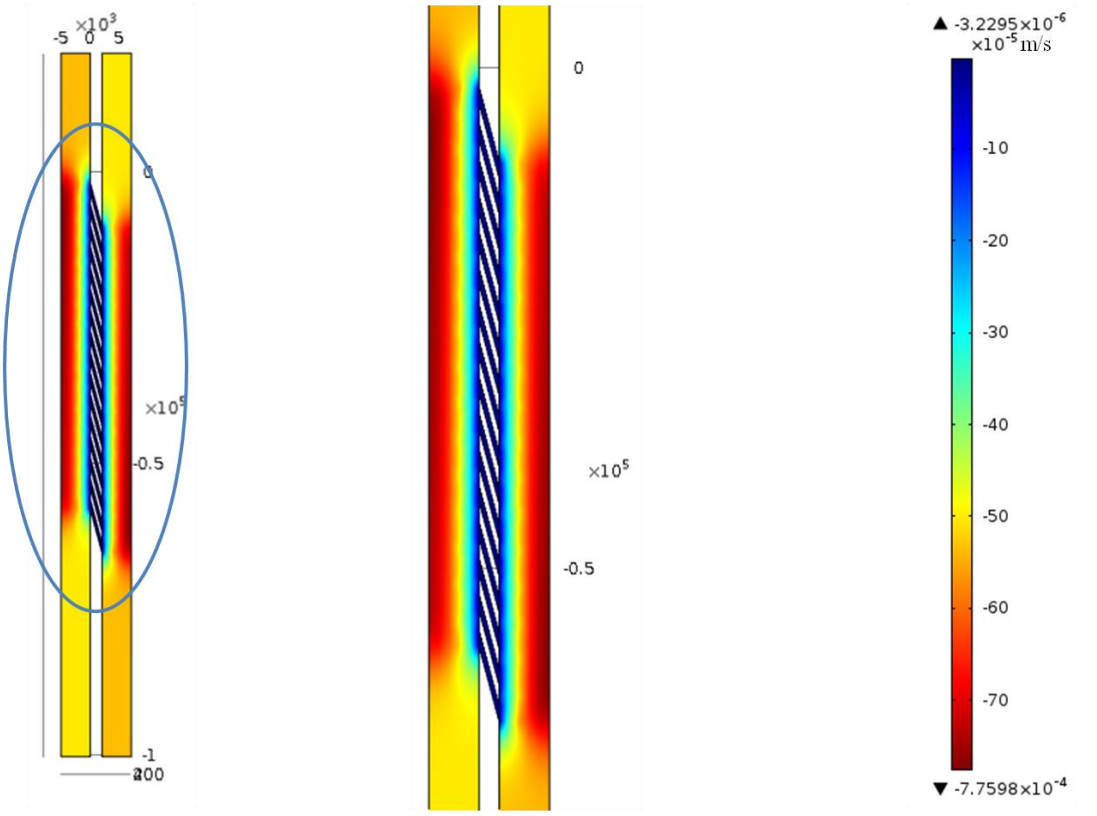

f $\theta = -75^\circ$

Figure 5.11 Y direction velocity components (Slip boundary condition)

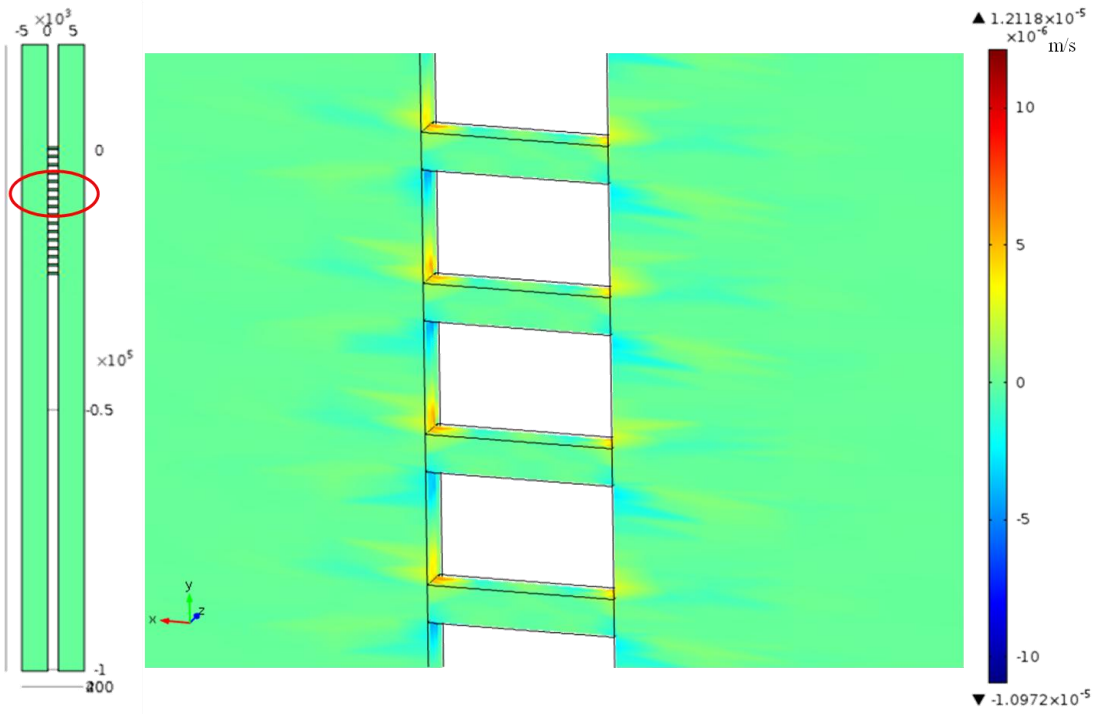

a $\theta = 0^\circ$

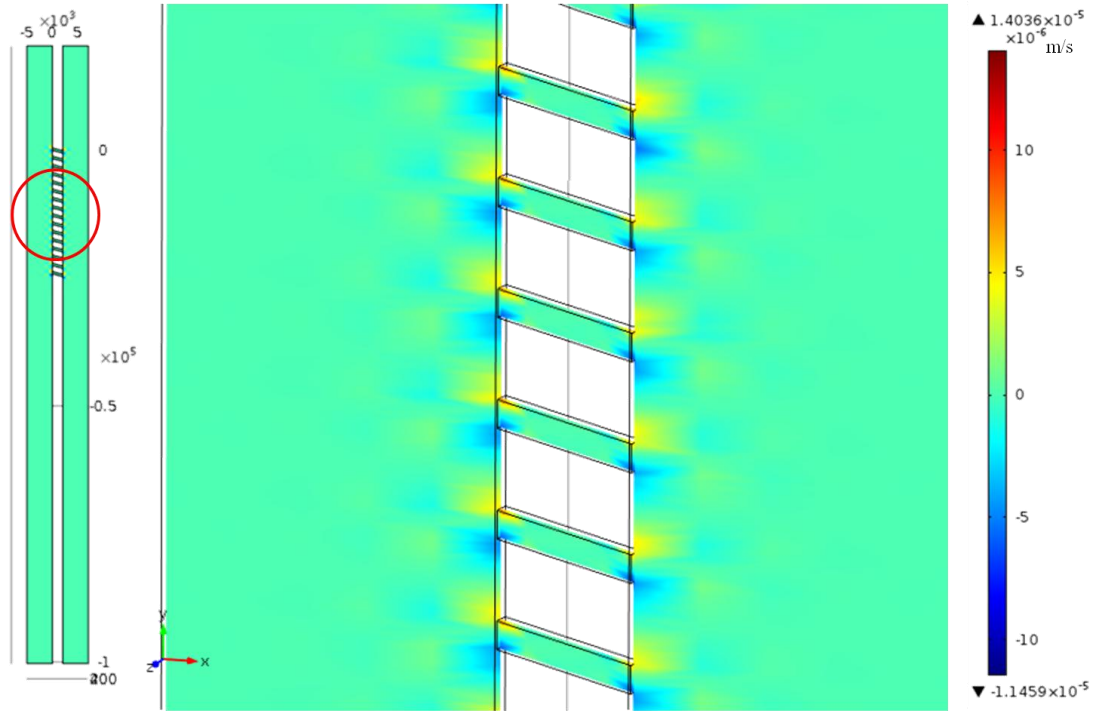

b $\theta = -15^\circ$

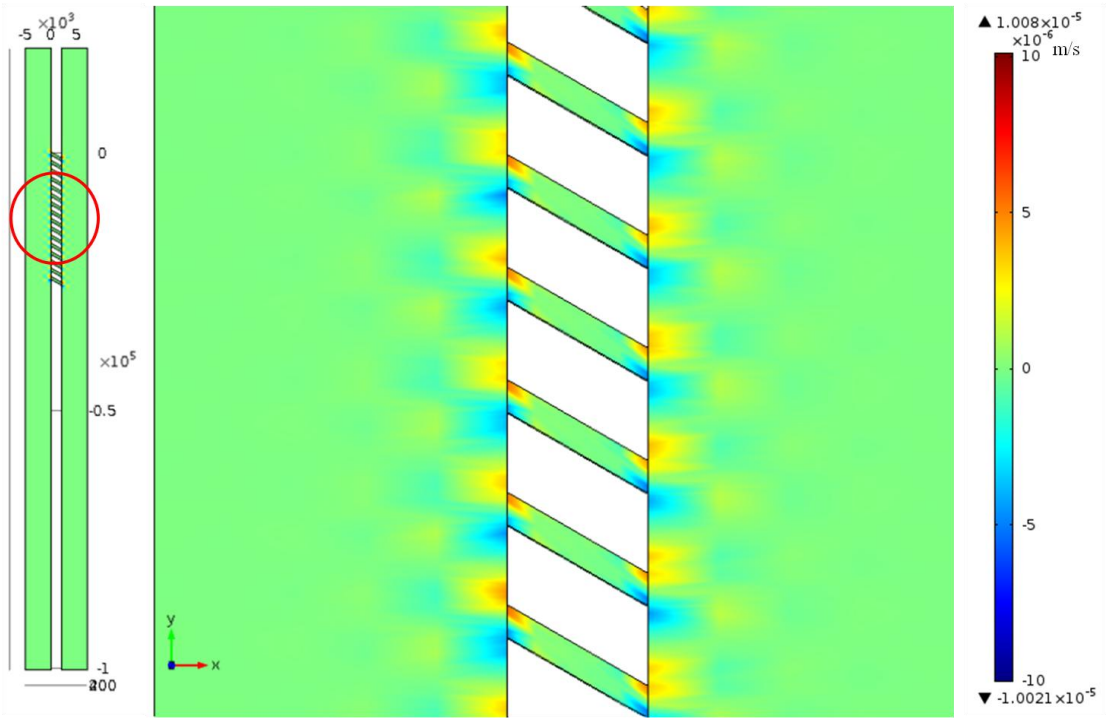
×10³
-5 0 5
0
×10⁵
-0.5
-1
y
x
▲ 1.008×10⁻⁵
×10⁻⁶
m/s
10
5
0
-5
-10
▼ -1.0021×10⁻⁵

c θ = -30°

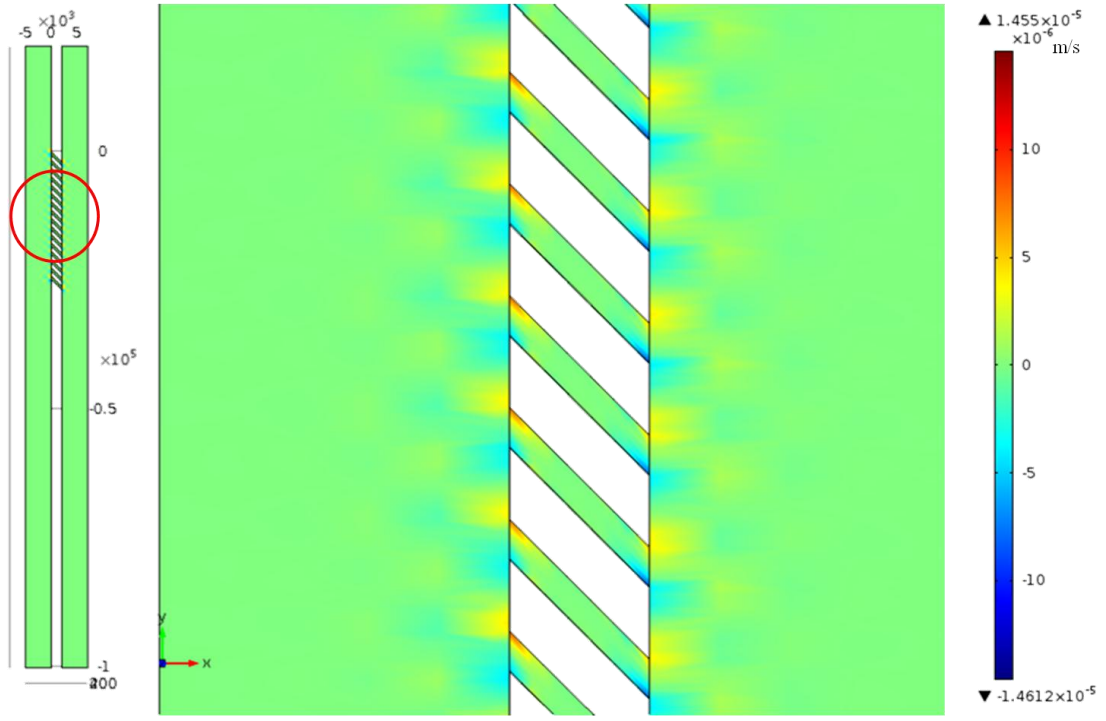
×10³
-5 0 5
0
×10⁵
-0.5
-1
y
x
▲ 1.455×10⁻⁵
×10⁻⁶
m/s
10
5
0
-5
-10
▼ -1.4612×10⁻⁵

d θ = -45°

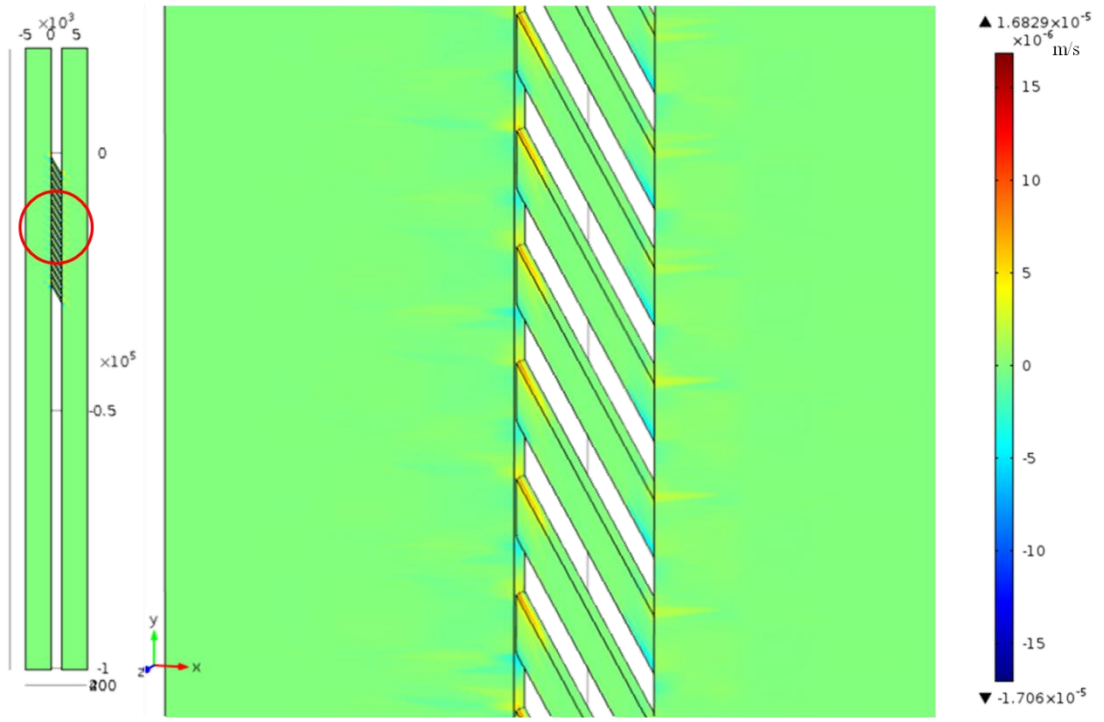

e θ = -60°

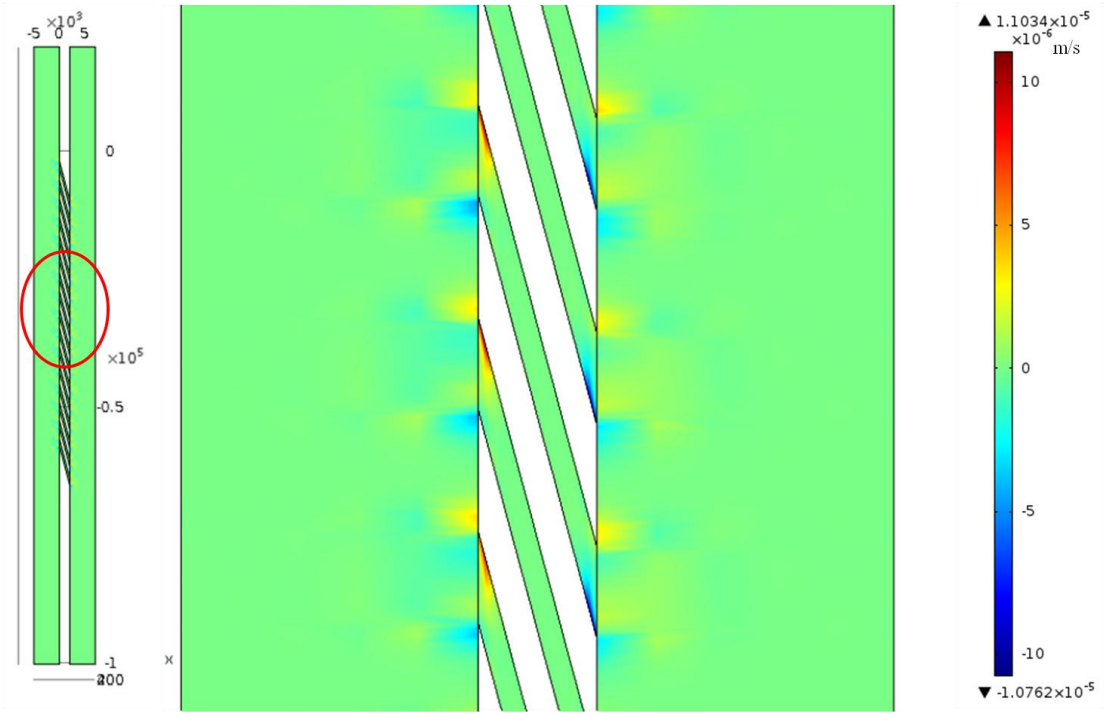

f θ = -75°

Figure 5.12 Z direction velocity components (Slip boundary condition)

5.3.2 Velocity Streamline

When $\theta = 0°$ (Figure 5.13a), the two vortexes occupy almost the whole area of a sieve channel. By raising the angle magnitude, higher convection appears across the sieve channels while the vortex in the sieve channels decreases. When the angle magnitude is large (Figure 5.13 e & f), streamlines across the sieve channel are obvious while the vortexes disappears. These phenomena were not observed in the simulations under no-slip boundary condition in section 5.2.3. The convection in the sieve channels reduces the possibility of clogging and jamming inside the channels.

The velocity streamlines shown in Figure 5.13 clearly present the low velocity layer. The flow goes around the cross sections and leaves a blank area which is the low velocity layer. The low velocity area is formed due to the vortices in the sieve channels. Comparing with the simulation results in section 5.2.3, the streamlines are still concave towards sieve channels around the cross section but much smoother.

5.3.3 Pressure

Figure 5.14 shows the contour pressure for different angles. The pressures beside the sieve channel are equal, although the value of the pressure varies rapidly at the cross section. There are apparent overpressures at the top edges of the sieve entrances. It is able to be seen that the pressure at the bottom of a sieve channel entrance is lower than the pressure at the top of the adjacent sieve channel entrance. Therefore the pressure gradient along the interface of the cross section slows down the flow along the interface. This is why there is a low velocity layer at the cross section.

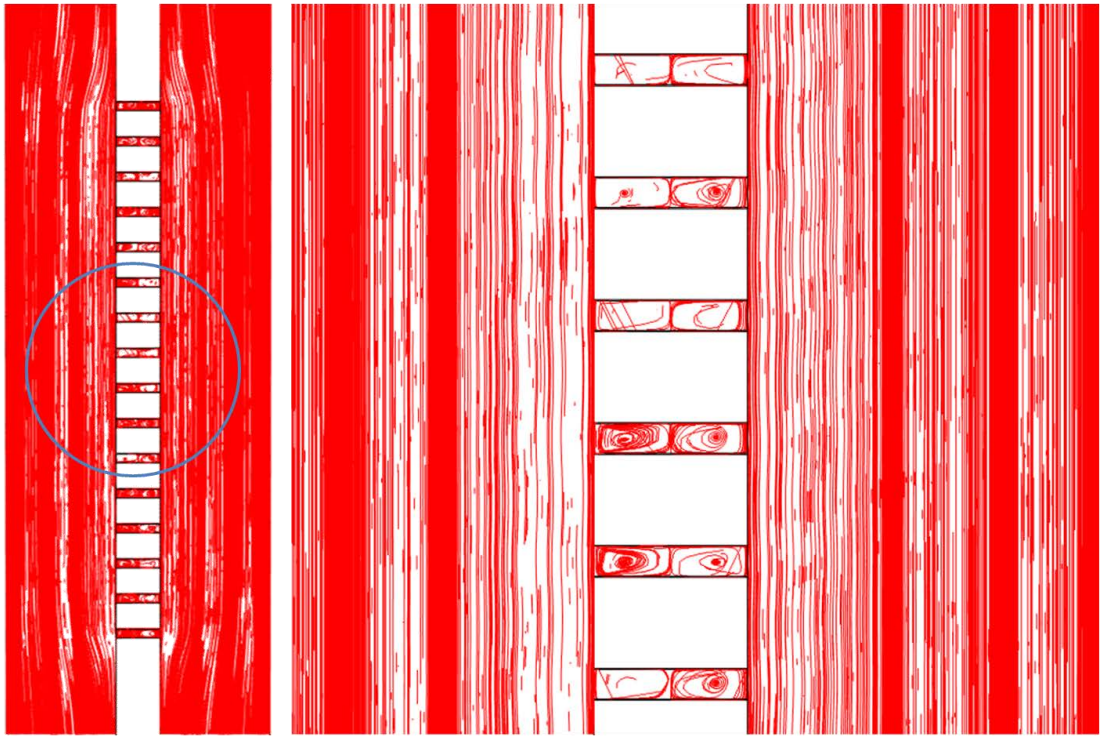

a $\theta = 0^\circ$

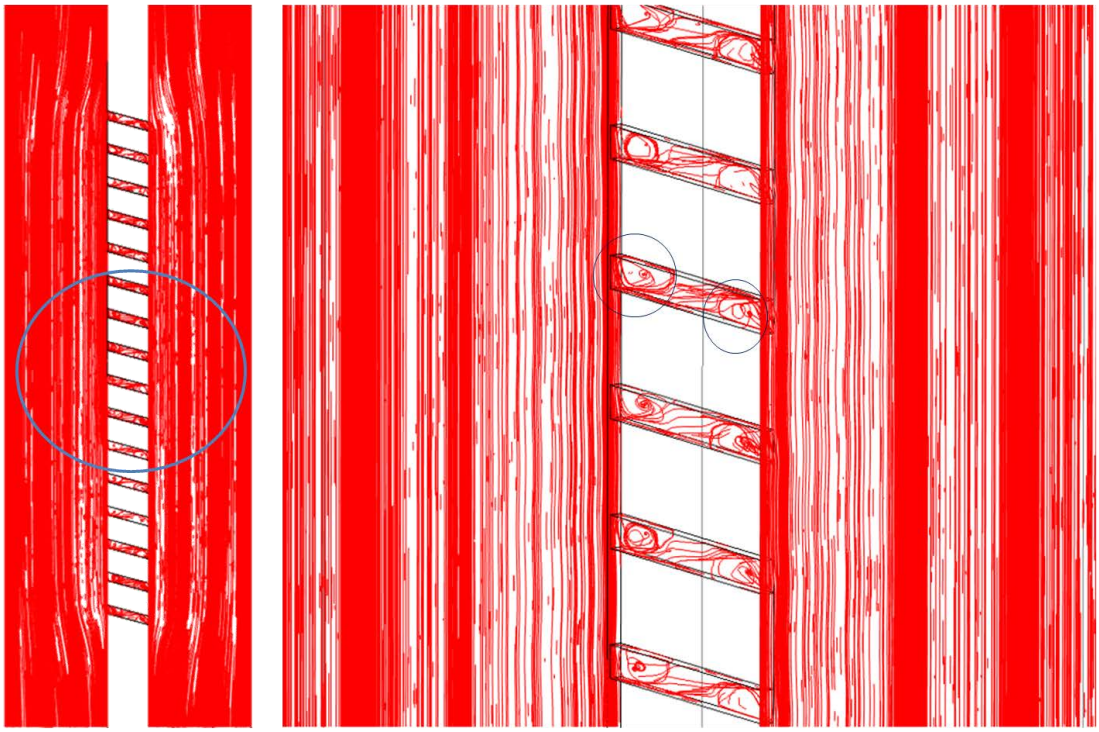

b $\theta = -15^\circ$

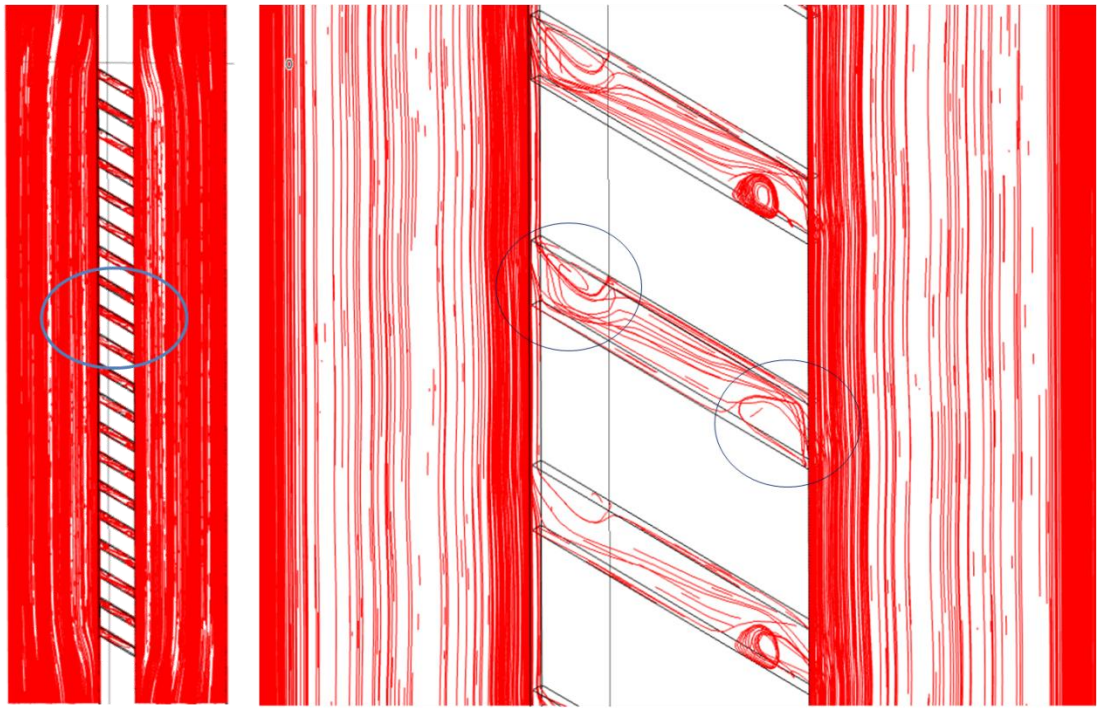

c $\theta = -30^\circ$

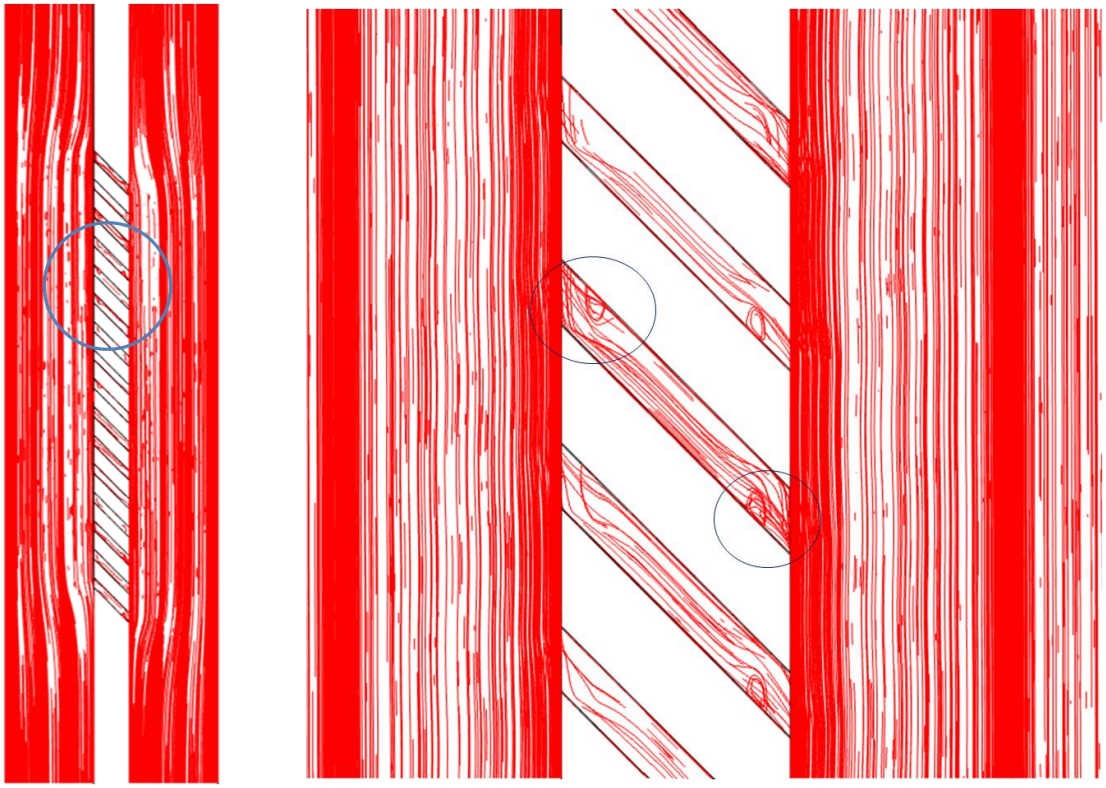

d $\theta = -45^\circ$

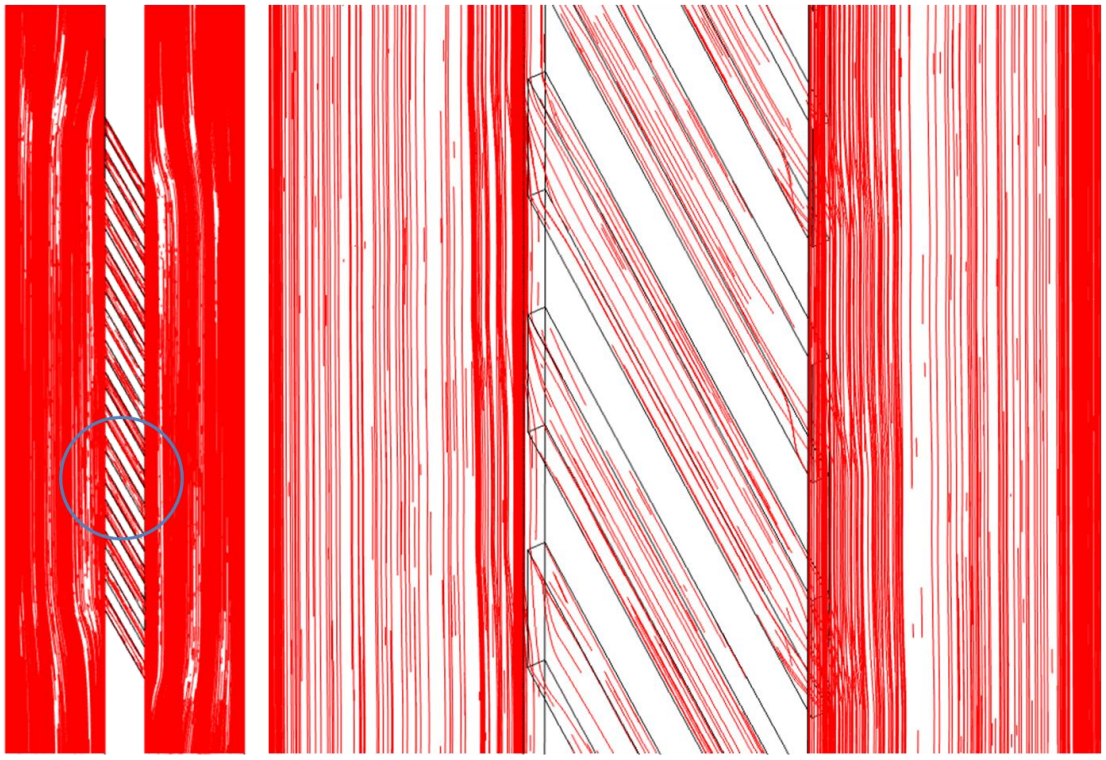

e $\theta = -60^\circ$

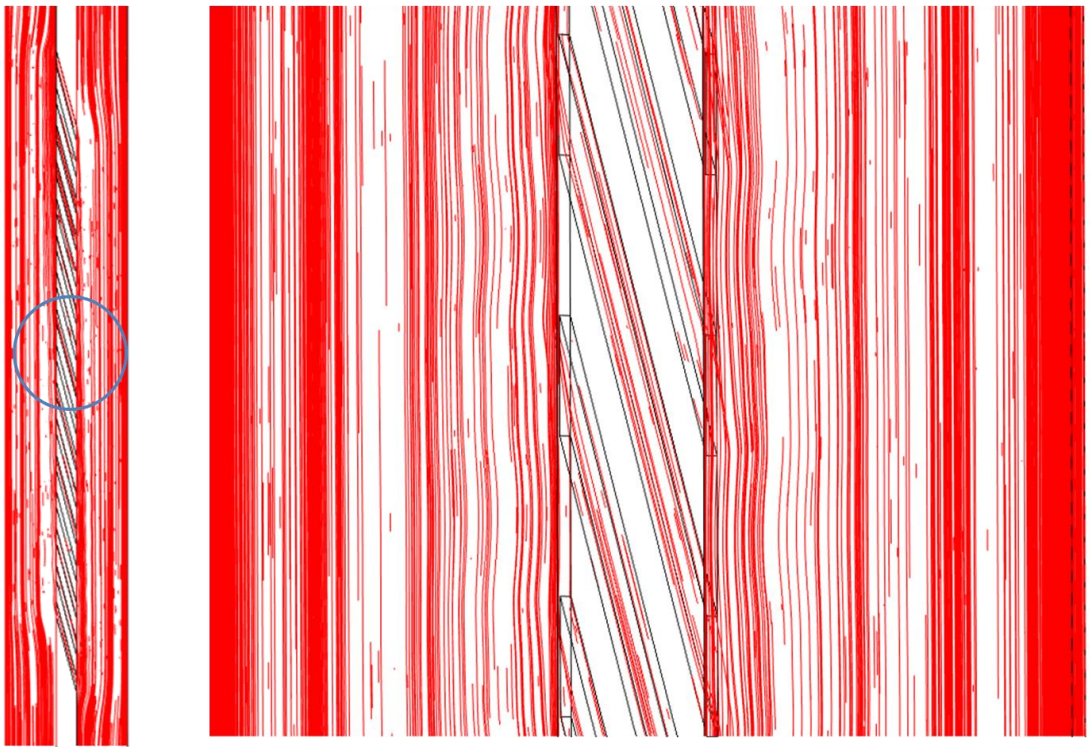

f $\theta = -75^\circ$

Figure 5.13 Velocity streamlines of angular H shaped channels series with slip boundary condition

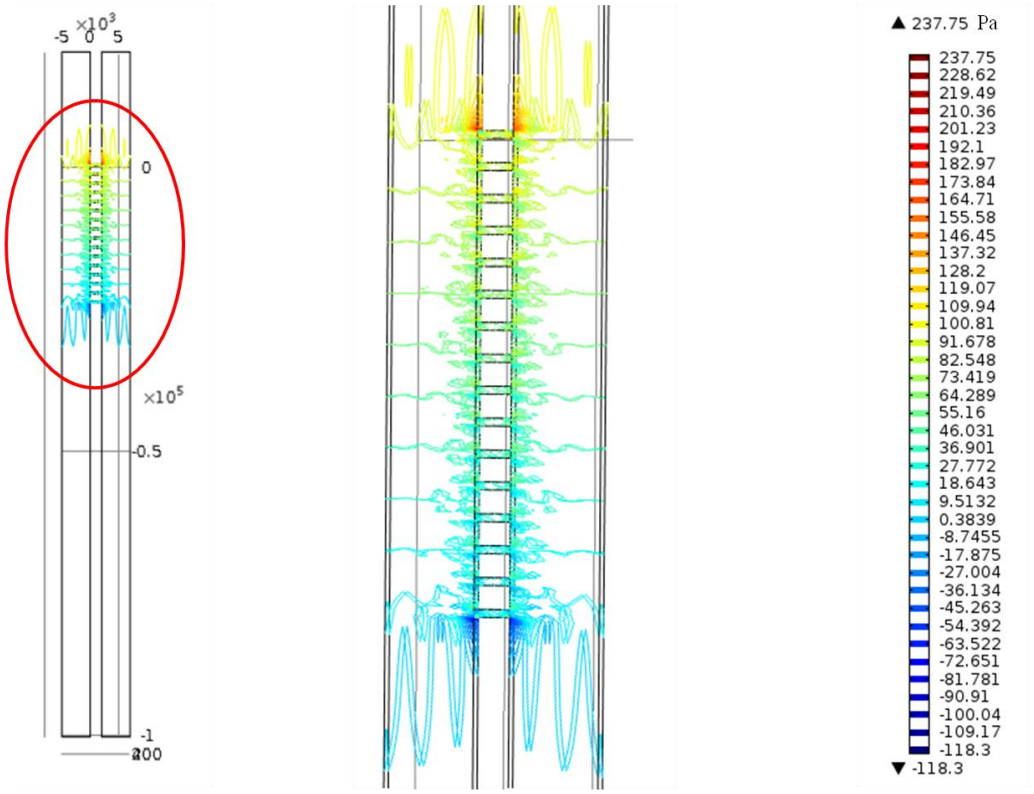

a $\theta = 0^\circ$

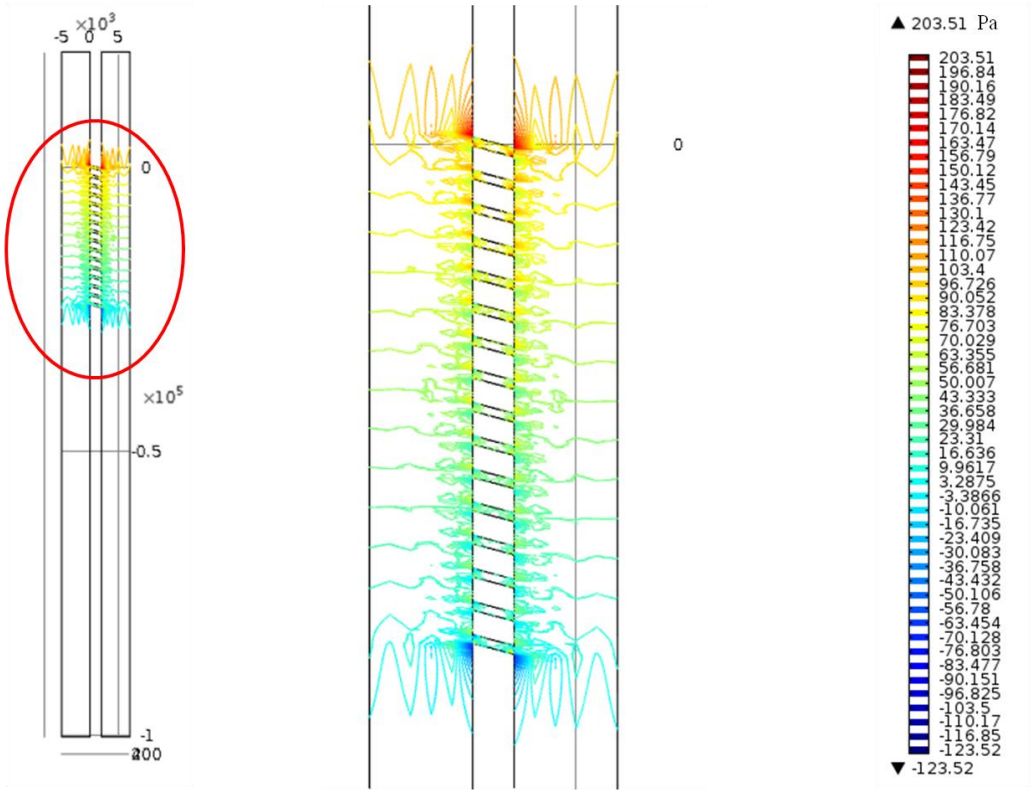

b $\theta = -15^\circ$

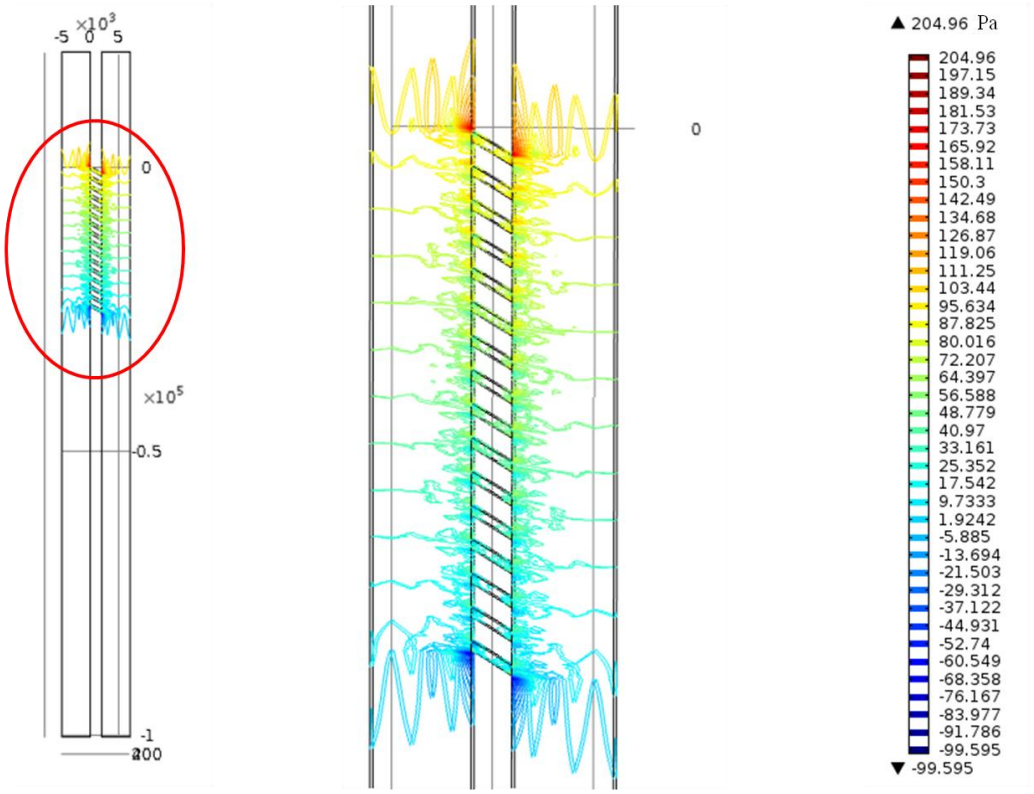

c $\theta = -30^\circ$

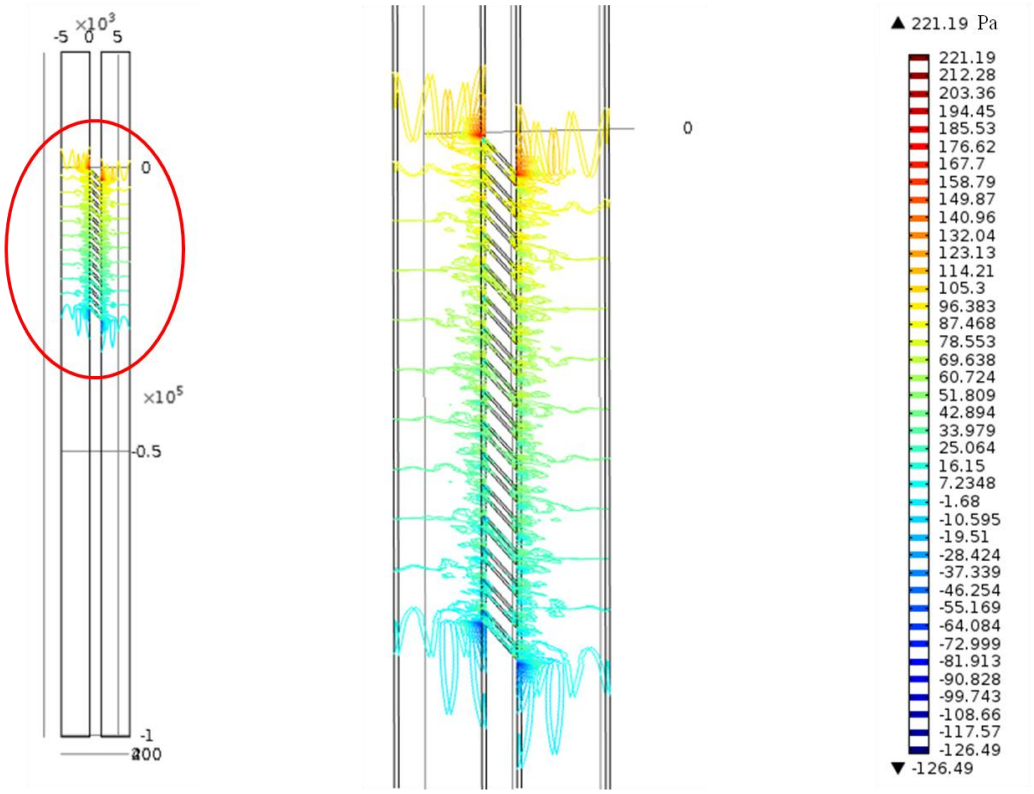

d $\theta = -45^\circ$

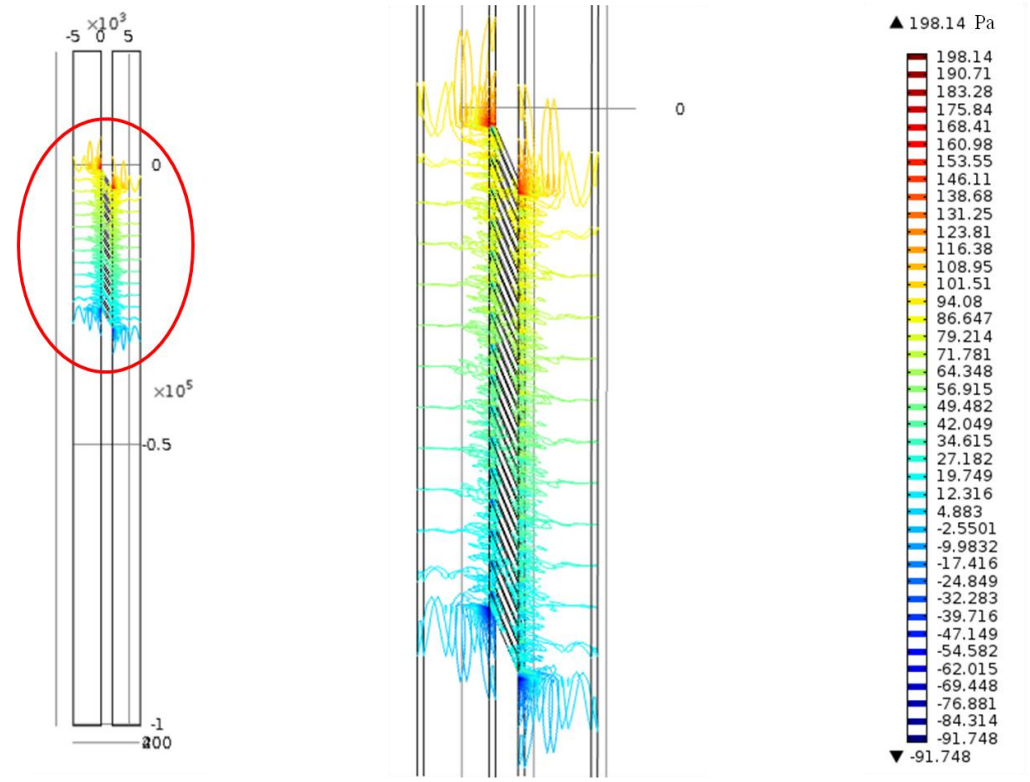

e θ = -60°

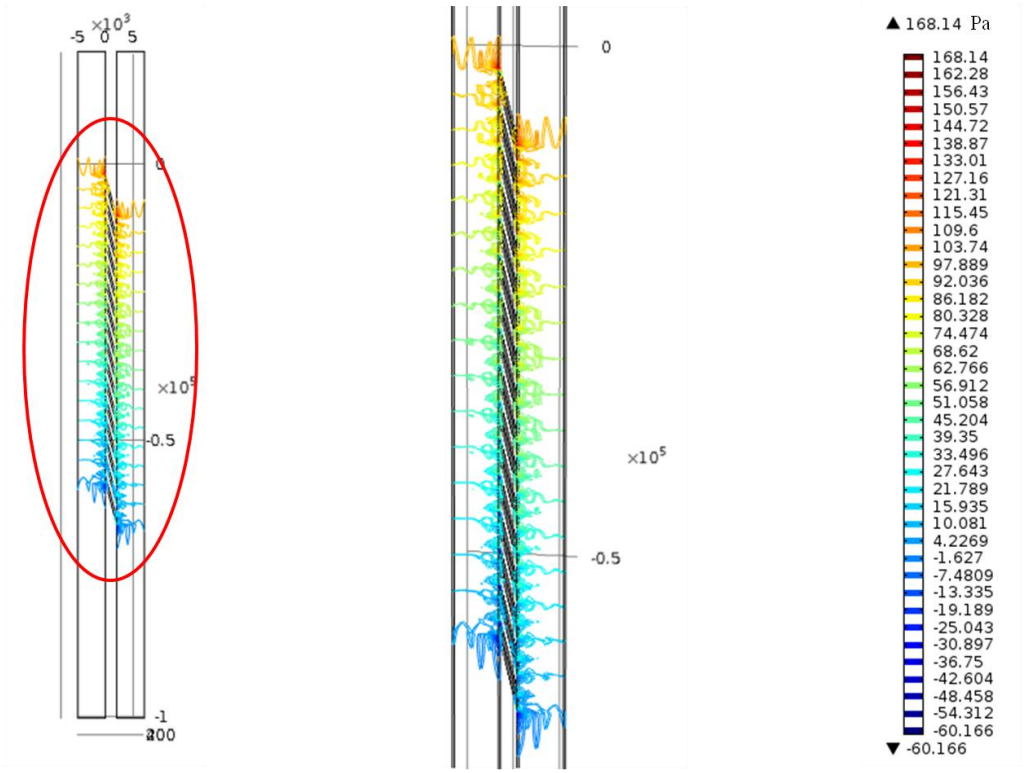

f θ = -75°

Figure 5.14 Contour pressure of angular H shaped channels series (Slip boundary condition)

5.3.4 Conclusions

When the slip boundary condition is applied for studies of filters based on H shaped channels, the surface velocity at the solid-liquid interface is not zero. Overall higher velocity is achieved. However, a low velocity layer occurs on the interfaces of the sample inlet channel-sieve channels and capture channel-sieve channels. This is because of the high roughness of the interface [161]. In the low velocity layer area, diffusion is the main transport process. The flow goes around the low velocity layer reducing the contact of component with the sieve surface. Considering the slip on the filter interface, the H channel series therefore reduce the possibility of adhesion at the entrances of the sieve channels. The vortexes in the sieve channel with small angle magnitude acts as a mixer thus increase the diffusion flux. On the other hand, the dead volume increases the chance of clogging.

Although the flow rate in the sieve channel increases with the angle magnitude and is higher than the flow rate in the no-slip situation; the proportion of fluid flows into the sieve channel drops down (When $\theta = -75°$, the sieve channels occupy 3.36% of the inlet sample solutions flow under the slip condition; while 10.19% under the no-slip boundary condition), therefore the concentrating effect is weakened. As the value of flow velocity in the sieve channel is still low, diffusion still dominates the transport process in the sieve channels. Thus the improvements caused by the convection across the sieves are still limited under the free slip boundary condition. As the flow rate in the sieve channel with no-slip boundary condition is even lower, only large magnitude angle is valuable to be applied with slip flow filtration.

5.4 3D Modelling of Three-Level Angular Semi-H Shaped Filter

5.4.1 Model settings and meshing

The three-level filter consisted of one 20 μm × 270 μm × 800 nm (width × length × depth) sample inlet channel; 200 200 nm ×2 μm× 200 nm, 20 400 nm × 2 μm × 400 nm and 2 800 nm × 2 μm × 800 nm sieve channels; and also three capture channels of which the depths were all 800 nm. The angle of the sieve channels was set as -60°. The density and dynamic viscosity were 1.50 kg/m^3 and 0.03 Pa·s respectively. Transport of Diluted Species (*chds*) and Laminar Flow (*spf*) modules were used in this simulation. Figure 5.15 shows the settings of those modules.

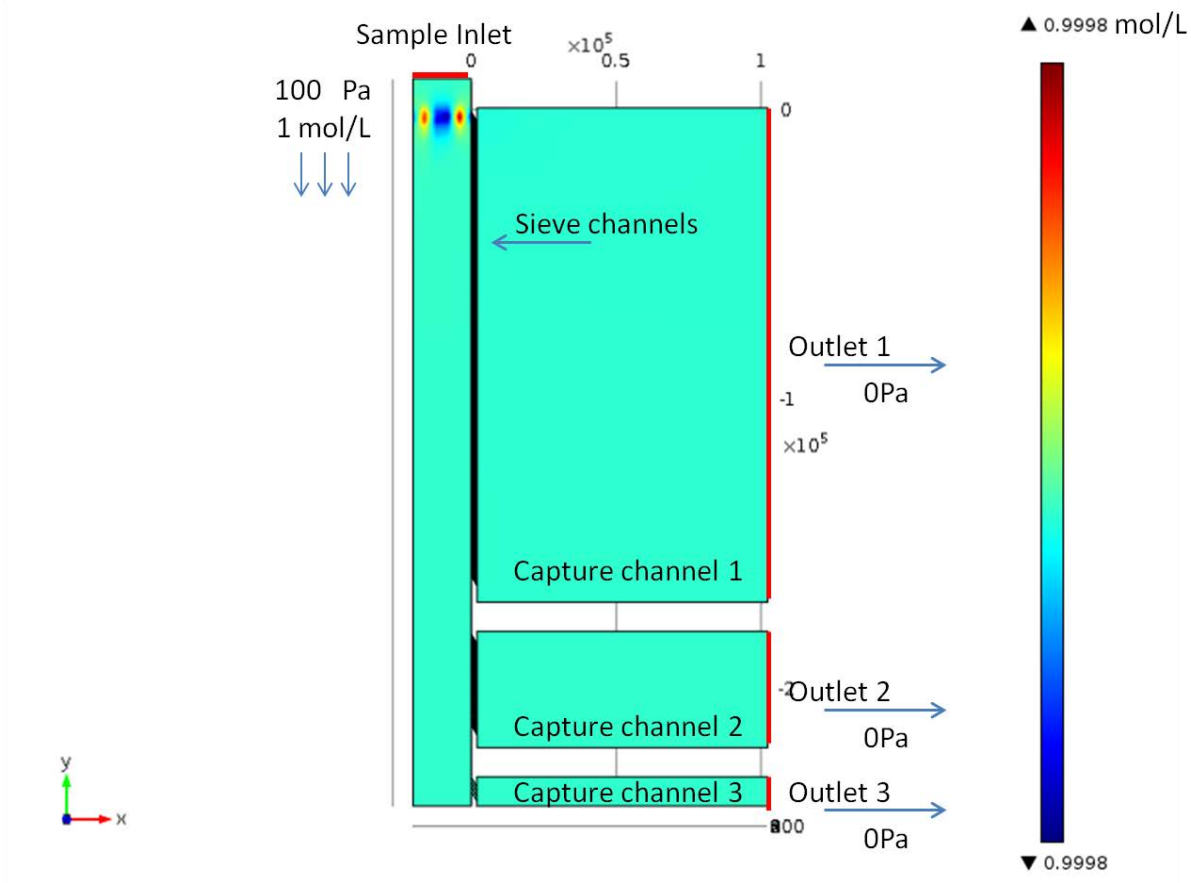

Figure 5.15 Static concentration of particles smaller than 200 nm

User control mesh was selected to build the mesh. Figure 5.16 shows the mesh of this model. The meshing process was similar as section 5.2. Firstly the 2D free triangular mesh was drawn on the interface between the sample inlet channel and the sieve channels (yz-plane). This was then swept along the x-axis to build the 3D triangular prism mesh of the sample inlet channel and sieve channels. Thirdly a free triangular mesh was drawn on the interface between the sieve channels and capture channels (yz-plane). Then this free triangular mesh was swept along the x-axis to form the mesh of the capture channels. The size of the free triangular mesh was from 100 nm to 625 nm and the size of swept element was from 200 nm to 1,000 nm.

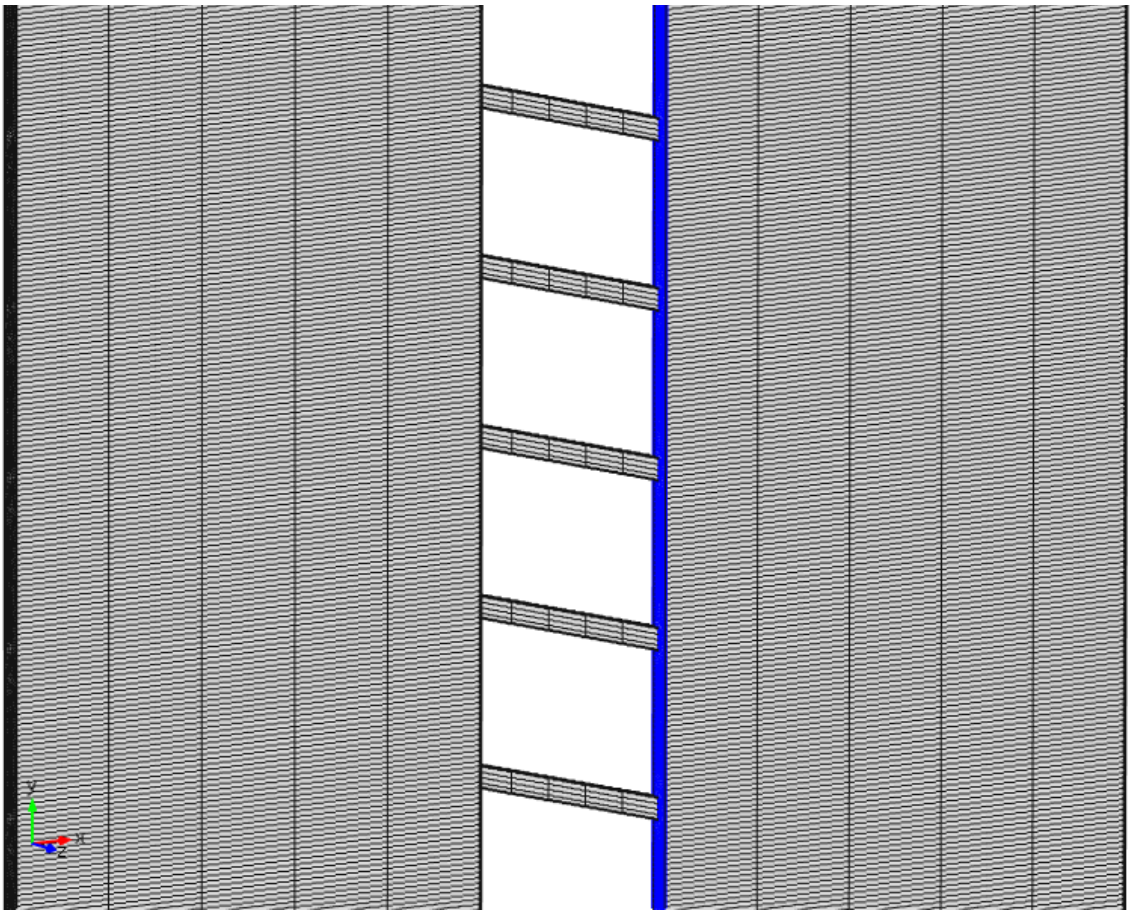

Figure 5.16 3D Mesh of the three-level angular semi-H shaped filter.

5.4.2 Velocity magnitudes

Table 5.3 exhibits the velocity magnitudes in different positions of the three-level filter. For the sieve channels and capture channel, the highest velocity value is found in the third level. However, in the sample inlet channel, the velocity reduces when the diameter of the sieve channel entrance increases. By calculating the surface integration of velocity at the inlet and outlets, the flow rate of each channel can be found and is given in Table 5.4. As the sample inlet flow separates sequentially into three levels of capture channels, it is understandable that the flow rate in the sample inlet channel drops down during every level of filtration. Among the capture channels, level 3 has the biggest sieve size. Even if the number of third level sieve channels is the least (two), the flow rate of Level 3 is still the highest of the capture channel due to the high flow rate allowed by the big entrance of the sieve channels. Figure 5.17 exhibits the velocity magnitude on yz-planes. The x component of velocity on yz-planes around level 1 &2; and 2&3 are shown in Figure 5.18 a &b.

Table 5.3 Velocity magnitudes at the middle of each channel (m/s)

Level	Sample inlet channel	Sieve channel	Capture channel
1	4.28e-8	1.87e-8	2.95e-9
2	3.08e-8	8.44e-8	9.8e-9
3	2.57e-8	4.77e-7	5.97e-8

Table 5.4 rate at each outlet of the three-level semi-H shaped filter (m^3/s)

Sample inlet	Capture 1	Capture 2	Capture 3
7.57139e-19	1.00056e-19	1.59884e-19	4.97199e-19

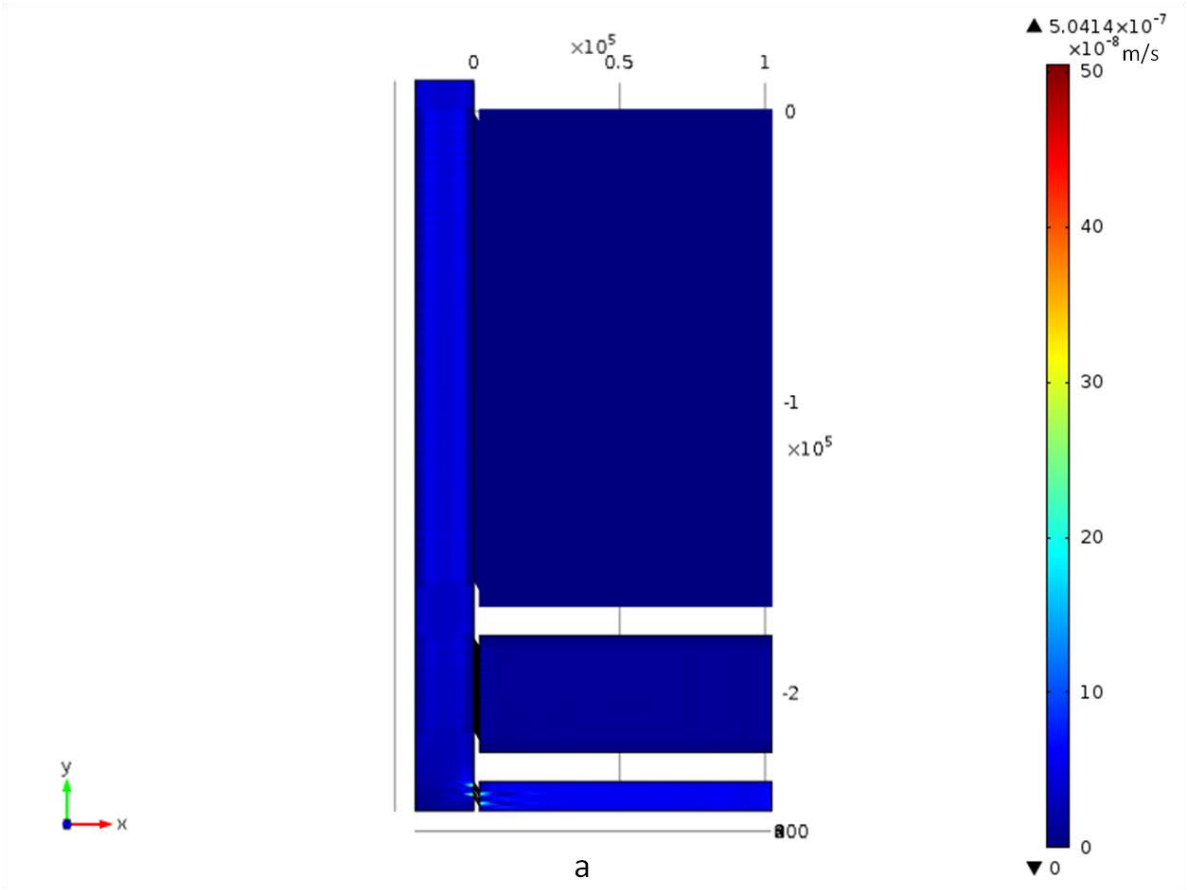

Figure 5.17 Magnitude of the three-level semi-H shaped filter.

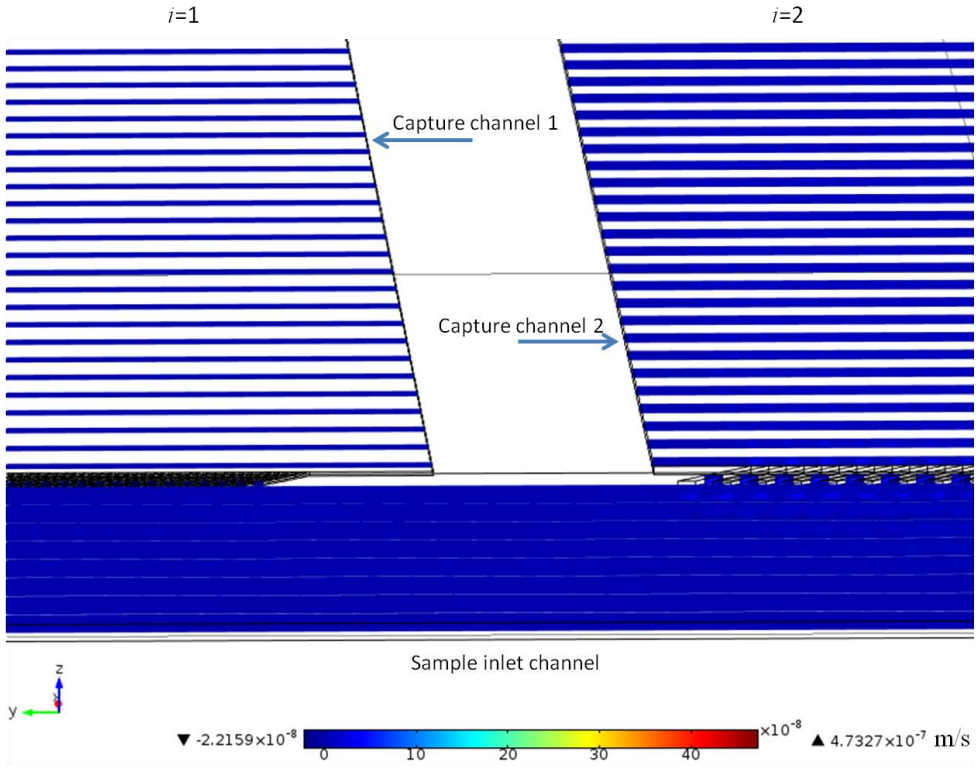

a

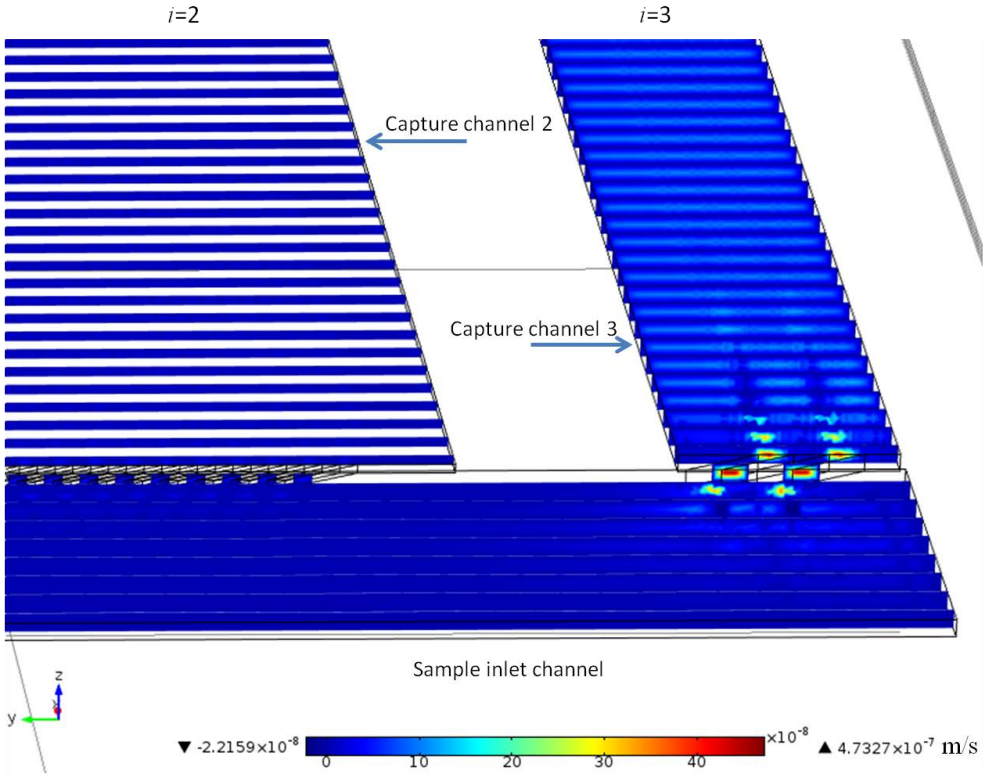

b

Figure 5.18 X direction velocity component on yz-planes slices:

(a) level 1 and 2; (b) level 2 and 3.

5.4.3 Flow Streamline

Figure 5.19a shows the streamline of the velocity field of the three-level filter based on semi-H shaped channels. Figure 5.19b and c describes the streamline at the second and third level respectively. It can be seen that most streamlines which start from the inlet flow across the third level sieve channels. Thus the flow rate in capture channel 3 is the highest of the three capture channels. The first level captures the least flow due to the small diameter of the sieve entrances in spite of the number of sieve channels being the most for level 1.

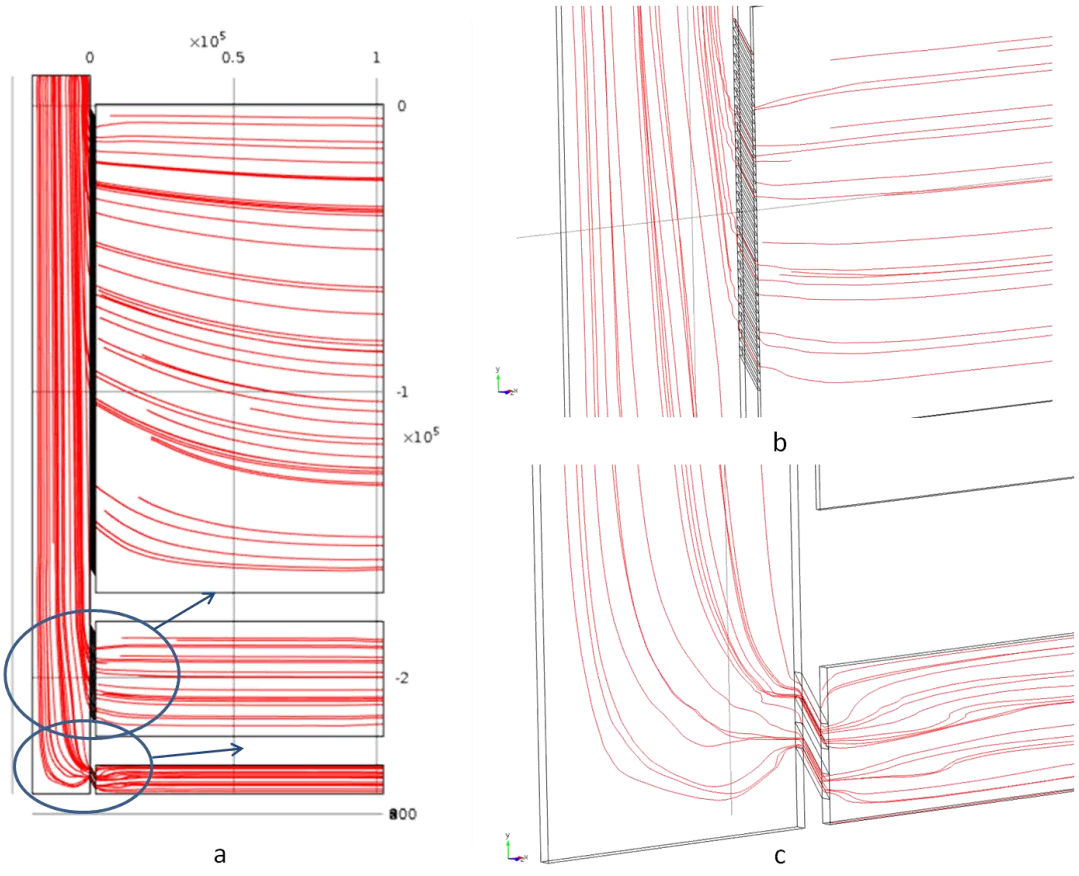

Figure 5.19 Velocity streamline of the three-level semi-H shaped filter

5.4.4 Pressure

The pressure distribution in the three-level filter based on semi-H shaped filter is exhibited in Figure 5.20. Although the initial outlet pressure is 0Pa; the pressure at the end of capture channel 1, 2 and 3 is 53, 51 and 47 Pa respectively. It has been mentioned in section 4.2.1 that the pressure drops down quickly in the sieve channels. For that model of a one level semi-H shaped channel series, the pressure at the bottom cross section of the sample inlet channel and last sieve channel is low. Thus the last sieve channel which connects the sample inlet channel and capture channel drags the pressure at each end into equilibrium. The pressure in the sieve channels decrease rapidly because the pressure in the sample channels drops down heavily. In Figure 5.20 there is a clear contour pressure line which shows the pressures at each end of the last sieve channel of the first level are the same. That is why the pressures at the outlets are not zero.

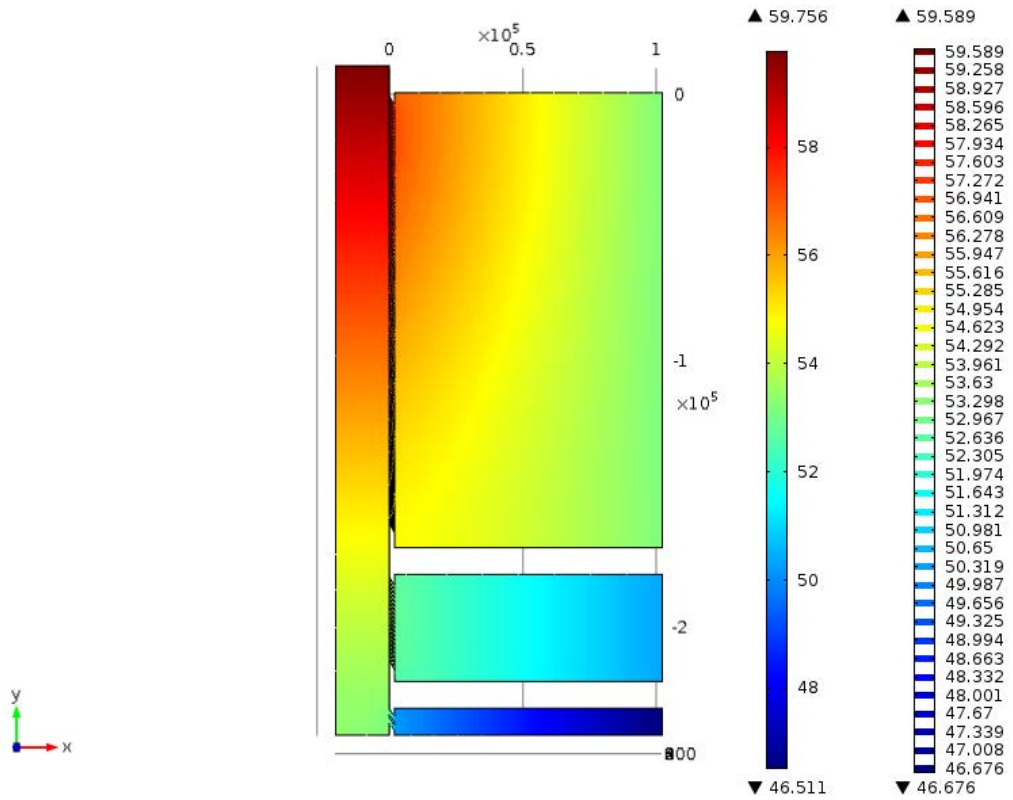

Figure 5.20 Pressure in the three-level filter based on semi-H shaped channels. (Pa)

5.4.5 Concentration

The inlet concentrations of all three components are 1 $\mathrm{mol/m^3}$; the concentrations at each outlet are described in Table 5.5. The results are the same as for three different sized filtrations with paper filters or membrane filters used in the laboratory. Thus this three-level filter is one feasible way to microminiaturize the filtration process down to the chip level. However, it is not able to purify middle diameter components from the mixtures of small, middle and big particles. This problem limits its application for multi component purification when pure middle sized components are wanted. A multi-level filter based on H shaped channels is able to meliorate the purification process.

Table 5.5 Concentration after multilevel filtration ($\mathrm{mol/m^3}$)

	$i=1$	$i=2$	$i=3$
$j=1$	1	1	1
$j=2$	0	1	1
$j=3$	0	0	1

5.4.6 Conclusions

Firstly, there is relatively high flow in the sample inlet channel which is helpful to reduce adhesion on the sample inlet channel-sieve channels interface.

Secondly, the closed sample inlet channel (no outlet) results in a lower flow comparing with an open sample inlet channel (one outlet at the bottom of sample channel). Thus closed sample inlet should be avoided in design.

Thirdly, the concentration results illustrate that multi-level filter based on semi-H shaped channels is able to separate mixtures into multi group. However, it can only remove the bigger group from target components, but cannot remove the smaller group. Thus multi-level filters based on semi-H shaped channels have a limited capability for multi sized component separation. A multi-level filter based on H shaped channels is able to improve the purification process further.

5.5 Summary

Aiming at more accurate simulation of filter based on H shaped filter, 3D models of angular H shaped channel series were built and studied in this chapter. The flow properties and angle effects were analysed. This study was helpful for understanding the flow process in filter based on H shaped channels. Overall the angle was shown to have limited improvement of flow rate in sieve channels. However the possibility of adhesion increases because the angle enhances the trap effect around cross section area by enlarging the cross section.

Then slip boundary condition was applied with the same models. The flow rates were improved comparing with the ones with no-slip boundary condition. Low velocity layers were observed around cross section among sample inlet channel, sieve channels and capture channel. This layer protected the cross section from unwanted contact with big components therefore reducing the chance of adhesion and clustering. The convection in sieve channels was observed when the angle magnitude was bigger than 30°. Thus large angle showed potential improvements of adhesion and clustering inside sieve channels.

A 3D simulation on a three-level filter based on semi-H shaped channels was reported as well. The pattern simulated was designed for the verification chip in Chapter 6. A closed sample inlet channel resulted in a pumping difficulty comparing with an open one. What is more, the simulation results illustrated the limited capability of separation of multi sized components mixture.

CHAPTER 6

CHIP DESIGN AND FABIRCATION

6.1 Introduction

This chapter illustrates the methodology of filter chip design. A whole multi-level nanofilter design path contains application demand analysis, detection requirement analysis; geometric design, interface design, material selection and fabrication process design six steps. Two multilevel filter test chips for dextran and dyed nano spheres separation were designed by this path as examples to demonstrate the methodology of filter chip design.

A new applicable fabrication process for micro- and nano- filter chips was described and demonstrated. In this manufacturing process, firstly photolithography was applied to achieve the 2D pattern of micro structures which were the sample inlet, capture and dilute channels; and then RIE was used to build the 3D pattern of these channels. The fine channels, nanosieve channels, were etched by Focused Ion Beam. After bonding the silicon substrate with a glass cover, a chip of multilevel filter was finally made. Fabrication experiments were described in this chapter and the recipes of each step were given. Other alternative fabrication routes were introduced briefly by the end of this chapter.

6.2 Design Flow of Multi-level Nanofilter Chip

Based on the three-level filter models analysed in section 4.5.1 which were the core and main pattern of the filter chips, two test versions of three-level filter chips were designed in this section. Whereas the geometric model of a multi-level filter has been already built based on the demand of the application, during the design several questions still should be answered. The first question is how to detect the flow and components in it? Then secondly besides the core pattern of the channels of multi-level filters, how to design the connection interface with other devices such as pumps and detection instruments, the question is, what kinds of materials are suitable for these applications? And finally the fourth to be answered is how these materials should be fabricated to build a patterned chip? After these questions are answered, combining with the geometric model of a multi-level filter, a design of chip is able to be developed. Figure 6.1 shows the whole design progress.

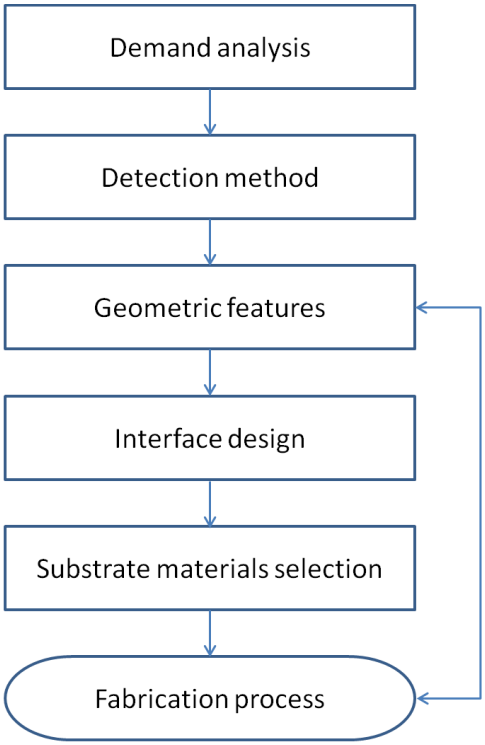

Figure 6.1 Flow process diagram for multilevel filter design

6.2.1 Detection Requirement Analysis

A straight forward way to show the filtration is by separating different size and colour dyed particles, such as commercial dyed nanospheres and fluorescent dextran. The capture solution of each level will show a different colour, which is a rainbow filtration. If the rainbow was observed, the sample inlet channel and capture channels should be visible. This is an example that detection methods affect geometric features design. The concentration is able to be detected under a microscope or more precisely by absorption photometry[162, 163]. For optical detection, the chip is desired to be transparent on at least one side, which should be considered during material selection. If a fluorescent microscope was applied for a real-time detection, the chip diameter and connection interface should be designed to allow adjustment of the stage of microscope.

6.2.2 Geometric features design

By analysing the components in the solutions for separation, main geometric features of multilevel filter chips can be designed. The width and depth (a_i) of n ($0 < i \leq n$) level sieve channels can be decided under the condition $a_j < a_i < a_{j+1}$. For a three-level filter, $n = 3$, maximally four different size component groups can be purified. The minimum width (w) and depth (d) of the sample inlet channel is governed by the size of the largest component, which is ($w > a_{j=n+1}, d > a_{j=n+1}$). The diameter of dextran is as shown in Table 6.1, thus the sieve size a_i for each level can be 2.33-29.4 nm, 29.4-54 nm and bigger than 54 nm respectively. Considering the EDL of channels and the fabrication method used, a set of value is able to be decided. For example, one set of a_i are 20, 40 and 80 nm respectively, which are suitable for Focused Ion Beam milling. The width (w) and depth (d) of the sample inlet channel could be 2,000 nm and 1,000 nm, which are easily achieved by

photolithography and RIE etching. These values were used in some simulations in Chapter 4. It should be noticed that there are no experimental data for an accurate fluorescent dextran diameter. What is able to found is that the dyed particles are small (molecule weight comparing with 3kDa dextran), thus the theoretical diameter (imagining the shape of component is a sphere) of fluorescent dextran conjugate is similar with but bigger than the dextran itself. Therefore the diameter values in Table 6.1 are still to be referenced when designing the filter.

Table 6.1 Diameter of commercial dextran

j	Molecule Weight	Diameter a_j (nm)	Fluorescent Label	Colour
1	3kDa	2.33	ThermoFisher Dextran Texas Red Neutral	Red
2	500kDa	29.4	ThermoFisher Dextran Fluorescein	Blue
3	2,000kDa	54	ThermoFisher Dextran Tetramethylrhodamine	Green

The details of the dyed micro and nano spheres are shown in Table 6.2, and from these it is able to design and test three-level filters to show the design process and fabrication process in a more straight forward way, i.e. a rainbow filtration. For example, Visiblex^{TM} Visible Dyed Nanospheres 1008(30nm red), 1011(300nm yellow), 1012(500nm purple) and 1004(800nm blue) can be used for a three-level filter test, in which the three-level sieves size are 200, 400 and 600nm respectively. Comparing with dextran conjugates, dyed nanosphere can be applied more easily with a uniform geometric shape and diameter. What is more, the detection of dyed nanosphere does not demand a fluorescent microscope which is not available in Micro-engineering and Nano-technology Research Group. For a verification experiment, dyed nanospheres are a better choice, while the dyed dextran conjugates are more suitable for bio-particles filtration. In this section, two chips were designed. One was a

chip aiming at demonstrating the fabrication process and observing the filtration phenomena. This chip was designed for dyed nanospheres. The other one was a three-level filter design for bio-particles separation and fluorescent microscope detection. Commercial dextran has a set of standard molecular masses and is widely used in bioscience, so that it is undoubtedly a good indicative component for filtration studies.

Table 6.2 Size map of commercial dyed nanospheres

Name	Size (nm)	Colour
Visiblex™ Visible Dyed Nanospheres 1001	30	Blue
Visiblex™ Visible Dyed Nanospheres 1002	200	Blue
Visiblex™ Visible Dyed Nanospheres 1003	500	Blue
Visiblex™ Visible Dyed Nanospheres 1004	800	Blue
Visiblex™ Visible Dyed Nanospheres 1008	30	Red
Visiblex™ Visible Dyed Nanospheres 1009	500	Red
Visiblex™ Visible Dyed Nanospheres 1011	300	Yellow
Visiblex™ Visible Dyed Nanospheres 1012	500	Purple

6.2.3 Connection Interface Design

At beginning, a test chip aiming at demonstrating the fabrication process and filtration was designed. Here it is named as verification chip. It was designed to be as simple as possible. The sample inlet was a hole on the silicon substrate which connected with a polycarbonate or silica tube. However it is hard to avoid leaking by sealing to the silicon wafer with pipes. One way to solve this problem is packaging the chip and pipe together with PDMS. Another solution is connecting the tubes with the glass side, which is applied on most commercial microfluidic chips. Thus in the later design of multi-level filter chip a commercial connecter was used. All pipes were connected with the inlet holes on glass cover (Figure 6.2).

Figure 6.2 Commercial interface for an four channels chip (http://www.dolomite-bio.com)

6.2.4 Materials Selection

As it was mentioned in the literature review, several materials are widely used for Lab-on-Chip devices, which are silicon, glass, PDMS, metal and other polymers.[164] For microfluidics devices, glass is a common choice for substrates, especially in industry, due to the low cost, fabrication accuracy, and harshness of environment that it will withstand. Another reason is that the transparency of glass makes optical detection to be realisable, which is crucial for biomedical applications. However, the fabrication techniques limit the application of glass for nanostructures. Whereas the multi-level filter contains several different depth structures, it is difficult to make each level sieve channels on the same surface by wet etching which is currently the main fabrication method for glass due to the low cost and high throughput. Femtosecond laser machining and other alternative techniques are able to manufacture 3D nano structures on glass; however the cost is relatively high. Thus glass is a candidate substrate material. PDMS and other polymers are not suitable for nano channels due to their low mechanical strength. What's more the possibility of reaction with sample fluid also limits the application of polymers.

For nanofluidics devices, a silicon wafer is one of the best substrate materials due to the difficulty of reaction of the silicon with the fluidic samples, the low cost, good mechanical properties and the highly developed silicon fabrication techniques. Considering the widely

accessible equipments in laboratories, especially in the clean room of University of Birmingham, the silicon wafer is a great option for a patterned nanofilter demonstration. Meanwhile, glass was selected as the cover material for the compatibility with optical detection.

6.2.5 Fabrication Process Design

When the materials have been selected, fabrication methods and their recipes can be given based on the geometry conditions. For the multi-level filter based on H shaped channels fabrication process, various 3D fabrication techniques, such as Focused Ion Beam milling, femtosecond laser machining, gray scale e-beam lithography, nanoimprint lithography and scanning probe lithography are able to be used. The main difficulty is the fabrication of all levels of channels with different sizes on one chip. Considering the size map of components in human blood, the size of channels shall need to cover nanometres to microns.

Focused Ion Beam (FIB) is one way to manufacture 3D nano structures which was introduced in chapter 2.[132, 133, 135] The disadvantages are that FIB milling is expensive and time consuming. Thus it is not an economic way for large volume structure milling such as micro channels.

Laser machining is an alternative technique for micro channels fabrication. The etch rate of silicon can be more than $2 \times 10^5\ \mu m/s$ for micro channels.[165] The single femtosecond laser pulses technique can be used for nano channel fabrication on glass substrates or transparent polymer layer with a high repetition rate (GHz)[166] for a rapid writing speed (400m/s, the depth of channel depends on the laser pulse fluence [167]). The principle of femtosecond laser machining is the laser induced breakdown caused by the optical energy transferring to the material (glass or transparent polymer). The ionizations during this

transfer process permanently change the phase or structure of the material so that the exposure area can dissolve in solvent.[168] (For silica glass the solvent is water[169]). However, due to the strong two-photon absorption of semiconductors such as silicon at the fundamental wavelength of commonly used femtosecond lasers, this technique currently cannot be used for nano scale silicon modification.[170]

Another alternative technique for the 3D nano structures manufacturing on one chip is electron beam (e-beam) greyscale lithography of which the resolution can be 20nm [171, 172]. Comparing with FIB milling, on one hand e-beam lithography is faster and more economic; on the other hand e-beam lithography requires a resist layer. If 3D silicon structures are demanded, RIE could be applied to transfer the structures from the resist mould to the silicon substrate. During the transfer process (such as RIE etch and wet etch), there are unavoidable degradations of structures such as edge smoothing. If the accurate different thickness resist mould was achieved, for some applications (for example, when the fluids do not react with the resist and the mechanical strength requirement is low) there should be no necessity of a silicon mould.

Nanoimprint lithography is another option for batch fabrication, which is a potential way for commercial manufacturing [173-175]. The basic principle of nanoimprinting is to transfer the structures from the mould to the resist layer under pressing; and then transfer the structures from the resist to substrate, typically by anisotropic etching. As nanoimprint lithography needs a mould, it has the geometric accuracy degradation problems during the transfer of structures, which is similar to grey scale e-beam lithography. When the moulds for nanoimprint are ready, for trial experiments, the moulds are applicable thus there are no

necessity of the later imprint process if the amounts of experiment on each sized are little. Therefore nanoimprint is not an economic way for laboratory study.

Scanning probe lithography was reported as a top-down 3D manufacturing method for nano structures by Yongda Yan *et al* [176]. In this report, a $20\ \mu m \times 20\ \mu m$ portrait, in which peak-valley height was 120 nm, was machined with an atomic force microscope on a polished aluminium disc in 10min. Thus the scanning probe lithography is a low cost technique with high accuracy. This method is only suitable for nano scale structures and requires a precision-stage system. Mostly, scanning probe lithography is used as a bottom-up method for self-assembly manufacturing.[177-179] The basic principle is using the probe tip (scanning tunnelling microscopy or atomic force microscopy) to modify the surface and then proceeding the self-assembly fabrication. The materials and the relatively low geometric accuracy of patterns limit this bottom-up scanning probe lithography to be applied in nanofluidics.

No matter which fabrication techniques are chosen, the final manufacturing step is bonding the silicon chips with glass covers. Then a multi-level filter chip will be achieved. Here is an example fabrication path which was designed to fulfil the conditions in University of Birmingham. Considering the accessible facilities (mask aligner, DRIE and FIB) in clean room here, the femtosecond laser machining, greyscale e-beam lithography and probe scanning lithography are not available. Due to the high cost and low efficiency of FIB system, the micro and nano structures are designed to be fabricated separately for trial experiments of multi-level filter based on H shaped channels. For the micro channels, such as the sample inlet channel and all capture channels, photolithography combined with RIE is a common fabrication process for silicon which was introduced in section 2.5. After micro structures

manufacturing with photolithography and RIE, the nano structures can be etched by FIB on diced chips. Then the silicon chip can be bonded with a glass cover. It should be highlighted that this fabrication process has not been seen in other publications. The reason why not combine photolithography with e-beam lithography is the difficulty of spinning resist on an uneven surface. The greyscale e-beam lithography, femtosecond laser machining and scan probe lithography are not available with the machine in the laboratory here. Figure 6.3 shows this fabrication process. Photolithography is applied first with a silicon wafer to build a photoresist mask for shallow RIE etching. After the shallow RIE etching, a photoresist mask is fabricated on the back side of silicon substrate. Then DRIE is used for a penetration etch from the back side of the wafer. Then the substrate is cleaned and the nano channels are fabricated by FIB milling. Finally a glass cover is bonded with the silicon substrate by anodic bonding. This fabrication process was verified with experiments described below.

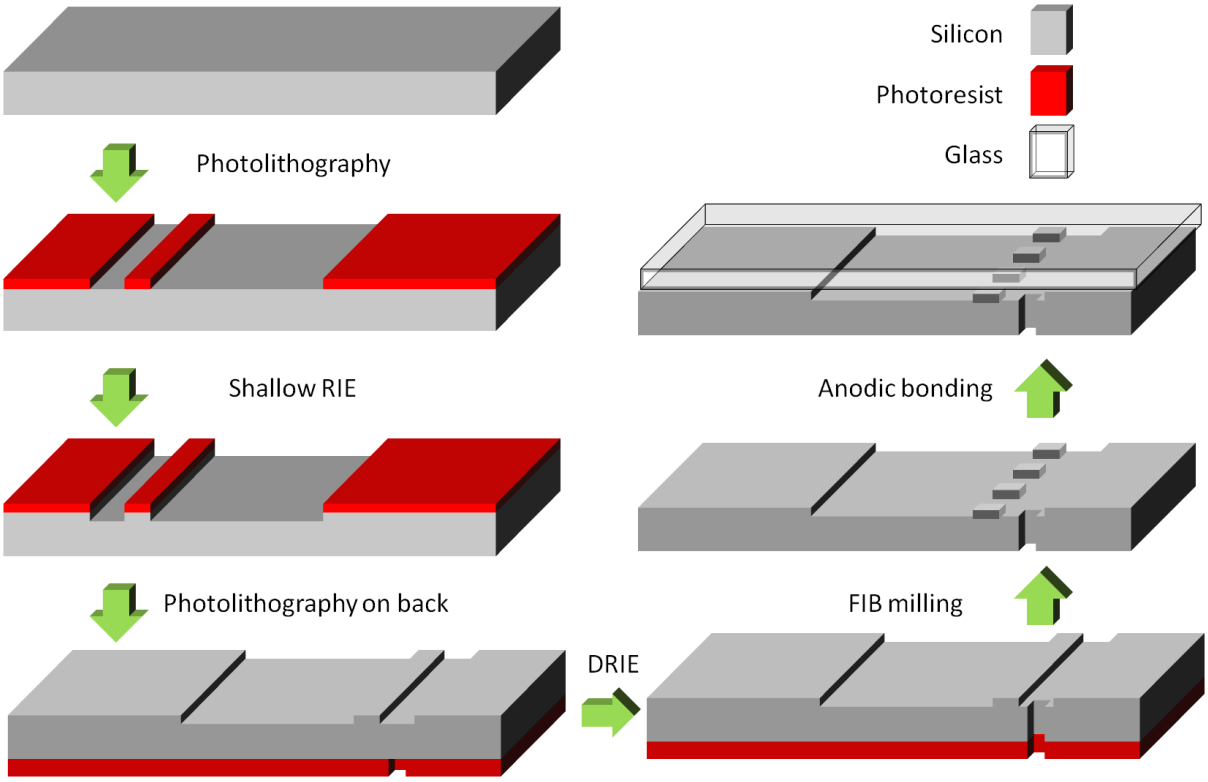

Figure 6.3 Fabrication process for multi-level nanofilter chip

6.3 Photolithography

6.3.1 Mask for Photolithography

For both the verification chip and the multi-level filter chip, two masks were needed. One was designed for the micro channels, and the other was for the inlet and outlet connection. The first question that needed to be answered is which type of photoresist is suitable for each mask application. Key factors are the etch resistance and thickness of photoresist. For different depth RIE etching, different type and different thickness of photoresist are available. Considering the depth of micro channels which is around 1μm and the etching rate of silicon and photoresist, a thin photoresist layer is enough. Therefore MICORPOSIT™ S1800 G2 series negative photoresist was used for the micro channels fabrication. As the penetration etchings on back side asked for a thick photoresist layer and high etch resistance, negative photoresist MEGAPOSIT SPR 220-7.0 was chosen for the back side photolithography.

Software AutoCAD2008 was used to draw masks. Figure 6.4 shows the four inch chromium mask designed for the top side of the verification chip. This mask was fabricated by Delta Mask B.V[1]. There were two symmetric three-level filters on one chip which were designed for contrast experiments. The round reservoir in the middle was designed for connection with the penetrated inlet hole etched from back the side of the silicon wafer. The width of the wall between the inlet channel and capture channels was 2 m which was the minimum size that can be achieved by the Canon PLA-501FA mask aligner available in the Birmingham clean room. The width of the sample inlet channel and capture channels is 20 m and $1\,\mathrm{mm}$

[1] Delta Mask B.V. Nijmansbos 56, 7543 GJ ENSCHEDE, The Netherlands. Website: www.deltamask.nl

respectively (visible by human eyes). There were two special chips with a dilute channel as well.

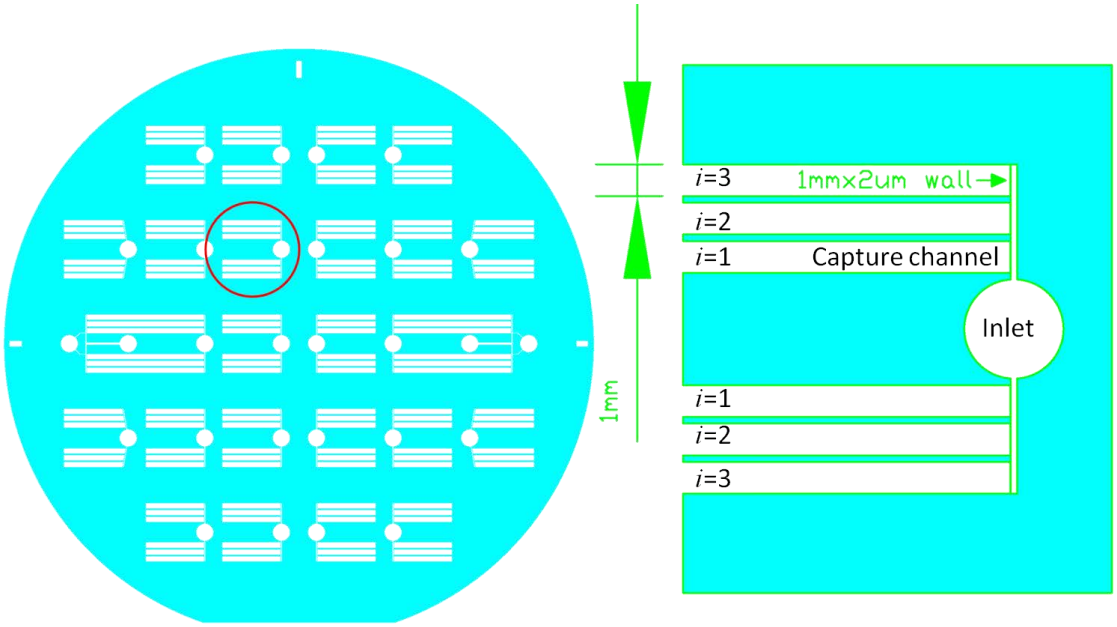

Figure 6.4 (a) Top side mask for the verification chip photolithography; (b) Top view of a chip.

Figure 6.5 illustrates the back side mask for the verification chip which was printed on transparency film. The photoresist used for this mask was MEGAPOSIT SPR 220 which was a negative resist and had a high etch resistance. The round holes were designed for penetration etching from the back side of the silicon wafer; the produced through hole would then connect with the round reservoir on the top side. The radius of the through hole was smaller than the radius of the reservoir to enhance the tolerance of alignment error.

Figure 6.6 exhibits the mask drawing of the top side of a multi-level filter chip design (not to scale otherwise some details cannot be seen). The size of this chip is the same as a microscope slide (15 mm x 45mm). The U shaped channel at the bottom is the sample inlet. The other three channels are capture channels 1, 2 and 3 from bottom to top respectively. The diameter of four channels is 2 m and the width of the wall left for the sieves is 2 m.

The hole for connection was designed to be fabricated on the glass cover with another mask which is shown in Figure 6.7.

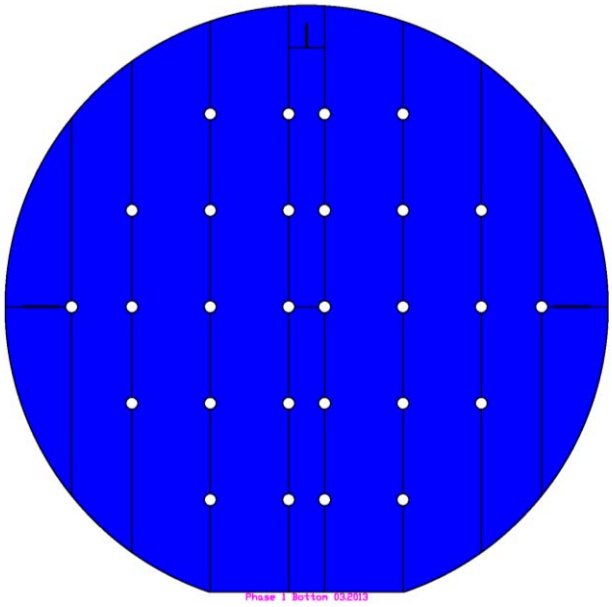

Figure 6.5 Back side mask drawing for the verification chip.

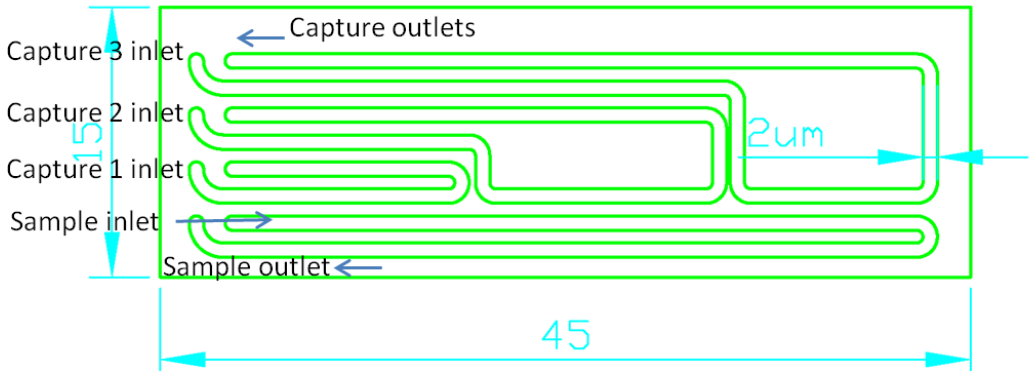

Figure 6.6 Three-level nanofilter chip micro channel map.

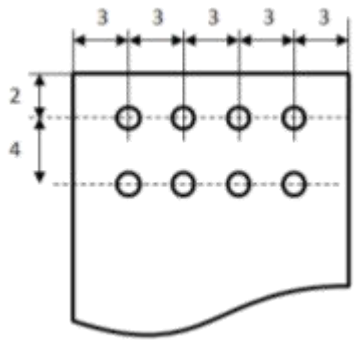

Figure 6.7 Interface map for glass cover.

6.3.2 Photolithography Experiments

Several experiments were carried out with the masks designed for the verification chip to find the appropriate photolithography recipes. All these experiments were made with EMS 1000-1 hot plate, EMS Model 4000 Photoresist Spinner and Canon PLA-501FA Mask Aligner in the clean room of the Micro-engineering and Nano-technology Research Group (Figure 6.8).

a b

Figure 6.8(a) EMS 1000-1 hot plate (Left), EMS Model 4000 Photoresist Spinner (Right); (b) Canon PLA-501FA Mask Aligner

Table 6.3 records the experiments of the top side photolithography of the verification chip with S1805photoresist. All reused wafers were cleaned before use. It can be seen that pre-treatment with primer is necessary for a good coating. The wafer should be cooled down on a hot plate rather than in air after soft bake, otherwise the resist peeled off easily during developing. The wafer can be agitated slightly and carefully during the dip in developer.

Table 6.3 Photolithography recipe exploration on photoresist S1805

No.	VT1	VT2	VT3	VT4
Pre-treatment	New wafer, none primer	New wafer, none primer	Reused wafer, none primer	Reused wafer, none primer
Spin speed	3000 rpm	3000 rpm	3000 rpm	3000 rpm
Spin time	30s	30	30	30
Softbake	115℃, 60s	115℃, 60s	115℃, 60s	115℃, 60s
Cool down	On hot plate	On hot plate	On hot plate	On hot plate
Exposure time	7s	3s	3s	2.9s
Develop	MF™-319, Dip in	MF™-319, Dip in	MF™-319, Dip in	MF™-319, spray wash
Result	Over exposure, good adhesion	Lack of develop	Over exposure, Weak adhesion	2μm wall peeled off,
NO.	VT5	VT6	VT7	VT8
Pre-treatment	Reused wafer, none primer	Reused wafer, none primer	Reused wafer, none primer	Reused wafer, 2min primer
Spin speed	3000 rpm	4000 rpm	4000 rpm	4000 rpm
Spin time	30	30	30	30
Softbake	115℃, 60s	115℃, 60s	115℃, 60s	115℃, 60s
Cool down	In air	On hot plate	On hot plate	On hot plate
Exposure time	2.9s	3s	2.5s	2.4s
Develop	MF™-319, dip in	MF™-319, Dip in	MF™-319, dip in	MF™-319, dip in
Result	Over exposure, Weak adhesion	Over exposure, Weak adhesion	Over exposure, Insufficient development	Appropriate exposure & development, good adhesion

The recipe used in experiment No. VT8 gave the best result and its reproducibility was very good in later RIE experiments. Consequently, the progress of top side photolithography can be operated with the recipe of No. VT8. The spinner was broken once when these experiments were taken. During the broken period the spin speed was not available at 3000rpm so 4000rpm was used instead. Thus there were two different spin speeds in this table. The thickness of coated S1805 photoresist at 4000rpm was acceptable for shallow RIE etching, which will be described in the RIE experiment section.

The recipe for the back side photolithography of verification chip with photoresist SPR 220-7.0 is shown in Table 6.4. From the results, group No. VB2 shows a best exposure and development.

Table 6.4 Photolithography experiment on photoresist SPR 220-7.0

No.	VB1	VB2	VB3
Pre-treatment	2min primer	2min primer	2min primer
Spin speed	3000rpm	3000rpm	3000rpm
Spin time	30s	30s	30s
Softbake	30s step-down to 115℃, 90s	30s step-down to 115℃, 90s	30s step-down to 115℃, 90s
Cool down	On hot plate	On hot plate	On hot plate
Exposure time	7.7s	7.5s	7.3s
Develop	Dip in MF-24A	Dip in MF-24A	Dip in MF-24A
Result	Over exposure	Appropriate exposure, good adhesion, sufficient development	Lack of exposure

6.4 Reactive Ion Etch

When the photoresist pattern on the top side of the silicon wafer was achieved, RIE was applied to transform the photoresist pattern to the silicon substrate. The system used here was a STS Multiplex ICP DRIE etcher (Figure 6.9) which was designed for deep RIE etching. A group of experiments were made to explore an appropriate recipe for shallow etching with the STS Multiplex ICP DRIE etcher.

Figure 6.9 STS Multiplex ICP DRIE etcher

First a group of experiments without a passivate step were designed to figure out a recipe as a start point which could be optimized with further experiments. The RF power was 600W for all experiments. Table 6.5 describes the results where the depth value was detected by AMBIOS XP-200 Surface Profiler (Figure 6.10). Before surface profiler detection, the photoresist was removed by MICROPOSIT REMOVER 1165 and the wafer was dried in nitrogen gas. It can be seen that No. ET1 and ET6 show results which are desired. However the etch rate is slightly high for etching a 1 μm shallow pattern when SF_6 Flow is 130sccm. Thus the etch time should be well controlled. The RF platen power affects the etch rate slightly. For a lower etch rate, a lower power is better.

Figure 6.10 AMBIOS XP-200 Surface Profiler

Table 6.5 RIE experiment without passivate process

NO.	SF_6 Flow (sccm)	RF Platen Power (W)	Etch time (s)	Depth (m)
ET1	130	12	20	1.0
ET2	130	12	60	2.5
ET3	130	12	120	4.7
ET4	130	12	180	5.8
ET5	130	12	240	All photoresist removed
ET6	130	30	20	1.1
ET7	130	30	60	2.5
ET8	130	30	120	All photoresist removed
ET9	130	30	180	All photoresist removed
ET10	130	30	40	1.9
ET11	130	12	40	1.8

Then a C_4F_8 passivation step was introduced to the etch process. The RF platen power for the passivation was zero to create an isotropic deposition. Table 6.6 records the results. It is apparently that the etch rate is not steady when there are several cycles. By observing the real time value in the Progress Control-ICP window, it was seen that the SF_6 and C_4F_8 flow rate was not steady in each cycle whereas the long term average value was steady. That is why a longer process time is necessary. Thus reducing the SF_6 Flow and increasing the cycle numbers are options for a more steady etch.

Table 6.6 RIE experiment with 130sccm SF6 Flow

No.	SF_6 Flow (sccm)	RF Platen Power (W)	Etch time (s)	C_4F_8 flow (sccm)	Passivate time (s)	Cycle	Depth (m)
EPT1	130	12	10	100	7	4	1.6
EPT2	130	12	10	100	7	4	1.6
EPT3	130	12	10	100	7	4	1.5
EPT4	130	12	10	100	7	6	2.1
EPT5	130	12	10	100	7	12	4.0
EPT6	130	30	10	100	7	4	2.3
EPT7	130	30	10	100	7	6	3.2
EPT8	130	12	8	100	7	5	1.4
EPT9	130	12	8	100	7	5	1.5
EPT10	130	12	6	100	5	5	0.7
EPT11	130	12	6	100	5	5	0.62
EPT12	130	12	6	100	5	6	0.7
EPT13	130	12	6	100	5	6	0.8
EPT14	130	12	6	100	5	7	1.5

The depth values in No.EPT10-14 show the possibility that there was a thin SiO_2 layer on the silicon substrate due to the dip in developer. Therefore it is necessary to bake the wafer after developing and do the RIE etching as soon as possible afterward.

Table 6.7 exhibits experiments which reduced the SF_6 flow. After each etching, a 5 min O_2 clean (45sccm O_2 flow, RF coil 600W, RF platen 30w) was applied on EPT15-30 to remove the photoresist instead of using a chemical remover. The depth varies when SF_6 flow is 100sccm (No.EPT15-17) and 80sccm (No.EPT18-22), so that the SF_6 flow was reduced again to 60sccm. No.EPT23-28, 29-34 are two groups of repeat experiments which etched three and four cycles respectively with 60sccm SF_6 flow. The variances are 0.0077 and 0.0308 m^2 respectively. The recipe used in experiment No.EPT35-37 achieved a steady and appropriate depth by increasing the cycle number to five. Figure 6.11 shows the SEM picture of No. EPT37. The silicon structures were well patterned. The bottom of the etching area was very smooth while the side wall was straight but rough. A little photoresist is observed to remain in Figure 6.11b, therefore a longer O_2 clean is desired. The dust which can be viewed in 6.11 a & c was introduced during the chip transfer from clean room to the SEM centre.

Table 6.7 RIE recipe explore experiments

No.	SF_6 Flow (sccm)	RF Platen Power (W)	Etch time (s)	C_4F_8 flow (sccm)	Passivate time (s)	Cycle	Depth (m)
EPT15	100	12	8	80	7	4	1.2
EPT16	100	12	8	80	7	4	1.0
EPT17	100	12	8	80	7	5	1.3
EPT18	80	12	8	60	7	6	1.55
EPT19	80	12	8	60	7	4	0.97
EPT20	80	12	8	60	7	5	1.3
EPT21	80	12	8	60	7	8	2.3
EPT22	80	12	8	60	7	16	5.2
EPT23	60	8	8	50	7	3	0.42
EPT24	60	8	8	50	7	3	0.6
EPT25	60	8	8	50	7	3	0.4
EPT26	60	8	8	50	7	3	0.6
EPT27	60	8	8	50	7	3	0.4
EPT28	60	8	8	50	7	3	0.45
EPT29	60	8	8	50	7	4	1.1
EPT30	60	8	8	50	7	4	0.9
EPT31	60	8	8	50	7	4	0.7
EPT32	60	8	8	50	7	4	0.5
EPT33	60	8	8	50	7	4	0.7
EPT34	60	8	8	50	7	4	0.6
EPT35	60	8	8	50	7	5	1.2
EPT36	60	8	8	50	7	5	1.2
EPT37	60	8	8	50	7	5	1.2
EPT38	60	8	8	50	7	6	1.5

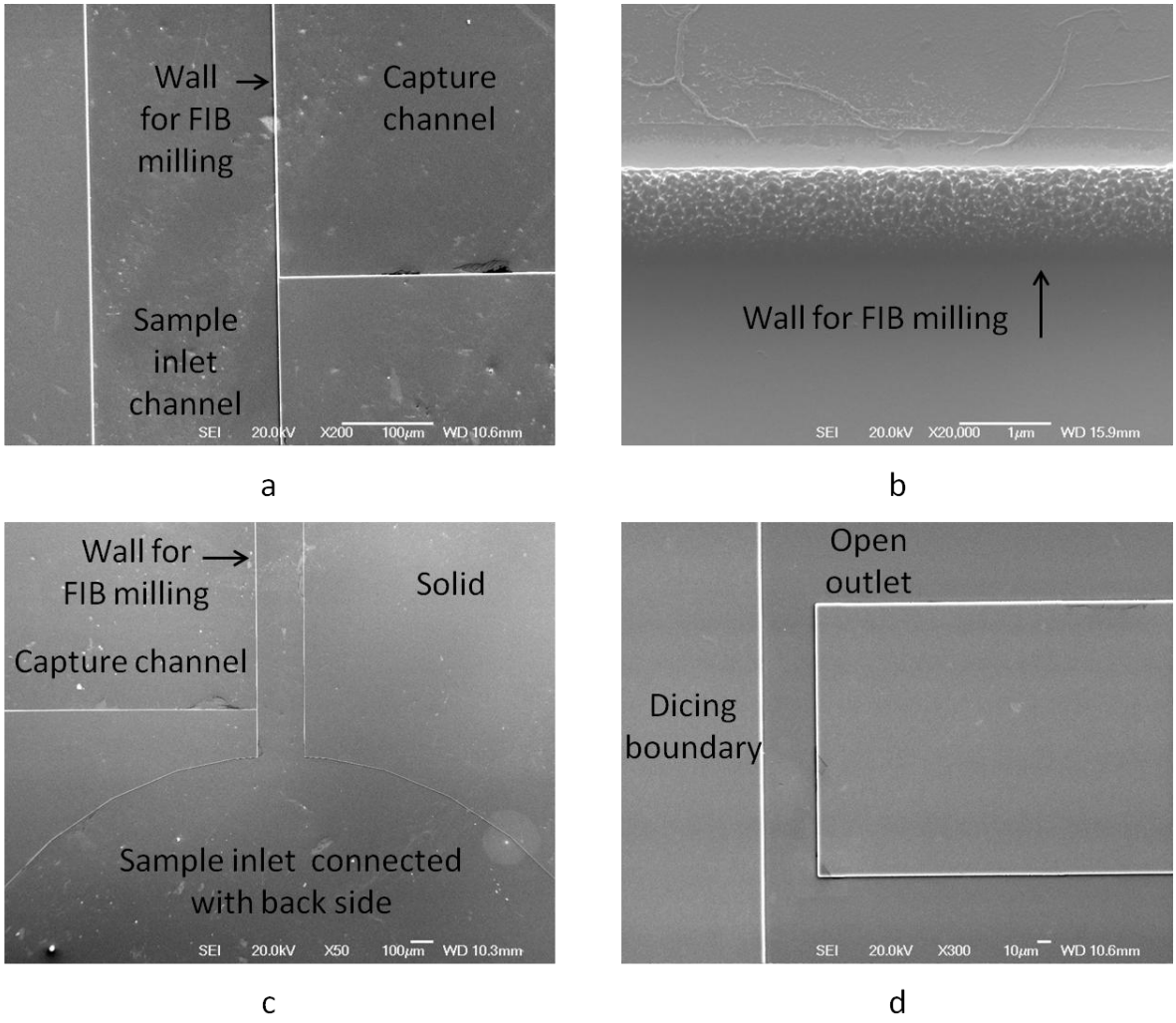

Figure 6.11 SEM pictures (a) Wall separate sample inlet and capture channel; (b) Side view of the wall; (c) Inlet hole which was designed to connect a penetration hole etched from back side; (d) Open outlet of capture channel and dicing boundary.

The recipe for back side etch is described in Table 6.8. For a 200 m thickness wafer it takes about 145 min.

Table 6.8 DRIE recipe for penetration etching

	Flow	RF coil	RF platen	Time
Etch	SF_6 130 sccm	600 W	12 W	10 s
Passivate	C_4F_8 85 sccm	600 W	0 W	7 s

6.5 Focused Ion Beam Milling

After RIE etching the micro structure of the verification chip had been achieved, then FIB was applied to mill the fine sieve channels. Equation 6.1 defines the milling rate R which can be found in user manual of FEI Dual-Beam Strata 235 Focused Ion Beam.

$$R = \frac{dA}{It} \qquad \text{Equation 6.1}$$

Where d is the milling depth,

A is the scanning area,

I is the beam current,

t is the milling time.

The 30keV gallium beam milling rate for silicon is R =0.15$\mu m^3/nA \cdot s$. Table 6.9 describes the beam current and its corresponding milling spot size. As the diameter of sieve channels on the verification chip are 200, 400 and 600nm respectively; the beam current for each level of sieves can be deicide. The length of sieve channels is 2000nm. Therefore the milling time is able to be calculated using Equation 6.1.

Table 6.10 exhibits the recipe for each size of sieves and the corresponding milling time needed. The quantity of channels were calculated with Equation 3.12 when $\gamma = 1$. The whole milling process takes 84.5min and 96.5min for the verification chip and multi-level filter chip respectively. However this time does not consider the time cost for cross section clean which is necessary for a nanochannel FIB milling. If the milling area was same as the aimed channel area, the two entrances of the nanochannel should be over milling one side and lack of milling the other side due to the alignment error. To avoid this phenomenon, a two steps milling are normally applied for cross section milling. A smaller area is milled with high beam current first. Then the edges left of cross section are cleaned with a low beam

current milling. Normally the ion beam current used for each cross section clean is a quarter of its milling beam current. The sieve channels pattern is able to be designed and edited using the xP V2.25 software for FEI Dual-Beam Strata 235 FIB. Figure 6.12 exhibits the FEI Dual-Beam Strata 235 FIB system.

Table 6.9 Different beam currents and the corresponding milling spot size
[Source: FIB manual for FEI Dual-Beam Strata 235]

Beam current (pA)	Milling spot size (nm)	Best use
1	6	Very high-resolution imaging, High aspect ratio holes, High-resolution imaging
10	10.0	Quick imaging
30	12.5	Navigation imaging
50	15.0	Milling submicron holes Final milling on cross sections
300	25.0	Milling micron-sized holes
500	30.0	Intermediate/final milling on cross sections
3000	60.0	Initial milling for small cross sections
5000	100.0	Initial milling for medium cross sections
7000	150.0	Initial milling for medium-large cross sections

Table 6.10 FIB milling time for different level sieves

$d = a_i$ (μm)	A (μm^2)	Milling beam current I (pA)	Milling time for one channel (s)	Quantity of channels	Total pattern time (min)
0.2	0.4	1000	0.53	6000	53.33
0.4	0.8	3000	2.13	1500	17.78
0.6	1.2	4000	1.2	667	13.34
0.02	0.04	10	0.53	6000	53.33
0.04	0.08	10	1.94	1500	35.56
0.08	0.16	70	1.22	375	7.62

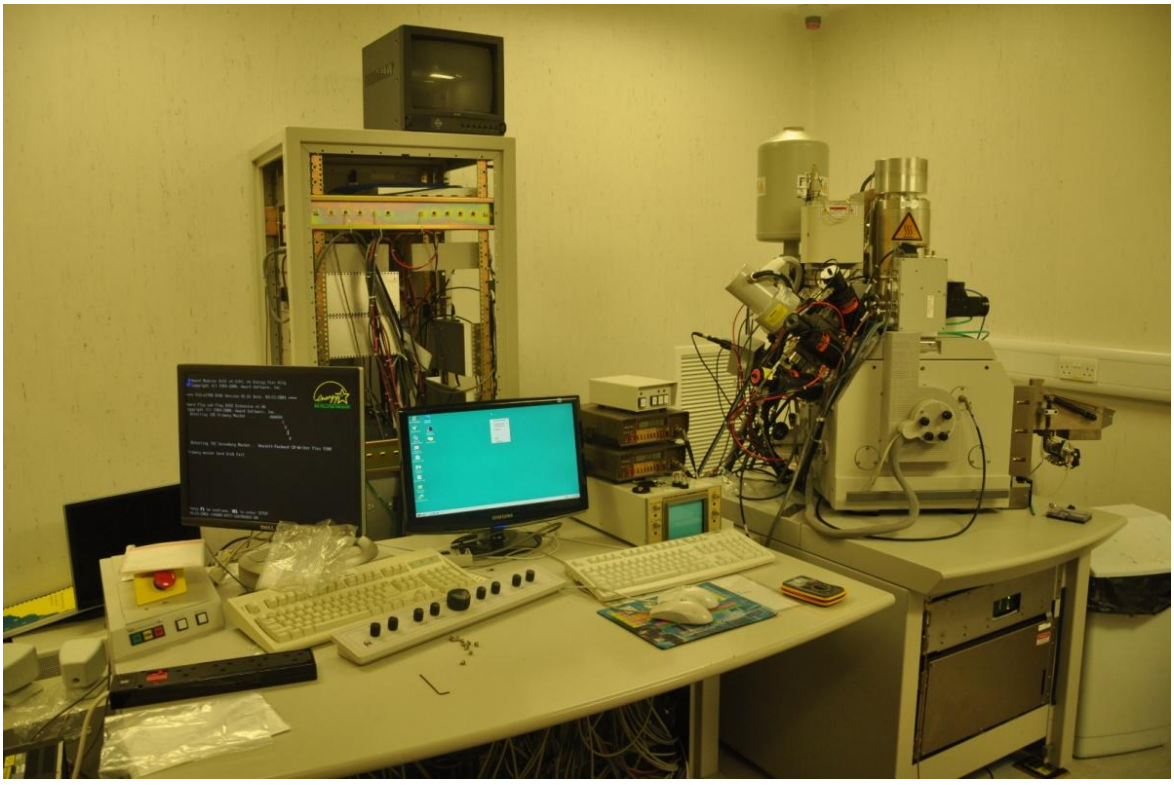

Figure 6.12 FEI Dual-Beam Strata 235 Focused Ion Beam

A trial milling was made on the verification chip (No.EPT10) and its results are shown in Figure 6.13. The current of 30 keV gallium beam used in this trial milling was 5nA and dwell time of 10 μs. Milling time was 5.87s and a $2 \times 2.2 \times 1$ μm^3 cross section was achieved. The

/

RIE etch depth was 0.7 μm. As the width of milling area is wider than the wall (2 μm), it is clearly shown in the picture that at the bottom besides the wall there was milled two holes. The holes beside sieve channels can trap components therefore increase the possibility of clogging. Thus a better alignment is necessary.

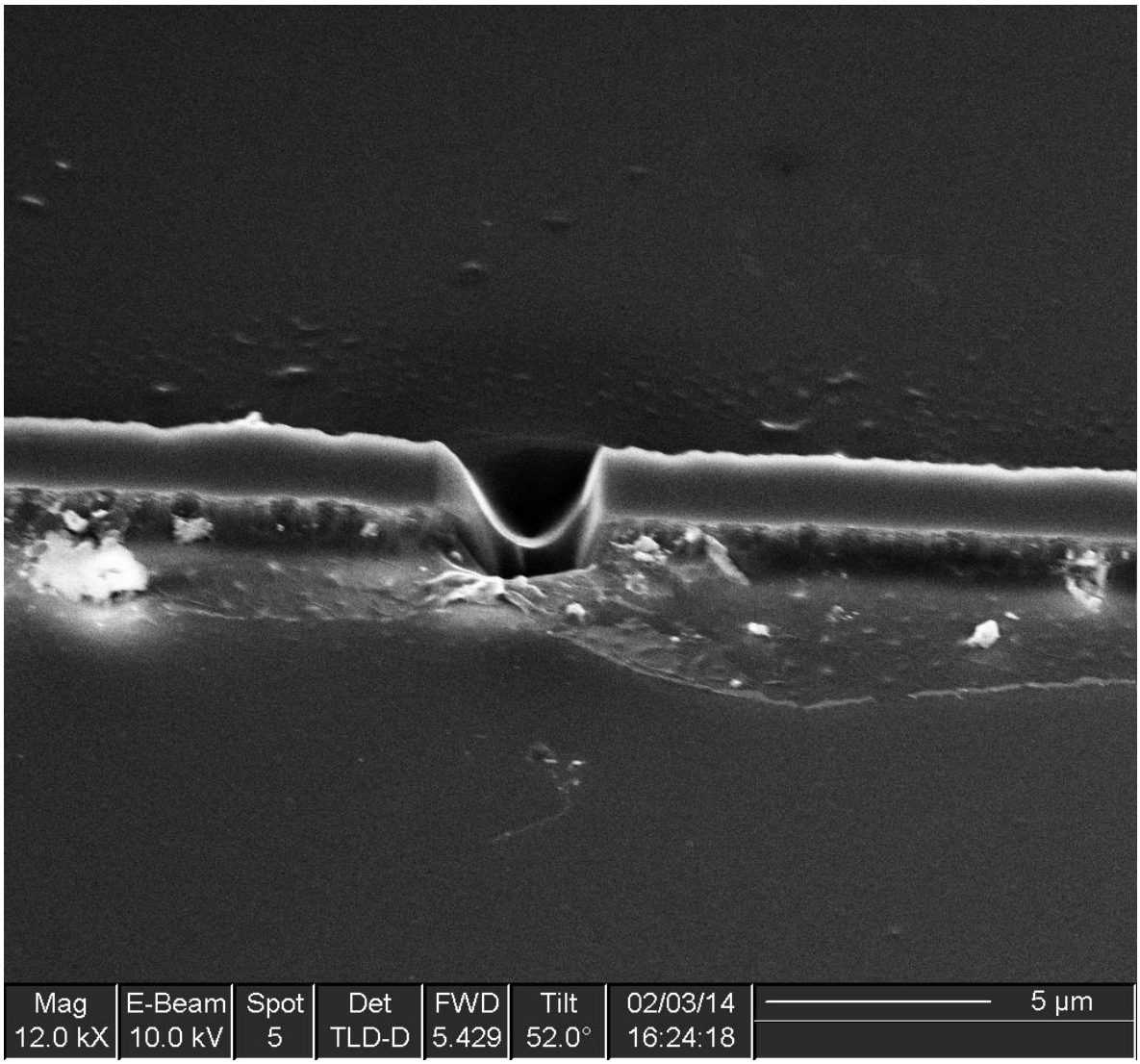

Figure 6.13 SEM image of FIB milled channel

The two steps milling is helpful to improve the geometry features of cross section. High ion beam current and long dwell period results in a sloped side wall in the sieve channel which is shown clearly in the figure. The sediment caused by chemical photoresist remover can be

viewed along the wall. After the chemical removal of photoresist, a nitrogen flow was applied to dry the surface. The silicon wall blocked the nitrogen flow thus kept the remover solution near the bottom of wall which presented as the dirty vestige under SEM. Therefore a physical removal method, O_2 clean taken by STS Multiplex ICP DRIE etcher, was applied to avoid the photoresist pollution. Consequently this is not a successful fine channel milling experiment; however, it demonstrates the feasibility to fabricate a nanofilter combining RIE etching and FIB milling and points out the cautions for nanochannel milling. Due to the machine failure of FEI Dual-Beam Strata 235 Focused Ion Beam and STS Multiplex ICP DRIE etcher, experiments on FIB milling was stopped at this point. Further fabrication on the recipes shown in Table 6.10 will be made in the future.

6.6 Wet Etch and Bonding

6.6.1 Wet Etch of Glass

After FIB milling, the silicon structure part of the chip is all fabricated. Then the glass covers with connection holes for the multilevel filter chip are made by wet etching. A typical glass wet etching process flow that could be used for fabricating the glass covers is described as below. First a hard resist mask is coated with the glass wafer. Hard bake is recommended for photoresist mask to enhance the adhesion of photoresist to glass wafer. Secondly prepare glass etching solution. Add 85ml DI water, buffered HF (5ml), and 9-10ml HCL into a Teflon container sequentially and stir with a plastic stirrer carefully. Thirdly, put the glass substrate into the etching solution and stir constantly. The etch rate is approximately $1\mu m/min$ at room temperature. Fourthly after etch rinse the substrate in DI water and then remove the resist. Finally clean up all materials.

6.6.2 Anodic Bonding

The last step of the fabrication process is bonding the silicon substrate with the glass cover. Several techniques are able to bond silicon with glass. Most methods applied adhesives or soft material to seal two wafers together, such as adhesive bonding (epoxies, silicones, photoresist, etc.), glass frit bonding and solder bonding. However this changes the dimensions of the micro and nanostructures at the interface, especially nanoscale structures, due to flow of adhesive into the features. Anodic bonding is one way to bond silicon and glass without adhesives. The silicon and glass wafers are heated (300-500℃, depending on glass type) to mobilize the ions in the glass. When a high voltage is applied, the ions migrate from the interface forming a depletion layer. The high electric field attract silicon and glass to contact firmly where an anodic reaction takes place. Due to the permanent high strength bond, accurate alignment, free thermally matched stress, no flow of glass, no adhesives and low cost; anodic bonding is widely used in research and industry, especially in the microfluidics area. It is also able to be applied on chip level which is necessary for the application in this section. Commercial bonding services are available. For example, Applied Microengineering Limited (AML) is a company in Oxfordshire offering various bonding services including anodic bonding. The chips fabricated in this section were planned to be bonded in this company.

6.7 Alternative fabrication routes

As it was introduced in section 6.2.5, various alternative fabrication routes are available for manufacturing of multi-level filter based on H shaped channels. In this section, more details on the alternative fabrication routes are given.

For silicon substrate, greyscale e-beam lithography combined with etch (dry or wet), dicing and anodic bonding technique is one option for multi-level filter based on H shaped channels. The first step is coating the wafer with resist and soft baking. The pattern is drawn in the e-beam pattern control system and this is then used to control the greyscale e-beam writing process to form exposed features. Finally the development process results in different depth micro and nano channels on the resist. No mask is needed. Then reactive ion etch or wet etch is able to transfer the pattern on resist mould to the silicon substrate. O_2 clean or chemical remover can be used for removing the various thicknesses of resist. After cleaning the silicon wafer, a glass cover wafer is bonded onto it. Finally filter chips are achieved after dicing. This method requires well controlled RIE process to minimize the structure degradations during structure transfer. Apparently, the use of greyscale e-beam lithography avoids the need for alignment process of different masks to create the features and so increases the accuracy of cross section and the fabrication efficiency. By choosing resists with high etch selectivity; the writing time can be further reduced. However the depth errors of e-beam writing will be amplified after RIE step if thin resists are used.

Imprint lithography requires a mould (silicon or metal) as a stamp which can be fabricated by the e-beam lithography or FIB milling (silicon) and lift-off (metal).[180, 181] When the mask has been fabricated, the silicon wafer needs to be coated with a layer of imprint polymer. Then the imprint stamp is pressed against the polymer layer accompanied with heating or UV light exposure. For a silicon filter, RIE shall be applied to transfer the structure on polymer mould to silicon wafer, which is similar with the process of e-beam lithography. For a metal filter, lift-off method is used for the final manufacturing.[182] The metal layer on the substrate needs to be coated before the polymer layer. The anodic bonding and

dicing are the last two steps of this fabrication route. Nanoimprint lithography with RIE and anodic bonding suits for large volume manufacturing of filter chips. Once the stamp has been made, the pattern cannot be changed easily. Thus for trial experiments of multi-level filter based on H shaped channels, the imprint stamps can fulfil the requirements of experiments with higher flexibility.

For use of glass as a substrate, femtosecond laser machining is a convenient method for 3D fabrication. As it was mentioned in section 6.2.5, femtosecond laser pulses change the phase or structure of silica glass. The exposure area is able to dissolve in water. Theoretically, bonding is not necessary. All 3D structure of multi-level filter can be machined inside one glass bulk after femtosecond laser writing and then dipping in water to dissolve the modified glass area. However, the dissolving process of nanochannels in this situation will be extremely slow. It is better to machine the channels on the surface of glass substrate and then bonding with a glass cover. This fabrication route can produce totally transparent chips which are applicable for more optical detection method comparing with the silicon-glass chips.

If the micro and nano channels are fabricated separately, besides the example fabrication route, there are various options. Laser machining, electro discharge machining, powder blasting (glass only), casting, injection moulding (polymer only) and hot embossing (polymer only) etc can be used to replace the photolithography step for microchannel manufacturing[164]. Femtosecond laser machining (glass), e-beam lithography, greyscale e-beam lithography and scanning probe lithography etc are capable for the fabrication of nanochannels.

The greyscale e-beam lithography, nanoimprint lithography and femtosecond laser machining can manufacture all channels in one step. Due to their high resolution, the distance among channels can be sub-micron or even less. Therefore the shorter length of sieve channels results in shorter fabrication time and shorter transport time comparing with the two steps (microchannel and nanochannel) fabrication routes. The nanoimprint lithography suits for large volume chips manufacturing with medium set up cost, while the greyscale e-beam lithography and femtosecond laser machining can be applied for medium volume produce.

6.8 Summary

In this chapter the methodology the design of the multi-level filter based on H shaped channel was described, which contains six steps: application demand analysis, detection requirement analysis; geometric design, interface design, material selection and fabrication process design. For each step, examples were given and analysed based on the multi-level filter. One verification chip aiming at demonstrating fabrication process and basic filtration was designed as an example of the design flow. Another example was a three-level nanofilter chip.

A new path to fabricate a nanofilter was designed as an example of fabrication route design considering the cost and the accessible facilities in University of Birmingham. Then experiments were made to explore recipes for each step of fabrication. Reliable and reproducible recipes for S1805 and SPR 220 photolithography were achieved. RIE experiments gave a recipe which resulted in a 1.2μm depth etching for the top side of both verification and three-level nanofilter chips. Penetration etch from the back side of the

verification chip had been done as well. Recipes for different level sieve channel FIB milling were discussed. The discussion of a trial milling experiment demonstrated the feasibility of a fabrication process of multi-level nanofilter combining ICP RIE and Focused Ion Beam, and pointed out cautions for FIB nanochannel milling. Nevertheless the failure of equipments halted the following fabrication later fabrication process. The wet etch progress for the glass cover of three-level nanofilter chips and available bonding technique were briefly illustrated. Finally, alternative manufacturing processes were illustrated briefly. Further fabrication will be made in near future.

CHAPTER 7

DISCUSSION AND CONCLUSIONS

7.1 Introduction

In this chapter, firstly the validation of the simulations exhibited in the former chapters is introduced. Based on the validated results, overall discussions on the flow properties and the mass transfer are made to link all former chapters together. The comparisons between multi-level filter based on H shaped channel and other published methods, and the methodology of chip design are discussed as well. The chapter concludes with a summary of the thesis followed by the presentations of the main conclusions of the research and the ideas for future work.

7.2 Validation of the Simulations

7.2.1 Dumbbell channel model

The dumbbell channel contains a sudden contraction and a sudden expansion in width. The flow stream of Newtonian fluid through a dumbbell channel can be calculated by Navier-Stokes equations (Equation 2.9 & 10). The flow properties in channel with sudden contraction [151, 152, 183, 184] and sudden expansion [185-193] were studied and verified by many researchers. The contraction structure contracts the flow while the expansion structure expands the flow in contrast. The researches demonstrated that there is a pressure drop after pass a sudden contraction. Figure 7.1 draws the simulation result of

contour pressure in dumbbell channel of section 3.2.1. The pressure drop can be seen clearly, which fits the published results of sudden contraction [152, 184, 194].

Vortices forms near the corners of the barriers and the wall (before the contraction and after the expansion). The turbulent flow caused by the barriers is affected by Reynolds number [183, 184, 186, 187, 190]. In the micron and nano scale, the Reynolds number ($\mathrm{Re} = \rho v l/\mu$) is low, typically $\mathrm{Re} < 1$.[195, 196] Thus in micro- and nano- dumbbell channels, the transition from laminar to turbulent flow cannot occur.[151, 189] What's more, the convections of the vortex around the corner of the barrier and wall are so weak, that the eddy (dead-volume) length is small and the weak vortex cannot be seen in the coarse streamline graph (Figure 3.2a). Figure 7.2 redraws the streamline with a density of 400 (the density of Figure 3.2a is 20). Four closed eddy regions were formed around the corner of the barrier and the wall. The vortex near the entrance wall of sieve channel cannot appear due to the low Reynolds number.

Similar results can be found in lot of publications such as Mills[197], Bullen *et al* [184], Pike et al [185], Hawa [187], and Biswas *et al* [191] etc. The separated flow after the expansion is applied in Pinched Flow Fractionation (PFF) for micro components separation (Figure 2.5)[56]. The angle of expansion used in PFF is designed to eliminate the dead-volumes (vortex area). The angle issue was discussed in Jeremy and Stefan's review [190]. If the length of sieve channel is small, the barrier can be viewed as a symmetric channel with an orifice plate inside. Laminar flow through an orifice plate is a classic fluidic case and has been studied by numerous scholars[194, 197].

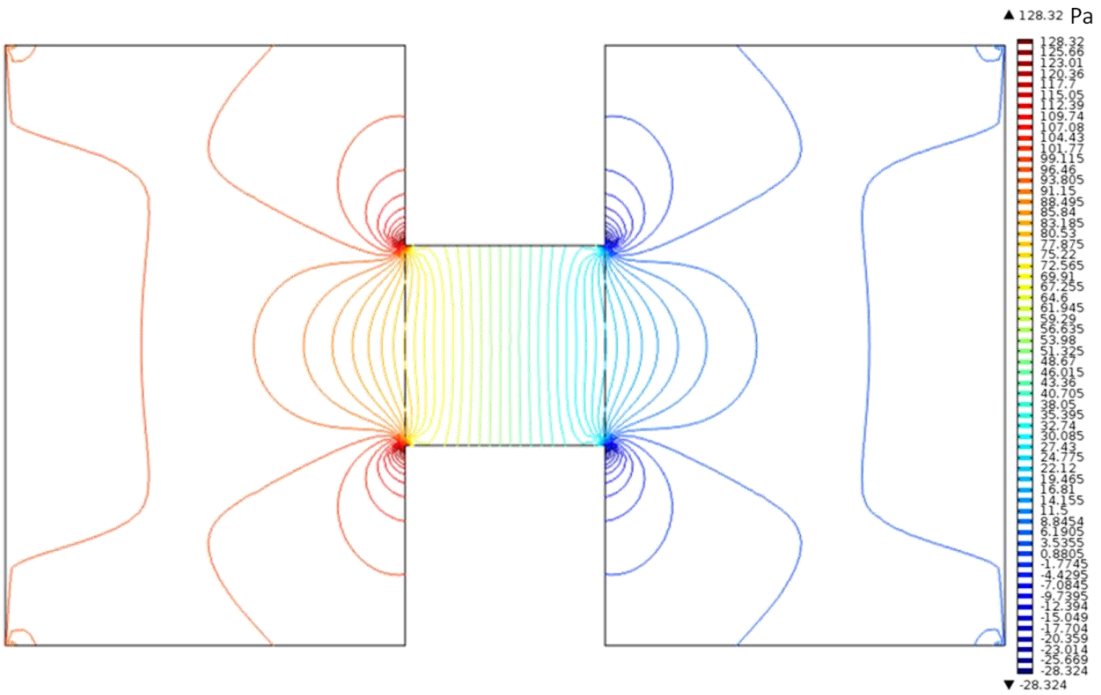

Figure 7. 1 Contour pressure of dumbbell channel

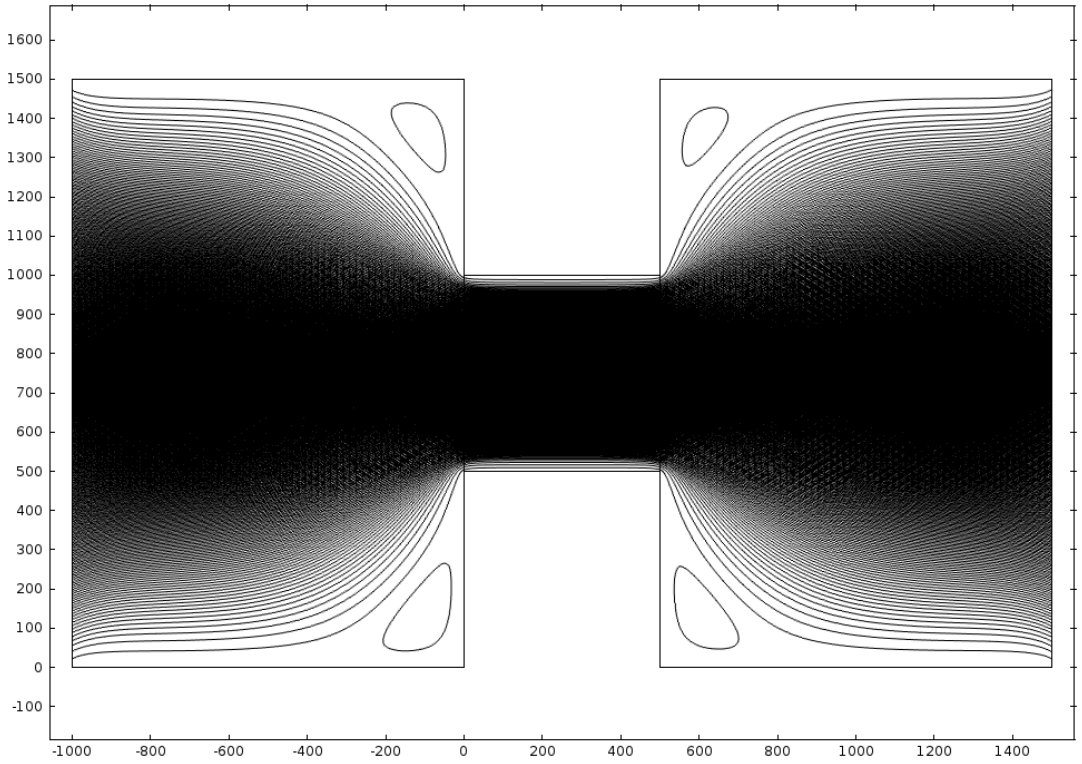

Figure 7.2 Velocity streamline through dumbbell channel

7.2.2 Semi-H shaped channel model

The left part of semi-H shaped channel is a T junction (bifurcation) while the right part is a channel with extension in width which was introduced in last section (7.2.2). The vortices (maximum around 1.2e-5m/s) in dead-volume region are too weak to be shown in streamline graph (Figure 3.3). For the bifurcation part, comparing with the studies when $Re > 1$ [198, 199], the main difference is the vortex region. Due to the low Reynolds number, vortices cannot develop in the sieve channel and main channel. Similar streamlines with low Reynolds number were published in the article of Lin *et al* [200] and Sugaya *et al* [63]. The diameter of each branch of the T channel in Lin's work was the same, whereas in section 3.2.2 of this thesis the size of sieve channel is smaller than the sample inlet channel. Thus in the semi-H shaped channel fewer stream flows into the sieve branch by contrast with the inlet flow. Rainer *et al* reported a bifurcation blood cell filter which was h-shaped [201]. The bifurcation described the same principle of the semi-H shaped channel. Sugaya analysed the separation process in HDF, which is an application of semi-H channel series. Other similar results about laminar flow around a sharp edge in microchannel can be found in Todd's review[196].

The right part which is an extension channel was used for continuous separation in the PFF method[56]. Similar separation phenomenon was also observed in the HDF [62]. In that report the micro components flowed through the long sieve channel into the outlet with different directions. However, due to the alignment effect missing in the long sieve channel, the separation efficiency of the extension stream was low. These results support the analysis of semi-H shaped channels in this thesis.

When the semi-H channel is extended to semi-H channel series (section 4.2), a model of cross-flow filtration is built. Kim *et al* studied the particle trajectories and sieving in a two dimensional cross-flow filtration process (without the capture channel) [153]. The results of simulation in section 4.2 show consistency of flow properties comparing with Kim's results. Detailed analysis of the cake layer formation was introduced in Kim's paper.

Similar structure of semi-H channel series was also applied in hydrodynamic filtration (HDF Figure 2.7) [62, 202, 203]. The fine capillary in Figure 2.7a allows liquid to flow though under a low flow rate while blockings any micro components. In contrast, the capillary in Figure 2.7b illustrates a typical cross-flow filtration process, similarly with the simulation in section 4.2. The streamline towards the sieve channel concentrates and aligns the particles. Experiment results of Yamada's work exhibited the fluorescent flow stream and filtration of blood cells.[62] Consequently the COMSOL simulations about semi-H shaped channel and its series are validated theoretically and experimentally.

7.2.3 H shaped, angular H shaped channel model and multi-level filtration

For the symmetric H shaped channel, apparently there is no convection in the sieve channel connecting the three channels. Thus the model can be viewed as two symmetric channels with two symmetric rectangular traps (expansion and then contraction in width). Thus the streamlines in Figure 3.4, 4.7a and 5.3a are the same kind of the streamline of laminar flow passing a trap[203, 204]. They are similar to the trace of the big group in semi-H shaped channel as well. When the depth of the trap increases, vortex is possible to occurs [151]. The streamlines in Figure 5.3&13 demonstrate the vortices in the sieve channels.

Østergaard *et al* reported an application of active H-shaped channel separation with magnetic enhanced selectivity[205]. In this report, the magnetic particles pass the sieve channel under a magnetic force to realize the single particle detection. No publication about passive filtration based on H-shaped channel has been seen, neither the angular H-shaped channel applications. However, based on the results on H shaped channel and H shaped channel series, the properties of angular H shaped channel are easy to understand with the basic fluidic principles.

The stream in H shaped and angular H shaped channel series with slip flow showed higher resistance (shear stress) of flow near the cross section (Figure 5.9 & 13). Here the cross section can be viewed as a rough surface. Comparing with the smooth side wall, the shear stress increases with roughness. Similar numerical simulation results on gaseous flow were given by Ji *et al* [206] and Cao *et al* [207]. Kunert and Harting gave a similar conclusion in their numerical research on fluid flow in microchannel[208]. Lilly *et al* demonstrated this phenomenon with experimental evidence[209]. Bonaccurso *et al* validated the relationship of roughness and shear rate of liquid flow in completely wetting microchannel[161].

Consequently, in this section 7.2, by comparing with all these validated publications, the simulations of dumbbell, semi-H and H shaped channel and their series are validated. Therefore the settings of the simulation software COMSOL Multiphysics® are correct. Because the simulations of multi-level filtration used the same settings and the structure of multi-level filter is combination of semi-H or H shaped channel series which have already been validated, therefore the simulations on multi-level filters have a reliable basis. What's more, the hydrodynamic filtration demonstrates the applicability of multi-level separation in sequence; and the Brownian ratchet[86] and the hydrodynamic cell trapping[210] gives

examples of filtration based on diffusion rather than convection. So the results of multi-level filter simulation presented in this thesis are both meaningful and reliable.

7.2.4 Summary of the validation

Over all, this section validates the simulations in chapter 3-6 with analytical models, numerical models and published experiment results. The results about dumbbell channel, which is the basis of the dead-end filtration, fitted the studies of dead-end filtration and flow properties in a channel with an orifice (sudden contraction and sudden expansion in width) (section 7.2.1). Then the model of semi-H channel was validated by the research results on cross-flow filtration, bifurcation of flow and sudden expansion of flow in width (section 7.2.2). The H shaped channel was also demonstrated by the publications on trap effects, surface roughness effects and example of H shaped channel applications (section 7.2.2). Based on these analyses, the series of dumbbell, semi-H and H shaped channel were also demonstrated. Related research and publication were introduced in section 7.2.3. The three-level filter based on the semi-H channel series was also validated in section 7.2.3 by the reports on cross-flow filtration and HDF. Hence the settings and results of the COMSOL Multiphysics® were confirmed to be correct and reliable. Thus the simulations of multi-level filter based on H shaped channels which used the same modules and settings can be inferred as meaningful and reliable ones. After validated the models used in this thesis, discussions with more details can be made.

7.3 Discussions

7.3.1 Laminar flow

In this thesis, three models, dumbbell, semi-H and H channel were studied as fundamental elements of the filter with barrier. In structure, the right parts of the dumbbell channel and the semi-H channel are the same (sudden expansion) which was mentioned in section 3.1. And the structures of the left part of semi-H channel and the left part of H channel are same, while the left and right parts of H channel are symmetric. In section 3.2 and section 7.2, it can be seen that the same expansion structure results in a similar expansion flow.

As the dead volume regions besides the cross section in the left part of the dumbbell channel (dead-end filtration) (Figure 7.2) are eliminated by switching the structure to a semi-H channel (cross-flow filtration) (Figure 3.3), the semi-H structure (cross-flow) significantly improves the usage time of the filter with less clogging in contrast with dumbbell structure (dead-end) [211, 212].

The streamlines from the inlet towards the sieve channel in the semi-H model (Figure 3.3) illustrates the flow bifurcation at the cross section (structure bifurcation). This phenomenon results in a concentrating and an alignment of micron and submicron particles towards the side wall of the inlet channel. It is more obvious when there are a set of bifurcations (Figure 5.19). This concentrating phenomenon is the main principle of hydrodynamic filtration[62] and hydrodynamic cell trapping[210].

For the H shaped channel, two parallel symmetric inlet channels were set up with the same inlet/outlet pressure. There is no convection across the sieve channel due to the symmetric pressure besides the sieve channel. The concave streamline towards the cross section

exhibits the trap effect. On the one hand, there is no dead volume in the sample inlet and capture channel of the H channel model, which reduces the cake layer formation in both sides of a filter; but on the other hand, the concentrating effect is not available in the symmetric H shaped channel.

Vortices were observed in the sieve channels. In section 3.3.1, no vortex was seen in the H channel model, due to the low aspect ratio (length/width) of the sieve channel (Figure 3.4).

If the pressure in the sample inlet channel and the capture channel are not symmetric, there are convections through the sieve channel from the higher pressure region to the lower pressure region. For the particles with low diffusion coefficient, the higher pressure on the sample side can increase the total flux in the sieve channel; what's more it also concentrates and aligns the micro particles along the cross section, in a similar manner to the angular H shaped channels.

Because the angle of angular H channel destroys the symmetry of the structure, the pressures on either side of the sieve channel are not equal anymore. Consequently the fluid convection across the sieve channel occurs under a pressure gradient (Figure 3.13 & 14). Comparing with the semi-H channel, however, the pressure difference on either side of the sieve channel of an angular H-shaped channel is small. In other words, the convection across the sieve channel is low. In contrast to the symmetric H channel model, this low convection potentially can be taken advantaged of concentrating and alignment of the particles.

In structure, the semi-H channel series (section 4.2 & 5.4) is a periodic sequence of semi-H channels. Thus the flow in a semi-H channel series has similar properties as for a single semi-H channel. However, due to the bifurcations of flow at each cross section, the flow can be

separated into several layers corresponding to each sieve channel. The convection in sieve channel can be estimated by studying these streamline layers. As the streamlines flow into the sieve channels occupy a large proportion of the total inlet stream when there is a large amount of the sieve channels, the semi-H channel series enhance the concentrating and alignment effect in the sample inlet channel compared with a single semi-H channel.

Similarly, in structure, the H shaped channel series is a periodic series of H shaped channels. Because there is no convection transfer across the sieve channel, in contrast with the semi-H channel series, the laminar flow in H shaped channel series shows strict periodicity (section 4.3 & 5.2-4). Due to the low convection in the sieve channel of angular H-shaped channel series (section 4.4 & 5.2-4), each angular sieve channel corresponds with a thin layer of streamline. When the angle is positive, the convection flux is backward against the diffusion flux. Therefore the trap effect at the cross section can be weakened. When the angle is negative, inversely, the trap effect is enhanced. The variation of convection is slight when the magnitude of angle is small for both situations.

As the same pressure settings were used for the dumbbell, semi-H and H shaped channel simulations, the flow rates of the capture outlets can be compared and it was found that the highest to the lowest were the H shaped channel, dumbbell channel and the semi-H channel. This rank relates to the amount of pressure drop in the sieve channel of dumbbell and semi-H channels. In industry, commonly both dead-end filtration and cross-flow filtration require a high pressure at the original solution side for higher efficiency [213-215].

The simulations on H and angular H shaped channel series with slip boundary condition exhibited significantly higher flow rate both in the inlet channels and the sieve channels comparing with the no-slip ones. The asymmetric laminar flow in the sample inlet and

capture channel reduces the chances of components to contact with the filter surface. The trap and alignment effect at the cross section were weakened as well (Figure 5.13).

The multi-level filter consisting of different semi-H channel series can be analysed by the streamline layers. The different width and depth of sieves result in different convection flow rate into the sieve channel.[62] The multi-level filter based on H shaped channels is a sequence of several periodic H shaped channel series with different periods. Thus the flow correspondingly shows periodicity with different periods.

7.3.2 Mass transfer in the sieve channels

The static flux in a dumbbell channel, semi-H channel and the semi-H channel series mainly refers to the convection flux. The main reason is that there is only one inlet of these three models. The gradient of concentration is zero. Based on the Equation 2.5, the streamline of velocity can be used to describe the principle of the separation process. For the semi-H channel series and the multi-level filter based on semi-H channels, the diffusion flux dropped down till the concentration of the small group was uniform during the passive filtration. Here it was assuming that the volume of the inlet is large enough thus the sample concentration is fixed at the inlet. For a small volume multi-level filtration of micro components, such as the HDF, the diffusion can be neglected however the concentration may not be uniform due to the concentrating effect [62, 63].

For the micro components in a microchannel, components can be viewed as a solid phase so that the diffusion can be neglected. (That is why HDF are applicable for micro-particles.) For the nano-particles which cannot simply be viewed as solid phase in microchannel, the

diffusion cannot be neglected. Therefore the phenomenon of the concentrating and alignment towards the filter interface is weakened by reducing the particle sizes.

In contrast, the H shaped channel has two inlets, the sample inlet and the buffer (capture channel) inlet. The concentration difference of the two inlets causes diffusion between the sample and buffer inlets (Figure 3.5 & 3.16). As there is no convection linking the two parallel channels, the mass transfer process is dominated by diffusion.

For the semi-H filter, Yamada and other researchers reported that even if the micro particle is smaller than the diameter of the branch sieve channel, particles cannot enter the sieve channel due to the particles' shape and rotation, and the low flow rate into the sieve channel[62, 63]. The width of streamline band was used in these reports to analyze the separation process. By adding sieve channels, in other words, adding the flow rate into capture channel, the small particles can finally transfer into the capture channel by convection. When the diffusion cannot be neglected, the velocity streamline is only able to estimate the convection flux. In the sieve channel of the symmetric H shaped model, only diffusion occurs. The diffusion flux can be calculated with the Fick's law. For the asymmetric H shaped channel such as the angular H shaped channel, both convection and diffusion should be considered. The smaller that the magnitude of angle is, the lower the convection is.

In section 3.3, it was demonstrated that when the entrance diameter of the sieve channel is smaller than the entrance diameter of the inlet channel, the diffusion flux is lower than half of the total flux of the small group. Thus H shaped channel series was introduced to overcome this. The integration of flux on the total cross section increases with the number of sieve channels until the integration value equal to half of the integration of flux on the

sample inlet (Figure 3.5 & 4.8). Also the reason why $\gamma = 1$ is an insufficient estimation for Equation 3.12 is because the diffusion is anisotropic therefore there is a lower flux through the sieve channels [161].

The mass transfer process in the angular H shaped channel series contains the diffusion flux and the convection flux which is caused by the asymmetric pressure distribution. The convection flux relates to the angle and pump pressure settings. Meanwhile the diffusion flux can be analysed by the same principle of the H shaped channel series. As the diffusion coefficient declines with the increasing diameter of particles, the convection flux occupies a higher proportion in the mass transfer of larger components. The angular effect on the capture concentration is weakened however, due to the lower convection towards the sieve channel. Thus the convection caused by the angle shows potential for the concentrating and alignment of micro components or reducing the adhesion.

One of the basic principles of the multi-level sequence filtration is to collect particles from the sample solution by size sequence. So the amount of each substance in the main channel reduces by the size order. It is an easy way to sort the particles by size. For the particles which can pass through more than one level of sieves, the highest concentration of them is always obtained at the first level where they can enter. For the aim of multi species purification, the concentration at later levels (where the species can pass through) is demanded to be as low as possible; so that the effects of these particles on later levels can be minimized. The HDF is an example of the sequence filtration principle. However the small group cannot be completely removed from the main channel, therefore the separation efficiency is below 100% [62, 63]. The Alignment along the main channel side wall varies the concentration distribution. The concentrating and alignment effects of micro-particles in the

main channel of HDF increase the separation efficiency comparing with the multi-level filter based on the H shaped channels.

The multi-level filter based on semi-H shaped channels is a similar device as HDF. However, the sizes of particles are not limited to microns. The section 4.2.2 and 5.4 studied the properties of a three-level filter based on the semi-H channels. For the nanoparticles, concentrating towards the cross section was not observed in the simulations. Because the transfer of solutes accompanies with the transfer of solvent, the static concentrations of all groups were uniform everywhere where they can enter. The simulations on semi-H shaped channel and its series illustrated this issue as well.

Apparently the multi-level filter based on semi-H shaped channels cannot fit the requirement of purification just mentioned which asks for the concentrations of the components (besides the target component) to be as low as possible. If the particles were transferred independently from the solvent, however, the reduced amount of substance in one side should result in a correspondingly reduced concentration. Typically, external fields are implemented for the independent transfers of some species (section 2.2 & 2.3.3.5). The diffusion is another transfer phenomenon of which the solute transfers separately from the solvent. H shaped channel is one design for passive diffusion separation. Thus the multi-level filter based on H shaped channels is applicable for the purification. This design was put forwards in section 3.5 and analyzed in section 4.5.

Due to the diffusion flux among each level of the multi-level filter based on H shaped channels, the concentration for the component j at each level i ($i \geq j$) is not exactly the geometric sequence described by the Equation 3.9. The Equation 3.14 was put forwards to estimate the error of Equation 3.9 and was verified by simulation in section 4.5.1. The

simulation results shown in Table 4.6 demonstrate that the concentration $c_{i,j}$ of a component j at level i $(i = j)$ increases with the distance l_i between adjacent levels $(i \text{ and } i+1)$. In contrast, the concentration $c_{i+1,j}$ decreases with the increasing distance L_i. Figure 7.3 exhibits the concentration curve along the sample inlet channel of the model in section 4.5.1. The first sieve channel starts at $x = -40\mu\text{m}$ and ends at $x = 0\mu\text{m}$. When the demanded error δ_i is small (0.5%), the distance l_i is the longest in the figure thus the concentration gradient (negative) at the section between adjacent levels $i \text{ and } i+1$ is the highest. The concentration decline is limited by the condition $c_{i,j}^{\text{Sample}} - c_{i+1,j}^{\text{Sample}} \leq 2^{-i}\, c_{0,j}^{\text{Sample}}$; $i, j = 1,2,\dots,n$. Even though the magnitude of concentration gradient is low, the total concentration variation is the largest due to the long l_i. That is why the $c_{2,1}^{\text{Simulated}}$ obtained is the lowest value when $\delta_i = 0.5\%$. When the distance reduces, the interaction among each level is enhanced; thus the magnitude of concentration gradient increases. Due to the continuous condition, the concentration gradient before level i decreased as well. As the entrance length is fixed, the concentration at the entrance of level i drops down. Overall, the estimate function reflects the tendency of concentration changing with the distance l_i accurately. It fits the results of simulations and gives sufficient estimate of the error in Equation 3.9 when the design error is small.

As the distances among each level of a multi-level filter based on H shaped channel can be designed based on the Equation 3.9, models of multi-level filter were built and verified in section 4.5. The simulation on the multi-level filter with a dilute channel illustrates that higher filtration efficiency can be achieved. For this principle, the small groups $(j < i)$ can be washed out from the sample inlet channel by adding dilute levels. Figure 7.4 is a percentage stacked chart describing the concentration composition of each level (without or with dilute

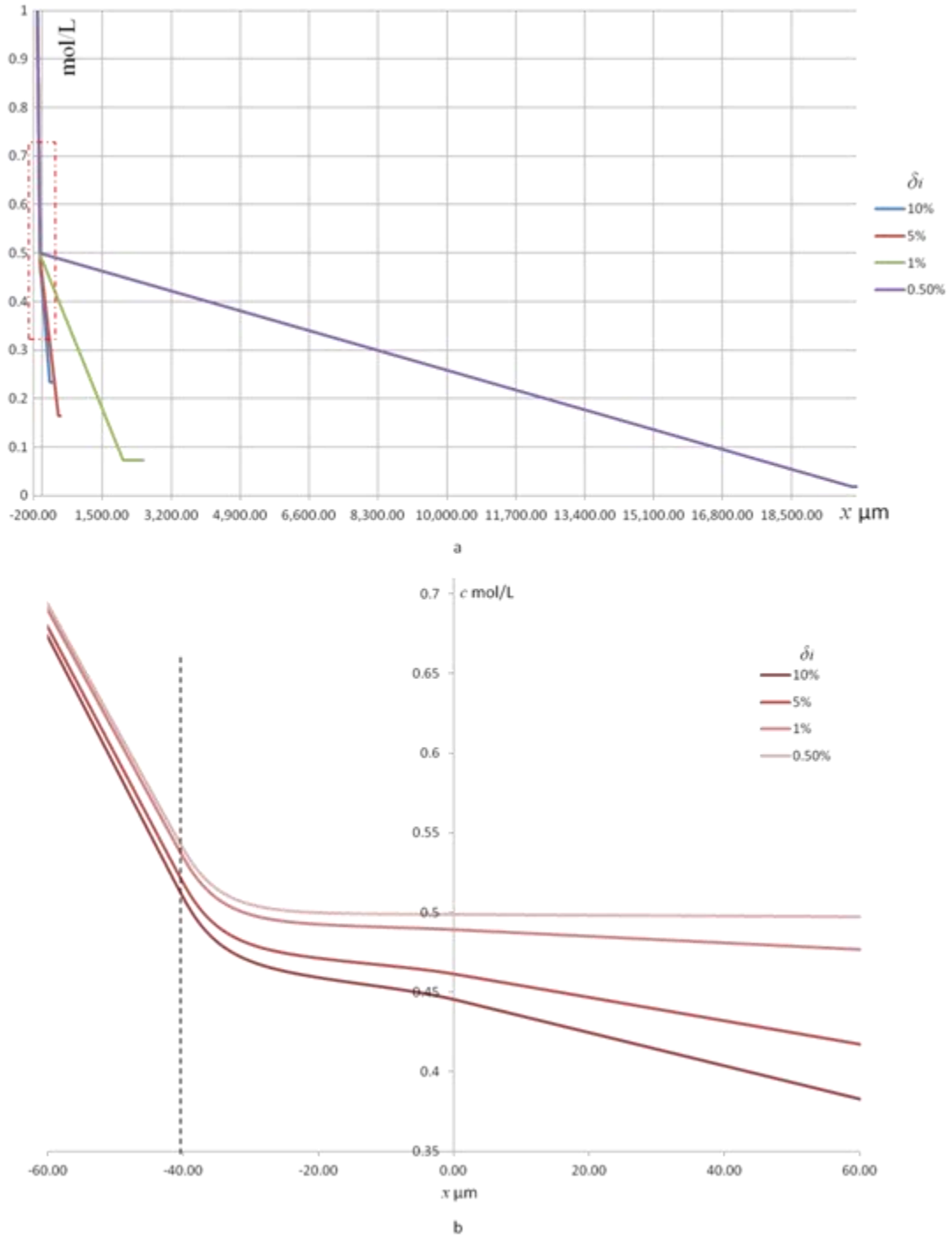

Figure 7.3 (a) The concentration along the sample inlet channel $c_{i,j}^{\text{Sample}}(x)$; (b) the concentration variation around level 1 (the red region in (a))

channel) according to Table 4.8. The concentration variation can be seen straightforwardly. Apparently the dilute channel increased the separation efficiency. The short distances among each levels resulted in a low separation efficiency in level 2 and 3. The values in the

outlet of level 3 and the main channel show that the amount of sieve channels in the third level in insufficient.

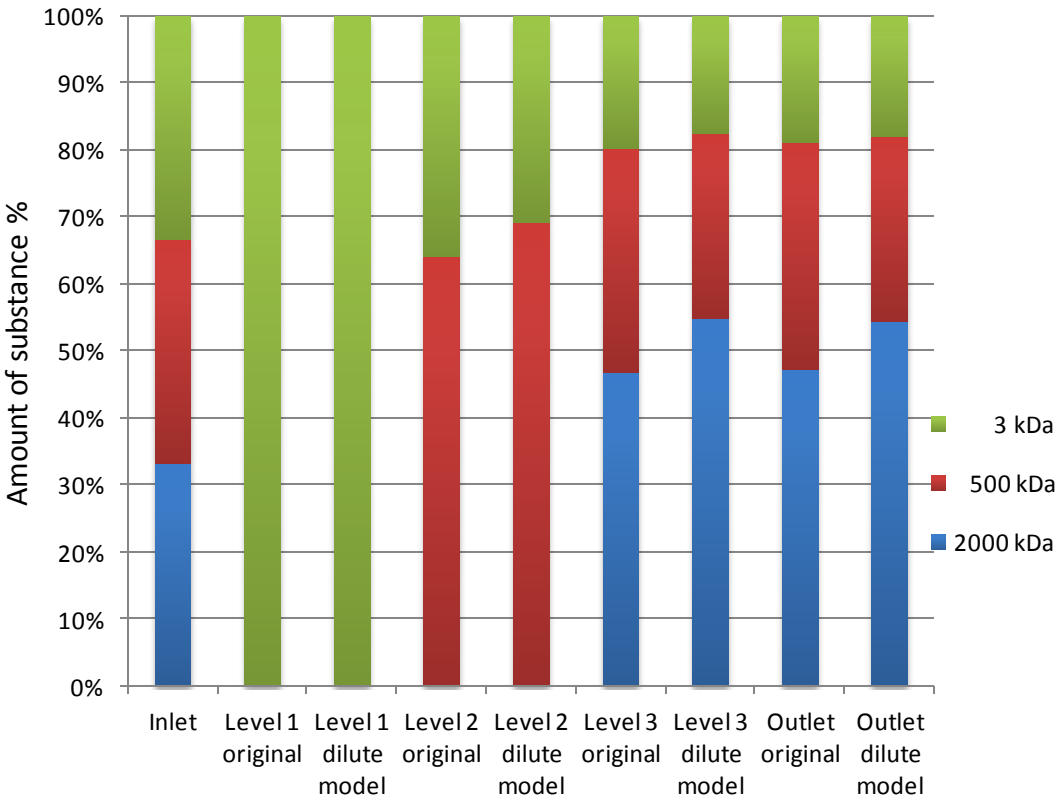

Figure 7.4 The ratios of components at the outlets of three-level filters without (original) or with a dilute channel (dilute model)

The results and discussions in section 3.4, 4.4, and 5.2-4 shows that the angular effect on the mass transfer is weak. The convection introduced by the angle is low comparing with the main flow in the inlet channels. This convection flux can vary the time for mass transfer. The static concentration is not affected by the angle in continuous separation process. The angular H shaped channels are potentially able to align and concentrate the micro particles. Slip flow weakens the angular effect on concentrating the flow.

7.3.3 The chip design methodology

The design work is crucial for transferring from a geometric model to an applicable device. A design methodology was discussed in section 6.2. According to this methodology, two types of multi-level filter chip which had been simulated in section 4.5 and 5.4 were designed as demonstrations. Alternative fabrication routes and test plans were introduced and discussed. The fabrication was unfinished due to facilities failure in the clean room.

7.3.4 Comparing with other methods

Nicole reviewed the continuous flow separation in microfluidics devices and summarized a table to compare different techniques (Table 7.1)[20]. The first seven techniques are passive continuous separation methods without external fields, while the others are active continuous separation methods. The flow rate of passive continuous separation mainly relates to the channel diameter and pumping methods. In these methods, only the lateral displacement and Brownian ratchet are applicable for nano particles. The pinched flow fractionation, filtration obstacles are strict separation methods with specific designed structures for specific composition of solutions while the others are not strict separation methods. Although the hydrodynamic filtration cannot separate micro-components completely, it achieves a very high throughput and adjusts to composition variation easily. Generally, the comparisons of these methods are not straightforward. There are no “one size fits all” separation methods currently.

Table 7.1 Listing of continuous flow separation methods with details of the forces utilised, the basis of separation and the applicable samples. The data for flow rates and throughput were taken from the selected reference, if provided

Method	Separation induced by	Separation based on	Sample	Flow rate /throughput	Ref.
Pinched flow fractionation	Laminar flow regime	Size	Microparticles, cells	70 cm/s 40 000 particles/h	[56]
Hydrodynamic filtration	Laminar flow regime	Size	Microparticles	1 mm/s 100 000s particles/ h	[62]
Bifurcation	Laminar flow	Size, shape	Blood	5 mL/h 1–3 mm/s	[201]
Filtration obstacles	Diffusion and obstacles	Size	Blood	5–12 µL/min 10–20 mm/s	[216]
Lateral displacement	Obstacle array	Size	Particles (0.8, 0.9, 1.0 µm) DNA (61 kbp, 158 kbp)	20 µm/s (DNA) 100 pg/h (DNA)	[60]
Brownian ratchet	Diffusion and obstacles	Size	DNA	2 µm/s 10 pg/ h	[86]

Hydrophoretic separation	Pressure gradient from slanted obstacles	Size	Microparticles	1 to 3 cm/s 10 000s beads h^{-1}	[217]
DNA prism	Obstacle array and electric field	Size	DNA	10 ng/h	[218]
Entropic trap array	Dams and electric field	Size	DNA	10 pg/h	[69]
Repulsion array	Dams, electric double layers	Charge to size ratio	Proteins	300 pg/h	[69]
Free-flow electrophoresis	Homogeneous electric field	Charge to size ratio	Proteins, amino acids	6 mm/s	[219]
Free-flow isoelectric focusing	pH gradient	Isoelectric point	Proteins and cells	9 mm/s	[220]
Magnetophoresis	Inhomogeneous magnetic field	Size, magnetisation	Magnetic particles, cells	1.2 mm/s 10 000s cells/h	[67]

Dielectrophoresis	Inhomogeneous electric field	Size, polarisability	Microparticles, cells	up to 4 mm/s 100 000s cells h^{-1}	[66]
Acoustophoresis	Acoustic pressure	Size, density, compressibility	Microparticles, cells	11 cm s^{-1}	[221]
Optical lattice	Optical force	Size, refractive index	Microparticles, cells	30 µm s^{-1} 90 000 particles h^{-1}	[222]
Sedimentation	Gravity	Density, size	Microparticles, droplets	6 mm s^{-1} slowed to 1 mm s^{-1}	[223]

The multi-level filter based on H channels is applicable for both micron and nano particle passive separations by size. It is not a complete separation device but has a very high flow rate dealing with more than two sized target components separation. The separation efficiency can be improved by adding dilute levels and extending the distance between each level.

For the multi-level filter based on H shaped channel, theoretically the maximum flow rate is dominated the sample composition (concentration), the diffusion coefficient and the area of cross section. Therefore by adding to the amount of sieve channels, the flow rate is able to reach a very high level. The flow rate/throughput (1.01mm/s, section 5.3.1) in the slip

models of H shaped channel series under a low pump pressure (100Pa) is similar as the one of hydrodynamic filtration[62].

7.4 Summary

In this thesis, a new type multi-level micro and nano filter based on H shaped channels was developed. The design methodology of this type multi-level micro and nano filter was built. A new fabrication process for multi-level filter chip was put forward and verified by experiment. 2D and 3D modelling simulations on filters based on H shaped channels were presented and discussed.

The research started at analysis of dumbbell channels which were the basic constituents of traditional dead-end filters (section 3.2.1). Then the inlet flow direction was changed from perpendicular with the filter surface to parallel with the filter surface aiming for a higher flow rate and a lower possibility of blocking. Therefore semi-H shaped channels (cross-flow filtration) were introduced as an improvement of dumbbell channels (section 3.2.2). For further improvements upon semi-H shaped channels, the flow properties and transport process in H shaped channels were studied (section 3.3), which is the fundamental basis of the research in this thesis. After discussions about angle effect of angular H shaped channels (section 3.4), a new design of multi-level filter based on H shaped channels was put forwards. The theoretical concentrations after sufficient diffusion were given by analytical formulas. Based on the geometric diameter of filter channel, an estimate equation about the number of sieve channels for sufficient diffusion was put forward. The relationship of capture concentration error and the distance between two adjacent levels was described by a formula as well.

It is meaningful to understand the transport process in each level of multi-level filter which consists of one sample inlet channel, one capture channel and a plurality of parallel same sized sieve channels. Chapter 4 studied the flow properties and mass transfer process of the filters based on semi-H shaped channels, H shaped channels and angular H shaped channels. During these studies, the estimate equation on quantities of sieve channel was verified (section 4.3.1 and 4.4.1). Then the multi-level filters were simulated by finite element software COMSOL Multiphysics®. Meanwhile, the formula describing capture concentration error which is introduced by the distance between two adjacent levels was verified. Therefore the main features of a multi-level filter based on H shaped channels can be designed with mathematic tools.

For a better understanding of the flow properties in nanofilter based on H shaped channels and the angle effects, 3D modelling of H shaped and angular H shaped channels series were made as reinforcement (section 5.2). Whereas the no-slip boundary condition does not reflect the real flow movement on solid-liquid interface in various situations, slip boundary condition was applied with the 3D models in section 5.3 as a control group of the simulations in section 5.2. The angular H shaped channels series showed higher flow rate and lower possibilities of adhesion and clustering in slip boundary condition simulations. The improvements of flow rate in sieve channels due to angle effect were observed in both conditions, especially no slip condition. After all, a simulation of a three-level filter based on angular semi-H shaped channels was studied and discussed. A multi-level filter based on semi-H shaped channels is a feasible way to microminiaturize several filtration processes down to chip level. This simulation can be viewed as a verification of the verify chip designed in section 6.2.

A six steps design flow of multi-level filer chips based on H shaped channels was put forward and verified, which is i) application demand analysis, ii) detection requirement analysis, iii) geometric design, iv) interface design, v) material selection and vi) fabrication progress design. Two multi-level filter chips were designed following this design path as examples (section 6.2). For fabricating the pattern of multi-level filters which consist of multi depth structures, a new fabrication process was put forward (section 6.2.5). Fabrication experiments on photolithography (section 6.3), Reactive Ion Etch (section 6.4) and Focus Ion Beam (section 6.5) were taken and reported. The wet etch and bonding processes were introduced. These experiments demonstrated the feasibility of this fabrication process and gave reasonable recipes for this fabrication process.

The simulations in chapter 3-5 were validated in chapter 7. Then the overall discussions were illustrated. Comparisons with other continuous separation techniques were discussed. Consequently, the main conclusions of the research were summarised in the following section along with suggestions for future work (in section 7.6) to take the research forward.

7.5 Conclusions

The conclusions obtained during this research are summarized as following:

The dumbbell channel is the basis of dead-end filters. Dead volumes form before and after the barriers thus easily to be blocked by clogging. (Section 3.2.1 & 7.2.1)

Semi-H shaped channels, which are the basis of cross-flow filters, using the bifurcation structure to eliminate the dead volume before the barriers hence reducing the possibility of clogging and jamming. (Section 3.2.2)

The flow rate in the sample inlet channel is high; however, the pressure drops severely across the sieve channel and the flow rate in the capture channel is low, which is the pumping problem. (Section 3.2.2)

Convection is the main mass transfer process in semi-H shaped channels. (Section 3.2.2)

The static capture concentration is the same as the inlet concentration. (Section 3.2.2)

H shaped channels eliminate all dead volumes around the barriers therefore further reduce the possibility of adhesion on both cross-sections and slow down the cake layer formation process. (Section 3.3.1)

High flow rate are achieved in both the sample inlet and capture channels compared with the semi-H shaped channels. (Section 3.3.1)

Diffusion is the main transport phenomenon in the sieve channel while there is no convection across the sieve channel in a symmetric H shaped channels. (Section 3.3.2&3)

The capture concentration of single H shaped channel filter is less than 50% of sample concentration (the second law of thermodynamics) (Section 3.3.2&3).

For a higher capture concentration, more than one sieve channels are needed, which is the H shaped channels series. (Section 3.3.2)

The angular H shaped channels enhance the convection in sieve channel due to the asymmetric structure, thus both convection and diffusion occur in the sieve channel. (Section 3.4.1)

The semi-H shaped channel series are typical cross-flow structures. The H shaped channel series improve the flow rate in the capture channel. (Section 4.2.2 & 4.3.2)

Osmosis was observed in H shaped channel series. (Section 5.2.4 & 5.3.1)

The sufficient numbers of sieves in H shaped channel series for the maximum capture concentration (50% of the sample inlet concentration) can be estimate by the formula $N_i \geq \gamma \frac{wd}{a_i^2}$ (Equation 3.12). One typical value is γ=1 which means that the pore area equals to the sample inlet area. (Section 4.3.1)

The length of the cross-section area affects the diffusion. Longer length is helpful to increase the capture concentration (up to 50% of the inlet concentration). (Section 4.3.1)

Vortices were observed in the sieve channels of H shaped channel series. When the no-slip boundary condition was used, the areas of vortices were small. (Section 5.2.3) When the boundary condition was set as slip, the vortices developed bigger and occupied whole sieve channels. (Section 5.3.2) The vortices increase the diffusion flux.

The increasing magnitude of the angle of the sieve channels enhances the convections through the sieve channels while reduces the vortices area, especially when the flow slips on the boundary interface. (Section 5.2.3 & 5.3.2)

The convection through the negative angular sieve channels concentrates and aligns micro particles along the cross section. It is also helpful to increase the total mass transfer flux in the multi-level filter; therefore higher flow rate is applicable. (Section 5.2.3 & 5.3.2)

The flow rate across the sieve channels increase with the angle magnitude. This angle effect reduces when the width and depth of the sieve channel reduce. (Section 5.2.4 & 5.3.1)

By connecting different level filters (semi-H or H shaped channels series) sequentially; a multi-level micro- and nano- filter is built. (Section 3.5.1)

For the multi-level filter based on semi-H shaped channels, the flow rates are low in the capture channels compared with the flow rate in the sample inlet channel (Table 4.1); hence a high pumping pressure and long filtration time are required. (Section 4.2.3 & 5.4.2-4)

The capture concentration can be described as $c_{i,j}^{\text{Capture}} = 0,\ i < j;\ c_{i,j}^{\text{Capture}} = c_{0,j}^{\text{Sample}},\ i \geq j$. Therefore the multi-level filtration based on the semi-H shaped channel is not a complete separation method. (Section 4.2.3 & 5.4.5)

For the multi-level filter based on H shaped channels, the flow rates in both the sample inlet and capture channel are high compared with the multi-level filter based on Semi-H shaped channels; therefore solving this pumping problem. (Section 4.5.2)

The capture concentration in multi-level filter based on semi-H shaped channels fulfils the condition $c_{i,j\leq i}^{\text{Capture}} > c_{i+1,j\leq i}^{\text{Capture}}$ and $c_{i,j>i}^{\text{Capture}} = 0$. (Section 3.5.1 & 4.5.1)

Assuming each level is isolated from the others, the ideal concentration in each level is $c_{i,j}^{\text{Capture}} = c_{i,j}^{\text{Sample}} = 2^{-i} \cdot c_{0,j}^{\text{Sample}} \quad (i = 1,2,\dots,n)$(Equation 3.9). When a dilute channel is added, the concentration is described as below (Equation 3.10 and 3.11),

$$c_{i,j}^{\text{Capture}} = c_{i,j}^{\text{Sample}} = \begin{cases} \frac{1}{2} \cdot c_{0,j}^{\text{Sample}} & i = 1 \\ \frac{2}{9} \cdot \left(\frac{3}{4}\right)^{i} \cdot c_{0,j}^{\text{Sample}} & i > 1 \end{cases}, \quad c_{i}^{\text{Dilute}} = \begin{cases} \frac{1}{4} \cdot c_{0,j}^{\text{Sample}} & i = 1 \\ \frac{1}{3}\left(\frac{3}{4}\right)^{i-1} \cdot c_{0,j}^{\text{Sample}} & i > 1 \end{cases}$$

Consequently no matter whether there is a dilute channel, $c_{i,j=i}^{\text{Capture}} > c_{i,j\neq i}^{\text{Capture}}$. (Section 3.5.1)

The dilute channel and dilute sieves are simple but efficient way to increase the separation efficiency. (Section 3.5.1)

The interaction among each level, actually, introduces an error in Equation 3.9-11. The error and the distance between two adjacent levels can be described by the estimation function: $l_i \geq \frac{N_i w_i}{2\delta_i}$ (Equation 3.15). Apparently, a long distance l_i can reduce the error of Equation 3.9-11. This estimation function fits the results of simulations and gives sufficient estimate of the error in Equation 3.9 when the design error is small.

Overall the multi-level filter based on H shaped channels obtains a rapid, high throughput, large scale range (nanometres to microns) purification of complex mixtures on chip level. The high flow rates in this filter reduce the adhesion on the solid-liquid interface, which reduces the possibility of blocking of the sieves. During the filtration process, the mixture sample is diluted level by level thus also reducing the possibility of clogging. The inlet fluid of the captures channels is able to be a buffer to keep the pH value and osmotic pressure during the filtration process. Thus it is propitious for keeping the cytoactivities, while traditional filtration is not capable to keep the bio-environment for cells. This type of multi-level filter is easily extended by connecting different size filter chips in series. With additional dilute channel and dilute sieve channels, higher size selectivity can be achieved.

The methodology of designing a multi-level filter chip based on H shaped channels was established. It is a six steps path which is i) application demand analysis, ii) detection requirement analysis, iii) geometric design, iv) interface design, v) material selection and the last step vi) fabrication progress design. (Section 6.2)

Among the alternative fabrication process which are able to fabricate different widths and depths channels on the same chip, a new fabrication process was introduced and demonstrated. During this fabrication progress of a chip, it is flexible to design and modify

the patterns of sieve channels with FIB. Angular sieve channels are able to be fabricated with this process as well.

7.6 Future Work

A new fabrication process has been put forward in this thesis. Although most parts of this process have been demonstrated with experiments, the anodic bonding process is still waiting to be done.

After the multi-level filter chips are fabricated, test experiment of these chips need to be done. Dyed nanospheres and dyed dextran can be uses as indicators. Further phase demonstrations on separation of blood cells and serum, microvesicles, and proteins etc shall be taken to demonstrate the filter chips.

As the fabrication process which was put forward in thesis is not suitable for industry fabrication, other fabrication processes are desired, such as nano-imprint[173]. The recipes of these fabrication processes are crucial for commercialization of multi-level filter chips based on H shaped channels.

For the boundary condition of flow, surface roughness [161, 224, 225] and wetting [226, 227]are key factors. As the SEM figure of ICP RIE results showed a rough side wall, the study of its nano-roughness may introduce potential improvements of the filter. When the surface of sieve channels is super-hydrophobic[52, 53, 85], there is layer of gas[228]. How will this air layer affect the filtration process needs to be assessed?

When most components in the mixture are approximate sphere, the sieve channels are able to be replaced by a long weir. It is helpful to accelerate the transport process across the sieve channel and enhance the tolerance of clogging around cross section. How to design

the length of the weir and what will be happened for the deformable components? What is the advantage of the multi-level filter based on long weir compared with the pillars?

Droplets in micro channels is a hot topic recently[229]. If the inlet flow is droplets rather than continuous flow, the length of the sieve channel is considerable comparing with the scale of droplets. Thus the angle effect on connection could be observed in angular H shaped channels. So it is a potential improvement of micro- or nano- filters based on H shaped channels. Hence the effects of droplet flow should be studied.

List of References

1. Lee, K.K. and C.H. Ahn, *A new on-chip whole blood/plasma separator driven by asymmetric capillary forces.* Lab on a Chip, 2013. **13**(16): p. 3261-3267.
2. Yada, S., et al., *Isolation and characterization of two groups of novel marine bacteria producing violacein.* Mar Biotechnol (NY), 2008. **10**(2): p. 128-32.
3. Washizu, M., *Electrostatic actuation of liquid droplets for micro-reactor applications.* Industry Applications, IEEE Transactions on, 1998. **34**(4): p. 732-737.
4. de la Escosura-Muniz, A. and A. Merkoci, *A Nanochannel/Nanoparticle-Based Filtering and Sensing Platform for Direct Detection of a Cancer Biomarker in Blood.* Small, 2011. **7**(5): p. 675-682.
5. Yamada, M., et al., *Rapid Quantification of Disease-Marker Proteins Using Continuous-Flow Immunoseparation in a Nanosieve Fluidic Device.* Analytical Chemistry, 2009. **81**(16): p. 7067-7074.
6. Yao, T., et al., *Enhancement of surface plasmon resonance signals using a MIP/GNPs/rGO nano-hybrid film for the rapid detection of ractopamine.* Biosensors and Bioelectronics, 2016. **75**: p. 96-100.
7. Mei, J.V., et al., *Use of filter paper for the collection and analysis of human whole blood specimens.* The Journal of nutrition, 2001. **131**(5): p. 1631S-1636S.
8. Xu, P., C. Bellona, and J.E. Drewes, *Fouling of nanofiltration and reverse osmosis membranes during municipal wastewater reclamation: membrane autopsy results from pilot-scale investigations.* Journal of Membrane Science, 2010. **353**(1): p. 111-121.
9. Laursen, I., et al., *Second‐generation nanofiltered plasma‐derived mannan‐binding lectin product: process and characteristics.* Vox sanguinis, 2007. **92**(4): p. 338-350.
10. Vijay, Y., et al., *Nanofilter for hydrogen purification.* International journal of hydrogen energy, 2003. **28**(9): p. 1015-1018.
11. Ralhan, R., et al., *Discovery and verification of head-and-neck cancer biomarkers by differential protein expression analysis using iTRAQ labeling, multidimensional liquid chromatography, and tandem mass spectrometry.* Molecular & Cellular Proteomics, 2008. **7**(6): p. 1162-1173.
12. Ji, H.M., et al., *Silicon-based microfilters for whole blood cell separation.* Biomedical microdevices, 2008. **10**(2): p. 251-257.
13. Watanabe, H. and H. Rikumaru, *Using non-woven fabric filter*. 1987, Google Patents.
14. Giddings, J.C., *Field-flow fractionation: analysis of macromolecular, colloidal, and particulate materials.* Science, 1993. **260**(5113): p. 1456-1465.
15. Kim, W.-S., et al., *Size determination of diesel soot particles using flow and sedimentation field-flow fractionation.* Analytical chemistry, 1999. **71**(15): p. 3265-3272.
16. Yang, J., et al., *Cell separation on microfabricated electrodes using dielectrophoretic/gravitational field-flow fractionation.* Analytical chemistry, 1999. **71**(5): p. 911-918.

17. Loeschner, K., et al., *Detection and characterization of silver nanoparticles in chicken meat by asymmetric flow field flow fractionation with detection by conventional or single particle ICP-MS.* Analytical and bioanalytical chemistry, 2013. **405**(25): p. 8185-8195.
18. Barahona, F., et al., *Simultaneous determination of size and quantification of silica nanoparticles by asymmetric flow field-flow fractionation coupled to ICPMS using silica nanoparticles standards.* Analytical chemistry, 2015. **87**(5): p. 3039-3047.
19. Giddings, J.C., *A system based on split-flow lateral-transport thin (SPLITT) separation cells for rapid and continuous particle fractionation.* Separation Science and Technology, 1985. **20**(9-10): p. 749-768.
20. Pamme, N., *Continuous flow separations in microfluidic devices.* Lab on a Chip, 2007. **7**(12): p. 1644-1659.
21. Jiang, Y., A. Kummerow, and M. Hansen, *Preparative particle separation by continuous SPLITT fractionation.* Journal of Microcolumn Separations, 1997. **9**(4): p. 261-273.
22. Small, H., *Hydrodynamic chromatography a technique for size analysis of colloidal particles.* Journal of colloid and interface science, 1974. **48**(1): p. 147-161.
23. Chmela, E., et al., *A chip system for size separation of macromolecules and particles by hydrodynamic chromatography.* Analytical chemistry, 2002. **74**(14): p. 3470-3475.
24. Gardeniers, H. and A.V. Den Berg, *Micro-and nanofluidic devices for environmental and biomedical applications.* International Journal of Environmental Analytical Chemistry, 2004. **84**(11): p. 809-819.
25. Silebi, C. and J. DosRamos, *Separation of submicrometer particles by capillary hydrodynamic fractionation (CHDF).* Journal of colloid and interface science, 1989. **130**(1): p. 14-24.
26. Miller, C., et al., *Characterization of miniemulsion droplet size and stability using capillary hydrodynamic fractionation.* Journal of colloid and interface science, 1994. **162**(1): p. 11-18.
27. DosRamos, J.G. *Recent developments on resolution and applicability of capillary hydrodynamic fractionation*. in *ACS SYMPOSIUM SERIES*. 2004: Washington, DC; American Chemical Society; 1999.
28. Clementi, L.A., et al., *Capillary hydrodynamic fractionation of hydrophobic colloids: Errors in the estimated particle size distribution.* Particuology, 2014. **17**: p. 97-105.
29. Svedberg, T. and H. Rinde, *The ultra-centrifuge, a new instrument for the determination of size and distribution of size of particle in amicroscopic colloids.* Journal of the American Chemical Society, 1924. **46**(12): p. 2677-2693.
30. Schachman, H.K., *Ultracentrifugation in biochemistry*. 2013: Elsevier.
31. Schoch, R.B., J.Y. Han, and P. Renaud, *Transport phenomena in nanofluidics.* Reviews of Modern Physics, 2008. **80**(3): p. 839-883.
32. Giddings, J.C., F. Yang, and M.N. Myers, *Flow-field-flow fractionation: a versatile new separation method.* Science, 1976. **193**(4259): p. 1244-1245.
33. Vickrey, T.M. and J.A. Garcia-Ramirez, *Magnetic field-flow fractionation: theoretical basis.* Separation Science and Technology, 1980. **15**(6): p. 1297-1304.
34. Müller, D., et al., *Nanoparticle separation with a miniaturized asymmetrical flow field-flow fractionation cartridge.* Frontiers in chemistry, 2015. **3**.
35. Gossett, D.R., et al., *Label-free cell separation and sorting in microfluidic systems.* Analytical and bioanalytical chemistry, 2010. **397**(8): p. 3249-3267.

36. Lenshof, A. and T. Laurell, *Continuous separation of cells and particles in microfluidic systems.* Chemical Society Reviews, 2010. **39**(3): p. 1203-1217.
37. Provder, T., *Particle size distribution II: assessment and characterization*. 1991: American Chemical Society.
38. Mullins, M.E. and C. Orr, *Particle sizing by capillary hydrodynamic chromatography.* International Journal of Multiphase Flow, 1979. **5**(1): p. 79-85.
39. Noel, R.J., et al., *Capillary hydrodynamic chromatography.* Journal of Chromatography A, 1978. **166**(2): p. 373-382.
40. Svedberg, T. and J.B. Nichols, *Determination of size and distribution of size of particle by centrifugal methods.* Journal of the American Chemical Society, 1923. **45**(12): p. 2910-2917.
41. Ünlü, M., M.E. Morgan, and J.S. Minden, *Difference gel electrophoresis. A single gel method for detecting changes in protein extracts.* Electrophoresis, 1997. **18**(11): p. 2071-2077.
42. Schägger, H. and G. von Jagow, *Blue native electrophoresis for isolation of membrane protein complexes in enzymatically active form.* Analytical biochemistry, 1991. **199**(2): p. 223-231.
43. Polikarpov, N., et al., *Dendritic glycopolymers as dynamic and covalent coating in capillary electrophoresis: View on protein separation processes and detection of nanogram-scaled albumin in biological samples.* Journal of Chromatography A, 2015. **1378**: p. 65-73.
44. Zhu, Z., J.J. Lu, and S. Liu, *Protein separation by capillary gel electrophoresis: A review.* Analytica chimica acta, 2012. **709**: p. 21-31.
45. Li, W., et al., *Single protein molecule detection by glass nanopores.* ACS nano, 2013. **7**(5): p. 4129-4134.
46. Pikal, M.J., *The role of electroosmotic flow in transdermal iontophoresis.* Advanced drug delivery reviews, 1992. **9**(2): p. 201-237.
47. Fu, J.P., et al., *A patterned anisotropic nanofluidic sieving structure for continuous-flow separation of DNA and proteins.* Nature Nanotechnology, 2007. **2**(2): p. 121-128.
48. Geng, Z., et al., *Continuous blood separation utilizing spiral filtration microchannel with gradually varied width and micro-pillar array.* Sensors and Actuators B: Chemical, 2013. **180**: p. 122-129.
49. Zhu, L., et al., *Filter-based microfluidic device as a platform for immunofluorescent assay of microbial cells.* Lab on a Chip, 2004. **4**(4): p. 337-341.
50. Yuen, P.K., et al., *Microchip module for blood sample preparation and nucleic acid amplification reactions.* Genome Research, 2001. **11**(3): p. 405-412.
51. Wilding, P., et al., *Integrated cell isolation and polymerase chain reaction analysis using silicon microfilter chambers.* Analytical biochemistry, 1998. **257**(2): p. 95-100.
52. Andersson, H., et al., *Micromachined flow-through filter-chamber for chemical reactions on beads.* Sensors and Actuators B: Chemical, 2000. **67**(1): p. 203-208.
53. Andersson, H., W. van der Wijngaart, and G. Stemme, *Micromachined filter-chamber array with passive valves for biochemical assays on beads.* Electrophoresis, 2001. **22**(2): p. 249-257.
54. Denhardt, D.T., *A membrane-filter technique for the detection of complementary DNA.* Biochemical and biophysical research communications, 1966. **23**(5): p. 641-646.

55. Guell, C., P. Czekaj, and R.H. Davis, *Microfiltration of protein mixtures and the effects of yeast on membrane fouling.* Journal of Membrane Science, 1999. **155**(1): p. 113-122.
56. Yamada, M., M. Nakashima, and M. Seki, *Pinched flow fractionation: continuous size separation of particles utilizing a laminar flow profile in a pinched microchannel.* Analytical chemistry, 2004. **76**(18): p. 5465-5471.
57. Lu, X. and X. Xuan, *Continuous microfluidic particle separation via elasto-inertial pinched flow fractionation (eiPFF).* Analytical chemistry, 2015.
58. Austin, R.H., *Continuous separation of biomolecules by the laterally asymmetric diffusion array with out-of-plane sample injection.* Electrophoresis, 2002. **23**(20): p. 3496-3503.
59. Jia, Y., Y. Ren, and H. Jiang, *Continuous dielectrophoretic particle separation using a microfluidic device with 3 - D electrodes and vaulted obstacles.* Electrophoresis, 2015.
60. Huang, L.R., et al., *Continuous particle separation through deterministic lateral displacement.* Science, 2004. **304**(5673): p. 987-990.
61. Inglis, D.W., et al., *Critical particle size for fractionation by deterministic lateral displacement.* Lab on a Chip, 2006. **6**(5): p. 655-658.
62. Yamada, M. and M. Seki, *Hydrodynamic filtration for on-chip particle concentration and classification utilizing microfluidics.* Lab on a Chip, 2005. **5**(11): p. 1233-1239.
63. Sugaya, S., M. Yamada, and M. Seki, *Observation of nonspherical particle behaviors for continuous shape-based separation using hydrodynamic filtration.* Biomicrofluidics, 2011. **5**(2): p. 024103.
64. Russom, A., et al., *Differential inertial focusing of particles in curved low-aspect-ratio microchannels.* New journal of physics, 2009. **11**(7): p. 075025.
65. Kuntaegowdanahalli, S.S., et al., *Inertial microfluidics for continuous particle separation in spiral microchannels.* Lab on a Chip, 2009. **9**(20): p. 2973-2980.
66. Doh, I. and Y.-H. Cho, *A continuous cell separation chip using hydrodynamic dielectrophoresis (DEP) process.* Sensors and Actuators A: Physical, 2005. **121**(1): p. 59-65.
67. Pamme, N. and C. Wilhelm, *Continuous sorting of magnetic cells via on-chip free-flow magnetophoresis.* Lab on a Chip, 2006. **6**(8): p. 974-980.
68. Coakley, W.T., *Ultrasonic separations in analytical biotechnology.* Trends in biotechnology, 1997. **15**(12): p. 506-511.
69. Fu, J., et al., *A patterned anisotropic nanofluidic sieving structure for continuous-flow separation of DNA and proteins.* Nature nanotechnology, 2007. **2**(2): p. 121-128.
70. Fu, J. and H.J. Caulfield, *Designing spectral sensitivity curves for use with Artificial Color.* Pattern Recognition, 2007. **40**(8): p. 2251-2260.
71. Banerjee, S., S. Mondal, and S. De, *Gel controlling dead-end membrane filtration: Theory revisited (vol 99, pg 77, 2012).* Separation and Purification Technology, 2013. **109**: p. 148-148.
72. Qu, P., G. Gesan-Guiziou, and A. Bouchoux, *Dead-end filtration of sponge-like colloids: The case of casein micelle.* Journal of Membrane Science, 2012. **417**: p. 10-19.
73. Li, X. and J. Li, *Dead-End Filtration*, in *Encyclopedia of Membranes*, E. Drioli and L. Giorno, Editors. 2015, Springer Berlin Heidelberg: Berlin, Heidelberg. p. 1-3.

74. Bacchin, P., M. Meireles, and P. Aimar, *Modelling of filtration: from the polarised layer to deposit formation and compaction.* Desalination, 2002. **145**(1-3): p. 139-146.
75. Rajha, H.N., et al., *Effect of alternative physical pretreatments (pulsed electric field, high voltage electrical discharges and ultrasound) on the dead-end ultrafiltration of vine-shoot extracts.* Separation and Purification Technology, 2015. **146**: p. 243-251.
76. Simon, A., et al., *Low-frequency ultrasound to improve dead-end ultrafiltration performance.* Separation Science and Technology, 2000. **35**(16): p. 2619-2637.
77. Iritani, E., Y. Mukai, and Y. Kiyotomo, *Effects of electric field on dynamic behaviors of dead-end inclined and downward ultrafiltration of protein solutions.* Journal of Membrane Science, 2000. **164**(1): p. 51-57.
78. Liu, D., et al., *Intensification of polyphenols extraction from grape seeds by high voltage electrical discharges and extract concentration by dead-end ultrafiltration.* Separation and Purification Technology, 2011. **81**(2): p. 134-140.
79. Benkahla, Y., et al., *Cake growth mechanism in cross-flow microfiltration of mineral suspensions.* Journal of Membrane Science, 1995. **98**(1): p. 107-117.
80. Lu, W.M. and K.J. Hwang, *Cake formation in 2 - D cross - flow filtration.* AIChE Journal, 1995. **41**(6): p. 1443-1455.
81. Pan, Y., et al., *Prediction of particle deposition and layer growth in the preparation of a dynamic membrane with cross-flow microfiltration.* Rsc Advances, 2015. **5**(108): p. 89015-89024.
82. Seminario, L., et al., *Pore blocking and permeability reduction in cross-flow microfiltration.* Journal of Membrane Science, 2002. **209**(1): p. 121-142.
83. Kyllönen, H., et al., *Experimental aspects of ultrasonically enhanced cross-flow membrane filtration of industrial wastewater.* Ultrasonics sonochemistry, 2006. **13**(4): p. 295-302.
84. Bowen, W.R. and H.A. Sabuni, *Pulsed electrokinetic cleaning of cellulose nitrate microfiltration membranes.* Industrial & engineering chemistry research, 1992. **31**(2): p. 515-523.
85. Andersson, H., et al., *Hydrophobic valves of plasma deposited octafluorocyclobutane in DRIE channels.* Sensors and Actuators B: Chemical, 2001. **75**(1): p. 136-141.
86. Duke, T.A.J. and R.H. Austin, *Microfabricated Sieve for the Continuous Sorting of Macromolecules.* Physical review letters, 1998. **80**(7): p. 1552-1555.
87. Segre, G. and A. Silberberg, *Behavior of macroscopic rigid spheres in Poiseuille flow.* J. Fluid Mech., 1962. **14**.
88. Di Carlo, D., et al., *Continuous inertial focusing, ordering, and separation of particles in microchannels.* Proceedings of the National Academy of Sciences, 2007. **104**(48): p. 18892-18897.
89. Morijiri, T., et al., *Microfluidic counterflow centrifugal elutriation system for sedimentation-based cell separation.* Microfluidics and nanofluidics, 2013. **14**(6): p. 1049-1057.
90. Masaeli, M., et al., *Continuous inertial focusing and separation of particles by shape.* Physical Review X, 2012. **2**(3): p. 031017.
91. Alvankarian, J., A. Bahadorimehr, and B.Y. Majlis, *A pillar-based microfilter for isolation of white blood cells on elastomeric substrate.* Biomicrofluidics, 2013. **7**(1): p. 014102.

92. Yang, S., A. Ündar, and J.D. Zahn, *A microfluidic device for continuous, real time blood plasma separation.* Lab on a Chip, 2006. **6**(7): p. 871-880.
93. Lenshof, A., C. Magnusson, and T. Laurell, *Acoustofluidics 8: Applications of acoustophoresis in continuous flow microsystems.* Lab on a Chip, 2012. **12**(7): p. 1210-1223.
94. Steffen, D. and R.A. Weinberg, *The integrated genome of murine leukemia virus.* Cell, 1978. **15**(3): p. 1003-1010.
95. Hosokawa, K., M. Omata, and M. Maeda, *Immunoassay on a power-free microchip with laminar flow-assisted dendritic amplification.* Analytical Chemistry, 2007. **79**(15): p. 6000-4.
96. Inoue, A., et al., *I-shaped microchannel array chip for parallel electrophoretic analyses.* Analytical Chemistry, 2007. **79**(5): p. 2168-73.
97. Guo, T.-Y., et al., *Chitosan beads as molecularly imprinted polymer matrix for selective separation of proteins.* Biomaterials, 2005. **26**(28): p. 5737-5745.
98. Pappenheimer, J., E. Renkin, and L. Borrero, *Filtration, diffusion and molecular sieving through peripheral capillary membranes.* Am. J. Physiol, 1951. **167**(13): p. 2578.
99. Renkin, E.M., *Filtration, diffusion, and molecular sieving through porous cellulose membranes.* The Journal of general physiology, 1954. **38**(2): p. 225-243.
100. Deen, W., *Hindered transport of large molecules in liquid ‐filled pores.* AIChE Journal, 1987. **33**(9): p. 1409-1425.
101. Han, J., J. Fu, and R.B. Schoch, *Molecular sieving using nanofilters: past, present and future.* Lab on a Chip, 2008. **8**(1): p. 23-33.
102. Fu, J., P. Mao, and J. Han, *Nanofilter array chip for fast gel-free biomolecule separation.* Applied Physics Letters, 2005. **87**(26): p. 263902.
103. Fu, J., J. Yoo, and J. Han, *Molecular sieving in periodic free-energy landscapes created by patterned nanofilter arrays.* Physical review letters, 2006. **97**(1): p. 018103.
104. Diehl, F., K.W. Kinzler, and B. Vogelstein, *Single-molecule PCR on microparticles in water-in-oil emulsions*. 2014, Google Patents.
105. Yoon, S.-H., et al., *Effect of calcium ion on the fouling of nanofilter by humic acid in drinking water production.* Water Research, 1998. **32**(7): p. 2180-2186.
106. Hillman, R.S. and I. Gibbons, *Blood separation device comprising a filter and a capillary flow pathway exiting the filter*. 1992, Google Patents.
107. Chung, K.H., et al., *Magnetically-actuated blood filter unit attachable to pre-made biochips.* Lab on a Chip, 2012. **12**(18): p. 3272-3276.
108. Tayyaba, S., M.W. Ashraf, and N. Afzulpurkar, *Design, Simulation, and Fabrication of Microneedles and a Blood Filter for Use in a Hemofiltration System.* Automation Science and Engineering, IEEE Transactions on, 2013. **10**(2): p. 252-266.
109. Ng, E., et al., *Multi-Dimensional Nanostructures for Microfluidic Screening of Biomarkers: From Molecular Separation to Cancer Cell Detection.* Annals of Biomedical Engineering, 2015: p. 1-16.
110. Rammer, P., et al., *BAMLET activates a lysosomal cell death program in cancer cells.* Molecular cancer therapeutics, 2010. **9**(1): p. 24-32.
111. Viswanathan, S., et al., *Graphene–protein field effect biosensors: glucose sensing.* Materials Today, 2015.
112. Jian, L., *APPLICATION OF NANOFILTER MEMBRANE IN WATER TREATMENT [J].* Environmental Engineering, 2001. **1**: p. 006.

113. Yuan, F., et al., *Vascular permeability in a human tumor xenograft: molecular size dependence and cutoff size.* Cancer research, 1995. **55**(17): p. 3752-3756.
114. Skalak, R. and P. Branemark, *Deformation of red blood cells in capillaries.* Science, 1969. **164**(3880): p. 717-719.
115. Bessey, O.A., O.H. Lowry, and M.J. Brock, *The quantitative determination of ascorbic acid in small amounts of white blood cells and platelets.* Journal of Biological Chemistry, 1947. **168**(1): p. 197-205.
116. Chen, C., et al., *Microfluidic isolation and transcriptome analysis of serum microvesicles.* Lab on a Chip, 2010. **10**(4): p. 505-511.
117. Taylor, R. and R. Krishna, *Multicomponent mass transfer*. Wiley series in chemical engineering. 1993, New York: Wiley. xxxiv, 579 p.
118. Weissberg, H.L., *Effective diffusion coefficient in porous media.* Journal of Applied Physics, 1963. **34**(9): p. 2636-2639.
119. Grathwohl, P., *Diffusion in Natural Porous Media: Contaminant Transport.* SorptionrDesorption and, 1998.
120. Constantin, P. and C. Foias, *Navier-stokes equations*. 1988: University of Chicago Press.
121. Chaturani, P. and R.P. Samy, *Pulsatile flow of Casson's fluid through stenosed arteries with applications to blood flow.* Biorheology, 1985. **23**(5): p. 499-511.
122. Tirtaatmadja, V., D.E. Dunstan, and D.V. Boger, *Rheology of dextran solutions.* Journal of Non-Newtonian Fluid Mechanics, 2001. **97**(2): p. 295-301.
123. Van Zant, P. and Chapman, *Microchip fabrication: a practical guide to semiconductor processing*. Vol. 5. 2000: McGraw-Hill New York.
124. O'Toole, M., E. Liu, and M. Chang. *Multilevel resist for photolithography utilizing an absorbing dye: simulation and experiment*. in *1981 Microlithography Conferences*. 1981: International Society for Optics and Photonics.
125. Kumar, A. and G.M. Whitesides, *Features of gold having micrometer to centimeter dimensions can be formed through a combination of stamping with an elastomeric stamp and an alkanethiol ''ink"followed by chemical etching.* Applied Physics Letters, 1993. **63**(14): p. 2002-2004.
126. Anhoj, T.A., et al., *The effect of soft bake temperature on the polymerization of SU-8 photoresist.* Journal of Micromechanics and Microengineering, 2006. **16**(9): p. 1819.
127. O'Neill, F.T. and J.T. Sheridan, *Photoresist reflow method of microlens production Part I: Background and experiments.* Optik-International Journal for Light and Electron Optics, 2002. **113**(9): p. 391-404.
128. del Campo, A. and C. Greiner, *SU-8: a photoresist for high-aspect-ratio and 3D submicron lithography.* Journal of Micromechanics and Microengineering, 2007. **17**(6): p. R81.
129. Henry, M.D., *ICP etching of silicon for micro and nanoscale devices*. 2010, California Institute of Technology.
130. Wagner, J.J. and W.W. Brandt, *DC plasma etching of silicon by sulfur hexafluoride. Mass spectrometric study of the discharge products.* Plasma Chemistry and Plasma Processing, 1981. **1**(2): p. 201-215.
131. Garrity, M.P., T.W. Peterson, and J.F. O'Hanlon, *Particle formation rates in sulfur hexafluoride plasma etching of silicon.* Journal of Vacuum Science & Technology A, 1996. **14**(2): p. 550-555.
132. Melngailis, J., *Focused ion beam technology and applications.* Journal of Vacuum Science & Technology B, 1987. **5**(2): p. 469-495.

133. Talbot, C.G., N. Richardson, and D. Masnaghetti, *Ic modification with focused ion beam system*. 1992, Google Patents.
134. Stewart, D.K., A.F. Doyle, and J.D. Casey Jr. *Focused ion beam deposition of new materials: dielectric films for device modification and mask repair, and tantalum films for x-ray mask repair*. in *SPIE's 1995 Symposium on Microlithography*. 1995: International Society for Optics and Photonics.
135. Utke, I., P. Hoffmann, and J. Melngailis, *Gas-assisted focused electron beam and ion beam processing and fabrication.* Journal of Vacuum Science & Technology B, 2008. **26**(4): p. 1197-1276.
136. Nikawa, K., *Applications of focused ion beam technique to failure analysis of very large scale integrations: A review.* Journal of Vacuum Science & Technology B, 1991. **9**(5): p. 2566-2577.
137. Krohn, V. and G. Ringo, *Ion source of high brightness using liquid metal.* Applied Physics Letters, 1975. **27**(9): p. 479-481.
138. Volkert, C.A. and A.M. Minor, *Focused ion beam microscopy and micromachining.* MRS bulletin, 2007. **32**(05): p. 389-399.
139. Davies, N., et al., *Development and experimental application of a gold liquid metal ion source.* Applied Surface Science, 2003. **203**: p. 223-227.
140. Seliger, R., et al., *A high‐intensity scanning ion probe with submicrometer spot size.* Applied Physics Letters, 1979. **34**(5): p. 310-312.
141. Miyauchi, E., et al., *Selective Si and Be implantation in GaAs using a 100 kV mass‐separating focused ion beam system with an Au–Si–Be liquid metal ion source.* Journal of Vacuum Science & Technology B, 1983. **1**(4): p. 1113-1116.
142. Matsui, S., et al., *Three-dimensional nanostructure fabrication by focused-ion-beam chemical vapor deposition.* Journal of Vacuum Science & Technology B, 2000. **18**(6): p. 3181-3184.
143. Tseng, A.A., *Recent developments in micromilling using focused ion beam technology.* Journal of Micromechanics and Microengineering, 2004. **14**(4): p. R15.
144. Phaneuf, M., *Applications of focused ion beam microscopy to materials science specimens.* Micron, 1999. **30**(3): p. 277-288.
145. Wang, V., J. Ward, and R. Seliger, *A mass‐separating focused‐ion‐beam system for maskless ion implantation.* Journal of Vacuum Science & Technology, 1981. **19**(4): p. 1158-1163.
146. Liu, C., A. Datta, and Y. Wang, *Ordered anodic alumina nanochannels on focused-ion-beam-prepatterned aluminum surfaces.* Applied Physics Letters, 2001. **78**(1): p. 120-122.
147. Masuda, H., et al., *Highly ordered nanochannel-array architecture in anodic alumina.* Applied Physics Letters, 1997. **71**(19): p. 2770-2772.
148. Vasile, M., et al., *Focused ion beam milling: depth control for three-dimensional microfabrication.* Journal of Vacuum Science & Technology B, 1997. **15**(6): p. 2350-2354.
149. Kawakatsu, T., S.-i. Nakao, and S. Kimura, *Effects of size and compressibility of suspended particles and surface pore size of membrane on flux in crossflow filtration.* Journal of Membrane Science, 1993. **81**(1): p. 173-190.
150. Chang, S., A.G. Fane, and T.D. Waite, *Analysis of constant permeate flow filtration using dead-end hollow fiber membranes.* Journal of Membrane Science, 2006. **268**(2): p. 132-141.

151. Oertel, H., *Prandtl's essentials of fluid mechanics*. 2nd ed. Applied mathematical sciences. 2003, New York: Springer. xii, 723 p.
152. Abdelall, F., et al., *Pressure drop caused by abrupt flow area changes in small channels.* Experimental Thermal and Fluid Science, 2005. **29**(4): p. 425-434.
153. Kim, M.-m. and A.L. Zydney, *Theoretical analysis of particle trajectories and sieving in a two-dimensional cross-flow filtration system.* Journal of Membrane Science, 2006. **281**(1): p. 666-675.
154. Barker, T.B., *Quality by experimental design*. Quality and reliability. 1985, New York, Milwaukee: M. Dekker; ASQC Quality Press. xiv, 384 p.
155. Cochran, W.G. and G.M. Cox, *Experimental designs*. 2d ed. A Wiley publication in applied statistics. 1957, New York,: Wiley. 611 p.
156. Goldstein, S., *Fluid mechanics in the first half of this century.* Annual Review of Fluid Mechanics, 1969. **1**(1): p. 1-29.
157. Lauga, E., M. Brenner, and H. Stone, *Microfluidics: the no-slip boundary condition*, in *Springer handbook of experimental fluid mechanics*. 2007, Springer. p. 1219-1240.
158. Tretheway, D.C. and C.D. Meinhart, *Apparent fluid slip at hydrophobic microchannel walls.* Physics of Fluids (1994-present), 2002. **14**(3): p. L9-L12.
159. Brochard, F. and P. De Gennes, *Shear-dependent slippage at a polymer/solid interface.* Langmuir, 1992. **8**(12): p. 3033-3037.
160. Craig, V.S., C. Neto, and D.R. Williams, *Shear-dependent boundary slip in an aqueous Newtonian liquid.* Physical review letters, 2001. **87**(5): p. 054504.
161. Bonaccurso, E., H.-J. Butt, and V.S. Craig, *Surface roughness and hydrodynamic boundary slip of a Newtonian fluid in a completely wetting system.* Physical review letters, 2003. **90**(14): p. 144501.
162. Tingzhao, W. and G. Yingqi, *A Review: Advances in Atomic Absorption Spectrometry and Atomic Fluorescence Spectrometry.* Analytical Laboratory, 1987: p. Z1.
163. Baruthio, F., et al., *Determination of manganese in biological materials by electrothermal atomic absorption spectrometry: a review.* Clinical chemistry, 1988. **34**(2): p. 227-234.
164. *Microfluidics Design for Manufacture Guidlines*. in *MF5 European Open Day* 2014. Cambridge, UK.
165. Bloomstein, T. and D. Ehrlich, *Stereo laser micromachining of silicon.* Applied Physics Letters, 1992. **61**(6): p. 708-710.
166. Keller, U., *Recent developments in compact ultrafast lasers.* Nature, 2003. **424**(6950): p. 831-838.
167. Herbstman, J.F. and A.J. Hunt, *High-aspect ratio nanochannel formation by single femtosecond laser pulses.* Optics express, 2010. **18**(16): p. 16840-16848.
168. Gattass, R.R. and E. Mazur, *Femtosecond laser micromachining in transparent materials.* Nature photonics, 2008. **2**(4): p. 219-225.
169. Li, Y., et al., *Three-dimensional hole drilling of silica glass from the rear surface with femtosecond laser pulses.* Optics letters, 2001. **26**(23): p. 1912-1914.
170. Grojo, D., et al., *Limitations to laser machining of silicon using femtosecond micro-Bessel beams in the infrared.* Journal of Applied Physics, 2015. **117**(15): p. 153105.
171. Stavis, S.M., E.A. Strychalski, and M. Gaitan, *Nanofluidic structures with complex three-dimensional surfaces.* Nanotechnology, 2009. **20**(16): p. 165302.

172. Kim, J., D. Joy, and S.-Y. Lee, *Controlling resist thickness and etch depth for fabrication of 3D structures in electron-beam grayscale lithography.* Microelectronic Engineering, 2007. **84**(12): p. 2859-2864.
173. Chen, Y., *Applications of nanoimprint lithography/hot embossing: a review.* Applied Physics A, 2015. **121**(2): p. 451-465.
174. Chou, S.Y., P.R. Krauss, and P.J. Renstrom, *Nanoimprint lithography.* Journal of Vacuum Science & Technology B, 1996. **14**(6): p. 4129-4133.
175. Jin, P., et al., *Replication of micro-optical elements with continuous relief by ultraviolet embossing with thiol-ene-based resist.* Applied optics, 2011. **50**(21): p. 4063-4067.
176. Yan, Y., et al., *Top‐Down Nanomechanical Machining of Three‐Dimensional Nanostructures by Atomic Force Microscopy.* Small, 2010. **6**(6): p. 724-728.
177. Liu, G.-Y., S. Xu, and Y. Qian, *Nanofabrication of self-assembled monolayers using scanning probe lithography.* Accounts of Chemical Research, 2000. **33**(7): p. 457-466.
178. Piner, R.D., et al., *"Dip-pen" nanolithography.* Science, 1999. **283**(5402): p. 661-663.
179. Krämer, S., R.R. Fuierer, and C.B. Gorman, *Scanning probe lithography using self-assembled monolayers.* Chemical Reviews, 2003. **103**(11): p. 4367-4418.
180. Schleunitz, A. and H. Schift, *Fabrication of 3D nanoimprint stamps with continuous reliefs using dose-modulated electron beam lithography and thermal reflow.* Journal of Micromechanics and Microengineering, 2010. **20**(9): p. 095002.
181. Morita, T., et al., *Three-dimensional nanoimprint mold fabrication by focused-ion-beam chemical vapor deposition.* Japanese journal of applied physics, 2003. **42**(6S): p. 3874.
182. Kuo, C.W., et al., *Fabrication of Large‐Area Periodic Nanopillar Arrays for Nanoimprint Lithography Using Polymer Colloid Masks.* Advanced Materials, 2003. **15**(13): p. 1065-1068.
183. Durst, F. and T. Loy, *Investigations of laminar flow in a pipe with sudden contraction of cross sectional area.* Computers & fluids, 1985. **13**(1): p. 15-36.
184. Bullen, P., et al., *The determination of pipe contraction pressure loss coefficients for incompressible turbulent flow.* International journal of heat and fluid flow, 1987. **8**(2): p. 111-118.
185. Pike, D.J., et al., *Flow Cell Design for Effective Biosensing.* Sensors, 2013. **13**(1): p. 58-70.
186. Durst, F., A. Melling, and J. Whitelaw, *Low Reynolds number flow over a plane symmetric sudden expansion.* Journal of Fluid Mechanics, 1974. **64**(01): p. 111-128.
187. Hawa, T. and Z. Rusak, *The dynamics of a laminar flow in a symmetric channel with a sudden expansion.* Journal of Fluid Mechanics, 2001. **436**: p. 283-320.
188. Fearn, R., T. Mullin, and K. Cliffe, *Nonlinear flow phenomena in a symmetric sudden expansion.* Journal of Fluid Mechanics, 1990. **211**: p. 595-608.
189. Durst, F., J. Pereira, and C. Tropea, *The plane symmetric sudden-expansion flow at low Reynolds numbers.* Journal of Fluid Mechanics, 1993. **248**: p. 567-581.
190. Hawkes, J.J. and S. Radel, *Acoustofluidics 22: Multi-wavelength resonators, applications and considerations.* Lab on a Chip, 2013. **13**(4): p. 610-627.
191. Biswas, G., M. Breuer, and F. Durst, *Backward-Facing Step Flows for Various Expansion Ratios at Low and Moderate Reynolds Numbers.* Journal of Fluids Engineering, 2004. **126**(3): p. 362-374.

192. Rocha, G.N., R.J. Poole, and P.J. Oliveira, *Bifurcation phenomena in viscoelastic flows through a symmetric 1 : 4 expansion.* Journal of Non-Newtonian Fluid Mechanics, 2007. **141**(1): p. 1-17.
193. Rocha, G. and P. Oliveira, *Viscoelastic Flows in 1-to-4 Sudden Expansions.* IBEREO'04 Encontro Ibérico de Reologia: p. 403-408.
194. Erhard, P., et al., *Prandtl-essentials of fluid mechanics*. Vol. 158. 2010: Springer Science & Business Media.
195. Stone, H.A. and S. Kim, *Microfluidics: basic issues, applications, and challenges.* AIChE Journal, 2001. **47**(6): p. 1250-1254.
196. Squires, T.M. and S.R. Quake, *Microfluidics: Fluid physics at the nanoliter scale.* Reviews of modern physics, 2005. **77**(3): p. 977-1026.
197. Mills, R., *Numerical solutions of viscous flow through a pipe orifice at low Reynolds numbers.* Journal of Mechanical Engineering Science, 1968. **10**(2): p. 133-140.
198. Miranda, A.I., P. Oliveira, and F.T.d. Pinho, *Steady and unsteady laminar flows of Newtonian and generalized Newtonian fluids in a planar T ‐ junction.* International journal for numerical methods in fluids, 2008. **57**(3): p. 295-328.
199. Kazakidi, A., et al., *Effect of reverse flow on the pattern of wall shear stress near arterial branches.* Journal of The Royal Society Interface, 2011. **8**(64): p. 1594-1603.
200. Lin, C.-H., L.-M. Fu, and Y.-S. Chien, *Microfluidic T-Form Mixer Utilizing Switching Electroosmotic Flow.* Analytical chemistry, 2004. **76**(18): p. 5265-5272.
201. Jäggi, R.D., R. Sandoz, and C.S. Effenhauser, *Microfluidic depletion of red blood cells from whole blood in high-aspect-ratio microchannels.* Microfluidics and nanofluidics, 2007. **3**(1): p. 47-53.
202. Novo, P., et al., *High spatial and temporal resolution cell manipulation techniques in microchannels.* Analyst, 2016. **141**(6): p. 1888-1905.
203. Mizuno, M., et al., *Magnetophoresis-Integrated Hydrodynamic Filtration System for Size- and Surface Marker-Based Two-Dimensional Cell Sorting.* Analytical chemistry, 2013. **85**(16): p. 7666-7673.
204. Khabiry, M. and N. Jalili, *A Microfluidic Platform Containing Sidewall Microgrooves for Cell Positioning and Trapping.* 2015.
205. Østergaard, S., et al., *A novel approach to the automation of clinical chemistry by controlled manipulation of magnetic particles.* Journal of Magnetism and Magnetic Materials, 1999. **194**(1–3): p. 156-162.
206. Ji, Y., K. Yuan, and J. Chung, *Numerical simulation of wall roughness on gaseous flow and heat transfer in a microchannel.* International Journal of Heat and Mass Transfer, 2006. **49**(7): p. 1329-1339.
207. Cao, B.-Y., M. Chen, and Z.-Y. Guo, *Effect of surface roughness on gas flow in microchannels by molecular dynamics simulation.* International Journal of Engineering Science, 2006. **44**(13): p. 927-937.
208. Kunert, C. and J. Harting, *Roughness induced boundary slip in microchannel flows.* Physical review letters, 2007. **99**(17): p. 176001.
209. Lilly, T., et al., *Numerical and experimental investigation of microchannel flows with rough surfaces.* Physics of Fluids (1994-present), 2007. **19**(10): p. 106101.
210. Banaeiyan, A.A., et al., *Hydrodynamic Cell Trapping for High Throughput Single-Cell Applications.* Micromachines, 2013. **4**(4): p. 414-430.
211. Rushton, A. and V.M. Matsis, *Studies of Constant Rate Filtration in Dead-End and Cross-Flow Modes.* Filtration & Separation, 1994. **31**(6): p. 643-646.

212. Grangeon, A., et al., *Cross-flow filter membrane and method of manufacturing it*. 2004, Google Patents.
213. Balannec, B., et al., *Comparative study of different nanofiltration and reverse osmosis membranes for dairy effluent treatment by dead-end filtration.* Separation and Purification Technology, 2005. **42**(2): p. 195-200.
214. Koenders, M.A., E. Liebhart, and R.J. Wakeman, *Dead-end filtration with torsional shear: Experimental findings and theoretical analysis.* Chemical Engineering Research & Design, 2001. **79**(A3): p. 249-259.
215. Shamsuddin, N., D.B. Das, and V.M. Starov, *Filtration of natural organic matter using ultrafiltration membranes for drinking water purposes: Circular cross-flow compared with stirred dead end flow.* Chemical Engineering Journal, 2015. **276**: p. 331-339.
216. Sethu, P., A. Sin, and M. Toner, *Microfluidic diffusive filter for apheresis (leukapheresis).* Lab on a Chip, 2006. **6**(1): p. 83-89.
217. Choi, S. and J.-K. Park, *Continuous hydrophoretic separation and sizing of microparticles using slanted obstacles in a microchannel.* Lab on a Chip, 2007. **7**(7): p. 890-897.
218. Huang, L.R., et al., *A DNA prism for high-speed continuous fractionation of large DNA molecules.* Nature biotechnology, 2002. **20**(10): p. 1048-1051.
219. Zhang, C.-X. and A. Manz, *High-speed free-flow electrophoresis on chip.* Analytical chemistry, 2003. **75**(21): p. 5759-5766.
220. Xu, Y., et al., *Sub-second isoelectric focusing in free flow using a microfluidic device.* Lab on a Chip, 2003. **3**(4): p. 224-227.
221. Petersson, F., et al., *Continuous separation of lipid particles from erythrocytes by means of laminar flow and acoustic standing wave forces.* Lab on a Chip, 2005. **5**(1): p. 20-22.
222. MacDonald, M., G. Spalding, and K. Dholakia, *Microfluidic sorting in an optical lattice.* Nature, 2003. **426**(6965): p. 421-424.
223. Huh, D., et al., *Gravity-driven microfluidic particle sorting device with hydrodynamic separation amplification.* Analytical chemistry, 2007. **79**(4): p. 1369-1376.
224. Galea, T.M. and P. Attard, *Molecular dynamics study of the effect of atomic roughness on the slip length at the fluid-solid boundary during shear flow.* Langmuir, 2004. **20**(8): p. 3477-3482.
225. Zhu, Y. and S. Granick, *Limits of the hydrodynamic no-slip boundary condition.* Physical review letters, 2002. **88**(10): p. 106102.
226. De Gennes, P.-G., *Wetting: statics and dynamics.* Reviews of modern physics, 1985. **57**(3): p. 827.
227. De Gennes, P.-G., F. Brochard-Wyart, and D. Quéré, *Capillarity and wetting phenomena: drops, bubbles, pearls, waves*. 2013: Springer Science & Business Media.
228. Ruckenstein, E. and N. Churaev, *A possible hydrodynamic origin of the forces of hydrophobic attraction.* Journal of colloid and interface science, 1991. **147**(2): p. 535-538.
229. Teh, S.-Y., et al., *Droplet microfluidics.* Lab on a Chip, 2008. **8**(2): p. 198-220.